Applications of Quantum Electro-Optic Control and Squeezed Light

Ping Koy Lam

B. Sc., University of Auckland, 1991.
M. Sc., The Australian National University, 1996.

A thesis submitted for the degree of
Doctor of Philosophy
of the Australian National University

December 1998

To

PP, MM and FF.

Declaration

This thesis is an account of research undertaken between May 1995 and November 1998 in *the Department of Physics, Faculty of Science, Australian National University, Canberra, Australia* and *Laser Zentrum Hannover, Hannover, Germany.*

Except where acknowledged in the customary manner, the material presented in this thesis is, to the best of my knowledge, original and has not been submitted in whole or part for a degree in any university.

Ping Koy Lam
December, 1998

Acknowledgements

I sincerely thank my supervisor Prof. Hans -A. Bachor, Prof. David E. McClelland and Prof. Craig M. Savage for their continual support in the research work undertaken in this thesis. Their assistance and advice in many situations throughout the course of my studies are invaluable to the completion of this thesis.

I have been gifted with the opportunities of working with many talented colleagues and lab partners. I am grateful to Dr. Andrew G. White, Dr. Timothy C. Ralph, Dr. Jiangrui Gao, Dr. Matthew B. Taubman, Elanor H. Huntington, Dr. Charles C. Harb, Dr. Malcolm B. Gray, Daniel A. Shaddock, Jinwei Wu, and Ben C. Buchler for sharing their expertise with me. The running and execution of a complicated experiment is most of the time too difficult for an individual alone to handle. The word "we" used in this thesis is therefore by no means only a convention. Specifically, in part II of this thesis, I used we to include Dr. Andrew G. White, Dr. Jiangrui Gao, Dr. Matthew B. Taubman, Markus Bode and Ben C. Buchler. In part III, "we" changes its definition to Dr. Timothy C. Ralph and Elanor H. Huntington.

In spite of the short stay at the Laser Zentrum Hannover in Germany, I am glad to have earned the acquaintance of Dr. Ingo Freitag and Markus Bode. Their generosity in sharing knowledge as well as friendship has made my working experience in the Zentrum both fun and lucrative.

The success of an experiment also depends a lot on its apparatus and equipments. I am indeed privileged to have the technical supports from Brett Brown, Paul McNamara, Russell Koehne and Joe Harb. All of them have made the design and setup of the experiment a great deal smoother.

As an international PhD student who had to faced many administrative hurdles, I thank Felicity Davey, Jennifer Wilcoxon and Zeta Hall for their patience and advice in always providing the best solutions. Again, I owe the opportunity of my PhD studies to Prof. Hans -A. Bachor for overcoming the initial tussle with the system.

Without friends to see me through, my years of postgraduate studies would have been unbearable. I thank Dr. Andrew G. White, Dr. Joseph J. Hope, Dr. Glenn M. Moy, Dr. Charles C. Harb, Dr. Timothy C. Ralph and Joseph B. K. Tan for providing the occasional distractions from the, at times, monotonous lab work and tedious calculations.

To me the biggest sacrifice made for this PhD studies is the time I did not get to spend with my family. I thank my Mum, Mum-in-law, Chin Koi, Yoong Koy, Fui Foon and Koon Chye for their understanding of, and encouragement on, my aim to become a scientist. It is their support which propel me onwards in the hardest of times. Knowing that all of them are always there, although most of the times τ km away, where $\tau > 5000$ km, is still enough to make my life happier. I also thank my many nephews and nieces who provided so much joy during my short visits home.

Finally, I thank my wife Poh Ping, for her loving company and for sharing the stress and hardship faced by an overworked PhD student.

Abstract

In this thesis, we report the observations of optical squeezing from second harmonic generation (SHG), optical parametric oscillation (OPO) and optical parametric amplification (OPA). Demonstrations and proposals of applications involving the squeezed light and electro-optic control loops are presented.

In our SHG setup, we report the observation of 2.1 dB of intensity squeezing on the second harmonic (SH) output. Investigations into the system show that the squeezing performance of a SHG system is critically affected by the pump noise and a modular theory of noise propagation is developed to describe and quantify this effect. Our experimental data has also shown that in a low-loss SHG system, intra-cavity nondegenerate OPO modes can simultaneously occur. This competition of nonlinear processes leads to the optical clamping of the SH output power and in general can degrade the SH squeezing. We model this competition and show that it imposes a limit to the observable SH squeezing. Proposals for minimizing the effect of competition are presented.

In our OPO setup, we report the observation of 7.1 dB of vacuum squeezing and more than 4 dB of intensity squeezing when the OPO is operating as a parametric amplifier. We present the design criteria and discuss the limits to the observable squeezing from the OPO. We attribute the large amount of squeezing obtained in our experiment to the high escape efficiency of the OPO. The effect of phase jitter on the squeezing of the vacuum state is modeled.

The quantum noise performance of an electro-optic feedforward control loop is investigated. With classical coherent inputs, we demonstrate that vacuum fluctuations introduced at the beam splitter of the control loop can be completely cancelled by an optimum amount of positive feedforward. The cancellation of vacuum fluctuations leads to the possibility of noiseless signal amplification with the feedforward loop. Comparison shows that the feedforward amplifier is superior or at least comparable in performance with other noiseless amplification schemes. When combined with an injection-locked non-planar ring Nd:YAG laser, we demonstrate that signal and power amplifications can both be noiseless and independently variable.

Using squeezed inputs to the feedforward control loop, we demonstrate that information carrying squeezed states can be made robust to large downstream transmission losses via a noiseless signal amplification. We show that the combination of a squeezed vacuum meter input and a feedforward loop is a quantum nondemolition (QND) device, with the feedforward loop providing an additional improvement on the transfer of signal. In general, the use of a squeezed vacuum meter input and an electro-optic feedforward loop can provide pre- and post- enhancements to many existing QND schemes.

Finally, we proposed that the quantum teleportation of a continuous-wave optical state can be achieved using a pair of phase and amplitude electro-optic feedforward loops with two orthogonal quadrature squeezed inputs. The signal transfer and quantum correlation of the teleported optical state are analysed. We show that a two dimensional diagram, similar to the QND figures of merits, can be used to quantify the performance of a teleporter.

Contents

Declaration **v**

Acknowledgements **vii**

Abstract **ix**

1 Introduction **1**
- 1.1 Overview 1
- 1.2 Publications 2
- 1.3 Thesis plan 4

I Theoretical Models and Experimental Techniques **7**

2 Models in Quantum Optics **9**
- 2.1 Heisenberg uncertainty principle and quantum noise 9
- 2.2 Squeezing of the quadrature variances 10
- 2.3 Rigorous solution and the linearized formalism 12
  - 2.3.1 Linearization of the annihilation operator 12
  - 2.3.2 The quantum sideband picture 14
  - 2.3.3 The ball-on-stick picture 16
- 2.4 Theory of the measurement processes 18
  - 2.4.1 Direct detection 18
  - 2.4.2 Self-homodyning 20
  - 2.4.3 Homodyning with a local oscillator 21
  - 2.4.4 Inefficient measurements 21
  - 2.4.5 Mode mismatch in homodyne measurements 22

3 Experimental Techniques **25**
- 3.1 The lasers 25
- 3.2 Propagation of light beams 26
  - 3.2.1 Mode-matching 26
  - 3.2.2 Polarization optics and dichroics 28
- 3.3 Mode Cleaners 29
  - 3.3.1 Intensity noise cleaner 29
  - 3.3.2 Spatial mode cleaner 31
- 3.4 The nonlinear medium 31
- 3.5 Design considerations of the nonlinear resonators 32
  - 3.5.1 Standing wave and traveling wave cavities 32
  - 3.5.2 Monolithic, hemilithic and external mirror cavities 33
  - 3.5.3 Dielectric and evanescent coupling 34
- 3.6 The servo-control systems 35

3.7 Detection of light field . . . 35
3.8 Data retrieval . . . 36

II Generation of Squeezed States 39

4 The Second Order Optical Nonlinearity 41
4.1 Introduction . . . 41
4.2 Optical $\chi^{(2)}$ processes . . . 42
4.3 Conditions for $\chi^{(2)}$ interactions . . . 42
4.3.1 Conservation of energy . . . 43
4.3.2 Conservation of momentum: Phase matching . . . 43
4.3.3 Cavity resonance . . . 46
4.4 The $\chi^{(2)}$ Hamiltonian . . . 48
4.5 A mechanical analogy . . . 49

5 Squeezing in Second Harmonic Generation 51
5.1 Introduction . . . 51
5.2 Modular theory of noise propagation . . . 52
5.3 The experiment . . . 54
5.4 Comparison between experiment and theory . . . 56
5.5 Summary . . . 58

6 Interacting Second Order Nonlinearities 61
6.1 Cooperating and competing nonlinearities . . . 61
6.2 Competing nonlinearities: intra-cavity SHG and NDOPO . . . 62
6.2.1 Power clamping . . . 63
6.2.2 Limit to squeezing . . . 66
6.3 Summary . . . 69

7 Classical Properties of a Doubly Resonant Optical Parametric Oscillator 71
7.1 Introduction . . . 71
7.2 Experimental setup . . . 72
7.3 Output power and pump depletion . . . 74
7.4 Coarse and fine tuning capabilities . . . 75
7.5 Summary . . . 77

8 Squeezed Vacuum Generation 79
8.1 Introduction . . . 79
8.2 Experimental setup . . . 80
8.2.1 The second harmonic generator . . . 80
8.2.2 The optical parametric oscillator . . . 82
8.2.3 The mode cleaner . . . 82
8.2.4 The homodyne system . . . 83
8.3 A simple theory for OPO . . . 83
8.4 Classical regenerative gain . . . 84
8.5 Limits to vacuum squeezing . . . 85
8.6 Squeezing results . . . 89
8.7 Summary . . . 90

III Applications of Quantum Electro-Optic Control 91

9 Quantum Electro-Optic Control of Light 93
9.1 Introduction 93
9.2 Classical and quantum control theory 94
9.2.1 Classical feedback and feedforward 94
9.2.2 Quantum limit of control theory 96
9.3 Noiseless optical amplification 96
9.3.1 Examples of noiseless amplification 99
9.4 Experimental setup 99
9.5 Theoretical modelling 100
9.6 Experimental results of noiseless amplification 105
9.6.1 Quantum noise limited input 105
9.6.2 Squeezed input 106
9.7 Signal and power amplification 108
9.7.1 Experimental setup and results 111
9.8 Summary 112

10 Quantum Nondemolition Measurement with Electro-Optic Control 115
10.1 Introduction 115
10.2 Criteria for QND measurements 116
10.3 The beam splitter 119
10.4 Electro-optic feedforward as a QND measurement 121
10.5 Pre- and post- enhancement of a QND measurement 124

11 Quantum Teleportation of Continuous Variables 127
11.1 Introduction 127
11.2 Teleportation with classical channels 129
11.3 Teleportation with quantum and classical channels 132
11.3.1 The requisite EPR state 132
11.3.2 Quantum teleportation results 133

12 Conclusions 137
12.1 Summary of the squeezing results 137
12.2 Summary of the electro-optic feedforward control results 137
12.3 Future research 138
12.3.1 Mode-locked OPO via competing nonlinearities 138
12.3.2 Implementations of QND measurement and quantum teleportation 138
12.3.3 The squashed state of light 139

A Measuring Signal and Noise with a Spectrum Analyser 141

B Photodetector Circuit Diagrams 143

C PID Controller Circuit Diagrams 145

D Temperature Controller Circuit Diagrams 149

E Laser Controller Circuit Diagrams 151

F Q-Switched Second Harmonic Generation 155
F.1 Introduction 155
F.2 Q-switched NPRO 155
F.3 Results 157
F.4 Conclusions 159

G Optical Homodyne Tomography of Information Carrying Laser Beams 161
G.1 Introduction 161
G.2 Standard homodyne detection 162
G.3 Modulation 163
G.4 Optical homodyne tomography 164
G.5 Wigner function reconstruction 165
G.6 Experimental results 166
  G.6.1 Varying the depth of phase modulation 166
  G.6.2 Switched phase modulation 167
  G.6.3 Asynchronous detection (variable phase ψ). 167
G.7 Discussion and summary 167

Bibliography 171

List of Figures

1.1 Historical results of squeezing experiments. 1
1.2 Structure of the thesis 5

2.1 Photon number distributions of squeezed and coherent states 11
2.2 Flow chart for modeling quantum optical systems 13
2.3 Quantum and classical sideband correspondence 14
2.4 Sideband pictures of PM, AM and quantum noise 16
2.5 Correspondence between Wigner and the ball-on-stick representation . . . 17
2.6 The ball on stick explanations of squeezing 18
2.7 Schematics of detection systems 19

3.1 Precise mode matching of a Gaussian beam 28
3.2 Examples of nonlinear optical resonators 33
3.3 Probability distribution functions of noise and signal 37

4.1 Overview of the basic $\chi^{(2)}$ nonlinear interactions 43
4.2 Phase matching function for MgO:LiNbO$_3$ 45
4.3 Nonlinear coupling strength as a function of wavelength 46
4.4 Resonance conditions of parametric oscillators 47
4.5 Mechanical analogy of nonlinear optics 50

5.1 Block diagram of the modular propagation of noise in SHG 52
5.2 Setup of the second harmonic generation experiment. 55
5.3 Mode cleaned spectrum of the second harmonic generator pump field . . 57
5.4 Theoretical and experimental spectra of the SHG 58

6.1 Simple examples of cooperating and competing nonlinearities 62
6.2 Effect of temperature tuning on nonlinearities 64
6.3 Optical modes of the intra-cavity competing nonlinearities OPO 65
6.4 Optical clamping of the second harmonic power 66
6.5 Theoretical plots of second harmonic squeezing with competition 67
6.6 Experimental plots of second harmonic squeezing with competition 68

7.1 Schematic of the classical OPO experiment 73
7.2 Classical OPO output power 74
7.3 Depletion of the harmonic power of the classical OPO 76
7.4 Phase matching plot of the classical OPO 77
7.5 Mode pair analysis of OPO output 78

8.1 Experimental setup of the squeezed vacuum generator 81
8.2 Theoretical prediction of the classical gain 85
8.3 Classical gain of the squeezed vacuum generator 86
8.4 Limits of the OPO squeezing 87

8.5 Magnitudes of squeezing and anti-squeezing noise variance 88
8.6 Noise variance of the squeezed vacuum 89
8.7 Noise variance of the OPA output 90

9.1 Simple feedback and feedforward loops 95
9.2 Optical amplifiers in phase space representation 97
9.3 The schematic of electro-optic feedforward 100
9.4 Schematic of the in-loop circuit 100
9.5 In-loop electronics transfer function 101
9.6 Calculated results of signal transfer coefficient 103
9.7 Contour plots of the signal transfer coefficient 104
9.8 Results of T_s with 50% in-loop reflection 105
9.9 Results of T_s with 90% in-loop reflection 106
9.10 Noiseless amplification with squeezed input signal 107
9.11 Signal and power amplifiers 108
9.12 Transfer function of an injection locked ring laser 109
9.13 Schematic of the combined feedforward-injection locked amplifier 111
9.14 Maximum T_s for varying in-loop reflectivity 112
9.15 Normalized output variance of the injection locked laser 113

10.1 Schematic of a QND experiment 116
10.2 2-D QND measurement diagram 119
10.3 Beam splitter with squeezed vacuum input 121
10.4 Feedforward as a QND 122
10.5 QND performances with squeezed vacuum and feedforward 124
10.6 Schematic of the pre- and post- enhanced QND measurement 125

11.1 Simple transmission scheme 129
11.2 Classical teleportation scheme 130
11.3 Performance of the classical teleporter 133
11.4 Quantum teleportation scheme 134
11.5 EPR entanglement 135
11.6 Performance of the quantum teleporter 136

12.1 Squashed state of light 139

B.1 Circuit diagram of 1064 nm photodetector 143
B.2 Circuit diagram of 532 nm photodetector 144

C.1 Gain and integrator stages of UniPID 5.0 145
C.2 Differentiator stage of UniPID 5.0 146
C.3 Driver and roll-off stage of UniPID 5.0 146
C.4 Circuit diagram of piezo-electric actuator M1 PID 147
C.5 Circuit diagram of high voltage PZT amplifier 148

D.1 Front end interface of milli-Kelvin temperature controller 149
D.2 PID circuit of milli-Kelvin temperature controller 150
D.3 Power supply of milli-Kelvin temperature controller 150

E.1 Laser controller fast input schematic 151

E.2 Fast input (HV) amplifier of laser controller 152
E.3 Slow input of laser controller 153
E.4 Laser controller power supply 154

F.1 Q-switched laser crystal assembly 156
F.2 Q-switched SHG 157
F.3 Output pulse frequency and width 158
F.4 SHG conversion efficiency 158

G.1 Optical homodyne tomography experimental setup 163
G.2 Data processing of OHT experiment (a) 165
G.3 Data processing of OHT experiment (b) 166
G.4 Data processing of OHT experiment (c) 167
G.5 Wigner function of phase modulation 168
G.6 Wigner function of a classical mixture state 169
G.7 Wigner function of phase-unlocked scheme 169

List of Tables

3.1 Optics list . . . 27
3.2 Mode cleaners . . . 30
3.3 Photodiodes . . . 35

5.1 Parameters of the Nd:YAG laser . . . 56

9.1 Signal transfer coefficients for the combined amplifier . . . 112

A.1 Measured spectrum analyser quantities . . . 141
A.2 Corrected values . . . 142
A.3 Inferred values . . . 142

Alice being noiselessly amplified after having a magic drink
in her adventure in the Wonderland.

Chapter 1

Introduction

But certainly, for us who understand life, figures are a matter of indifference. I should have liked to begin this story in the fashion of the fairy-tales. . .

The Little Prince, Antoine de Saint-Exupéry

1.1 Overview

Squeezing was first demonstrated by Slusher *et al.* via four wave mixing in an optical cavity [1] more than a decade ago. Since then many excellent theoretical developments and experimental demonstrations of the quantum optics of squeezed states have been carried out by many scientists of the field. The experimental achievements in the generation of squeezing field is summarized in Figure 1.1. From the figure[1] , we see that the magnitudes of the best squeezing results over a period of more than ten years have been steadily increased. However, what is not reflected in the figure is that the increase in the reported squeezing also comes with a corresponding increase in the stability of the generated squeezing: From the observation of a few milliseconds of fluctuations in

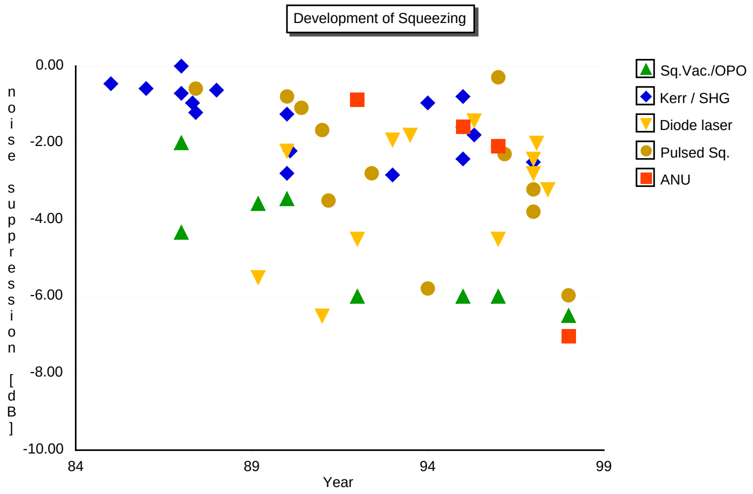

Figure 1.1: Historical results of squeezing experiments.

---

[1] By courtesy of H.-A. Bachor from the book "A guide to experiments in quantum optics"

light intensity lower than the standard quantum limit to the many “daylight” squeezing experiments of recent years where the sub-quantum noise behaviour of light were continuously and stably observed for many hours.

Both of these trends were brought about by advances in the many requisite technologies for a squeezing experiment: The availability of ultra-stable pump lasers (eg. Nd:YAG non-planar ring oscillator); The improvements in quantum efficiencies of photodiode semiconductor materials (eg. ETX-500 from Epitaxx); The invention and refinement of new stable locking techniques for optical experiments; The discovery of new nonlinear crystal materials (eg. PPLN) and the refinements and innovations in crystal growing, polishing and coating techniques. However, technological breakthroughs alone does not suffice. The design of a good quantum optics experiment also requires in-depth understandings of the physics of the involved nonlinear optical processes. This is one of the themes of this thesis.

With the availability of stable sources of strongly squeezed light, applications of the quantum state can then be successfully realized from the many proposed ideas. The applications of squeezed light proposed or demonstrated includes: The possibility of quantum non-demolition measurements; The improvements in sensitivities of spectroscopic, interferometric and anemometric measurements; and the facilitation of quantum effects investigation in optics. The search for new applications of squeezed light form the second theme of this thesis.

This thesis thus has two aims:

- *Generations of squeezed light*
  The first aim of this thesis is to investigate into the possible improvements on the methods of squeezed state generation. The system we have adopted is based on the continuous-wave (CW) nonlinear $\chi^{(2)}$ interaction processes. In this thesis, we report on squeezing results obtained from an optical second harmonic generator and an optical parametric oscillator (OPO). In the pursuit of larger and more stable quantum noise reductions, we were at times faced with the challenge of having to reconcile the discrepancies between theoretical predictions and experimental observations. However, it was through these incidences that new physics and understandings were found. One such example is the observation of competing nonlinearities in monolithic second harmonic generators. Whenever necessary detailed accounts of theoretical modeling of the experiments will be presented.

- *Applications of squeezed light*
  The second aim of this thesis is to investigate potential applications of the squeezed states of light. The focus of our effort in this regard is based on the use of electro-optic control loops. The limitations and potentials of a simple electro-optic feedforward loop is investigated experimentally. Results of the noiseless amplification of light is discussed. We also demonstrate that the combination of squeezed light and this form of light control lends itself to the possible implementations of quantum nondemolition measurements and quantum teleportations of optical states.

1.2 Publications

Most of the contents of this thesis have been published, or accepted for publication, in international journals or conference proceedings. Below is a list of publications resulting from work in this thesis:

1. M. S. Taubman, T. C. Ralph, A. G. White, P. K. Lam, H. W. Wiseman, D. E. McClelland and H.-A. Bachor,
   "A Reliable Source of Squeezed Light, and an Accurate Theoretical Model",
   Lasers in research & engineering: Proceedings of the 12th international congress, Springer-Verlag (1995).

2. A. G. White, M. S. Taubman, T. C. Ralph, P. K. Lam, D. E. McClelland, and H.-A. Bachor,
   "Experimental test of modular noise propagation theory for quantum optics",
   Phys. Rev. A **54**, 3400 (1996).

3. A. G. White, P. K. Lam, M. S. Taubman, M. A. M. Marte, S. Schiller, D. E. McClelland, and H.-A. Bachor,
   "Classical and quantum signature of competing $\chi^{(2)}$ *nonlinearities"*,
   Phys. Rev. A **55**, 4511 (1997).

4. P. K. Lam, T. C. Ralph, E. H. Huntington, and H.-A. Bachor,
   "Noiseless signal amplification using positive electro-optic feedforward",
   Phys. Rev. Lett. **79**, 1471 (1997).

5. P. K. Lam, H.-A. Bachor, E. H. Huntington, T. C. Ralph, A. G. White, M. S. Taubman, C. C. Harb and D. E. McClelland,
   "Making Squeezed Light Robust",
   Laser spectroscopy XIII international conference proceedings, World Scientific, 293 (1997).

6. I. Freitag, P. K. Lam, and A. Tünnermann,
   "Gütegeschaltete Miniatur-Ringlaser mit Frequenzkonversion",
   Laser und Optoelektronik **29**, 70 (1997).

7. T. C. Ralph, P. K. Lam, C. C. Harb, E. H. Huntington, A. G. White, M. S. Taubman, D. E. McClelland and H.-A. Bachor,
   "Optical engineering with squeezed light: laser noise spectra and noiseless amplifiers",
   Fifth international conference on squeezed states and uncertainty relations, 3 (1998).

8. P. K. Lam, T. C. Ralph, E. H. Huntington, D. E. McClelland, and H.-A. Bachor,
   "Noiseless electro-optic processing of optical signals generated with squeezed light",
   Opt. Ex. **2**, 100 (1998).

9. E. H. Huntington, P. K. Lam, T. C. Ralph, D. E. McClelland, and H.-A. Bachor,
   "Noiseless independent signal and power amplification",
   Opt. Lett. **23**, 540 (1998).

10. P. K. Lam, I. Freitag, M. Bode, A. Tünnermann, and H. Welling,
    "High average power Q-switched second harmonic generation with diode pumped Nd:YAG Laser",
    Electron. Lett. **34**, 666 (1998).

11. M. Bode, P. K. Lam, I. Freitag, A. Tünnermann, H.-A. Bachor, and H. Welling,
    "Continuously-tunable doubly resonant optical parametric oscillator",
    Opt. Commun. **148**, 117 (1998).

12. M. Bode, I. Freitag, A. Tünnermann, H. Welling, P. K. Lam and H.-A. Bachor,
"High power operation of a continuously-tunable doubly resonant optical parametric oscillator",
OSA Trends in Optics and Photonics **19**, Advanced Solid State Lasers, 136, (1998).

13. J. W. Wu, P. K. Lam, M. B. Gray and H.-A. Bachor,
"Optical homodyne tomography of information carrying laser beams",
Opt. Ex. **3**, 154 (1998).

14. T. C. Ralph and P. K. Lam,
"Teleportation with bright squeezed lights",
Phys. Rev. Lett. **81**, 5668 (1998).

15. T. C. Ralph, P. K. Lam, E. H. Huntington, B. C. Buchler, D. E. McClelland, and H.-A. Bachor,
"Quantum electro-optic control",
Optics & Photonics News **9**, 44 (1998).

16. T. C. Ralph, E. H. Huntington, C. C. Harb, B. C. Buchler, P. K. Lam, D. E. McClelland, and H.-A. Bachor,
"Understanding and controlling laser intensity noise",
Optical and Quantum Electronics, Accepted for (1999).

17. P. K. Lam, T. C. Ralph, B. C. Buchler, D. E. McClelland, H.-A. Bachor and J. Gao,
"Optimization and transfer of vacuum squeezing from an optical parametric oscillator",
J. Opt. B: Quantum and Semiclassical Optics, Accepted for (1999).

18. T. C. Ralph, P. K. Lam and R. E. S. Polkinghorne,
"Characterizing teleportation in optics",
J. Opt. B: Quantum and Semiclassical Optics, Accepted for (1999).

Other published papers by the author which are not included in this thesis are:

1. P. K. Lam and C. M. Savage,
"Complete atomic population inversion using correlated sidebands",
Phys. Rev. A **50**, 3500 (1994).

2. P. K. Lam, A. J. Stevenson and J. D. Love,
"Control and suppression of power transfer in couplers by periodic index modulation",
Electron. Lett. **31**, 1233 (1995).

3. P. K. Lam, A. J. Stevenson, J. D. Love,
"Coupling suppression by periodic index modulation in single-mode couplers",
Proceedings of the 19th Australian conferences on optical fibre technology (1995).

1.3 Thesis plan

This thesis is divided into three parts and the structure of this thesis is shown in Figure 1.2. In the first part of the thesis, we present the basic theoretical models and experimental techniques required as background knowledge for the study of CW quantum optical system. Since there are many textbooks in the field of quantum optics, the author has chosen to emphasis only more relevant fragments in details. The reading of this part can be omitted for readers who are familiar with current research work in CW quantum optical system.

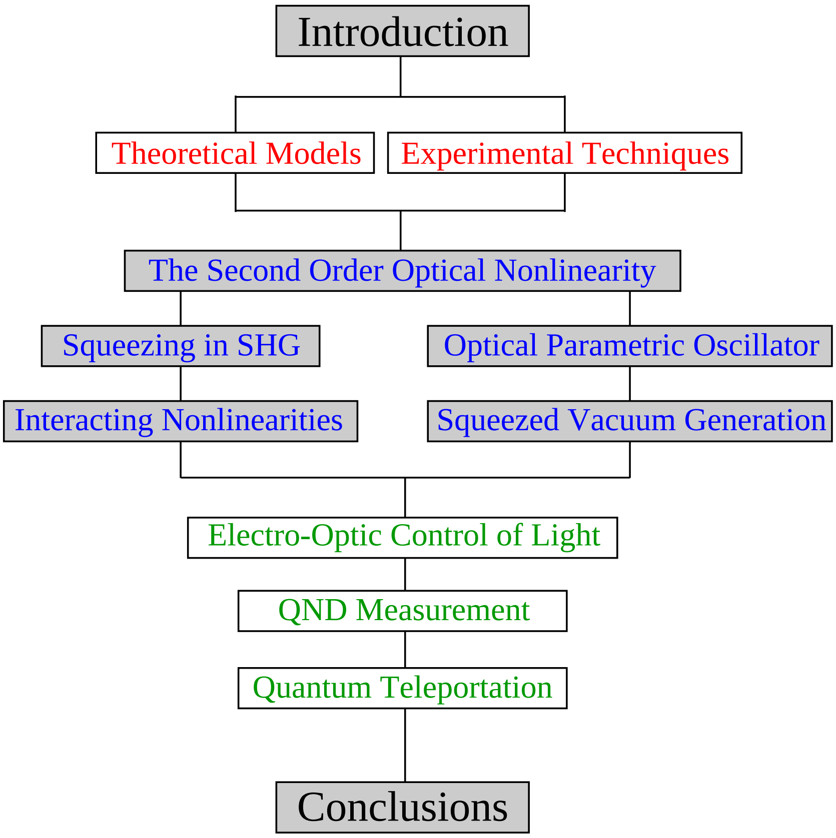

Figure 1.2: Structure of the thesis

In Chap. 2, we present theoretical models used in the analysis of the experimental results of this thesis. Although a rigorous quantum mechanical formalism is always sufficient in solving quantum optics problems, we have adopted the simpler but more intuitive approach of the *linearized formalism*. The sideband picture and ball-on-stick picture consequential to the linearized formalism is also discussed. Finally, the last section of the chapter derives, using the linearized formalism, measurement expressions of several photodetection schemes.

In Chap. 3, we outline experimental techniques and design criteria general to the setup of the experiments. We proceed along the beam path of an experiment to describe the beam manipulation, mode cleaning, nonlinear cavity design, servo control and detection of the light beam. Listings of optical components are also presented.

The second part of this thesis is concerned with the generations of squeezed states of light and the associated findings. We report squeezing from both the upconversion and downconversion processes of the second order $\chi^{(2)}$ nonlinear interaction.

In Chap. 4, we present an overview of second order nonlinear processes. Conditions necessary for the optimization of the $\chi^{(2)}$ effect as well as the general Hamiltonian of the $\chi^{(2)}$ nonlinear interaction are discussed. A simple mechanical analogy is also presented for the explanations of some nonlinear optics phenomena.

In Chap. 5, we examine the second harmonic amplitude squeezing of a frequency doubler. A modular theory for noise propagation is developed to explain the influence of pump noise in the squeezing performance of the second harmonic output.

In Chap. 6, the phenomena of interacting nonlinearities are discussed. We show that competing nonlinearities which facilitate the occurrence of intra-cavity nondegenerate optical parametric oscillation in frequency doublers lead to the optical clamping of the second harmonic output power. The study of the noise behaviour shows that the output squeezing of the system is degraded by the onset of competition.

In Chap. 7, a strongly pumped OPO is used for the study of the classical properties of parametric downconversion. The coarse and continuous frequency tuning ranges, threshold power, output power and pump depletion percentage of the OPO is characterized. This chapter serves as a preliminary study for the generation of squeezed vacuum using OPO.

In Chap. 8, an OPO with large escape efficiency is used to produce the squeezed vacuum state. We discuss the individual limits to the squeezing of the vacuum state and report more than 7 dB of vacuum squeezing and 4 dB of optical parametric amplifier (OPA) amplitude squeezing from the same system.

The last part of this thesis is concerned with the applications of electro-optic feedforward control loops and squeezed light.

In Chap. 9, an introduction to classical and quantum control theory is presented. We show that the electro-optic feedforward loop is a noiseless signal amplifier of the optical input and explain the results in terms of the cancellation of vacuum fluctuations. When used in conjunction with an injection-locked laser, we demonstrate that independently variable noiseless signal and power amplification is possible. With intensity squeezed light as input to the feedforward loop, we showed that the signal amplification can make an optical state robust to transmission losses.

In Chap. 10, the application of the electro-optic feedforward loop is extended to quantum nondemolition measurements. This is done with the injection of squeezed vacuum into the beam splitter of the electro-optic feedforward loop.

In Chap. 11, application of the electro-optic feedforward loop is pushed to its limit. With the use of two input squeezed sources and two feedforward loops, we show that the quantum teleportation of a CW optical state is possible. Experimental measures are proposed for quantifying the performance of a quantum teleporter.

Finally, Chap. 12 summarizes the main results of this thesis and present a brief outlook for future experimental work.

Part I

Theoretical Models and Experimental Techniques

Chapter 2

Models in Quantum Optics

> Great mathematical ideas do not blossom in workshops, as a rule, but on the other hand the theorist should not divorce himself from a healthy and intimate connection with practical questions.
>
> *J. L. Synge, Geometric optics: an introduction to Hamilton's method (1937).*

Overview

This chapter is concerned with the theoretical models and methods of analysis required for the experimental work of this thesis. The method of linearization of operators in quantum optics is presented. Two physical pictures, the sideband picture and the ball-on-stick picture, associated with the linearization of operators are described.

2.1 Heisenberg uncertainty principle and quantum noise

Quantum mechanics is known to be probabilistic since the formulation of the statistical interpretation by Born in 1926 [2]. This intrinsic statistical aspect of quantum mechanics coupled with our inability to specify each and every one of the continuum of modes in the electromagnetic field [3] give rise to "*quantum noise*" in optics [4].

In practice, the existence of quantum noise means that measurements of a physical quantity even from an ensemble of identically prepared states will still not be perfectly deterministic. The magnitude of this indeterminacy or fluctuations in measurements is succinctly summarized by the Heisenberg uncertainty principle (HUP). The HUP states that it is impossible to attain simultaneous precise knowledge of two noncommuting observables. If two observables are related to each other via the commutation relation,

$$[\hat{O}_-, \hat{O}_+] = \delta \tag{2.1}$$

then we have the following uncertainty relation

$$\Delta\hat{O}_- \ \Delta\hat{O}_+ \geq \frac{1}{2}|\delta| \tag{2.2}$$

where $\Delta\hat{O}$ is the standard deviation of the operator, given by

$$\Delta\hat{O} = \sqrt{\langle\hat{O}^2\rangle - \langle\hat{O}\rangle^2} \tag{2.3}$$

The standard example of this uncertainty relation is that of the momentum and position of a particle. Simultaneous determination of both quantities cannot be more precise than the given limit as explained in the *gedanken* experiment of the "Heisenberg microscope" [5]. We can translate the uncertainty relation to optics via the boson commutation relation and obtain

$$[\hat{a}, \hat{a}^\dagger] = 1 \tag{2.4}$$

$$\Delta\hat{a}\ \Delta\hat{a}^\dagger \geq \frac{1}{2} \tag{2.5}$$

Since the annihilation and the creation operators, $\hat{a}$ and $\hat{a}^\dagger$, are not Hermitian and therefore do not correspond to any physically measurable quantity, it is more relevant to re-express them in terms of the quadrature amplitudes

$$\hat{X}^+ = \hat{a} + \hat{a}^\dagger \tag{2.6}$$

$$\hat{X}^- = i(\hat{a} - \hat{a}^\dagger) \tag{2.7}$$

where $\hat{X}^+$ and $\hat{X}^-$ correspond to the amplitude and phase quadratures of the electric field, respectively. The Heisenberg uncertainty relation now becomes

$$[\hat{X}^+, \hat{X}^-] = 2i \tag{2.8}$$

$$\Delta\hat{X}^+\ \Delta\hat{X}^- \geq 1 \tag{2.9}$$

That is to say, if precise measurements were to be made on both the amplitude and phase quadratures an electric field, the results will be indeterministic to some extent. The fluctuations in both the quadrature amplitudes are referred to as the "*quantum noise*" of the electromagnetic field. The limit as predicted by HUP assuming that both quadrature amplitudes have the same uncertainty $\Delta\hat{X}^+ = \Delta\hat{X}^- = 1$. This is known as the "*standard quantum limit*".

2.2 Squeezing of the quadrature variances

The quantum state closest in resemblance to that of a laser output state is the coherent state $|\alpha\rangle$ [6]. A coherent state can be expressed in terms of the number or Fock states as

$$|\alpha\rangle = e^{-|\alpha|^2/2} \sum_{n=0}^{\infty} \frac{\alpha^n}{\sqrt{n!}} |n\rangle \tag{2.10}$$

where $|n\rangle$ is the Fock state representing an optical field with exactly n photons but with completely indeterminate phase. Coherent states have the following properties

$$\hat{a}|\alpha\rangle = \alpha|\alpha\rangle \tag{2.11}$$

$$\hat{D}_\alpha|0\rangle = |\alpha\rangle \tag{2.12}$$

Thus, coherent states are the eigenstates of the annihilation operator and can be obtained by having a displacement operator, $\hat{D}_\alpha$, acting on the vacuum state, where

$$\hat{D}_\alpha = e^{\alpha\hat{a}^\dagger - \alpha^*\hat{a}} \tag{2.13}$$

A more physical description of the coherent state can be found in the equations below

$$P(n) = \frac{|\alpha|^{2n}e^{-|\alpha|^2}}{n!} \tag{2.14}$$

$$\langle\hat{n}\rangle = |\alpha|^2 \tag{2.15}$$

$$\Delta\hat{n} = |\alpha| \tag{2.16}$$

$$\langle\hat{X}^+ + i\hat{X}^-\rangle = 2\alpha \tag{2.17}$$

$$\Delta\hat{X}^+ = 1 \tag{2.18}$$

$$\Delta\hat{X}^- = 1 \tag{2.19}$$

We note, firstly, that a coherent state has a Poissonian photon number distribution (see Figure 2.1). The average number of photons present in a coherent state $|\alpha\rangle$ is $|\alpha|^2$ and the standard error of the photon number is the square-root of the average photon number. We also note that the uncertainty of the amplitude quadrature and the phase quadrature are both equal to unity. This suggests that the phase and amplitude quadrature fluctuations of a coherent state are both at the standard quantum limit.

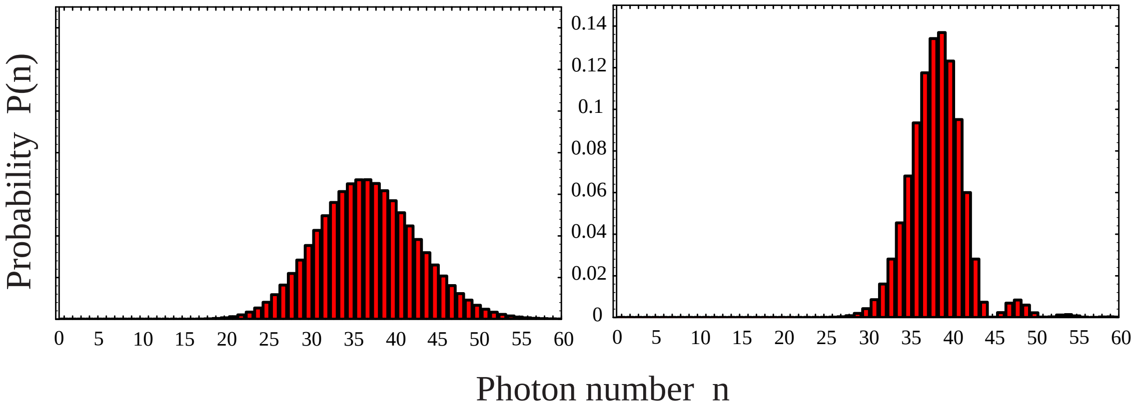

Figure 2.1: Photon number distributions of squeezed and coherent states. (a) coherent state with $\alpha = 6$, (b) squeezed state with $\alpha = 6$ and $r = 1$ (-4.3 dB).

Squeezed states of light can be obtained from a vacuum state using the displacement operator $\hat{D}_\alpha$, and the squeezing operator $\hat{S}_r$ given by

$$\hat{S}_r = e^{1/2(r^*\hat{a}^2 - r\hat{a}^{\dagger 2})} \tag{2.20}$$

where $|r|$ is called the *squeezing factor*. The squeezed state of light obtained from a vacuum state is represented by [1]

$$|\alpha, r\rangle = \hat{D}_\alpha\hat{S}_r|0\rangle \tag{2.21}$$

---

[1] Quadrature amplitude squeezing can also be obtained by $\hat{S}_r\hat{D}_\alpha|0\rangle$, this is known as the two photon coherent state [7]. The relationship between the two photon coherent state and squeezed state is given in Walls and Milburn [8].

and has the following properties

$$\begin{aligned}
P(n) &= \frac{1}{2^n n! \cosh(r)} (\tanh r)^n e^{-\alpha^2(1+\tanh r)} \left| H_n\left(\frac{\alpha e^r}{\sqrt{\sinh(2r)}}\right)\right|^2 && (2.22)\\
\langle \hat{n} \rangle &= |\alpha|^2 + \sinh^2 r && (2.23)\\
(\Delta \hat{n})^2 &= |\alpha \cosh r - \alpha^* \sinh r|^2 + 2\cosh^2 r \sinh^2 r && (2.24)\\
\langle \hat{X}^+ + i\hat{X}^- \rangle &= 2\alpha && (2.25)\\
\Delta \hat{X}^+ &= e^{-r} && (2.26)\\
\Delta \hat{X}^- &= e^{r} && (2.27)
\end{aligned}$$

where r is assumed real and $H_n(x)$ are the n^{th} ordered Hermite polynomials. The photon number distribution of squeezed state is no longer a simple Poissonian as shown in Figure 2.1. We note that with squeezed states, an asymmetry exist between the uncertainties of the orthogonal quadrature amplitudes.

In spite of the simplicity and elegance of the theoretical representation of the squeezed state presented in this section, many questions still remain. For example we have not yet acquired any physical understanding of the meaning of the displacement operator D_α and of the squeezing operator S_r. Do they correspond to any physical processes? What kind of system (Hamiltonian) is required for the generation of the squeezed state? These are some of the questions which the author attempts to answer in the course of the thesis.

2.3 Rigorous solution and the linearized formalism

The rigorous approaches adopted for the analysis and solution of quantum optical problems are described in many standard textbooks [4, 6, 8–10] and therefore shall not be discussed in this thesis. Instead the flowchart of one such approach is presented in Figure 2.2. Although the techniques of Fokker-Planck equation and quantum Langevin equation are very powerful, they normally do not provide an analytic solution nor a physically intuitive understanding. Most of the physics, unfortunately, is lost in the mathematics.

However, in situations where the quantum noise or fluctuations are small relative to the steady state optical amplitude, there is a much simpler method to a solution involving the linearization of operators. This method was first used in the context of quantum optics by Yurke [11] and Reynaud *et al.* [12]. As a consequence of this linearized formalism, we are able to use two complementary pictures: The quantum sideband picture and the ball-on-stick picture to aid our visualization of situations in quantum optics. These models will be presented in subsequent sections.

2.3.1 Linearization of the annihilation operator

When the steady state electromagnetic field has amplitude much larger than its fluctuations, we can write the annihilation operator of the given field as,

$$\hat{a}(t) \approx \alpha + \delta\hat{a}(t) \tag{2.28}$$

where α is a c-number representing the classical steady state component and $\delta\hat{a}(t)$ is the time-varying fluctuations of the annihilation operator. By writing the annihilation

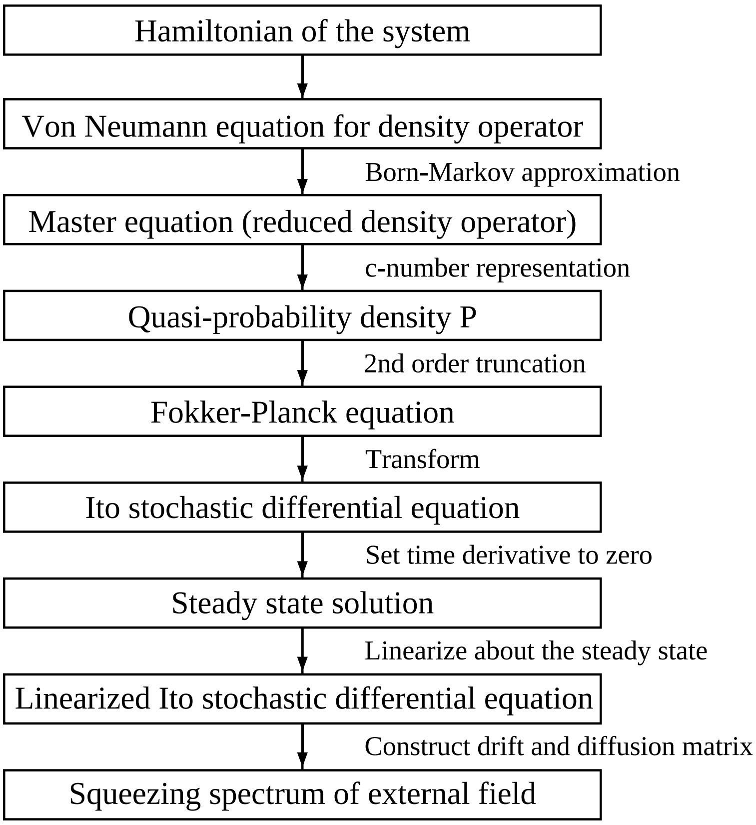

Figure 2.2: Flow chart for modeling quantum optical systems

operator in the given form, it is assumed that

$$\begin{aligned} \langle \delta\hat{a}(t) \rangle &= 0 & (2.29)\\ |\delta\hat{a}(t)| &\ll |\alpha| & (2.30) \end{aligned}$$

That is, on average the fluctuation term $\delta\hat{a}$ has no net contribution to the field amplitude and the fluctuations are perfectly centred at zero. The second condition states that the fluctuations is much smaller than the classical steady state component of the field. This allows us to make a first order approximation on an expression by neglecting higher order product terms of the quantum fluctuations δa. Because of the first order approximation of this operator, we find that the commutation relations are no longer of any consequence. We are thus left with a completely semi-classical c-number expression of a physical quantity.

As an example, let us apply the linearization procedure to the intensity (number) operator of an electromagnetic field. We find

$$\begin{aligned} \hat{n} &= \hat{a}^\dagger(t)\hat{a}(t) \\ &= [\alpha^* + \delta\hat{a}^\dagger(t)][\alpha + \delta\hat{a}(t)] \\ &= |\alpha|^2 + \alpha\,\delta\hat{a}^\dagger(t) + \alpha^*\delta\hat{a}(t) + \delta\hat{a}^\dagger(t)\delta\hat{a}(t) \qquad (2.31) \end{aligned}$$

Assuming that α is real, the first order approximation gives,

$$\hat{n} \approx |\alpha|^2 + \alpha\,\delta\hat{X}_a^+ \tag{2.32}$$

where $\delta\hat{a}^\dagger(t)\delta\hat{a}(t)$ is neglected and $\delta\hat{X}_a^+$ is the amplitude quadrature fluctuations of field a.

Throughout this thesis, we will use the described procedure of operator linearization for the modeling of experimental work. Because of its simplicity, we find that in most situations, analytic solutions in the form of transfer functions can be obtained. Thus giving more insights to the physics.

2.3.2 The quantum sideband picture

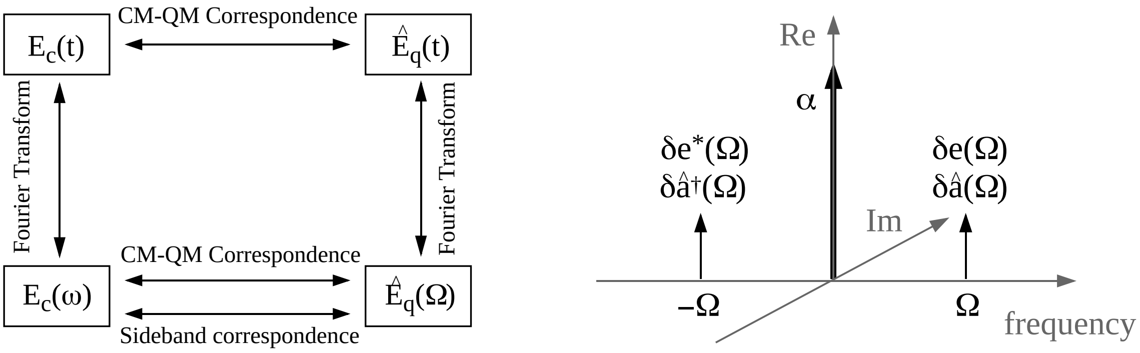

Figure 2.3: Quantum and classical sideband correspondence. *Left*: Conceptual schematic of the quantum-classical correspondence. Because of the canonical quantization of the electromagnetic field, most classical quantities have a quantum mechanical counterpart. Fourier transform can be performed to these quantities. In the Fourier domain, we find that the positive and negative classical sidebands of the electromagnetic field corresponds to the annihilation and creation operators, respectively. *Right*: Sideband diagram for an electromagnetic field. Ω represents a particular detection frequency; δe and δe^* are the upper and lower sidebands of a classical field; $\delta\hat{a}$ and $\delta\hat{a}^\dagger$ are the annihilation and creation operators of the quantum field.

The linearization of quantum mechanical operators described in the previous section enables the explanation of quantum optical problems with a direct analogue to situations in classical electromagnetics. We can therefore take advantage of this analogy and use the sideband picture of the electromagnetic field for visualizing quantum noise.

Figure 2.3 shows the conceptual schematic of the quantum sideband picture. Discussions of the correspondence between quantum mechanical operators and c-numbers in classical mechanics are available in many standard textbooks [8, 10]. Except for the quantum phase operator [8], most of the classical quantities have a unique quantum mechanical counterpart. The main difference between them are that in quantum mechanics, these physical quantities are operators and their orderings are important.

These correspondences are commonly made in the time domain, for example the quantum mechanical electric field vector is

$$\hat{E}_q(t) \;=\; i\sum_k \left(\frac{\hbar\omega_k}{2\epsilon_0}\right)^{1/2} \left(\hat{a}_k(t)e^{-i\omega_k t} - \hat{a}_k(t)^\dagger e^{i\omega_k t}\right) \tag{2.33}$$

$$= i\sum_k \left(\frac{\hbar\omega_k}{2\epsilon_0}\right)^{1/2} (\hat{X}_k^+(t)\sin(\omega_k t) - \hat{X}_k^-(t)\cos(\omega_k t)) \tag{2.34}$$

where k is the continuum of modes containing frequency and polarization information; $\hbar$ is the Planck constant; ϵ_0 is the permittivity of free space; and ω_k is the optical angular frequency of the field. The classical and quantum correspondences are

$$\hat{E}_q(t) \leftrightarrow E_c(t) \tag{2.35}$$
$$\hat{X}_k^+(t) \leftrightarrow X_k^+(t) \tag{2.36}$$
$$\hat{X}_k^-(t) \leftrightarrow X_k^-(t) \tag{2.37}$$
$$\hat{a}_k(t) \leftrightarrow e_k(t) \tag{2.38}$$
$$\hat{a}_k^\dagger(t) \leftrightarrow e_k^*(t) \tag{2.39}$$

We note that unlike the amplitude quadrature and phase quadrature operators the classical counterparts for the annihilation and creation operators, $e_k(t)$ and $e_k^*(t)$, do not corresponds to any familiar physical quantities. However, their meanings will become more apparent in the Fourier domain.

The Fourier transform of the electric field is given by

$$\tilde{\hat{E}}(\omega) = \int \hat{E}(t)e^{-i\omega t}dt \tag{2.40}$$

In the Fourier domain, we find that the time domain correspondences are still preserved.

$$\tilde{\hat{E}}_q(\omega) \leftrightarrow \tilde{E}_c(\omega) \tag{2.41}$$
$$\tilde{\hat{X}}_k^+(\omega) \leftrightarrow \tilde{X}_k^+(\omega) \tag{2.42}$$
$$\tilde{\hat{X}}_k^-(\omega) \leftrightarrow \tilde{X}_k^-(\omega) \tag{2.43}$$
$$\tilde{\hat{a}}_k(\omega) \leftrightarrow \tilde{e}_k(\omega) \tag{2.44}$$
$$\tilde{\hat{a}}_k^\dagger(\omega) \leftrightarrow \tilde{e}_k^*(\omega) \tag{2.45}$$

Furthermore $\tilde{e}_k(\omega)$ and $\tilde{e}_k^*(\omega)$ now have the meaning of being the upper and lower sidebands of the electric field. The Fourier transformations thus reveal that the annihilation and creation operators in quantum mechanics, are analogous to the upper and lower sidebands of a classical electromagnetic field

$$\delta e(\Omega) \leftrightarrow \delta\hat{a}(\Omega) \tag{2.46}$$
$$\delta e^*(\Omega) \leftrightarrow \delta\hat{a}^\dagger(\Omega) \tag{2.47}$$

as depicted by Figure 2.3.

With these correspondences established, we can now explain quantum noise and squeezing in terms of sidebands[2]. Classically, any form of modulation on an electric field can be decomposed into amplitude and phase modulation. An amplitude modulation has its upper and lower sidebands correlated with each other all the time. To first order, a phase modulation has a pair of sidebands (proportional to the first order Bessel

---

[2] Unless necessary to avoid confusion, all operators will not have explicit operator symbols from this point onwards in the thesis.

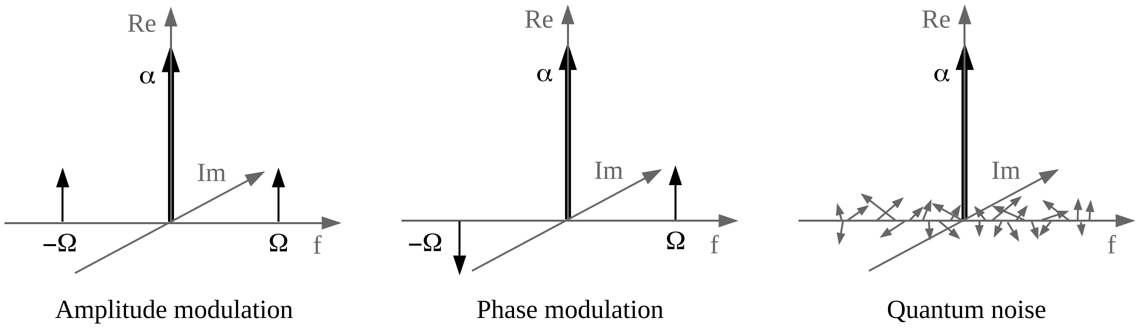

Figure 2.4: Sideband pictures of amplitude, phase modulations and quantum noise.

function J_1) which are anti-correlated with respect to each other. We can think of the quantum noise as a continuum of sidebands spanning all frequencies. These sidebands are uncorrelated with each other and on average, have a field strength equivalent to the square root of half a quantum, $\sqrt{\hbar\omega/2}$ (see Figure 2.4).

Linear processes such as absorption, optical mixing and resonator transmission, may affect the carrier and the sideband fields differently. However, they do not introduce any form of inter-sideband correlation. For example, in linear absorption all sidebands as well as the carrier field vectors experience the same amount of attenuation.

Nonlinear processes, on the other hand, differ in that they are capable of introducing correlations between the sidebands. For example, degenerate four-wave mixing correlates the $\pm\Omega$ sidebands so that their field vectors are parallel to each other and the carrier. The equal likelihoods of quantum fluctuations in any given quadrature therefore preferentially become amplitude modulation, thus causing a reduction in phase fluctuations. The squeezing of an electric field can therefore be thought of as the establishment of some form of correlation between this randomly fluctuating lower and upper sideband pairs. We have thus converted the quantum fluctuations into amplitude modulation for a phase squeezed field and vice versa.

2.3.3 The ball-on-stick picture

A common pictorial representation of quantum noise in many textbooks is the ball-on-stick picture of the electromagnetic field. In spite of its common usage in many situations, there is no formal definition to this pictorial representation. A common understanding is that this pictorial representation is an extension of the familiar phasor diagram of an electro-magnetic field in classical physics. The subtle difference is that the “ball” represents noise that is classical as well as quantum mechanical in origin. Because of this difference, we can regard the ball as a representation of a particular contour height (say e^{-1} or 1/2 of the full height) of a quasi-probability distribution function like the Q- or the Wigner function of a light state as shown in Figure 2.5. The “stick” length on the other hand is simply the classical steady state amplitude of the field. Hence the ball-on-stick picture is actually a superimposed picture of two separate representations: A contour circle of the quantum mechanical quasi-probability at a detection frequency Ω and a classical steady state field phasor.

Figure 2.6 depicts several useful examples of explanations for the squeezing of a coherent state via nonlinear optical processes. In Figure 2.6(a), we have a fundamental

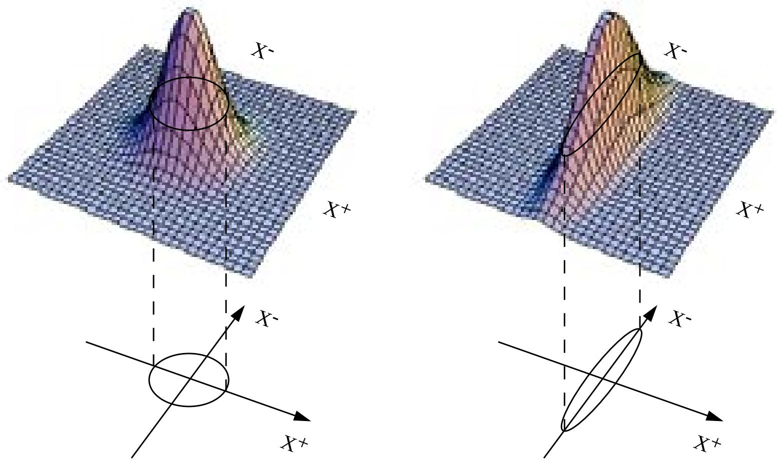

Figure 2.5: Correspondence between Wigner representation and the ball-on-stick representation

mode coherent input state with a certain optical field amplitude denoted by the stick length of the grey circle. This input minimum uncertainty state is subjected to a second order nonlinearity for the purpose of second harmonic generation. When the field amplitude of the fundamental mode fluctuates toward a larger value, the second harmonic generation will be more efficient and the fundamental mode will experience a bigger loss (55%, say). On the other hand, a fluctuation of field amplitude toward a smaller value will result in a less efficient second harmonic generation (smaller loss, say 45%). The net effect of this is a shrinking ball width along the length of the stick due to the intensity dependent loss nature of the process. However, since the initial state is a minimum uncertainty state, HUP requires that the orthogonal direction to the stick, be stretched by a corresponding amount to preserve the uncertainty product relation. The output of the fundamental field after second harmonic generation is thus represented by the black ellipse. This explains the output fundamental mode squeezing of a second harmonic generator.

Similarly Figure 2.6(b) shows that the intensity dependent phase shift from a $\chi^{(3)}$ Kerr medium can be squeezed at certain quadrature amplitude. In Figure 2.6(c) the vacuum fluctuations entering an optical parametric oscillator (OPO) is shown to be squeezed due to the phase dependence amplification or de-amplification by the parametric process. Finally in Figure 2.6(d) a coherent input to an optical parametric amplifier (OPA) is shown to be able to produce different quadrature squeezing depending on the relative phase of the coherent input field to the second harmonic pump field of the amplifier. In both Figure 2.6(c) and (d) we note that the effect of the parametric downconversion is similar to the existence of a stretching force along the X^+ axis and a compressing force along the X^- axis.

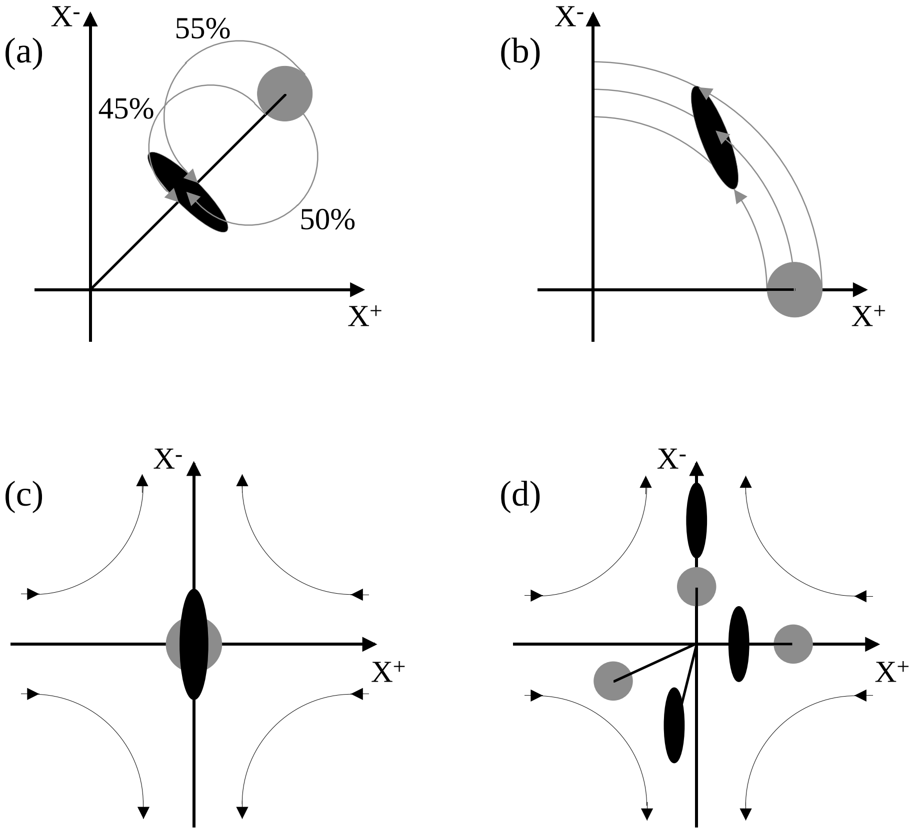

Figure 2.6: Explanations of squeezed state generations using ball-on-stick pictures. Grey circles denote input coherent and vacuum states and black ellipses represent squeezed output states. (a) Squeezing of the fundamental mode via second harmonic generation; (b) Kerr squeezing; (c) Vacuum squeezing via optical parametric oscillation; (d) Quadrature squeezing via optical parametric amplification.

2.4 Theory of the measurement processes

In this section, we use the linearized formalism to derive analytic expression for the basic measurement schemes used in this thesis.

2.4.1 Direct detection

One of the simplest continuous-wave (CW) optical measurements is the *direct detection* using a semiconductor photodiode. The photocurrent of the direct detection is proportional to the number of photons in the optical field,

$$n(t) = a^{\dagger}(t)a(t) \tag{2.48}$$

by linearizing the annihilation and creation operator and by the first order approximation of the quantum fluctuations, we find

$$i(t) \quad \propto \quad |\alpha|^2 + \alpha\,(\delta a^{\dagger}(t) + \ \delta a(t))$$

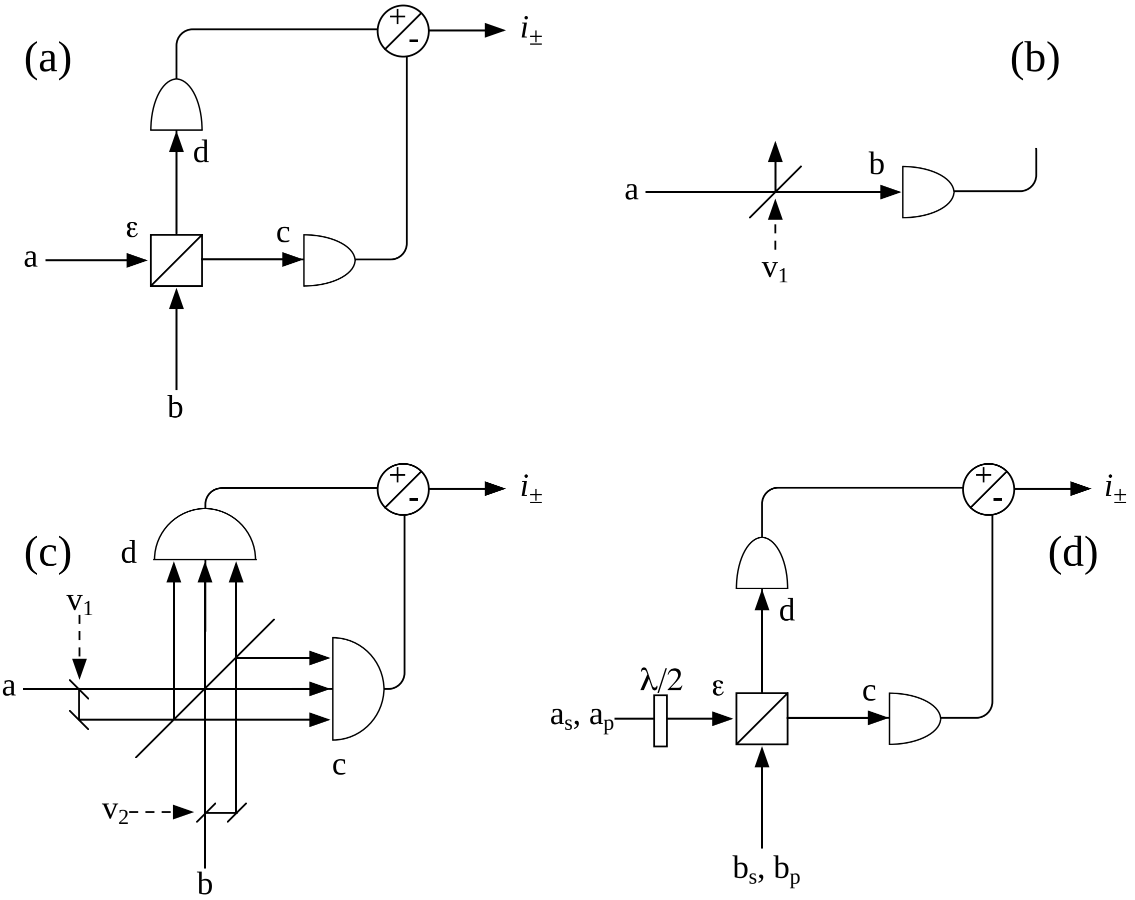

Figure 2.7: Schematics of a homodyning detection systems. (a) Mixing of two optical fields via a beam splitter. The detected photocurrents are added and subtracted with each other. (b) A model for inefficient detection. (c) Spatial mode mismatch: The mixing of the two input fields only occurs for the centre of the 3 arrows arriving at the final detectors. Part of the field a and b are left unmixed due to their spatial separation. (d) Polarization mismatch: The input signal a is polarization shifted by a half-wave plate, causing a lack of mixing with field b.

$$= |\alpha|^2 + \alpha\, \delta X_a^+(t) \tag{2.49}$$

We note that this expression contains a DC term (first term) which is proportional to the optical intensity as well as a fluctuation term of the amplitude quadrature (second term) that is proportionally scaled by the DC field amplitude. We can re-write this expression in Fourier representation using the Fourier transformed linearization equation of $a(\omega) \approx \alpha\, \delta(0) + \delta a(\omega)$, where $\delta(0)$ is a delta function centred at 0. This gives

$$\begin{aligned} n(\omega) &= a^\dagger(\omega) a(\omega) && (2.50) \\ &\approx |\alpha|^2 \delta(0) + \alpha\, \delta X_a^+(\omega) && (2.51) \end{aligned}$$

For quantum optics experiments, the analysis of the DC term is normally measured using a digital multimeter or an oscilloscope (CRO) and the radio-frequency (RF) spectrum is separately analyzed by the use of a spectrum analyser.

2.4.2 Self-homodyning

Figure 2.7(a) shows the general measurement scheme via optical mixing. A signal field a is injected into one of the input ports of the beam splitter. When the other input port is unused, the setup is known as *self-homodyning*. The output fields of the beam splitter are given by

$$c = \sqrt{1-\varepsilon}\, a + i\sqrt{\varepsilon}\, \delta v \tag{2.52}$$

$$d = i\sqrt{\varepsilon}\, a + \sqrt{1-\varepsilon}\, \delta v \tag{2.53}$$

where ε is the reflectivity of the beam splitter and δv is the vacuum field fluctuations entering the unused input port. We note that the reflection of an optical field experiences a 90° phase shift. The addition of the two input fields shown in Eqs. (2.52) and (2.53) are only valid with the following assumptions. Firstly, the two input fields must be of the same optical frequency (optical mode) and be coherently related to each other. Moreover, the inputs must occupy the same spatial extension (spatial mode). Finally, the inputs must be of the same polarization (polarization mode). Partial fulfilment of any of these conditions will lead to a decrease in detection efficiency as will be discussed in the last part of this section.

It is more convenient to express the two output fields of the beam splitter using only real numbers. This simplification can be done by making the substitutions of $\delta v \to \delta v \exp(-i\pi/2)$ and $d \to d \exp(+i\pi/2)$ into Eqs. (2.52) and (2.53) giving

$$c = \sqrt{1-\varepsilon}\, a + \sqrt{\varepsilon}\, \delta v \tag{2.54}$$

$$d = \sqrt{\varepsilon}\, a - \sqrt{1-\varepsilon}\, \delta v \tag{2.55}$$

If we assume that the beam splitter has a 50% reflectivity and $\varepsilon = 0.5$, the setup is called *balanced self-homodyning*. Linearization of the measured photocurrents gives

$$c^\dagger c \approx \frac{1}{2}\left[|\alpha|^2 + \alpha\left(\delta X_a^+ + \delta X_v^+\right)\right] \tag{2.56}$$

$$d^\dagger d \approx \frac{1}{2}\left[|\alpha|^2 + \alpha\left(\delta X_a^+ - \delta X_v^+\right)\right] \tag{2.57}$$

where we have assumed that the vacuum input has no coherent field amplitude. This leads us to the following conclusions. When the photocurrents of the detectors are added together, we retrieve back completely the same direct detection statistics of the input signal field a,

$$i_+ \propto c^\dagger c + d^\dagger d \tag{2.58}$$

$$\propto |\alpha|^2 + \alpha\, \delta X_a^+ \tag{2.59}$$

When the photocurrents are subtracted, we notice that the left over terms are that of the vacuum fluctuations scaled by the signal field amplitude.

$$i_- \propto c^\dagger c - d^\dagger d \tag{2.60}$$

$$\propto \alpha\, \delta X_v^+ \tag{2.61}$$

This means that in a balanced self-homodyne system, the sum and difference photocurrents can provide a calibration of the signal beam relative to the quantum noise limit of the input vacuum fluctuations. Balanced self-homodyning is hence useful for the measurement of amplitude quadrature squeezed light.

2.4.3 Homodyning with a local oscillator

Another interesting measurement scheme via optical mixing is when the second input field b, of Figure 2.7(a), is an intense optical field much stronger than that of the signal. This scheme is known as the *standard homodyne* measurement and we refer to the input state b as the optical local oscillator (LO). Again using the linearized formalism, we obtain

$$\begin{aligned} c^\dagger c &\approx \frac{1}{2}[|\alpha|^2 + |\beta|^2 + 2\alpha\beta\cos\theta + \qquad\qquad (2.62) \\ &\quad \alpha\,(\delta X_a^+ + \delta b e^{i\theta} + \delta b^\dagger e^{-i\theta}) + \beta(\delta X_b^+ + \delta a e^{-i\theta} + \delta a^\dagger e^{i\theta})] \\ d^\dagger d &\approx \frac{1}{2}[|\alpha|^2 + |\beta|^2 - 2\alpha\beta\cos\theta + \qquad\qquad (2.63) \\ &\quad \alpha\,(\delta X_a^+ - \delta b e^{i\theta} - \delta b^\dagger e^{-i\theta}) + \beta(\delta X_b^+ - \delta a e^{-i\theta} - \delta a^\dagger e^{i\theta})] \\ &\qquad\qquad\qquad\qquad (2.64) \end{aligned}$$

where θ denotes the relative phase difference between the coherently related LO and signal field and $b \approx \beta + \delta b$. We now instead assume that the coherent magnitude of the signal field is weak relative to the LO, $|\alpha| \ll |\beta|$, and neglect all terms without the strong LO coherent amplitude $|\beta|$, the first order approximation yields

$$c^\dagger c \approx \frac{1}{2}\left(|\beta|^2 + 2\alpha\beta\cos\theta + \beta(\delta X_a^{(\theta+\pi/2)} + \delta X_b^+)\right) \tag{2.65}$$

$$d^\dagger d \approx \frac{1}{2}\left(|\beta|^2 - 2\alpha\beta\cos\theta + \beta(\delta X_b^+ - \delta X_a^{(\theta+\pi/2)})\right) \tag{2.66}$$

Where $\delta X_a^\theta = \delta a e^{-i\theta} + \delta a^\dagger e^{i\theta}$ is the general quadrature amplitude of field a. The additional $\pi/2$ phase shift arises from the phase substitutions made earlier in this section. The sum and difference photocurrents are

$$i_+ \propto |\beta|^2 + \beta\,\delta X_b^+ \tag{2.67}$$

$$i_- \propto 2\alpha\beta\cos\theta + \beta\,\delta X_a^{(\theta+\pi/2)} \tag{2.68}$$

That is the sum photocurrent is to first order approximately that of the direct detection of the LO field. Because of the large coherent amplitude of the LO field, we are now able to make amplitude quadrature measurements of the input signal field from 0 to 360 degrees continuously by the scanning of the relative phase angle between the two fields. This continuous measurement of the signal quadrature amplitude is given by the difference photocurrent. The standard homodyning is hence a useful measurement in situation where the maximum squeezing quadrature is not the amplitude quadrature.

2.4.4 Inefficient measurements

The quantum efficiency of a photodetector, $\eta_{\rm det}$, can be modeled as shown in Figure 2.7(b) where a beam splitter with transmittivity of $\eta_{\rm det}$ is placed in front of an ideal detector with unity efficiency. This suggests that any loss or inefficiency experienced by a measurement scheme is similar to the interference of the signal field with an uncorrelated vacuum field.

An inefficient photodetector thus measures,

$$b^\dagger b = (\sqrt{\eta_{\rm det}}\, a^\dagger + \sqrt{1-\eta_{\rm det}}\, \delta v^\dagger)(\sqrt{\eta_{\rm det}}\, a + \sqrt{1-\eta_{\rm det}}\, \delta v) \tag{2.69}$$

$$\approx \eta_{\rm det}(|\alpha|^2 + \alpha\, \delta X_a^+) + \sqrt{\eta_{\rm det}(1-\eta_{\rm det})}\, \alpha\, \delta X_v^+ \tag{2.70}$$

This analysis can then be extended to inefficient homodyne systems.

2.4.5 Mode mismatch in homodyne measurements

When the two input optical fields to the beam splitter of a homodyne system are not perfectly mode matched, inefficiency in the homodyne measurement results. The mode mismatch of the fields can have several causes. Nonidentical polarization or partial non-polarization, difference in spatial modes, lack of optical coherence, all have the same detrimental effect to the homodyning. The schematic models of spatial mode mismatch and polarization mismatch are as shown in the Figure 2.7(c) and (d), respectively.

Since all the mentioned causes have a similar effect in the homodyne measurement, we shall only provide the analysis of polarization mismatch as shown in Figure 2.7 (d). An input signal a is homodyned with a LO b which has a slightly different polarization to that of the input field. Since orthogonally polarized fields do not interfere with each other, we need to decompose the LO state into the polarization of interest and its orthogonal state [13]

$$b_s = \sqrt{\eta}\, b + \sqrt{1-\eta}\, \delta v_b \tag{2.71}$$

$$b_p = \sqrt{1-\eta}\, b - \sqrt{\eta}\, \delta v_b \tag{2.72}$$

$$a_s = a \tag{2.73}$$

$$a_p = \delta v_a \tag{2.74}$$

where b is expressed as two components and $1-\eta$ represents the fraction of polarization mismatch. δv_b represents the orthogonally polarized input vacuum from the input port of b. Supposed that the input state of interest is s-polarized. The input p-polarization state is again simply a vacuum field δv_a. The beam splitter output state is then given by

$$c_{s,p} = \frac{1}{\sqrt{2}}(a_{s,p} + b_{s,p}) \tag{2.75}$$

$$d_{s,p} = \frac{1}{\sqrt{2}}(a_{s,p} - b_{s,p}) \tag{2.76}$$

where we now need to consider both polarizations explicitly. Since the detection of the light field using a photodetector is independent of polarization, the respective registered photocurrents on the detectors are given by the sum of both polarizations

$$\begin{aligned} \langle c_s^\dagger c_s + c_p^\dagger c_p \rangle = {} & \frac{1}{2}\langle a^\dagger a + b^\dagger b\rangle + \\ & \frac{1}{2}\Big\langle \sqrt{\eta}(a^\dagger b + b^\dagger a) + \sqrt{1-\eta}(a^\dagger \delta v_b + \delta v_b^\dagger a) + \\ & \sqrt{\eta(1-\eta)}(b^\dagger \delta v_b + \delta v_b^\dagger b) + \\ & \sqrt{1-\eta}\, b^\dagger(\sqrt{\eta}\delta v_b + \delta v_a) + \sqrt{1-\eta}(\sqrt{\eta}\delta v_b^\dagger + \delta v_a^\dagger) b \Big\rangle \end{aligned} \tag{2.77}$$

$$
\begin{aligned}
\langle d_s^\dagger d_s + d_p^\dagger d_p \rangle \;=\; & \frac{1}{2}\langle a^\dagger a + b^\dagger b \rangle + \\
& \frac{1}{2}\Big\langle -\sqrt{\eta}(a^\dagger b + b^\dagger a) - \sqrt{1-\eta}(a^\dagger \delta v_b + \delta v_b^\dagger a) + \\
& \sqrt{\eta(1-\eta)}(b^\dagger \delta v_b + \delta v_b^\dagger b) + \\
& \sqrt{1-\eta}\, b^\dagger(\sqrt{\eta}\delta v_b - \delta v_a) + \sqrt{1-\eta}(\sqrt{\eta}\delta v_b^\dagger - \delta v_a^\dagger) b \Big\rangle
\end{aligned}
\tag{2.78}
$$

where we have again made the first order approximation by neglecting the second order terms, like $\delta v_i \delta v_j$, of the vacua. The second terms of Eqs. (2.77) and (2.78) are due to interference of the bright fields. We note that a variation of the relative phase between the LO with the input signal field will produce a fluctuation in intensity proportional to $\sqrt{\eta}$. Hence the visibility of the interference is given by

$$
\mathrm{VIS} = \frac{I_{\max} - I_{\min}}{I_{\max} + I_{\min}} = \sqrt{\eta}
\tag{2.79}
$$

The difference photocurrent of the homodyning is given by

$$
\begin{aligned}
i_- \;&\propto\; \langle c_s^\dagger c_s + c_p^\dagger c_p \rangle - \langle d_s^\dagger d_s + d_p^\dagger d_p \rangle & (2.80)\\
&\approx\; \sqrt{\eta}\langle a^\dagger b + b^\dagger a \rangle + \sqrt{1-\eta}\langle a^\dagger \delta v_b + \delta v_b^\dagger a + b^\dagger \delta v_a + \delta v_a^\dagger b \rangle & (2.81)
\end{aligned}
$$

Again linearization and first order approximation of both the LO and signal field gives

$$
\begin{aligned}
i_- \;&\propto\; \sqrt{\eta}(2\alpha\beta + \alpha\, \delta X_b^+ + \beta\, \delta X_a^+) + \sqrt{1-\eta}(\alpha\, \delta X_a^+ + \beta\, \delta X_{va}^+) & (2.82)\\
&\approx\; 2\sqrt{\eta}\alpha\beta + \beta(\sqrt{\eta}\, \delta X_a^+ + \sqrt{1-\eta}\, \delta X_{va}^+) & (2.83)
\end{aligned}
$$

A comparison of this expression with that of the ideal homodyning (Eq. (2.68)) suggests that the field efficiency of the setup is decreased by a factor $\sqrt{\eta}$ which when translated to noise variance measurement, $V(\delta X_a^\theta) = (\Delta X_a^\theta)^2 = \langle (\delta X_a^\theta)^2 \rangle$, has an efficiency of η. We thus conclude that the homodyne efficiency of the system is given by

$$
\eta_{\mathrm{hom}} = \eta = (\mathrm{VIS})^2
\tag{2.84}
$$

Which means that the homodyne efficiency is dependent on the square of the interference visibility of the setup. This result is important in the detection of squeezed vacuum in Chap. 8.

Chapter 3

Experimental Techniques

In theory, there is no difference between theory and practice. But in practice, there is.

Anon

Overview

This chapter contains descriptions of the apparatus and techniques used in the experiments of this thesis. We discuss some generic design and equipment specifications required in quantum optics experiments. The first section starts with the laser source used. We then proceed along the beam path of the experiment to describe the beam manipulation, mode cleaning, nonlinear interaction, servo-control, and detection of the light beam. The final section ends with a description of the retrieval of experimental data.

3.1 The lasers

The lasers used in the work of this thesis are based on the diode pumped nonplanar ring oscillator (NPRO) Nd:YAG technology. This type of lasers was chosen because of its high beam quality (diffraction limited Gaussian) and its relatively low noise single-mode output [14, 15]. Semiconductor diode lasers are used as pump sources at the wavelength of 808 nm to the Nd:YAG crystal which lases via a 4-level transition giving 1064 nm light. A brief discussion of the NPRO laser geometry is given in Appendix F. The Nd:YAG laser crystal is sandwiched between a peltier element and a piezo-electric actuator. This assembly is then placed in a strong magnetic field which when combined with the NPRO geometry provides the Faraday effect necessary for single-mode operation [14].

Slow tuning of the laser frequency is achieved via control of the peltier temperature. Heating and cooling of the crystal changes the optical path length of the laser light and thus shifts the resonance frequency of the laser. With temperature control, tuning of many FSR of the laser cavity is easily achieved. However, the time constant of the temperature control is very large and can only be used to track the slow drifting ($\sim$10's of Hz) of the laser frequency. In addition, the heating of the Nd:YAG crystal can reduce the efficiency of the laser because the atomic levels population of the lasing medium is governed by the Maxwell-Boltzmann distribution. The operating temperature range of the laser is therefore restricted from 16°C and 40°C to avoid condensation and overheating, respectively.

Fast tuning of the laser can be achieved via supplying a voltage across the piezo-electric actuator. The mechanical stress experienced by the crystal has the same effect of slightly changing the optical cavity pathlength through a change in the crystal refractive index. However, this method normally only allows for small tuning ranges. Typically, the laser FSR are of the order of GHz and the fast tuning range achievable is only a small fraction of the FSR ($\sim$ 100's MHz). The locking bandwidth achieved via fast tuning, however, is better than temperature tuning at around 50 kHz. When a laser is used to lock to some external optical cavity as in Chap. 5, both tuning methods are used simultaneously to ensure good locking stability. Circuit diagrams of the laser controller is presented in Appendix E.

In this thesis, three NPRO Nd:YAG lasers were used in the experiments. The Lightwave-122 from Lightwave Inc. is used in the second harmonic generation and squeezing work. It has a maximum output power of around 200 mW and has a built-in noise-eater for the suppression of the laser resonant relaxation oscillation. Two lasers, Mephisto 350 and Mephisto 700, both from Laser Zentrum Hannover / InnoLight Inc. were used in most of the other experiments of this thesis. As stated by the model numbers, they have maximum output powers of 350 mW and 700 mW, respectively. The Mephisto 350, is specially designed with an optical input port and thus can be used as a slave laser in the injection locking setup used in Chap. 9. The Mephisto 700 is pumped by two separately controlled diode laser arrays, hence has a higher output power which is ideal for the simultaneous pumping of a SHG and the seeding an OPA. Further discussions on the NPRO laser and laser development work on a Q-switched laser is presented in Appendix F.

3.2 Propagation of light beams

Losses in optical elements are important considerations in quantum optics experiments. In the parts of the experiment before the nonlinear interaction, loss of the pump beam will result in a reduction of the available power for the ensuing frequency conversion process. This is particularly critical to some of the nonlinear interaction processes which require pump power higher than a given threshold, eg. the OPO. Because of the fragility of the quantum states of light, extreme care also has to be taken in the manipulation of the light beam after the nonlinear interaction process. Any loss of the output beam will result in a reduction in the observable quantum effect, eg. the amplitude quadrature squeezing of the light beam. Consequently, most of the components used in the experiments have to first satisfy a stringent low-loss requirement. A listings of the optical component used is shown in Table 3.1.

The steering of light beams in the experiment is done via dielectric mirrors specifically coated for high reflectance at the wavelength of interest. Typically, most of the deflector mirrors chosen have $R > 99\%$ when used at angles between 90° and 45°. These deflector mirrors are used on various high performance 2-axis mounts from Newport, Newfocus, Thorlabs and Lees. The precise alignment of the optical beam into a nonlinear optical cavity is achieved with the construction of a “Z-bend” by a pair of deflectors. In our experiment, these two deflectors were mounted on a home built common platform which provided 4-degrees (x, y, θ_x and θ_y) of uncoupled alignment.

3.2.1 Mode-matching

Once the alignment of the optical beam into a cavity is completed, the job is only half done since the size and shape of the beam must also be considered. A good mode matching of

Part Description	*Wavelength [nm]*	*Manufacturer*	*Model number*	*Comments*
Dielectric deflector mirror	1064 nm	Newfocus	5104	$R > 99\%$ @ $0 - 45\,^{\circ}$ 1” round
Dielectric deflector mirror	1064 nm	Rimkevicius	NA	$R > 99\%$ @ $0 - 45\,^{\circ}$ 1” square
Dielectric deflector mirror	1064 nm	Rimkevicius	NA	$R > 98\%$ @ $0 - 45\,^{\circ}$ 1” square
Lenses	1064 nm	Newport	KPXxxxAR.18	AR coat $R < 0.1\%$
Lenses	532 nm	Newport	KPXxxxAR.14	AR coat $R < 0.1\%$
Nonpolarizing beam splitter	1064 nm	Newport	05BC16NP.9	50/50 ± 2% 1/2” cube
Nonpolarizing beam splitter	1064 nm	CVI	BS1-1064-50-1025-45S	50/50 angle tune 1”round
Nonpolarizing beam splitter	532 nm	Newport	05BC16NP.3	50/50 ± 2% 10mm cube
Nonpolarizing beam splitter	532 nm	CVI	BS1-532-50-1025-45S	50/50 angle tune 1”round
$\lambda/2$ plate 0^{th} order	1064 nm	Newport	10RP02-34	loss $< 0.2\%$ 1” round
$\lambda/2$ plate 0^{th} order	1064 nm	Rimkevicius	NA	loss $< 0.5\%$ 1” round
$\lambda/2$ plate 0^{th} order	532 nm	Newport	10RP02-16	loss $< 0.2\%$ 1” round
$\lambda/2$ plate 0^{th} order	532 nm	Rimkevicius	NA	loss $< 0.5\%$ 1” round
$\lambda/4$ plate 0^{th} order	1064 nm	Newport	10RP04-34	loss $< 0.2\%$ 1” round
$\lambda/4$ plate 0^{th} order	1064 nm	Rimkevicius	NA	loss $< 0.5\%$ 1” round
$\lambda/4$ plate 0^{th} order	532 nm	Newport	10RP04-16	loss $< 0.2\%$ 1” round
$\lambda/4$ plate 0^{th} order	532 nm	Rimkevicius	NA	loss $< 0.5\%$ 1” round
Polarizing beam splitter	1064 nm	Newport	05BC16PC.9	1000:1 extinction 1/2” cube
Polarizing beam splitter	532 nm	Newport	05BC16PC.3	1000:1 extinction 10mm cube
Supermirror	1064 nm	Newport	10CV00SR.50T (high transmission)	$R > 99.99\%$ 1” round
Supermirror	1064 nm	REO	Special	user defined R 1” round
Long wave pass dichroic filter	$T = 1064$ nm $R = 532$ nm	Melles Griot	03BDL001	loss $< 0.2\%$ 1” round
Short wave pass dichroic filter	$T = 1064$ nm $R = 532$ nm	CVI	BSR-15-1025	loss $< 0.2\%$ 1” round
Short wave pass dichroic filter	$T = 1064$ nm $R = 532$ nm	CVI	SWP-45-RS1064-TP532-PW-1025	loss $< 0.2\%$ 1” round
Neutral density filters	All	Melles Griot	03FSG013	1”: OD = 0.04,0.1, 0.3,0.5,1.0,2.0,3.0.

Table 3.1: Optics list

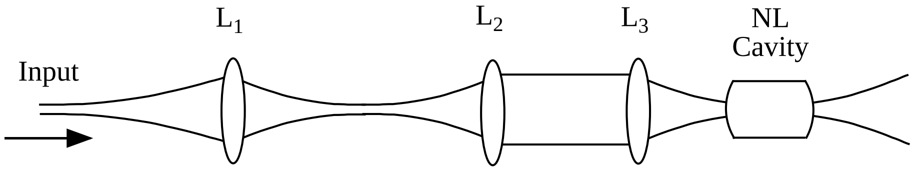

Figure 3.1: Precise mode matching of a Gaussian beam via telescopic lens arrangement. L_1 is used to achieve the desired beam waist. The L_2 and L_3 combination is used to translate the desired beam waist to the location of the nonlinear optical cavity.

a Gaussian beam into the cavity can increase the efficiency of the nonlinear interaction. This is because any unmatched part of an incident beam is simply reflected at the front surface of the cavity and does not take part in the nonlinear optical interaction. Moreover, because nonlinear optical processes are dependent on the optical intensity, the beam waist of the cavity is normally designed to be very narrow (of the order of 10 μm) for the strong focusing of optical field. The mode matching of a freely propagating Gaussian beam into nonlinear optical cavity thus requires high mechanical precision.

Figure 3.1 shows the use of a telescopic lens arrangement to achieve the approximate de-coupling of the waist size and waist position of a Gaussian beam. A lens L_1 is initially used to form the desired beam waist a distance away from the optical cavity. Any adjustment of the position of the lens always results in a simultaneously change of the waist size and the waist position. By using a combination of two lenses, L_2 and L_3 of the same focal length, we can de-couple the waist parameters. We first collimate the beam by placing lens L_2 a focal length away from the beam waist and then use L_3 to re-focus the beam back to its original waist size. Since the beam after L_2 is collimated, the position of L_3 is uncritical to the waist size of the final beam. Thus, by moving only lens L_3, we can adjust the position of the final beam waist without changing its size. The size of the waist can then be separately adjusted by moving both L_1 and L_2.

Obviously, the mode matching of an optical beam is an iterative process. The de-coupling of the waist size and position only simplifies the mode-matching procedure. The best mode-matching achieved using this technique was around 98%. We believe that the remaining 2% is due to the astigmatism of the input Gaussian beam from the source laser which can be compensated with the use of cylindrical lenses or anamorphic prisms.

3.2.2 Polarization optics and dichroics

As far as possible, zeroth order half-wave and quarter-wave plates are used in our experiments to ensure high beam quality. The polarization optics are used for several purposes. At the output of the laser, we used a combination of half-wave and quarter-wave plate to compensate the ellipticity in polarization of the NPRO output. A half-wave plate is also used in conjunction with a Faraday rotator to form a Faraday isolator which is essential in preventing optical feedback to the laser. When used in combination with a polarizing beam splitter, a half-wave plate can provide continuous variation of its transmitted and reflected beam power.

Dichroic mirrors or harmonically coated mirrors are used in our experiments to separate the fundamental from the second harmonic light. Table 3.1 shows the three different dichroics used. In general, the reflection of a beam from the dichroic experiences less loss compare to the transmission and the reflection of s-polarized light is also more efficient than the p-polarized light. Hence, the dichroic mirrors used in the second harmonic generation experiment, where the optical mode of interest is the second harmonic output, has high reflectivity for the s-polarized 532 nm light but high transmittivity for the p-polarized 1064 nm light. Conversely, in the OPO experiment high reflectivity for s-polarized 1064 nm is used, since the optical mode of interest is the low intensity or vacuum sub-harmonic output.

3.3 Mode Cleaners

Mode cleaners play important roles in most quantum optics experiments and measurements. In this section, we discuss the two different types of mode cleaners: Intensity noise cleaner and spatial mode cleaner. Both types of mode cleaners used are empty optical resonators either in a Fabry-Perot or ring configuration. However, there are subtle differences in their design criteria.

3.3.1 Intensity noise cleaner

An intensity noise cleaner is a device which is used for the filtering of high frequency intensity noise from a light source[1]. When light is incident on a locked optical cavity, intensity noise with frequencies higher than the cavity linewidth is reflected off the cavity while noise with frequency lower than the cavity linewidth is transmitted through. Thus an optical resonator can be thought of as a high-pass filter (optical capacitance) for the reflected light and a low pass filter (optical inductance) for the transmitted.

Suppose we have constructed a Fabry-Perot cavity using mirrors with reflectivities R_1 and R_2, and the cavity round trip pathlength and power loss is p and A, we can define the following parameters as given in [16]

$$g_{\mathrm{rt}} = \sqrt{R_1 R_2 (1-A)} \tag{3.1}$$

$$\mathcal{F} = \frac{\pi g_{\mathrm{rt}}}{1-g_{\mathrm{rt}}} \tag{3.2}$$

$$\mathrm{FSR} = \frac{1}{\tau} = \frac{c}{np} \tag{3.3}$$

$$\gamma_{\mathrm{tot}} = \frac{1-g_{\mathrm{rt}}}{\tau} \tag{3.4}$$

$$\mathrm{FWHM} = \frac{\gamma_{\mathrm{tot}}}{\pi\sqrt{g_{\mathrm{rt}}}} \tag{3.5}$$

where g_{rt} and τ are the loss parameter and the cavity round trip time; $\mathcal{F}$ and FSR are the finesse and free spectral range; γ_{tot} and FWHM are the total decay rate and the linewidth of the cavity; and n is the refractive index of the cavity spacer. Our aim of filtering as much high frequency intensity noise as possible from the transmitted beam without ex-

---

[1] Even though feedback control to the laser source (noise eater) can to some extent reduce the resonant relaxation oscillation as well as technical noise of a laser, this method does not produce quantum noise limited results. For a 50/50 beam splitter feedback system, the best performance of a laser noise eater is a noise suppression to 3 dB above the standard quantum limit from a noisy input. Since the generation of squeezed light relies on a quantum noise limited source, feedback control is, in general, inadequate.

Mode Cleaner	No. 1	No. 2	No. 3	No. 4
Type	Intensity	Both	Both	Both
Geometry	Ring	Linear	Linear	Ring
Path length	2.45m	160mm	170mm	400mm
Mirror Parameters	$R_1 = R_3 = 98\%$ $R_2 = 99.9\%$	$R_1 = R_2 = 99.98\%$ $A_1 = A_2 = 28.1$ppm $T_1 = T_2 = 196$ppm	$R_1 = 99.89\%$ $A_1 = 3190$ppm $T_1 = 0.103\%$ $R_2 = 99.98\%$ $A_2 = 2810$ppm $T_2 = 0.0196\%$	$R_2 = 99.99\%$ $T_1 = 1.8\%$ for p-pol $T_1 = 700$ppm for s-pol AR @ 1064 $< 0.1\%$
Finesse	138	14,000	5000	4000 s-pol 400 p-pol
FSR	122 MHz	940 MHz	880 MHz	750 MHz
FWHM	800 kHz	70 KHz	176 kHz	180 kHz s-pol 1.8 MHz p-pol
Powers	$P_{\text{refl}} \approx 60\%$	$P_{\text{trans}} = 75\%$ $P_{\text{refl}} = 8\ \%$	$P_{\text{trans}} \approx 60\ \%$	80% s-pol 95% p-pol

Table 3.2: Mode cleaners

periencing significant reduction in the transmitted optical intensity translate into the following two requirements on the mode cleaners:

- *Narrow cavity linewidth*
  Obviously, narrower linewidth is a desirable characteristic, since this leads to an extended filtering range (larger optical inductance). Narrow cavity linewidth can be achieved either by increasing the cavity length or by increasing the cavity finesse (increasing R_1, R_2 and reducing A). A length increase obviously is at the expense of mechanical stability. However, this may be necessary in situations where high reflectivity mirrors are not available. Furthermore, an increase in the cavity finesse increases the intra-cavity power which may sometimes exceed the damage threshold of the mirror coating [17].

- *High impedance matching*
  The reflected, circulating and transmitted power of an optical cavity locked on resonance are given by [16]

$$P_{\text{refl}} = \frac{(\sqrt{R_1} - (1-A)\sqrt{R_2})^2}{(1-g_{\text{rt}})^2} P_{\text{inc}} \tag{3.6}$$

$$P_{\text{circ}} = \frac{T_1}{(1-g_{\text{rt}})^2} P_{\text{inc}} \tag{3.7}$$

$$P_{\text{trans}} = \frac{T_1 T_2}{(1-g_{\text{rt}})^2} P_{\text{inc}} \tag{3.8}$$

We note that improvement in the transmission can be achieved when we have $P_{\text{refl}} = 0$ assuming a fixed amount of loss present. This corresponds to the impedance matching condition of

$$\sqrt{R_1} = (1-A)\sqrt{R_2} \tag{3.9}$$

3.3.2 Spatial mode cleaner

The purpose of the spatial mode cleaner in quantum optics experiments is to produce a spatially clean beam that has a Gaussian profile with diffraction limited beam quality. In Chap. 2 we have already seen that nonideal homodyning due to mode mismatch can degrade the efficiency of the homodyne measurement. The use of a spatial mode cleaner before the homodyning of optical beams can therefore improve the homodyne efficiency. Both narrow linewidth and high-impedance matching are still necessary for the construction of a good spatial mode cleaner. In addition, we also need to consider the eigenmode degeneracy of the optical cavity.

The difference in resonance frequencies of the $m^{\rm th}$ order to the $(m+1)^{\rm th}$ order eigenmode for a symmetric cavity with mirror radius R is given by

$$\delta\nu = \frac{1}{\pi}\frac{c}{np}\arccos(1-\frac{np}{2R}) \tag{3.10}$$

where $\delta\nu$ is the resonance frequency difference, p is the cavity perimeter and c is the speed of light. We note that for a confocal cavity $np = 2R$. This leads to $\delta\nu = c/2np = \mathrm{FSR}/2$. That is, all of the odd order confocal modes is degenerate at half of the FSR and all of the even order confocal modes is degenerate with the fundamental TEM_{00} spatial mode. When situation like this arises, the locking of a cavity at the fundamental resonance does not guarantee any rejection of the even order modes, since they are themselves resonant with the optical cavity. Thus, a good spatial mode cleaner requires

$$\delta\nu \neq \frac{r}{s}\mathrm{FSR} \tag{3.11}$$

for all small integer numbers of r and s. This is the condition which guarantees the nondegeneracy of high order spatial modes.

For the experiments of this thesis, four mode cleaners have been constructed. Table 3.2 shows their respective cavity parameters. The first intensity noise cleaner (No. 1) is used for the experiments on squeezed state generation via frequency doubling. Mode cleaners No. 2 and No. 3 are the second generation of mode cleaners which have significantly higher finesses and can be used as both spatial mode as well as intensity noise cleaners. In the experiments of squeezed vacuum generation, mode cleaner No. 3 is mainly used. The maximum incident power on mode cleaner No. 2 and No. 3 is 10 mW. Finally, mode cleaner No. 4 is based on a compact ring configuration similar to that described in [18]. This third generation of mode cleaner can also serve as both intensity noise and spatial mode cleaner. Furthermore, it has an extremely high damage threshold due to the special dielectric coating from Research Electro-Optics Inc. As much as 1 W of incident power can be incident on this cavity without any observable damage. Since the mode cleaner is in a ring cavity configuration, a change in the polarization state of the incident light can change the cavity finesse from 4000 to 400 due to the differences in mirror reflectivities.

3.4 The nonlinear medium

Bulk $\mathrm{MgO:LiNbO_3}$ was chosen as the nonlinear medium for the study of second harmonic generation and optical parametric oscillation. The reason is its relatively high nonlinearity and its compatibility with the Nd:YAG laser wavelength. The Magnesium oxide doping was introduced into bulk Lithium Niobate for the prevention of photorefractive damage. This doping sometimes introduces inhomogeneities and scattering to the nonlinear medium but the problems have been significantly reduced by improvements on the crystal growing and doping techniques. There are many other alternative nonlinear media, for example KTP is a commonly used $\chi^{(2)}$ nonlinear medium. However, for the frequency doubling and degenerate parametric downconversion with Nd:YAG wavelength, KTP crystal experiences beam “walk-off” and can only be used in a type II phase matched condition. Even though beam walk-off can be compensated by using a pair of oppositely oriented crystals in a single cavity, this complicates the setup and introduces additional losses. An alternative solution to this is to use KTP crystal for Nd:YAP laser wavelength (1.08 μm) as demonstrated in [19, 20]. Details on second harmonic generation with KTP crystals using Q-switched Nd:YAG laser are presented in Appendix F.

In recent years, periodically poled lithium niobate (PPLN) has shown great promise as a medium with many times higher nonlinearity to the bulk materials [21–23]. An attempt was made to use PPLN in the SHG setup[2]. We found that even though the available nonlinearity is higher, the periodic poling of the material can introduce higher losses. Since the factor of interest is in the ratio of nonlinearity to loss, the gain in using PPLN is not significant. Moreover, PPLN was demonstrated to have an anomalous self-focusing effect at the wavelength of 532 nm making the squeezed state generation via frequency doubling of Nd:YAG unsuitable. It is the author’s opinion that in spite of the modest nonlinearity of bulk $\mathrm{MgO:LiNbO_3}$, this material still remains to be one of the most suitable nonlinear material for the study of $\chi^{(2)}$ quantum effects.

3.5 Design considerations of the nonlinear resonators

Since the strength of optical nonlinearity is dependent on the intensity of the pump beam, methods have to be devised to attain the desired high optical field intensity. There are many possible methods of increasing the available intensity for nonlinear optical interactions. In some cases, the operation of lasers can be pulsed to produce short but very intense output light. Many experiments have utilized the Q-switching and mode-locking of lasers to generate squeezed states of light [24–27]. The technique used mostly in this thesis is that of the continuous-wave (CW) optical resonator method in which resonators were used to set up high intra-cavity field. By placing the nonlinear medium within the resonator, the intensity dependent nonlinear interaction is enhanced. Some of the more common optical resonators are shown in Figure 3.2. We can generally divide them into the following categories:

3.5.1 Standing wave and traveling wave cavities

Optical resonators can be formed either by a standing wave or a traveling wave between mirrors. Figure 3.2 (a, b and c) are examples of standing wave cavities. The advantage of a standing wave cavity is that it has lower loss due to fewer reflecting surfaces. However, in most setups a Faraday isolator is required to isolate the reflected light from the standing wave cavity to avoid feedback to the pump laser. In addition, standing wave cavity produces nodes and antinodes within the optical resonator. In some situation, this is undesirable as it may give rise to spatial hole burning effects.

---

[2] In collaboration with R. Batchko, C. C. Harb and R. L. Byer of Ginzton Laboratory, Stanford University

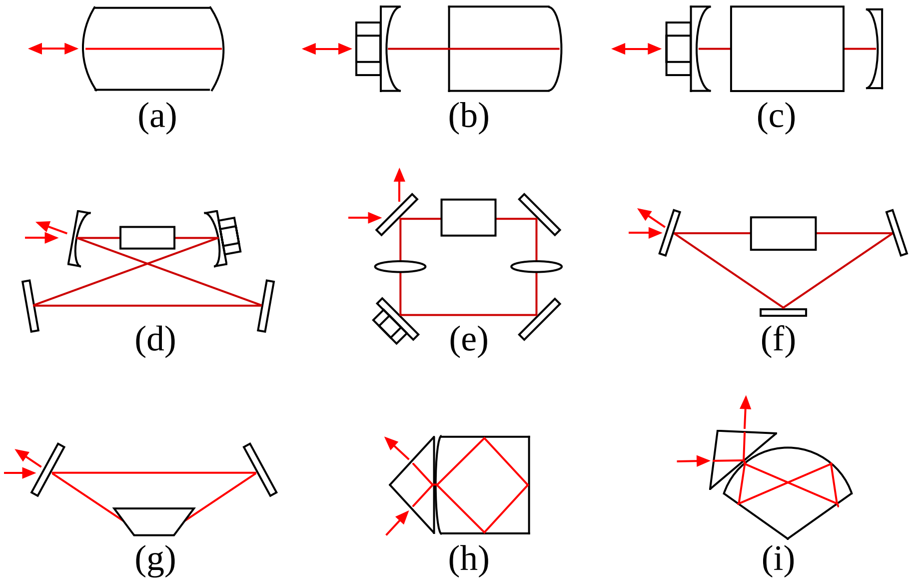

Figure 3.2: Nonlinear optical resonators: (a) Monolithic linear, (b) Hemilithic linear, (c) Straight cut linear, (d) Bow-tie, (e) Rectangular ring, (f) Triangular ring, (g) Brewster ring, (h) and (i) Monolithic TIR / FTIR cavities with outcoupling prisms.

The alternative to standing wave cavities are the ring or traveling wave cavities as shown in Figure 3.2 (d, e, f, g, h and i). The reflected light of a ring cavity is spatially separated from the incident light and thus does not require Faraday isolation. However, a ring cavity is in general less compact than a standing wave cavity. In situations where spatial mode quality is critical, an even number of reflections are necessary to avoid the inversion of any spatial inhomogeneity within the cavity. Thus, the most common configurations of rings, eg. “bow-tie” cavities, have 4 reflecting surfaces. The triangular cavity shown in Figure 3.2 (f) is generally not an ideal setup. Another rule for designing a ring cavity is to make each reflection as near to normal incidence as possible, particularly on mirrors with considerable curvature. This is to avoid spatial as well as polarization distortions.

Due to loss consideration, all of the squeezing experiments performed in this thesis uses linear standing wave cavities in favor of the ring cavities.

3.5.2 Monolithic, hemilithic and external mirror cavities

A monolithic cavity is one in which a single bulk crystal is used to form the spacer as well as the reflecting surfaces, (see Figure 3.2 a, h and i). The biggest advantage of a monolithic cavity is in its operational stability. Since the reflecting surfaces of the cavity are mechanically coupled with each other, the optical locking is usually robust. Furthermore, if the medium is clear, this geometry is very low loss due to the absence of media (crystal / air) interface within the cavity. Unfortunately, the stability of monolithic cavities comes with some inflexibility in the operation. For example, the finesse of the cavity is fixed by the dielectric coatings onto the monolith. It is only through repolishing and recoating that the cavity finesse can be altered. The optical length and most of the other cavity parameters of a monolithic are fixed as well. It is therefore normally difficult to scan the optical cavity more than a fraction of an FSR without exerting considerable amount of stress to the monolithic crystal. The monolithic cavity thus has less operational degrees of freedom but is mechanically very stable.

External mirror cavities with flat crystal as shown in Figure 3.2 (c, d, e, f and g), on the other hand, offer a lot of flexibility in the scanning and design optimization. Slight misalignment of the nonlinear crystal can even be used to find regions of varying finesses and nonlinearities arising from inhomogeneity in the end mirrors or nonlinear medium. However, because of the presence of two air / crystal interfaces, losses as well as dispersion in the external mirror cavities are normally higher than that of the monolithic cavities.

A compromise of the two geometries is the hemilithic (or semi-monolithic) cavity shown in Figure 3.2 (b). This system offers lower loss because of the single air / crystal interface but has good operational flexibility. Scanning the optical resonator by several FSR is easily achieved by using piezo-electric actuator mounted on the output coupling mirror. Because the output coupling surface is detached from the nonlinear medium, changes required in the cavity design are easily implemented with the swapping of the external mirrors.

For nonlinear optics experiment where there are more than one optical mode in a cavity, it is possible to construct a resonator which is monolithic for one mode but (say) hemilithic for the other. Once the advantages and limitations of the individual configurations are well understood, we can tailor a cavity design to suit the specifications of the experiment.

3.5.3 Dielectric and evanescent coupling

There are three methods of light reflection in an optical resonator. They are total-internal-reflection (TIR), frustrated total-internal-reflection (FTIR) and dielectric coating reflection. FTIR is achieved by placing a medium with matching refractive index close to the evanescent wave of a TIR light field. By minute adjustment of the separation, different amounts of light field can be coupled out of the evanescent light field. In both TIR and FTIR, the losses involved in the reflection and transmission are very small, limited only by the surface quality of the crystal. However, since TIR of light within a cavity can only be achieved at reflection angles larger than the critical angle of the air / crystal interface, both FTIR and TIR are not suitable for the construction of a linear cavity. It is also well known that the control of the transmittivity via FTIR is extremely sensitive to mechanical positioning due to the exponential decay of the evanescent wave amplitude. These are reasons why in recent years, quantum optics experiments are steering away from FTIR coupling setups as shown in Figure 3.2 (h and i).

The used of dielectric stacks as a reflection surface is now a matured technology. With losses as small as the parts-per-million (ppm) level, it is possible to construct an optical resonator with finesse of more than 100,000 from a linear standing wave cavity with dielectrically coated mirror pair. Reflectivity of the dielectric coating can be specified to $\sim \pm 0.2\%$ accuracy even for harmonically defined reflectivities (eg. 96% @ 1064 nm and 10% @ 532 nm). In addition, phase shifting of the light field due to dielectric reflection can also be specified. All of the crystals used in this thesis had their dielectric coatings done at the Laser Zentrum Hannover (LZH).

Photodiode model	*Measurement wavelength*	*Material*	*Quantum efficiency*	*Maximum power*
Hamamatsu S1721	532 nm	Silicon	90%	50 mW
Hamamatsu S1722	532 nm	Silicon	90%	50 mW
Hamamatsu S3590-04	532 nm	Silicon	88%	100 mW
EG&G FND-100	532 nm	Silicon	65%	30 mW
EG&G C30641G	1064 nm	InGaAs	80%	10 mW
EG&G C30642G	1064 nm	InGaAs	80%	25 mW
Epitaxx ETX-200	1064 nm	InGaAs	94%	25 mW
Epitaxx ETX-500	1064 nm	InGaAs	94%	$<$ 20 mW

Table 3.3: Photodiodes

3.6 The servo-control systems

In most of the experiments done in this thesis, the Pound-Drever-Hall method [28] is used as the method of locking optical cavities on resonance. We used home built proportional-integral-differential (PID) or servo units to provide the electronic feedback control to the experiment. Two different systems of PID[3] with comparable performance are shown in Appendix C.

The temperature control of nonlinear crystal is also achieved using a home built PID controlling unit as shown in Appendix D. The accuracy achieved in the temperature stability was inferred through the error signal of the feedback circuit and corresponds to a temperature fluctuation of ± 2mK. This is much better than most of the commercial temperature controller units.

3.7 Detection of light field

Table 3.3 shows the list of photodiodes used in the many experiments of this thesis. The steps taken to ensure high quantum efficiency performance from the photodiodes are: Initially the glass window of the photodiode was removed to eliminate reflection loss; The photodiodes are then aligned at or near Brewster angle to further reduce reflection off the semiconductor surface; Finally retro-reflecting mirrors were used to recapture the remaining reflected light from the first incidence.

The quantum efficiency of the photodiode was calculated by measuring the DC photocurrent of the photodiode and comparing it with the optical power of a given light

---

[3] By courtesy of Dr. M. S. Taubman for UniPID 5.O and Dr. M. B. Gray for M1

beam using the following expression

$$\eta_{\rm QE} = \frac{N_e}{N_{h\nu}} = \left(\frac{P}{h\nu}\right)\left(\frac{I}{e}\right) \tag{3.12}$$

where N_e and $N_{h\nu}$ are the number of electrons and photons, respectively, inferred from macroscopic measurements of the current I, and the optical power P. e is the electronic charge and $h\nu$ is the energy of the photon quantum. Using the above methods, two photodiodes were found to be best suited for our purpose. The first is the ETX-500 InGaAs diodes from Epitaxx. Quantum efficiency of up to 94% is attainable for measurement of Nd:YAG wavelength (1064 nm). The detection of the second harmonic of Nd:YAG (532 nm) however, is much less efficient. The use of silicon diodes S-1721 from Hamamatsu has achieved the best quantum efficiency of around 90%. Naturally, the accuracy of the quantum efficiency measurement is very much limited by the accuracy of the power meter used in the measurements which has a $\sim 5\%$ NIST traceable standard error.

The circuit diagrams used for the RF amplification of the photocurrents are given in Appendix B. A more detailed discussion on the design of theses photodetectors is given in the paper of Gray *et al.* [29].

3.8 Data retrieval

A RF spectrum analyser (SA) was frequently used for taking measurements of noise spectra in this thesis. An understanding of the operation of the instrument is thus fundamental to the analysis of the noise spectra and signal-to-noise ratio (SNR) measurements.

The SA used in the work of this thesis was a Hewlett Packard model 8568B with a frequency range from 100 Hz to 1.5 GHz. When necessary, a tracking generator model 8444A-OPT059 (500 kHz - 1.5 GHz) was set up for synchronous operation with this SA. For the simultaneous analysis of phase and amplitude transfer functions, a Hewlett Packard 3589A network analyser was used.

Most of the technical information of the SA is contained in the manual and the application notes of the equipment [30]. However, it is worthwhile to highlight one important detail that is often overlooked in the measurement of signal-to-noise using a SA.

For a deterministic signal, the peak signal voltage of $V_s^{\rm peak}$ measured by the envelope detector within the SA is converted to a root-mean-square (RMS) value with a scaling factor of $1/\sqrt{2}$ (-3 dB). A logarithmic amplifier is then used to convert this RMS value to dBm (log scale). The calibrated and converted reading is then filtered and displayed on screen.

In most commercially available spectrum analysers, it is assumed that the measurements are on deterministic modulation signals. The measurement of Gaussian noise hence poses a problem with the system calibration. Figure 3.3 shows the probability density functions of a deterministic modulation signal and a Gaussian noise source. Clearly, if inferences made on the peak noise voltage $V_n^{\rm peak}$ were similar to that of a deterministic modulation, a different value for the noise RMS will be obtained. The systematic errors can be summarized into three main factors:

- *Sinusoidal assumption error*
  This error arises from the incorrect inference of the Gaussian noise source as being deterministic and sinusoidal in nature. When the input Gaussian noise is band-

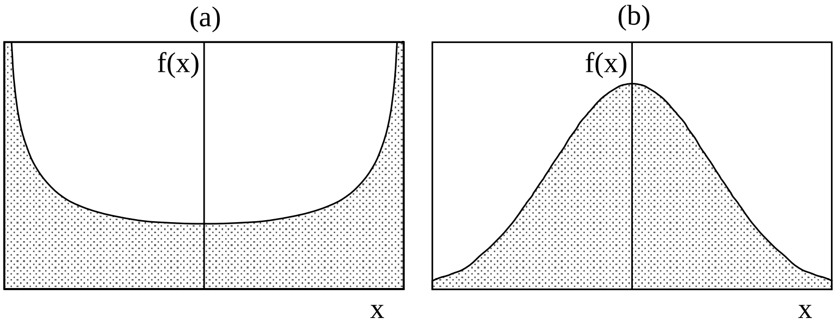

Figure 3.3: Probability distribution functions of (a) a deterministic sinusoidally modulated signal and (b) Gaussian noise. The y-axis is the probability density $f(x)$ and the x-axis the variable value x.

width limited, it changes into a Rayleigh distributed noise. A mean error of 1.05 dB will occur when Gaussian noise measurement is assumed to be sinusoidal.

- *Logarithmic amplifier error*
  Since the calibration of the logarithmic amplifier is only done for deterministic signals, the feeding of Rayleigh distributed noise through it will produce a skewed Rayleigh distribution causing a further mean error of 1.45 dB.

- *Resolution bandwidth error*
  The resolution bandwidth filter of the SA is typically the 3 dB width of the signal. With Gaussian noise, the equivalent bandwidth is typically 1.05 (0.21 dB) to 1.13 (0.53 dB) times greater than the signal bandwidth. Hence, this results in an error of around -0.5 dB.

The combined systematic error for noise measurement is hence approximately 2 dB (1.05 + 1.45 - 0.5). The reader is advised to peruse the equipment application notes [30] for a more technical discussion. A working numerical example of a typical signal-to-noise measurement is given in Appendix A.

Apart from the spectrum analyser, high speed digital CRO's (Hewlett Packard Infinium 500 MHz 2Gsa/s and Hewlett Packard 5460B 150 MHz) were also used in the retrieval of experimental data. In particular, work done on the reconstruction of Wigner function from measured quadrature phase amplitudes given in Appendix G requires the unprocessed photocurrent fluctuations of the detected light beam. In this case, we interfaced the digital CRO's with a Macintosh computer via an I/O card or a National Instruments LabVIEW program.

Part II

Generation of Squeezed States

Chapter 4

The Second Order Optical Nonlinearity

And now here is my secret, a very simple secret: It is only with the heart that one can see rightly; what is essential is invisible to the eye.

The Little Prince, Antoine de Saint-Exupéry (1940).

Overview

In this chapter we describe the general characteristics of second order $\chi^{(2)}$ nonlinear optical processes. Conditions required for the $\chi^{(2)}$ interactions are discussed and the general Hamiltonian of interactions presented.

4.1 Introduction

Until this century, the history of optics has always assumed that optical media were linear. The consequence of this assumption has led to many simple rules in optics: The principle of superposition in classical optics states the linear combination of any two solutions of an optics problem is also itself a solution; Propagation of light through an optical medium does not change the frequency of the light; Optical properties of a medium, such as refractive index and absorption coefficient, are independent of the intensity of light. With the invention of the laser in the 1960's, high optical intensities previously unattainable have revealed observations deviating from all of the simple rules stated above.

For light with frequencies far detuned from all of the atomic resonances, the most important optical parameter of a dielectric medium is the atomic polarization $\mathcal{P}$. The macroscopic polarization of a medium arises from the sum effect of minute displacements of the valence electrons from their normal orbit about the constituent atoms or molecules, that is the atomic dipole moments. When an electro-magnetic field traverses through a dielectric medium, a macroscopic polarization is induced. The induced polarization is capable of re-radiating its energy as an electro-magnetic field, thus changing the characteristics of the original incident field. For weak fields, the dielectric polarization mimics the traversing wave by oscillating at the same frequency with slight phase shift. This give rise to a change in the refractive index. For intense incident fields, the relationship between the polarization and applied field the can be expressed in a converging power series as

$$\mathcal{P} = \epsilon_o(\chi\mathcal{E} + \chi^{(2)}\mathcal{E}^2 + \chi^{(3)}\mathcal{E}^3 + \ldots) \tag{4.1}$$

where ϵ_o is the permittivity of free space, $\mathcal{E}$ is the applied electric field, χ is the linear susceptibility and $\chi^{(i)}$ are the i^{th} order nonlinear susceptibilities of the medium.

In spite of the very rapidly decreasing magnitudes of $\chi^{(i)}$ with increasing order, it is these nonlinear susceptibilities that give rise to a host of nonlinear optical phenomena. At high optical intensity where $\mathcal{E}$ is large, the principle of superposition no longer holds. Optical properties such as refractive index and absorption are now intensity dependent. Furthermore, the passage of light through a dielectric medium can produce new optical frequencies.

The focus of this part of the thesis is on the processes involving the $\chi^{(2)}$ nonlinearity and how such processes can produce squeezed light. We find that the second order nonlinearity $\chi^{(2)}$ alone, is sufficient to produce a host of interesting optical phenomena such as nonlinear absorption and gain, second harmonic generation (SHG), optical power clamping, optical parametric oscillation (OPO) and amplification (OPA). In the next section, we present a general description of the individual processes.

4.2 Optical $\chi^{(2)}$ processes

The basic optical processes involving the $\chi^{(2)}$ nonlinearity are illustrated in Figure 4.1. We note that a common feature of these processes is that it involves the interaction of 3 photons, $\chi^{(2)}$ processes are therefore also known as three-wave mixing processes. The processes can be divided into two complementary categories: The *up-conversions*, where two photons of lower energy combine to form a more energetic photon and the *down-conversions* where a single photon is converted into two photons of lower energies.

Upconversion processes include second harmonic generation where 2 photons of frequency ω are combined to form a photon of frequency 2ω. When the pair of incoming photons have different frequencies, $\omega - \Delta$ and $\omega + \Delta$, their combination is known as sum frequency generation.

Unlike the upconversion processes, some downconversion processes have associated threshold powers below which the dissociation of a 2ω photon into the sub-harmonic photons does not occur. These processes are called degenerate and non-degenerate optical parametric oscillation (DOPO and NDOPO). The threshold condition can be lifted when a seed field is introduced into the nonlinear medium. Thus, degenerate and non-degenerate parametric amplifications do not have a threshold power. We can also think of the DOPO and NDOPO as being vacuum seeded, that is to say it is the fluctuations of the vacuum field which trigger the dissociation of the 2ω photons.

4.3 Conditions for $\chi^{(2)}$ interactions

In this section, we examine the conditions necessary for the nonlinear interaction, specifically in the context of a CW pumped nonlinear medium in an optical resonator.

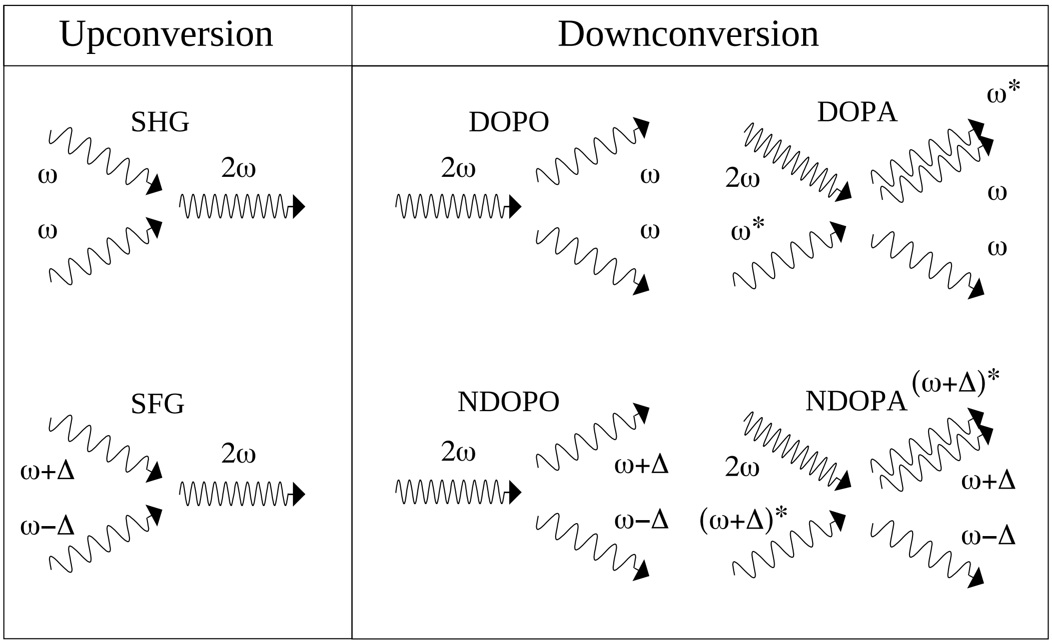

Figure 4.1: Overview of the basic $\chi^{(2)}$ nonlinear interactions. *Left*: The upconversion processes of second harmonic generation and sum-frequency generation. The Feynman-like diagram represent the destruction of two lower energy photons and the production of a higher energy (second harmonic) photon. The nonlinear atomic medium necessary for the photon-photon interaction is not shown for simplicity. *Right*: The downconversion processes. Degenerate and non-degenerate optical parametric oscillations are shown in the left column. Unlike the upconversion processes, the downconversions via $\chi^{(2)}$ are normally associated with a threshold power. By the introduction of a seed field, the right most column shows the process of degenerate and non-degenerate optical parametric amplifications. * denotes the seed photons.

4.3.1 Conservation of energy

Like all physical processes, the conservation of energy must be satisfied during the $\chi^{(2)}$ interaction. For three photons with frequencies ω_1, ω_2 and ω_3, we thus require

$$\omega_1 = \omega_2 + \omega_3 \tag{4.2}$$

This condition must be satisfied precisely for all nonlinear interactions.

4.3.2 Conservation of momentum: Phase matching

The conservation of momentum in a nonlinear optical process is often referred to as the phase matching condition. For the momentum of the three photons to be conserved, we require their optical wavevectors to fulfill the following equation.

$$k_1 + k_2 = k_3 \tag{4.3}$$

where the wavevectors are given by $k_i = n_i\omega_i/c_0$, n_i is the refractive index of the nonlinear medium experienced by the i^{th} field and c_0 is the speed of light in vacuum. When this equation holds exactly, the system is said to be *phase matched*. However, unlike the condition imposed by the conservation of energy, a small amount of phase mismatch is allowed at the expense of a reduction in the efficiency of the nonlinear process. To deal with situations where this occurs, we define the phase mismatch term $\Delta k \equiv (k_1+k_2)-k_3$. The simultaneous fulfilment of the conservation of energy and the phase matching condition thus imposes a relationship on the refractive indices. From here onwards we restrict our explanation to that of SHG or degenerate OPO where $\omega_1 = \omega_2$. Treatment of the non-degenerate processes is only a straight forward extension of the argument. The phase matching condition for the refractive indices is simply

$$n(\omega_1) = n(\omega_3) \tag{4.4}$$

Since in most dielectrics the refractive index is a function of the optical frequency (ie. dispersive), the above condition is seldom fulfilled. However, there are three methods of achieving phase matching in crystalline material where birefringence is present:

- *Type I phase matching*
  In type I phase matched material, the refractive index condition is satisfied when the polarizations of the two lower energy modes are the same but orthogonal to the polarization of the high energy mode ($\uparrow_{\omega_1} + \uparrow_{\omega_2} = \rightarrow_{\omega_3}$). Since the crystal is birefringent, a change in polarization angle with respect to the crystal axis can change the refractive index of the light beam. Angle tuning and temperature tuning can therefore be used to find the phase matched regime. *Noncritical* phase matching occurs when one of the polarizations is parallel with the optical axis (z), and the beam is free to propagate along any direction of the xy-plane. An example of type I noncritically phase matched system is the use of MgO:LiNbO$_3$ at Nd:YAG wavelength for second harmonic generation.

- *Type II phase matching*
  In type II phase matching, the refractive index condition is satisfied when the two lower energy modes are orthogonal with each other and the high energy mode has its polarization the same as one of the lower energy modes ($\uparrow_{\omega_1} + \rightarrow_{\omega_2} = \uparrow_{\omega_3}$). Phase matching can be similarly achieved via angle or temperature tuning. It is worth while to note that in many systems, type II phase matching gives rise to beam walk-off on one of the low frequency modes. Hence, such systems are not ideal for use in an optical cavity. However, with some effort the walk-off effect can be compensated by using a pair of oppositely oriented crystals. An example of type II phase matched system without beam walk-off is the use of KTP at Nd:YAP wavelength for second harmonic generation.

- *Quasi-phase matching*
  In a quasi-phase matched material, the phase matching is done via a periodic manipulation of the cumulated relative optical phase. By the short periodic inversion of the crystal domain, the phase mismatch is governed by

  $$\Delta k_{\mathrm{QPM}} = (k_1 + k_2) - k_3 - \frac{2\pi}{\Lambda} \tag{4.5}$$

  where Λ is the crystal inversion period. Hence, the condition imposed on the refractive indices is no longer required due to an additional periodic poling term. The advantage of periodic poling is that it can provide a means to access dielectric polarization with high nonlinearity which are otherwise unreachable with angle and temperature tuning. An example of quasi-phase matching is the use of periodically poled lithium niobate (PPLN) at Nd:YAG wavelength for the purpose of frequency doubling. In this situation, the polarization of all three modes are the same ($\uparrow_{\omega_1} + \uparrow_{\omega_2} = \uparrow_{\omega_3}$).

For the most of this thesis, the type I noncritical phase matched MgO:LiNbO$_3$ crystal is used with a Nd:YAG laser pump. The phase matching condition of this system, is succinctly summarized by the phase mismatch expression obtained from the Sellmeier equation [31]

$$\Delta k = -8666(1 - \frac{\lambda_0}{\lambda_s})^2 \mathrm{cm}^{-1} + 7.49(T - T_0)\mathrm{cm}^{-1}\mathrm{K}^{-1} \tag{4.6}$$

where $\lambda_0 = 1064$ nm and $T_0 = 107°\mathrm{C}$. The strength of a nonlinear interaction is given by a nonlinear coupling function, which we state without proof to be

$$g(\Delta k\ z) = \mathrm{sinc}\left[\frac{\Delta k\ z}{2}\right] e^{i\Delta k\ z/2} \tag{4.7}$$

where z is the length of the interaction region. Figure 4.2 shows a plot of this function. We note that the peak of the nonlinear interaction strength is a U-shaped curve as a function of temperature with its degeneracy point at around 107 °C. An increase in temperature above this point hence introduces frequency nondegeneracy of the subharmonic modes.

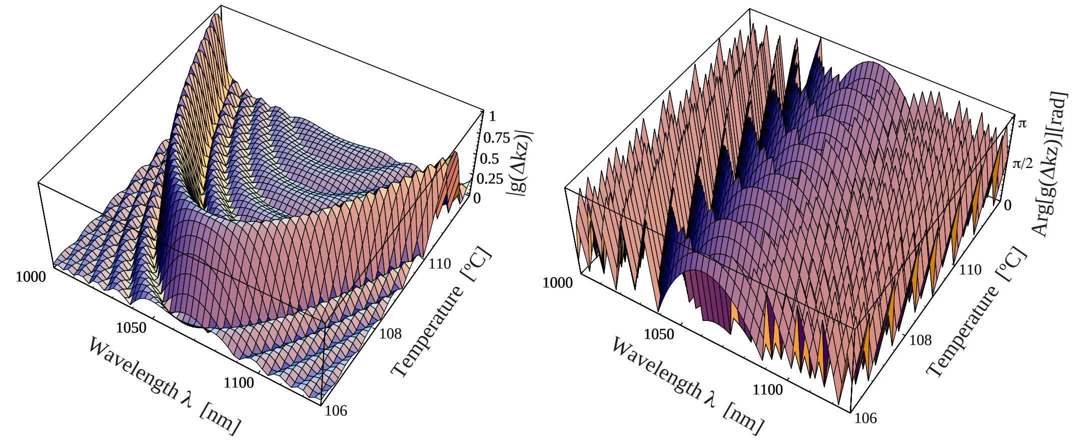

Figure 4.2: Phase matching function for MgO:LiNbO$_3$. *Left*: nonlinear coupling strength $|g(\Delta kz)|$ is plotted against the crystal temperature and the subharmonic wavelength (z = 1). *Right*: Similar plot for $\arg[g(\Delta kz)]$, unlike the strength of the nonlinear interaction, the nonlinear coupling phase varies rapidly across both temperature and wavelength.

More insight into the phase matching condition can be gained by looking at the cross-sectional views of the nonlinear coupling function. If a cross-section is taken along the temperature axis, we find that $|g(\Delta kz)|$ takes the shape of a sinc function. This describes the effect of temperature tuning. If a cross-section at the point of degeneracy were taken along the wavelength axis, we find a gain profile of the nonlinear crystal as shown in Figure 4.3. It is interesting to note that even at the point of degeneracy, the gain bandwidth of the medium is still quite broad. The magnified inset of the figure shows that a 1% decrease in the nonlinear coupling corresponds to a 12 nm gain width.

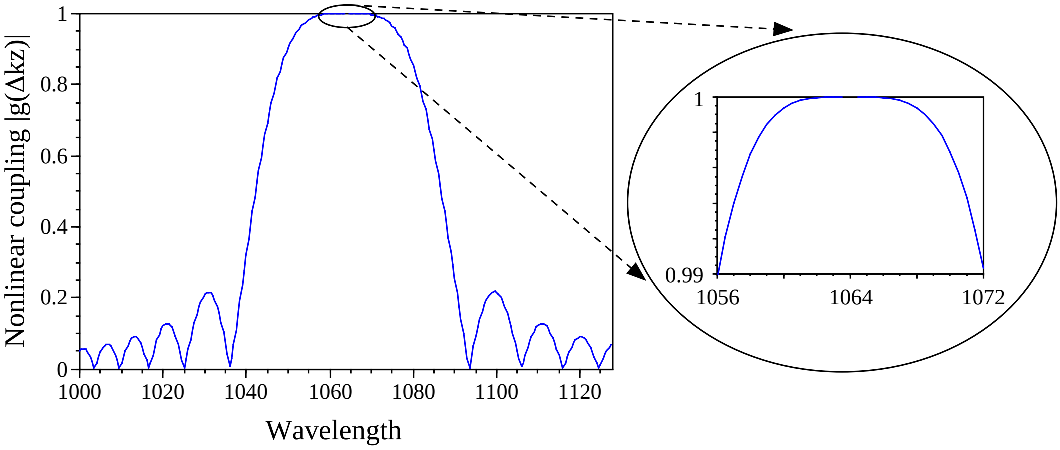

Figure 4.3: Nonlinear coupling $|g(\Delta kz)|$ for $\mathrm{MgO:LiNbO_3}$ at the degeneracy temperature of 107 °C as a function of wavelength.

4.3.3 Cavity resonance

The last set of conditions required for efficient nonlinear interaction within an optical cavity are the resonance conditions of the three interacting modes

$$\omega_1 = p\frac{\pi c_0}{n_1 L} \tag{4.8}$$

$$\omega_2 = q\frac{\pi c_0}{n_2 L} \tag{4.9}$$

$$\omega_3 = r\frac{\pi c_0}{n_3 L} \tag{4.10}$$

where p, q and r are positive integers, n_i is the refractive index of the $\mathrm{i^{th}}$ mode and L is the length of the cavity. These resonance conditions ensure that the nonlinear cavity maintains a high circulating power of the interacting modes, thereby enhancing the efficiency of the nonlinear process. Again, unlike the condition imposed by the conservation of energy, the cavity resonance conditions are not necessities, and nonlinear optical processes are even possible in a single-pass situation. However for the CW pump power used in most parts of this thesis, cavity resonance conditions play an important role in the nonlinear interaction. As discussed in Chap. 3, the designs of a nonlinear cavity can be diversely different. At times, it is more advantageous to have a cavity where one of the interacting modes is resonant while the other modes merely single or double pass through the nonlinear medium. In such situations, the nonresonant modes are not aware of the existence of any optical cavity conditions. Let us examine these situations with specific application to SHG and OPO in more detail.

- *Second harmonic generation*
  There are two different methods of SHG using a CW pump field on an optical cavity. The first method is to form an optical cavity of the fundamental pump field. This method is called singly (pump) resonant SHG. This enables the optical intensity of the fundamental field to build up within the cavity thus making the conversion to the second harmonic efficient. However, the second harmonic does not form a

cavity within the crystal and escapes after a single or double traversal of the cavity.

The second method of SHG is to provide optical resonances for both the fundamental and the second harmonic fields in the nonlinear cavity. Both modes then have to be locked on resonance. This is in general not guaranteed by only locking one of the modes as differential phase shifts may exist at the cavity reflection surfaces. However, it is apparent that there are advantages in making both cavities resonant since the effective nonlinearity of the system is further enhanced.

- *Optical parametric oscillation*
  An OPO is said to be *triply resonant* (TROPO) when all three of the interacting modes satisfy the cavity resonance conditions of Eqs. (4.8-4.10) (see Figure 4.4a). The TROPO is therefore the most efficient. However, such a system requires relatively complex locking in order to keep all three optical modes in simultaneous resonance.

  On the other hand singly resonant OPO (SRO), as shown in Figure 4.4(d), is the simplest in its operation. However, the threshold of such devices are orders of magnitude larger than the TROPO or the doubly resonant OPOs (DROs) (see Figure 4.4(b) and (c)). Note that a SRO where only the pump is resonant and both signal and idler are non-resonant is not a practical device due to the extremely large threshold.

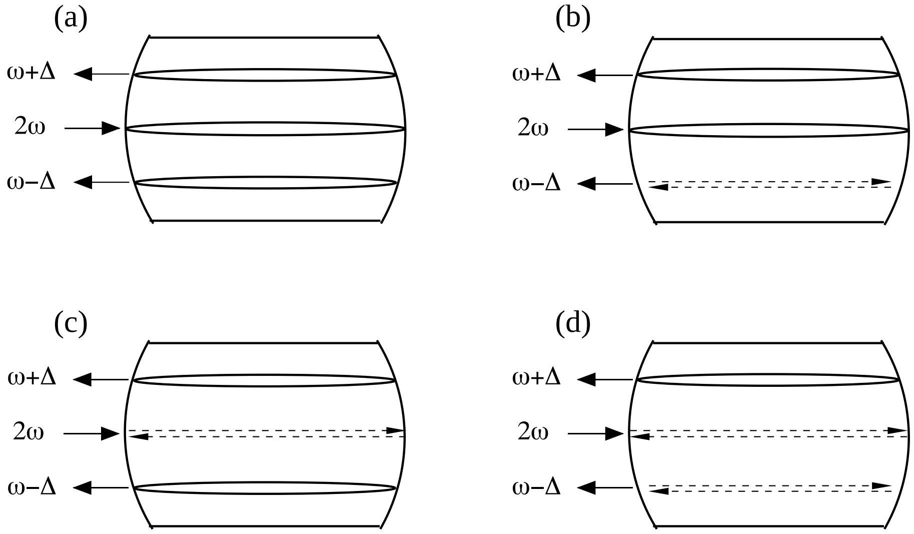

Figure 4.4: Resonance conditions of parametric oscillators. (a) Triply resonant OPO (TROPO); (b)Doubly resonant (pump and signal) OPO; (c) Doubly resonant (signal and idler) OPO and (d) Singly resonant OPO (SRO). $\omega + \Delta$ is commonly referred to as the signal output and $\omega - \Delta$ the idler output of the OPO.

For the MgO:LiNbO$_3$ material used in this thesis, the loss experienced by the second harmonic (532 nm) of the Nd:YAG wavelength is 4% cm^{-1}. This is comparatively larger than the 0.1% cm^{-1} loss experienced by the Nd:YAG wavelength (1064 nm). For this reason, the gain in making the second harmonic of the Nd:YAG resonant is minimal. We therefore decided on the simpler, singly (pump) resonant SHG and doubly (signal and idler) resonant OPO schemes for the generation of squeezed states.

4.4 The $\chi^{(2)}$ Hamiltonian

Let us depart from the descriptive nature of this chapter and turn to a more quantitative discussion of the $\chi^{(2)}$ processes. We start with the general Hamiltonian for 3-wave mixing [8, 32]

$$\begin{aligned}\hat{\mathcal{H}} &= \hbar\omega_1\hat{a}_1^\dagger\hat{a}_1 + \hbar\omega_2\hat{a}_2^\dagger\hat{a}_2 + \hbar\omega_3\hat{a}_3^\dagger\hat{a}_3 + \\ &\quad \frac{1}{2}i\hbar\kappa(\hat{a}_1^\dagger\hat{a}_2^\dagger\hat{a}_3 - \hat{a}_1\hat{a}_2\hat{a}_3^\dagger) + \\ &\quad i\hbar(E_1\hat{a}_1^\dagger e^{-i\omega_1 t} + E_2\hat{a}_2^\dagger e^{-i\omega_2 t} + E_3\hat{a}_3^\dagger e^{-i\omega_3 t} - \text{h.c.}) + \\ &\quad \hat{a}_1\hat{\Gamma}_1^\dagger + \hat{a}_1^\dagger\hat{\Gamma}_1 + \hat{a}_2\hat{\Gamma}_2^\dagger + \hat{a}_2^\dagger\hat{\Gamma}_2 + \hat{a}_3\hat{\Gamma}_3^\dagger + \hat{a}_3^\dagger\hat{\Gamma}_3 \end{aligned} \tag{4.11}$$

where $\hat{a}_i$ and ω_i ($i = 1, 2, 3$), denote the annihilation operators and angular frequencies for the signal, idler and second harmonic modes. κ is the $\chi^{(2)}$ second order nonlinearity of interest. E_i are the pump field amplitude of the respective modes. The last six terms of the Hamiltonian correspond to the Liouvillians describing the coupling between the discrete intra-cavity modes with the extra-cavity reservoir continuum. Terms from the first line of the Hamiltonian represent the rest energy of the system. The second line of the Hamiltonian are the interaction terms and the third line provides a description of the pumping of respective modes.

In its complete generality, this Hamiltonian contains both the classical and quantum dynamics of all of the $\chi^{(2)}$ interaction processes. Although this Hamiltonian can be solved rigorously using the master equation method, we shall only concern ourselves for the moment with the semi-classical solution of the system. The semi-classical equations of motion of the system are obtained by replacing the quantum mechanical operators $\hat{a}_i$ with the corresponding c-number field amplitudes α_i. Moreover, we can assume that the Liouvillian terms originating from the output coupling to an external reservoir cause exponential decays of the intra-cavity fields with total decay rates of γ_i. This leads us to a simpler system of equations

$$\begin{aligned}\dot{\alpha_1} &= -(\gamma_1 + i\Delta_1)\alpha_1 + \frac{1}{2}\kappa\alpha_2^*\alpha_3 + \sqrt{2\gamma_1^c}A_1^{\text{in}} \\ \dot{\alpha_2} &= -(\gamma_2 + i\Delta_2)\alpha_2 + \frac{1}{2}\kappa\alpha_1^*\alpha_3 + \sqrt{2\gamma_2^c}A_2^{\text{in}} \\ \dot{\alpha_3} &= -(\gamma_3 + i\Delta_3)\alpha_3 - \frac{1}{2}\kappa\alpha_1\alpha_2 + \sqrt{2\gamma_3^c}A_3^{\text{in}} \end{aligned} \tag{4.12}$$

where Δ_i represent the cavity detunings of the respective modes. We have used $\sqrt{2\gamma_i^c}A_i^{\text{in}}$ to replace the pumping terms of Eq. (4.11) and γ_i^c is the input coupling rate of the pump field A_i^{in}. In the case of SHG and DOPO where the two fundamental modes are degenerate, ie. $\alpha_1 = \alpha_2$, we can rederive the equation of motion to obtain

$$\begin{aligned}\dot{\alpha_1} &= -(\gamma_1 + i\Delta_1)\alpha_1 + \kappa\alpha_1^*\alpha_3 + \sqrt{2\gamma_1^c}A_1^{\text{in}} \\ \dot{\alpha_3} &= -(\gamma_3 + i\Delta_3)\alpha_3 - \frac{1}{2}\kappa|\alpha_1|^2 + \sqrt{2\gamma_3^c}A_3^{\text{in}} \end{aligned} \tag{4.13}$$

Where α_1 now represents the total field amplitude of the degenerate modes. Since in both our SHG and OPO systems the 532 nm mode is not resonant with the optical cavity, this results in much faster dynamics of the second harmonic (ω_3) mode. On the time scale of the evolution of the fundamental (ω_1) mode, the second harmonic appears to be constant. We can thus proceed by adiabatically eliminating the time derivative of the second harmonic mode by setting $\dot{\alpha}_3 = 0$. This gives us a steady state solution for the second harmonic

$$\alpha_3^{\mathrm{ss}} = \frac{-\kappa|\alpha|^2}{2\gamma_3} + \frac{\sqrt{2\gamma_3^c}A_3^{\mathrm{in}}}{\gamma_3} \tag{4.14}$$

where we have assumed $\Delta_3 = 0$. Substituting Eq. (4.14) into Eq. (4.13), we obtain

$$\dot{\alpha}_1 = -(\gamma_1 + i\Delta_1)\alpha_1 - \mu|\alpha_1|^2\alpha_1^* + \frac{\sqrt{2\gamma_3^c}A_3^{\mathrm{in}}}{\gamma_3}\alpha_1^* + \sqrt{2\gamma_1^c}A_1^{\mathrm{in}} \tag{4.15}$$

where the nonlinear interaction μ is defined as

$$\mu = \frac{1}{2}\frac{(\gamma_3 - i\Delta)}{(\gamma_3^2 + \Delta_3^2)}\kappa^2 \tag{4.16}$$

We note that the first term of Eq. (4.15) represents the linear loss of the fundamental mode. The second term of the equation can be regarded as an intensity dependent nonlinear loss or gain (depending on the pump conditions) by a simple redefinition of

$$\gamma_{\mathrm{nl}} = \mu|\alpha_1^{\mathrm{ss}}|^2 \tag{4.17}$$

Equation (4.15) derived in this section, is the most useful equation for this part of the thesis since it is capable of describing both second harmonic generation by setting $A_3^{\mathrm{in}} = 0$ and optical parametric oscillation by setting $A_1^{\mathrm{in}} = 0$. In the next few chapters, many results are obtained using Eq. (4.15) without explicit reference.

4.5 A mechanical analogy

For people who are more mechanically inclined, it is sometimes useful to translate the problem of nonlinear optics to a mechanical system involving springs and pendula. Figure 4.5 shows the translated paradigm. We can think of the atoms of a dielectric medium as particles that have both ends tied to two springs. The passage of electric field through an atom is equivalent to the mechanical perturbation of the particle. Obviously, the response of the system as shown in Figure 4.5(a) will produce an oscillation at the frequency of perturbation. This is the mechanical model for a linear optical medium. Figure 4.5(b) however, shows instead a particle that is held with two nonidentical springs. Moreover, one of the spring is stretched beyond the limit of Hooke's law. Mechanical perturbations of this system will result in anharmonic oscillations. A Fourier decomposition of the anharmonic oscillations will reveal new harmonic components of the mechanical oscillator analogous to optical second harmonic generation with a nonlinear dielectric.

The condition for phase matching discussed in this chapter also has a simple mechanical analogue. Figure 4.5(c) shows a particle hanging off a pendulum made from a piece of spring. From standard textbooks on classical mechanics, we found the angular frequency of the pendulum (ω_p) and the spring (ω_s) to be [33]

$$\omega_p \quad = \quad \sqrt{\frac{g(m + \mu/2)}{(m + \mu/3)L}} \tag{4.18}$$

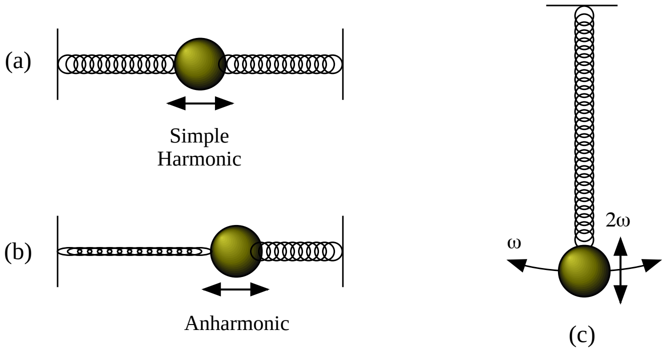

Figure 4.5: Mechanical analogy of nonlinear optics

$$\omega_s = \sqrt{\frac{\kappa}{(m+\mu/3)}} \tag{4.19}$$

where g is the gravitational acceleration, m and μ are the masses of the particle and the spring, κ is the spring constant and L is the load free rest length of the pendulum. The pendulum motion of the system is clearly coupled to the spring motion. For the system to have periodic solution, we require that the frequency of the spring oscillation be twice of that of the pendulum $2\omega_s = \omega_p$. This is the exact condition heuristically realized by all children on swings. The phase matching condition of this mechanical system is

$$L = \frac{4g(m+\mu/2)}{\kappa} \tag{4.20}$$

Let us now investigate driving the system with the fundamental pendulum mode. The first thing we note is that even with very small amount of pendulum displacement, we observe that the system will eventually couple some of the energy to the second harmonic spring mode. However, two solutions exist depending on the starting condition of the mechanical excitation: The smiley mode $\smile$ and the frowny mode $\frown$. In nonlinear optics, we find that 2 solutions with 180° phase difference exist for an OPO driven above threshold [32], suggesting a close correspondence between the two phenomena.

If on the other hand, the system is initially driven with the spring displacement, like a child trying to start the swing from rest, coupling to the pendulum mode is not as easily observed. The child on the swing needs an initial push to set the swing in motion. This corresponds to the threshold of the OPO in nonlinear optics. Naturally, like all analogies, there is a limit to the correspondence between the two systems. Nevertheless, the mechanical analogy still provides interesting perspectives to the phenomena in nonlinear optics.

Chapter 5

Squeezing in Second Harmonic Generation

Brick: “Well, they say nature hates a vacuum, Big Daddy.”
Big Daddy: ‘’ That’s what they say, but sometimes I think that a vacuum is a hell of a lot better than some of the stuff that nature replaces it with.”

Cat on a hot tin roof, Tennessee Williams

Overview

In this chapter, we discuss the generation of bright stable amplitude squeezed light using the second harmonic generation (SHG) process. We show that second harmonic squeezing is sensitive to the fundamental pump noise. A mode cleaner is used to make the pump field quantum noise limited and the SHG squeezing is subsequently improved. A transfer function approach to noise propagation without assuming a quantum noise limited pump source is presented. This approach is used to interpret the experimental results and to provide design improvements for future experiments. The relevant published paper to this chapter is

- *“Experimental test of modular noise propagation theory for quantum optics”*,
  A. G. White, M. S. Taubman, T. C. Ralph, P. K. Lam, D. E. McClelland, and H.-A. Bachor, Phys. Rev. A **54**, 3400 (1996).

5.1 Introduction

The first demonstration of squeezing by second harmonic generation (SHG) was made by Pereira *et al.* in 1988 [34]. In their experiment with a doubly resonant system, 0.6 dB of amplitude squeezing was observed for several milliseconds. The apparent instability of their experiment was chiefly due to dispersion which causes the fundamental and the second harmonic fields to drift in and out of phase with each other. This problem was overcome by Sizmann *et al.* [35] with the use of a monolithic doubly resonant cavity producing an improved results of 0.9 dB. Using the same technology, Kürz *et al.* [36, 37] observed 3.2 dB of amplitude squeezing on the fundamental beam for up to 10 s at a time. In all of these experiments, the observed squeezing was much less than that predicted by theory even when all experimental parameters were taken into consideration. This degradation or discrepancy was attributed to the difficulty in the fulfillment of the doubly resonant conditions. Technical difficulties have limited both the achievable nonlinearity as well as the stability of the observed squeezing.

Prompted by these difficulties, Paschotta *et al.* [38] pointed out that double resonance was not a necessary condition for the production of squeezing in an SHG system. In their work, they succeeded in obtaining 0.94 dB of stable second harmonic squeezing. Laser noise and thermal effects were the suspects in the limits to the amount of observed squeezing. In 1995 the ANU group observed that the second harmonic squeezing is severely degraded by the laser noise. An accurate theoretical model was developed by Ralph *et al.* [39] to explain the phenomenon. In the same year Tsuchida [40] observed 2.4 dB of squeezing from a singly resonant SHG which is the largest stable second harmonic squeezing reported to date. However, agreement between theory and experiment was again poor.

In this chapter, we examine the squeezing produced by a singly resonant SHG with the aim of developing an understanding of the apparent discrepancy between the observed and predicted amount of squeezing. One of the subjects of investigation is the effect of pump noise on the second harmonic squeezing.

The pump noise of a squeezed state generator is an important and often neglected factor in many analyses of experimental results. In some cases, eg. in the generation of squeezed vacuum state via a below threshold OPO, the pump noise to the squeezer is unimportant to first order [41]. However, this is not the case for squeezer relying on bright beams, such as the optical parametric amplifiers, second harmonic generators, Kerr media and rate-matched lasers. In these experiments with bright beams, the pump noise is propagated through the different stages of the experiment and will eventually "bury" or degrade the produced squeezing.

5.2 Modular theory of noise propagation

The cascaded approach to the noise propagation in quantum optics developed by Gardiner and Carmichael [42, 43] allows us to analyse and fully model the situation with a master equation approach. Unfortunately, this approach is not analytical, making the physical interpretation very difficult. In contrast, with the linearized formalism introduced in Chap. 2 we can simplify this cascaded approach to a more engineering like transfer function approach which is useful for describing optical systems of cascaded modules. In this section, we develop an analytical and simple modular theory for noise propagation for analysing the squeezed state generation in a SHG system.

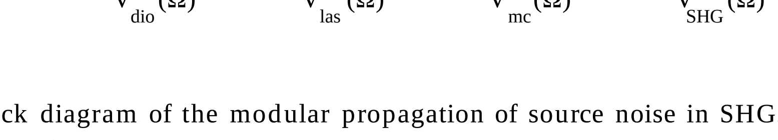

Figure 5.1: Block diagram of the modular propagation of source noise in SHG. The origin of the noise source is from the diode laser. $\omega_{\rm dio}, \omega_1$ and $2\omega_1$ are the 808, 1064 and 532 nm modes, respectively.

The conceptual layout of the experiment we are modeling is as shown in Figure 5.1. A SHG with output at $2\omega_1$ (532 nm) is driven by the output field of a mode cleaner at frequency ω_1 (1064 nm). The mode cleaner is resonant with an incident field from the Nd:YAG laser output and the Nd:YAG laser in turn is pumped by a diode laser array at frequency ω_{dio} (808 nm).

In order to model the noise propagation through each element of the experiment, the quantum-mechanical equations of motion of the field amplitudes for each element are derived, including the zero-point (vacuum) fluctuations terms. The equations of motion are then linearized with respect to the fluctuations, transformed to the frequency domain, and solved simultaneously for a solution of the cavity mode. An analytical expression of the noise variance spectrum of the output field is then found in terms of the cavity mode using the input-output formalism [44]. Explicit predictions can be made by solving the equations of motion and substituting the subsequent semi-classical values into the expression for the noise variance spectrum $V(\Omega)$.

The SHG under investigation in this chapter is a singly resonant system. That is, it is only resonant for the fundamental and not the generated second harmonic field. The intra-cavity field equation and the output spectrum for such a system are given by [38] as,

$$\dot{\alpha}_1 = -\kappa_1\alpha_1 - \mu|\alpha_1|^2\alpha_1 + \sqrt{2\kappa_c}A_1 \tag{5.1}$$

$$V_{\mathrm{SHG}}^{\mathrm{out}}(\Omega) = \frac{(\mu|\alpha_1|^2 - \kappa_1)^2 + \Omega^2 + 8\kappa_c\mu|\alpha_1|^2 V_{\mathrm{SHG}}^{\mathrm{in}}(\Omega) + 8\kappa_l\mu|\alpha_1|^2}{(3\mu|\alpha_1|^2 + \kappa_1)^2 + \Omega^2} \tag{5.2}$$

where α_1 is the fundamental field amplitude; μ is the strength of the $\chi^{(2)}$ nonlinearity; κ_1 is the total linear decay rate of the fundamental cavity; κ_c is the decay rate of the output coupling mirror; κ_l is the decay rate due to absorption and other losses; A_1 is the fundamental pump field; Ω is the angular detection frequency and $V_{\mathrm{SHG}}^{\mathrm{in}}$ is the amplitude spectrum of the incident pump field. The term $\mu|\alpha|^2$ is also commonly referred to as the nonlinear or two-photon decay rate. We note that for a coherent pump field of $V_{\mathrm{SHG}}^{\mathrm{in}}(\Omega) = 1$, optimum squeezing occurs at zero frequency in the limit of very large field amplitude:

$$V_{\mathrm{SHG}}^{\mathrm{out}}(0)|_{\alpha_1\to\infty} = \frac{1}{9} \tag{5.3}$$

giving predicted maximum second harmonic amplitude squeezing of 9.5 dB. Obviously a noisy, $V_{\mathrm{SHG}}^{\mathrm{in}} > 1$, incident pump field to the SHG will bury the squeezing of the output field.

An intensity noise cleaner formed by a Fabry-Perot cavity is a way of reducing high frequency intensity noise in a light beam. The intra-cavity field equation and intensity noise spectrum transfer function is given by

$$\dot{\alpha}_{\mathrm{mc}} = -\kappa_{\mathrm{mc}}\alpha_{\mathrm{mc}} + \sqrt{2\kappa_{\mathrm{mc}}^{\mathrm{loss}}A_{\mathrm{mc}}} \tag{5.4}$$

$$V_{\mathrm{mc}}^{\mathrm{out}}(\Omega) = \frac{2\kappa_{\mathrm{mc}}^{\mathrm{out}} - \kappa_{\mathrm{in}}^2 + \Omega^2 + 4\kappa_{\mathrm{mc}}^{\mathrm{in}}\kappa_{\mathrm{mc}}^{\mathrm{out}}V_{\mathrm{mc}}^{\mathrm{in}}(\Omega) + 4\kappa_{\mathrm{mc}}^{\mathrm{out}}\kappa_{\mathrm{mc}}}{\kappa_{\mathrm{mc}}^2 + \Omega^2} \tag{5.5}$$

where α_{mc} is the field amplitude of the mode cleaner; κ_{mc} is the total decay rate; A_{mc} is the incident driving rate; $\kappa_{\mathrm{mc}}^{\mathrm{in}}$ and $\kappa_{\mathrm{mc}}^{\mathrm{out}}$ are the decay rate of the input and output mirror of the mode cleaner. $V_{\mathrm{mc}}^{\mathrm{in}}(\Omega)$ is again the amplitude spectrum of the incident field.

The laser in this experiment is modeled as a three-level system using the equations of motion from [45], we obtain

$$\begin{aligned} \alpha_{\text{las}} &= \sqrt{\frac{J_2(\gamma - \gamma_1)}{2\kappa} - \frac{\gamma_1}{G}} && (5.6) \\ J_1 &= \frac{\gamma J_2}{\Gamma} && (5.7) \\ J_2 &= \frac{1 - 2\kappa/G}{\gamma/\Gamma + 2} && (5.8) \\ J_3 &= J_2 + \frac{2\kappa}{G} && (5.9) \end{aligned}$$

$$\begin{aligned} V_{\text{las}}^{\text{out}}(\Omega) = \; & 1 + \{(2\kappa_{\text{las}}^{c}{}^2[\Omega^2 + (G\alpha_{\text{las}}^2 + \gamma_t + \Gamma)^2] \\ & - 8\kappa_{\text{las}}^{c}\kappa_{\text{las}}G\alpha_{\text{las}}^2(G\alpha_{\text{las}}^2 + \gamma_t + \Gamma) \\ & + 2\kappa_{\text{las}}^{c}G^2\alpha_{\text{las}}^2(\Gamma J_1 V_{\text{las}}^{\text{in}}(\Omega) + \gamma_t J_3) && (5.10) \\ & + 2\kappa_{\text{las}}^{c}G[(\gamma_t + \Gamma)^2 + \Omega^2](J_3 + J_2) \\ & + 4\kappa_{\text{las}}^{c}\kappa_{\text{las}}^{\text{in}}[(G\alpha_{\text{las}}^2 + \gamma_t + \Gamma)^2 + \Omega^2]\} \\ & \times \\ & \{(2G\alpha_{\text{las}}^2\kappa_{\text{las}} - \Omega^2)^2 + \Omega^2(G\alpha_{\text{las}}^2 + \gamma_t + \Gamma)^2\}^{-1} && (5.11) \end{aligned}$$

where $G = \sigma_s \rho c'$ is the stimulated emission rate; σ_s is the stimulated emission cross section for the Nd:YAG; ρ is the density of Nd atoms in the laser medium; c' is the speed of light in the laser medium; γ_t and γ are the spontaneous emission rates for level $3 \to 2$, and $2 \to 1$ transitions, respectively. Γ is the rate of incoherent pumping of the lasing transition; κ_{las}^{c} and κ_{las}^{l} are the cavity decay rates for the output mirror and all other losses. $\kappa_{\text{las}} = \kappa_{\text{las}}^{c} + \kappa_{\text{las}}^{l}$ is the total decay rate; α_{las} and J_i are the laser field amplitude and the atomic population of the Nd atoms. Finally, $V_{\text{las}}^{\text{in}}$ is the amplitude quadrature spectrum of the diode laser pump field to the Nd:YAG laser. We note that Eq. (5.11) predicts a strong resonance at a frequency of $\Omega^2 = 2G\alpha^2\kappa_{\text{las}}^{c}$. This is the resonant relaxation oscillation of the laser.

All the equations for the noise variance in this section, can be concatenated together to give the output squeezing spectrum of the full system. Hence, the output squeezing spectrum can be analytically expressed in terms of all of the experimental parameters.

5.3 The experiment

Figure 5.2 shows the layout of the experiment. The laser used in this chapter is a Lightwave 122 diode pumped Nd:YAG NPRO capable of producing 200 mW of 1064 nm light. The output of the laser is passed through a ring mode cleaner (Mode cleaner No.1 of Table 3.2) formed by three mirrors. The total perimeter of the cavity is 2.45m and it has a cavity linewidth of 800 kHz. Supermirrors were not used in this experiment because the technology was not available to us at that time. Nevertheless, sufficient intensity noise reduction is achieved with this ring cavity mode cleaner since the detection frequencies for the SHG squeezing were at > 5 MHz, more than 6 cavity linewidths away. The locking of the mode cleaner is via two Pound-Drever-Hall configurations. The necessary phase modulation is achieved by modulating the fast frequency control port of the pump laser. Low frequency locking of the mode cleaner is achieved by feeding the resultant error sig-

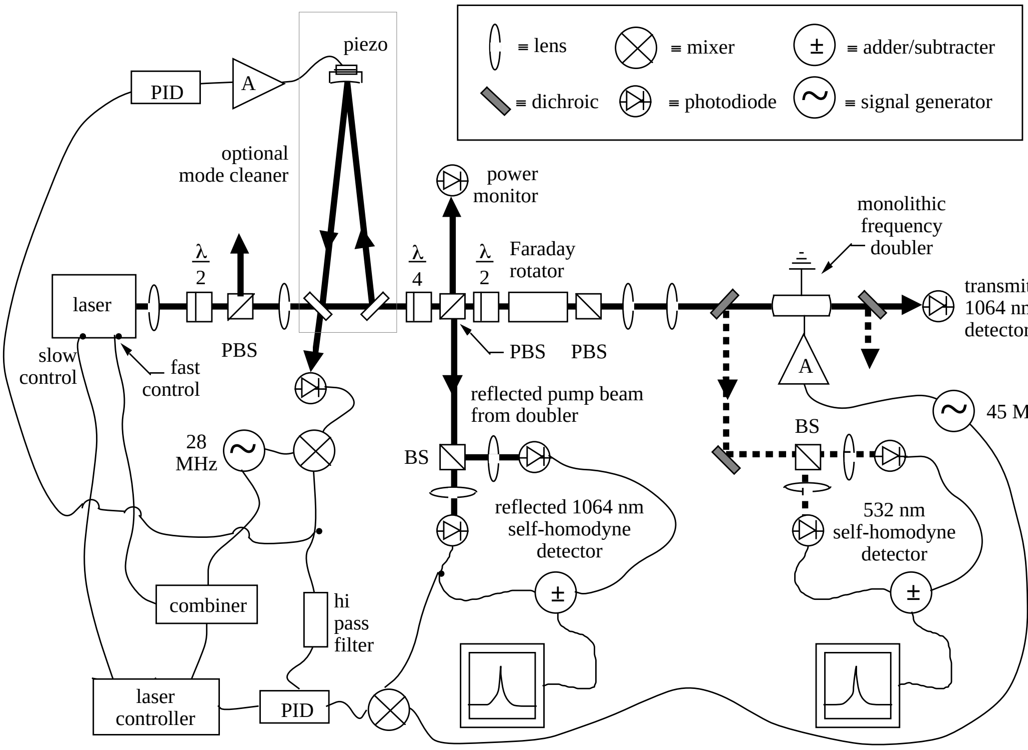

Figure 5.2: Setup of the second harmonic generation experiment.

nal from the beam reflected by the cavity to the piezo on one of the mirror of the mode cleaner. Due to the narrow linewidth and the physical extension of the cavity, this control alone is inadequate for a stable lock. An additional high-frequency locking is achieved by filtering the error signal and again feeding back to the fast control port of the laser. When locked the mode cleaner cavity transmits about 60% of the incident power, which is adequate for the pumping of the SHG crystal.

The SHG crystal is a standing-wave monolithic cavity made from bulk $\mathrm{MgO} : \mathrm{LiNbO_3}$. It has the dimensions of $5(x) \times 12.5(y) \times 5(z)$ mm, where z is the optical axis of the crystal. Both end faces of the monolith have radii of curvature $\mathrm{ROC} = 14.24$ mm which produce a cavity eigenmode waist of 32.8 μm for the TEM_{00} mode of 1064 nm light. The front face of the crystal has dielectric coating with reflectivities $99.60\pm$ 0.03% at 1064 nm and $\approx$ 4% at 532 nm. The dielectric coating of the back face is $99.96\pm$ 0.03% for both 1064 nm and 532 nm fields. The internal round trip loss of the fundamental light was estimated to be $0.10\pm$ 0.02% cm^{-1} whereas the loss at 532 nm is much higher at $\approx$ 4% cm^{-1}. The xy faces of the crystal is coated with a layer of gold to allow for good electrical contact with the electrodes used for electro-optic tuning and modulation of the nonlinear cavity. The crystal along with the electrodes are housed within a macor case and the entire assembly is then placed within a copper oven that is temperature stabilized at around $107°$C with a stability of ± 2 mK.

The nonlinear crystal was electro-optically modulated to produce a Pound-Drever-Hall error signal necessary for the locking. The reflected beam from the nonlinear cavity was measured and fed back to both the fast and slow controller of the Nd:YAG laser. The SHG crystal was pumped with 81 mW of mode matched fundamental light and produced 34 mW of second harmonic light. We note that at higher pump power, the second harmonic generation did not increase due to the onset of parasitic intra-cavity NDOPO. This will be the subject of discussion in the ensuing chapter.

The second harmonic light produced by the crystal was retrieved from the reflection of a dichroic plate immediately in front of the SHG crystal. A self-homodyne detection system was set up to analyse the amplitude noise of the second harmonic beam. Initially, a pair of EG&G FND-100 photodetectors were used for the measurement of the squeezed second harmonic beam. The external glass windows of the photodetectors were removed and both photodetectors were positioned close to the Brewster's angle to reduce reflection off the face of the photodiodes. Furthermore, any residual reflected lights from the photodetectors were retro-reflected back onto themselves to increase the quantum efficiency of the self-homodyning. We obtained a best quantum efficiency of $65\pm$ 5% for the second harmonic light at 532 nm.

The best squeezing result measured with this pair of photodetectors is 1.7 dB, corresponding to an inferred squeezing of $\approx$ 3 dB. In the later stages of the experiment, a new pair of Hamamatsu S1721 photodetectors were used. The best quantum efficiency obtained was 90%, this increased the amount of observed squeezing to around 2.1 dB whilst the inferred value was unchanged. Because of the simplicity in the locking of a singly resonant SHG system, the observed amplitude squeezing of the second harmonic has been shown to be stable for more than 5 hours [46, 47].

5.4 Comparison between experiment and theory

In this section, we compare the experimental results obtained from the SHG setup with the modular noise propagation theory developed in Sec. 5.2. As far as possible, the number of free parameters required for the modeling are minimized. This is done by first establishing several physical parameters of the laser. The values of the laser parameters for Nd:YAG listed in Table 5.1 was obtained from the book of *"Solid-State Laser Engineering"* by Koechner [48].

σ_s	$6.5\times10^{-23}\mathrm{m}^2$
ρ	1.38×10^{26} atoms.m^3
c'	$1.640\times10^{8}\mathrm{ms}^{-1}$
γ_t	$4.3\times10^{3}\mathrm{s}^{-1}$
γ	$3.3\times10^{7}\mathrm{s}^{-1}$
G	$1.47\times10^{12}\mathrm{s}^{-1}$

Table 5.1: Parameters of the Nd:YAG laser

The Lightwave-122 laser has a cavity perimeter of $p = 28.5$ mm, an input coupler reflectivity of $R =$ 96.8%, and a total internal round trip loss of 1.6%, and we thus obtained

$$\kappa^{c}_{\mathrm{las}} = 9.28\times10^{7} \qquad (5.12)$$

$$\kappa_{las} = 1.39\times10^{8} \qquad (5.13)$$

where the above quantities are in units of [s^{-1}]. The remaining parameter Γ can be determined by the fitting of the resonant relaxation oscillation (RRO) frequency of the laser.

For the pump power of the experiment, we find $\Gamma = 8.703\,\mathrm{s}^{-1}$.

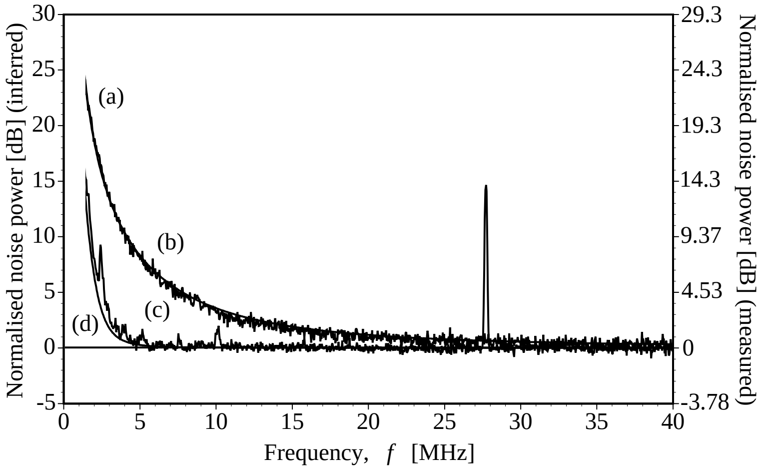

Figure 5.3: A comparison of the mode cleaner and laser output intensity noise spectra. Traces (a) and (b) are the experimental and theoretical traces for the output spectra of the laser, respectively. The intensity is not quantum noise limited at detection frequencies up to 40 MHz. Traces (c) and (d) are the equivalent for the mode cleaner output spectra. The output of the mode cleaner is quantum noise limited at detection frequencies higher than 7 MHz. The large peak at 27.6 MHz is the modulation signal for the Pound-Drever-Hall locking of the mode cleaner cavity.

We modelled the diode laser array as a white noise source which is 52 dB above the standard quantum limit, ie. $V_{\mathrm{dio}}^{\mathrm{in}} = 160,000$. This is consistent with the directly measured noise power of the diode arrays at detection frequencies of $\Omega < 50$ MHz. Figure 5.3 shows, at the same optical power, the output spectra of the Lightwave laser (a) and the locked mode cleaner (c). We observed that the mode cleaner has indeed reduced the intensity noise of the laser considerably. The output of the laser is not quantum noise limited ($<$ 0.25 dB) until beyond 45 MHz. However, with the noise filtering of the mode cleaner, the spectrum is quantum noise limited at above 7 MHz. Traces (b) and (d) are the theoretical predictions of traces (a) and (c), respectively, as obtained from Eqs. (5.5) and (5.11). The agreement between the theory and the experimental data is excellent.

Figure 5.4 shows the amplitude squeezing spectra of the second harmonic output. Traces (a) and (c) are the experimental results obtained without and with a mode cleaner. Again, we note significant noise reduction at low frequencies due to the noise filtering of the mode cleaner. Traces (b) and (d) are the corresponding theoretical predictions. The agreement between theory and experiment is again excellent. In Figure 5.4, the maximum squeezing shows an improvement from -0.5 dB at 23 MHz in (a) to -1.7 dB at 7.5 MHz in (c) with the application of a mode cleaner. Finally trace (e) is the calculated squeezing spectrum of the second harmonic output pumped by a coherent input (quantum noise limited at all frequencies). The figure clearly shows the necessity of the modular noise propagation theory since the naive prediction of a coherent state pump, which is quantum noise limited at all detection frequencies, is very different from the experimental results.

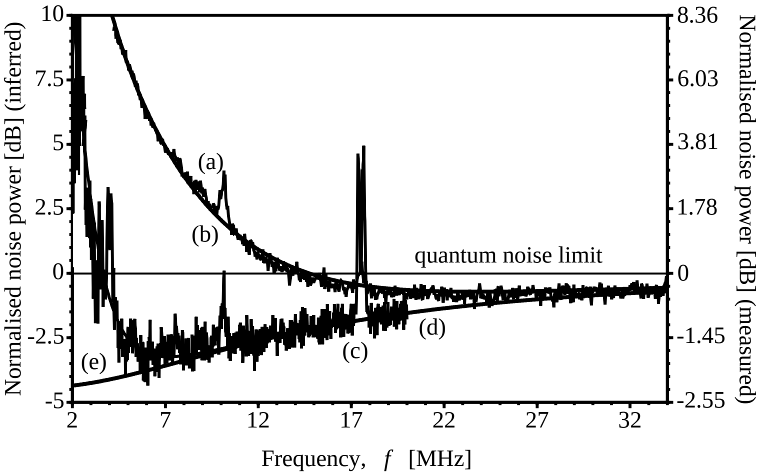

Figure 5.4: Theoretical and experimental spectra of the SHG. Traces (a) and (c) are the spectra obtained for the experiment run without and with the mode cleaner, respectively, after correction for electronic noise. The maximum squeezing in each case are 0.47 dB (0.75 dB inferred) at 23 MHz for trace (a) and 1.7 dB (3.0 dB inferred) at 7.5 MHz for trace (c). The small noise peak at 10 MHz on both traces is the residual noise from the locking system. Traces (b) and (d) are the theoretical plots corresponding to the experimental traces. Trace (e) is the theoretical prediction for the second harmonic squeezing with a coherent pump (quantum noise limited at all frequencies).

5.5 Summary

We have shown that the modular theory of noise propagation in SHG system is in excellent agreement with the experimental data of our singly resonant SHG. The analytic approach to the problem brings to light the contribution of the pump noise to the degradation of observed amplitude squeezing of the second harmonic field. Using a narrow linewidth mode cleaner, we were able to improve the observed second harmonic squeezing from 0.5 dB to 1.7 dB. Further improvement on the quantum efficiency of the photodetectors yield the best squeezing results of 2.1 dB for this setup. The inferred squeezing levels, however, are consistently limited at the 3 dB level. This is still significantly smaller than the theoretically predicted maximum squeezing of 1/9 (9.5 dB) for a singly resonant system. Even when realistic estimations of experimental imperfections (such as detector efficiency (85%), losses and finite cavity linewidth considerations) were made, the theory still predicts about 5.5 dB of observable squeezing. The largest observed second harmonic squeezing reported to date is only 2.4 dB [40].

The answer to the puzzle is the onset of parasitic intra-cavity NDOPO mode in SHG systems. This phenomenon will be discussed in detail in the next chapter. We can however, provide a list of requisites for the design of future experiments for the generation of large second harmonic amplitude squeezing:

- *Good mode cleaning*

  As discussed in Chap. 3, the use of supermirrors can improve significantly the performance of a mode cleaner. With reasonable cavity length of ≈ 150 mm, mode cleaner linewidth of < 100 kHz is nowadays easily achievable. This will make the fundamental pump for the SHG quantum noise limited from frequencies above

1 MHz. Thus enable the detection frequency to be lowered to regions of larger squeezing.

- *Large cavity linewidth*
  The nonlinear resonator must have large cavity linewidth. This is achievable by constructing a shorter nonlinear cavity. With the improvement of the $\chi^{(2)}$ nonlinearity in many new crystals, eg. PPLN, PPLT or BLIRA-free $\mathrm{KNbO_3}$, strong nonlinear interaction is possible with a crystal length of 5 mm or shorter. The large cavity linewidth of the nonlinear crystal can extend the range of large squeezing to higher detection frequencies.

- *Large intra-cavity dispersion*
  In the next chapter, we will show that the parasitic intra-cavity NDOPO modes degrade the second harmonic squeezing to a maximum of around 3 dB. Since the amount of second harmonic squeezing is dependent on the fundamental pump power, large cavity dispersion can be used to control or delay the onset of these parasitic modes, thus allowing larger amplitude squeezing of the second harmonic output.

Chapter 6

Interacting Second Order Nonlinearities

> Government and cooperation are in all things the laws of life; anarchy and competition the laws of death
>
> *Unto this last, John Ruskin (1862).*

Overview

In Chap. 5, we found that optical SHG can be used to produce stable bright amplitude squeezed light. However, in spite of the large amount of squeezing predicted by theory the largest inferred squeezing is less than 3 dB. In this chapter, we examine situations where two or more second order $\chi^{(2)}$ optical nonlinearities are interacting with each other or cascaded one after another. We have found that the onset of competing nonlinearities can lead to the optical clamping of the second harmonic generation and, in general, the degradation of the second harmonic squeezing. The relevant published paper to this chapter is

- *"Classical and quantum signatures of competing $\chi^{(2)}$ nonlinearities"*,
  A. G. White, P. K. Lam, M. S. Taubman, M. A. M. Marte, S. Schiller, D. E. McClelland, and H.-A. Bachor, Phys. Rev. A **55**, 4511 (1997).

6.1 Cooperating and competing nonlinearities

Cascaded nonlinearities or interacting nonlinearities can be categorized as *cooperating* or *competing*. By cooperating nonlinearities we refer to those where all nonlinear interactions, both upconversions and down conversions share the same modes. For example, the process of $\omega \rightarrow 2\omega \rightarrow \omega$, as shown in Figure 6.1(a), is a cascade of cooperating nonlinearities.

Competing nonlinearities, on the other hand, refer to a cascade of nonlinear interactions where new modes additional to the original fundamental and second harmonic modes are formed. One such example is the case of $\omega \rightarrow 2\omega \rightarrow \omega \pm \Delta$ as shown in Figure 6.1(b) or $\omega \pm \Delta_1 \rightarrow 2\omega \rightarrow \omega \pm \Delta_2$, where $\Delta_1 \neq \Delta_2$.

In as early as 1962, Siegman [49] predicted an interesting phenomenon resulting from cooperating nonlinearities. It was shown that the pump light transmitted through a DOPO system will experience optical power clamping. The transmitted pump light does not increase its intensity with increasing incident pump field to the DOPO. More recently,

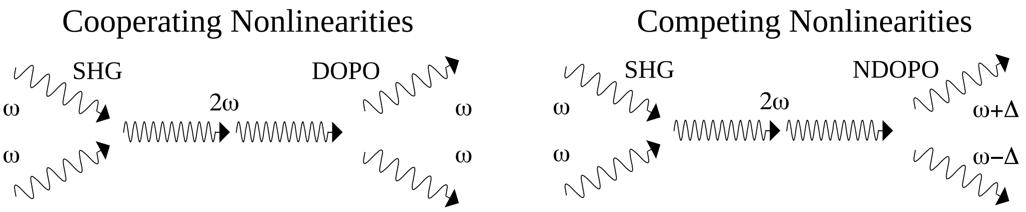

Figure 6.1: Simple examples of cooperating and competing nonlinearities.

large third order nonlinear effects have been observed via the cascade of two $\chi^{(2)}$ cooperating interactions [50, 51]. Extensive research was also carried out in CW system using a cavity [52, 53]. Optical Kerr effect and optical bistability are two of the physical phenomena observed in cooperating nonlinearity. It therefore holds promise for applications including optical switching, nonlinear optical amplification [54], squeezing and quantum nondemolition (QND) measurements.

In contrast, systems of competing nonlinearities have been mainly investigated for their potential as frequency tunable sources of light. Systems considered include: intra-cavity SFG and NDOPO [55, 56]; intra-cavity DFG and NDOPO [57]; and intra-cavity SHG and NDOPO [58–60] [61–63]. Intra-cavity NDOPO was first observed in an SHG system by Schiller *et al.* [58]. Quantum mechanical properties of the systems with competing nonlinearities are modeled in numerous papers by Marte [59, 64–66] in which non-classical features including enhancement of squeezing via competition was studied for quadruply resonant configurations.

We have experimentally observed both the cooperating and competing $\chi^{(2)}$ nonlinearities from the same monolithic SHG system described in Chap. 5. The purpose of this chapter is to present the quantum and classical signatures of competing nonlinearities. A simple theory is presented to explain their occurrences.

6.2 Competing nonlinearities: intra-cavity SHG and NDOPO

From Chap. 4 we note that by controlling the temperature of the crystal, the phase matching condition of the second order nonlinear system can be tuned from degeneracy (SHG / DOPO) to non-degeneracy (SFG / NDOPO). This seems to suggest that it is impossible to simultaneously observe intra-cavity NDOPO while the system is efficiently frequency doubling. The usual phase matching plot (see Figure 7.4) seems to support the same conclusion. However, a more detailed analysis reveals that even at the point of degeneracy, $\chi^{(2)}$ gain decreases very gradually with increasing nondegeneracy as shown in Figure 4.3.

Although the following analysis can be generalized to account for situations with more than one SFG / NDOPO mode pairs, we choose to model the situation using a set of 4-mode equations as in [59] by assuming that only one SFG / NDOPO mode pair is present,

$$\begin{aligned}
\dot{\alpha}_1 &= -(\gamma_1 + i\Delta_1)\alpha_1 + \kappa_1\alpha_3\alpha_1^* + -\sqrt{2\gamma_1^c}A_1^{\text{in}} \\
\dot{\alpha}_3 &= -(\gamma_3 + i\Delta_3)\alpha_3 - \frac{\kappa_1^*}{2}\alpha_1^2 - \kappa_2^*\alpha_s\alpha_i
\end{aligned}$$

$$\dot{\alpha}_{s,i} = -(\gamma_{s,i} + i\Delta_{s,i})\alpha_{s,i} + \kappa_2\alpha_3\alpha^*_{i,s} \tag{6.1}$$

where $\alpha_1, \alpha_3, \alpha_s$ and α_i are the field amplitudes for the fundamental, second harmonic, and the non-degenerate signal and idler modes, respectively. Their respective optical angular frequencies are $\omega, 2\omega, (\omega+\delta)$ and $(\omega-\delta)$. κ_1 is the original nonlinearity for the SHG and κ_2 is the new nonlinearity responsible for the SFG / NDOPO process. $A_1^{\text{in}} = \sqrt{P_1/h\nu_1}$ is the fundamental pump field amplitude and γ_1^{c} its output coupling decay rate. Finally, the detuning for the i-mode is given by Δ_i.

The system used in this study is the same setup as the SHG squeezing experiment of Chap. 5. The nonlinear crystal is only singly resonant where the fundamental mode sees an optical cavity formed by the monolith but the generated second harmonic is immediately coupled out of the monolith after double passing through the crystal. Before exiting the crystal, the second harmonic mode can still either downconvert back to the pump mode or initiate new pairs of NDOPO modes that also happen to meet the same cavity resonance condition as the fundamental pump. We again use the adiabatic elimination to neglect the fast dynamics of the second harmonic [1] by setting $\dot{\alpha}_3 = 0$. This gives

$$\begin{aligned}\dot{\alpha}_1 &= -(\gamma_1 + i\Delta_1)\alpha_1 - 2\sqrt{\mu_1\mu_2}\alpha_1^*\alpha_s\alpha_i - \mu_1|\alpha_1|^2\alpha_1 - \sqrt{2\gamma_1^{\text{c}}}A_1 \\ \dot{\alpha}_{s,i} &= -(\gamma_{s,i} + i\Delta_{s,i})\alpha_{s,i} - \sqrt{\mu_1\mu_2}\alpha_1^2\alpha^*_{i,s} - 2\mu_2\alpha_s\alpha_i\alpha^*_{i,s}\end{aligned} \tag{6.2}$$

where we have assumed that $\kappa_{1,2}$ are real numbers and the following substitutions for the nonlinear interaction rates μ_1 and μ_2 were made,

$$\mu_1 = \frac{\kappa_1^2}{2(\gamma_3 + i\Delta_3)} \tag{6.3}$$

$$\mu_2 = \frac{\kappa_2^2}{2(\gamma_3 + i\Delta_3)} \tag{6.4}$$

To simplify the subsequent analysis, we define

$$\bar{\gamma} = \sqrt{\gamma_s\gamma_i} \tag{6.5}$$

$$r = \sqrt{\frac{\mu_1}{\mu_2}} \tag{6.6}$$

$$N = \frac{P_1}{P_1^{\text{thr}}} \tag{6.7}$$

Where these scaled quantities are: The average decay rate for the NDOPO signal and idler pair, $\bar{\gamma}$; scaled nonlinear interaction rate, r; and the scaled fundamental pump power, N, defined with reference to the threshold power P_1^{thr} of the NDOPO.

6.2.1 Power clamping

For zero detunings, the threshold power for the onset of competing nonlinearities is given by

$$P_1^{\text{thr}} = h(2\nu)\frac{\bar{\gamma}}{\gamma_1^{\text{c}}}\frac{\gamma_1^2}{\sqrt{\mu_1\mu_2}}\frac{1}{4}\left(1 + r\frac{\bar{\gamma}^2}{\gamma_1^2}\right)^2 \tag{6.8}$$

---

[1] A more detailed solution of Eq. (6.1) without using adiabatic elimination is given in [59, 64–66] where several nonclassical features of the system are predicted.

Thus the threshold of the competing nonlinearities is dependent on a number of factors. Firstly, the nonlinearity μ_2 can be experimentally varied by a change in the *phase matching* temperature. At the point of degeneracy, we expect that $\mu_1 \geq \mu_2$, since this corresponds to the optimum phase matching temperature for the SHG / NDOPO process. For temperature lower than this point, μ_2 decreases much more rapidly than μ_1, making the threshold of competing nonlinearities higher. However, there is a limit to this control since the increase of the threshold is at the expense of lowering the efficiency of the SHG process. At temperature higher than the point of degeneracy, it is even possible to increase μ_2 to a value larger than μ_1. These three regimes of operation are summarized in Figure 6.2.

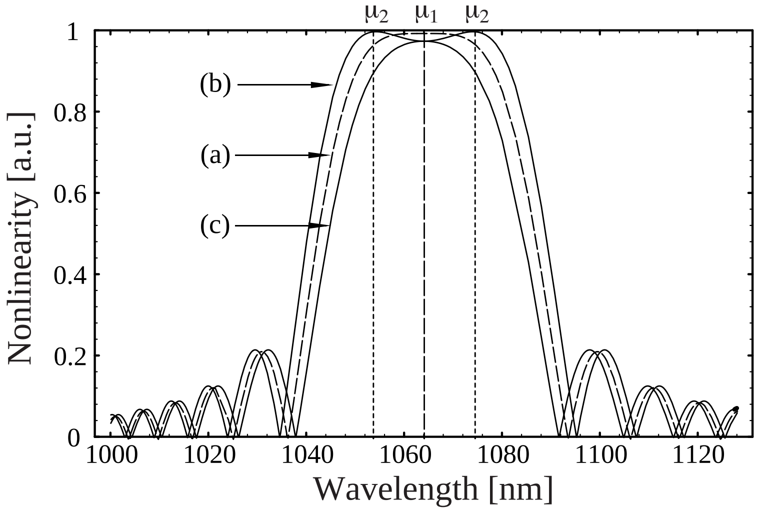

Figure 6.2: Effect of temperature tuning on nonlinearities. Figure shows plots of nonlinearity versus frequency. The phase matching temperature for SHG / DOPO is at $107°$. We assume that the NDOPO modes are those shown by the dotted lines with nonlinearity μ_2, and the solid line is the DOPO with nonlinearity μ_1. (a) When $T = 107°$ we have $\mu_1 \approx \mu_2$. (b) $T = 107.1°$, we find $\mu_2 > \mu_1$, operating at this temperature will give a low competing nonlinearities threshold. (c) $T = 106.9°$, at lower temperature, μ_2 decreases much more rapidly than μ_1.

The *coatings* on the monolithic crystal and the total *dispersion* of the cavity also affect the threshold of competing nonlinearities through the change in the decay rates of the NDOPO signal and idler modes. For broadband coatings [67], the threshold of competing nonlinearities can be very small. The existence of dispersion however will increase the threshold of competing nonlinearities. Since conservation of energy requires that the nondegenerate modes to be symmetrically detuned from degeneracy, the dispersion of the cavity will force either the signal or idler mode to be slightly detuned away from resonance. This will cause the NDOPO to become singly resonant resulting in an increase of threshold power.

At the point of degeneracy, SHG and DOPO processes are at their maximum efficiency. We can thus assume the following

$$\gamma_s, \gamma_i \leq \gamma_1 \tag{6.9}$$

$$\mu_2 \leq \mu_1 \tag{6.10}$$

that is, the phase matching as well as the resonance conditions of the monolith favors the

SHG / DOPO to SFG / NDOPO. The minimum threshold for the competing nonlinearities is therefore given by

$$P_1^{\min} = \frac{2h\nu\gamma_1^2}{\eta\mu_1}, \tag{6.11}$$

where $\eta = \gamma_{1^c}/\gamma_1$ is the cavity escape efficiency of the fundamental field.

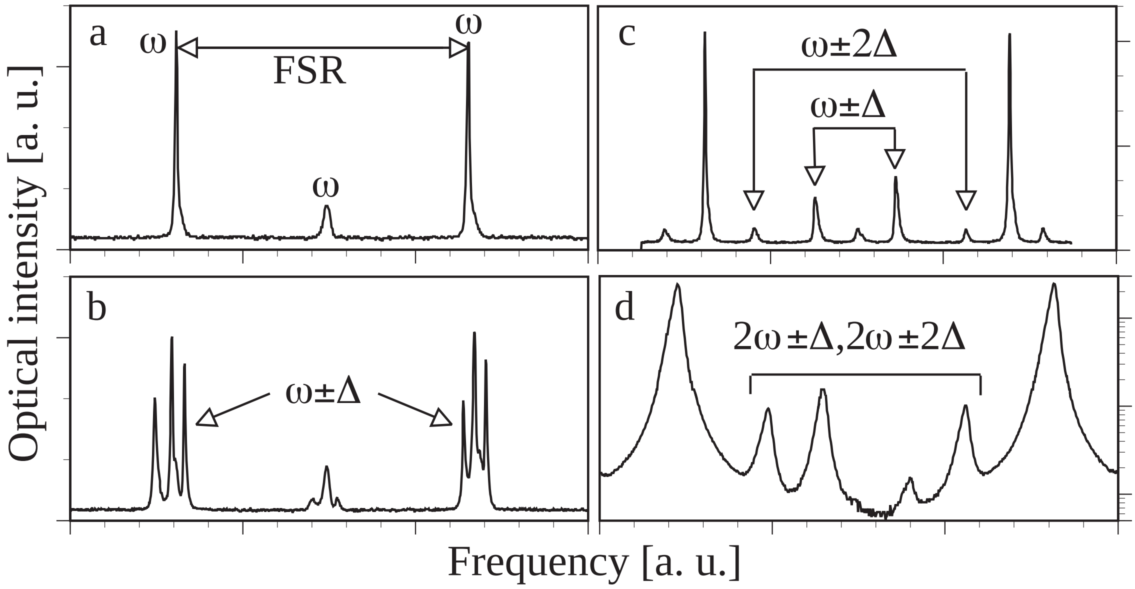

Figure 6.3: Optical spectrum analyser outputs of the intra-cavity NDOPO modes. Optical intensity is plotted against frequency (detuning of the OSA) in arbitrary units. (a) shows a single FSR scan of the OSA with only the 1064 nm input, the small peak in the middle of the FSR is due to imperfect alignment of the cavity. (b) the onset of intra-cavity NDOPO at $P_1 = 14$ mW gives rise to an additional pairs of fundamental modes at frequency $\omega \pm \Delta$. (c) At even higher fundamental pump power, $P_1 = 49$ mW, two pairs of nondegenerate fundamental modes emerged. Finally using another OSA for the second harmonic modes (d) shows that at $P_1 = 155$ mW, the intra-cavity NDOPO is strong enough to generate their own optical harmonic. The intensity scale is logarithmic for (d).

Above this threshold pump power ($N > 1$), the amplitudes of the signal and idler modes, $\alpha_{s,i}$ become large. This is the first signature of competition. Figure 6.3 shows the modal analysis of the fundamental and second harmonics of the system. Two separate scanning high finesse Fabry-Perot cavities were set up as optical spectrum analysers (OSA) for the reflected fundamental and second harmonic outputs of the monolith.

The output modes are analysed with respect to the detuning of the OSA cavity. For the scan of a single FSR, the odd order misalignment of the OSA shows up mid way between the resonant peak because of the confocal nature of the OSA. All higher even order modes of the OSA are degenerate with the resonant TEM_{00} mode. Thus, any other peaks shown in Figure 6.3 corresponds to new NDOPO modes. It is observed that increasing pump power can lead to more than a single pair of NDOPO modes as shown in Figure 6.3(c). When the pump power is further increased these NDOPO mode can themselves be strong enough to generate their own second harmonics. With a calibrated OSA, signal and idler modes from similar monolithic system were found to be as far detuned as up to 31 nm from degeneracy ($\nu_{i,s}$ =1033 nm, 1095 nm) [68].

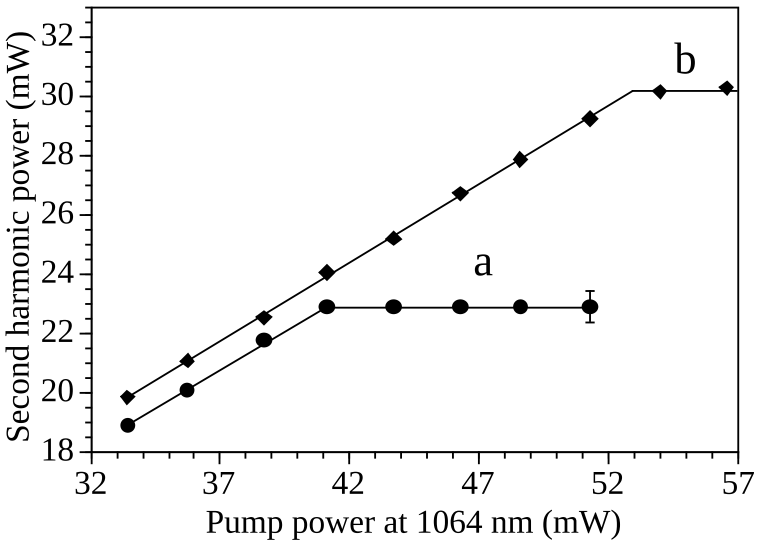

Figure 6.4: Second harmonic power is plotted against the fundamental pump power. (a) The second harmonic power is clamped at $P_2 = 23$ mW. By slightly changing the detuning of the monolithic cavity (b) shows that the clamping level can be shifted to higher power $P_2 = 40$ mW. The single error bar shown is the typical uncertainty of the measurements.

It is found from Eq. (6.1) that at pump power larger than the competition threshold, the second harmonic power is clamped at

$$P_3 = h2\nu\frac{\bar{\gamma}^2}{\mu_2} \tag{6.12}$$

A phenomenon analogous to the optical limiter proposed by Siegman [49] and also predicted by the quadruply resonant system in reference [59]. In the presence of competition, the second harmonic mode can have the choice of backconversions via DOPO and NDOPO.

6.2.2 Limit to squeezing

Naturally, the presence of competition also has its effect on the intensity noise of the second harmonic mode. For the quadruply resonant system, the predicted signature for competition is near-perfect squeezing on both the fundamental or the second harmonic mode in power regimes that are inaccessible in the absence of competition [64, 66]. However our system is not resonant at the second harmonics. The observed outcome of competition in this case is a degradation of second harmonic squeezing, in contrast to the enhancement provided in quadruply resonant competition.

From Chap. 5, we find that the squeezing spectrum for the second harmonic mode is given by

$$V_3(\Omega) = 1 - \frac{8\gamma_{\rm nl}^2 - 8\gamma_{\rm nl}\gamma_1^c(V_1^{\rm in}(\Omega) - 1)}{(3\gamma_{\rm nl}^2 + \gamma_1) + \Omega^2} \tag{6.13}$$

where $\gamma_{\rm nl} = \mu_1|\alpha_1|^2$ is the nonlinear loss rate of the system and $V_1^{\rm in}$ is the amplitude quadrature noise variance spectrum of the fundamental pump field. For a quantum noise limited input pump field $V_1^{\rm in}$ and a nonlinear loss dominated system $\gamma_{\rm nl} \gg \gamma_1$, the maximum observable squeezing is $V_3^{\rm max}(0) = 1/9$ (-9.5 dB) at frequencies close to DC. The largest amount of squeezing inferred from the experimental data in Chap. 5 is only around $V_3 = 1/2$ or -3 dB, in poor agreement with the prediction even when all nonideal conditions were taken into account. This discrepancy can now be understood as a consequence of the onset of competition. With competing nonlinearities, the modified noise spectrum for the second harmonic mode for pump power satisfying $N > 1$ becomes

$$V_3(\Omega) = 1 + \frac{2(N-1)B(\Omega) - 2NA(\Omega)}{(N-1)^2 B(\Omega) + \frac{C(N)\,N\,A(\Omega)}{r} + \left[\frac{\Omega\gamma_f}{2\bar{\gamma}}\right]^2 + \left[\frac{\Omega^2}{2\bar{\gamma}}\right]^2} \tag{6.14}$$

where we have assumed the ideal conditions of $V_1^{\rm in} = 1$ and $\gamma_1^c = \gamma_1$. The substitutions made were

$$\begin{aligned} \gamma_f &= \gamma_1 + r\bar{\gamma} && (6.15)\\ A(\Omega) &= r^2\Omega^2 && (6.16)\\ B(\Omega) &= \gamma_f^2 + \Omega^2 && (6.17)\\ C(N) &= \gamma_f/\bar{\gamma} + r(N+1) + 2(N-1) && (6.18) \end{aligned}$$

If we assume the condition of minimum competition threshold, Eq. (6.14) simplifies to

$$V_3(\Omega) = 1 + \frac{2(N-1-\bar{\Omega})}{4N^2\bar{\Omega} + (N-1-\bar{\Omega}^2)^2} \tag{6.19}$$

where $\bar{\Omega} = \Omega/(2\gamma_1)$. This gives a maximum squeezing of $V_3 = 1/2$ (-3 dB) at DC. When the threshold for competition is higher, the maximum squeezing is still at DC but has a larger value.

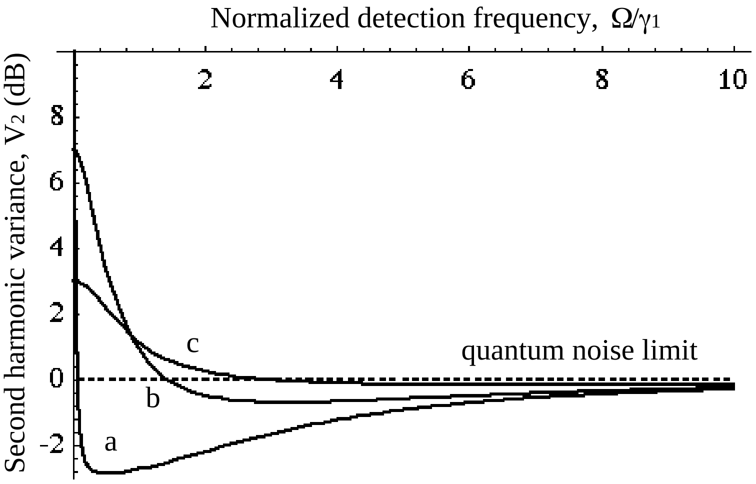

Figure 6.5: Theoretical plots of second harmonic squeezing in the presence of competition where we have assumed the minimum threshold condition $P_1^{\rm thr} = P_1^{\rm min}$. (a) $N = 1.001$, (b) $N = 1.25$ and (c) $N = 3$.

Figure 6.5 shows the theoretically calculated plots of the second harmonic squeezing spectra. At just above threshold, as in (a) of Figure 6.5, we note that the second harmonic is squeezed to an amount similar to that predicted by Eq. (6.13) for the same pump power. This shows that Eq. (6.13), which is valid only for $N \leq 1$, is continuous in its transition to Eq. (6.14) (or Eq. (6.19)) which is valid for $N \geq 1$. At power above the threshold, two effects come into play. Firstly, the increase in N pulls the second harmonic noise at all frequencies toward the noise level of the input field. Since the input is assumed to be quantum noise limited (or worse), the effect is to degrade the squeezing towards the quantum noise limit of $V_3 = 1$. This effect thus causes broadband degradation of the second harmonic squeezing as can be seen in (b) of Figure 6.5.

The second effect of competition is evident in (c) of Figure 6.5. We note that as the pump power is further increased to several times above threshold value, the low frequency end of the squeezing spectrum is severely degraded. In conventional OPO, the signal and idler amplitude quadratures are very noisy above threshold [69]. For a DOPO, the amplitude quadrature noise variance is quantum noise limited for $P_1 \geq 4P_1^{\rm thr}$ and 50% squeezed only for $P_1 > 25P_1^{\rm thr}$. Similarly, the noise from the many NDOPO pairs is transmitted to the amplitude of the second harmonic and hence causes squeezing to degrade.

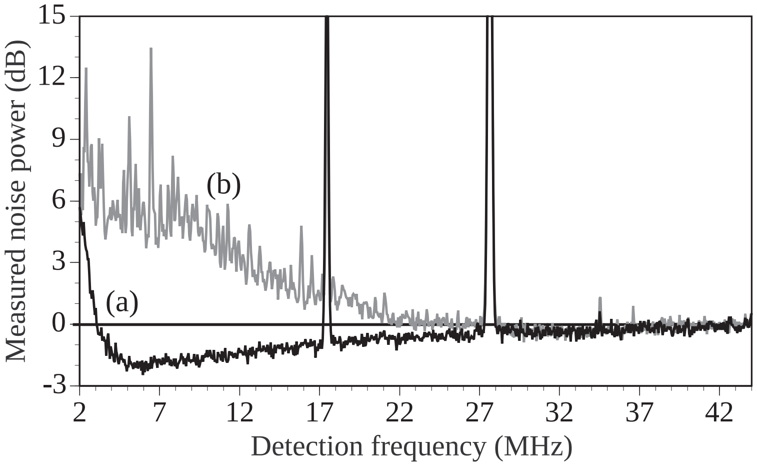

Figure 6.6: Experimental plots of the second harmonic squeezing spectra in the presence of competition. (a) In the absence of competition the second harmonic is squeezed, $P_1 = 74$ mW and (b) With competition, $P_1 = 60$ mW, lower frequency and broadband degradations completely destroy the second harmonic squeezing.

Figure 6.6 shows the experimentally observed squeezing spectra for the second harmonic mode. In plot (a) the competition is suppressed via a slight detuning of the fundamental mode. At below 6 MHz, the squeezing is degraded due to the laser pump noise. The maximum observed squeezing is 2.1 dB at around the 6 MHz region. The spikes at 17 MHz and 27 MHz are signals used for the locking of the monolithic cavity and the mode cleaner. When the threshold of the competing nonlinearities is surpassed, we observed the predicted broadband as well as low-frequency degradations of squeezing. This spectrum is much noisier in comparison with the plot of Figure 6.5(c). This is caused by the presence of more than one pair of NDOPO modes. Furthermore, the presence of the NDOPO modes causes instabilities in the locking system which further increases the noise in the system.

6.3 Summary

We have reported the observation of SHG and NDOPO in a monolithic cavity intended for the generation of second harmonic squeezing. Scanning optical spectrum analysers show the generation of new frequencies around both the fundamental and the second harmonic fields. One classical signature of competition is the clamping of the second harmonic output power. By slight changes in the cavity detuning, the clamping level of the second harmonic can be altered. This feature of competition may have applications as an optical limiter.

From the point of view of squeezed state generation, competition imposes a previously unsuspected limit to squeezing in the single resonant SHG setup. Even though enhancement of noise reduction was reported in theoretical work for the quadruply resonant SHG system, the onset of competition in our singly resonant SHG experiment degrades the amount of squeezing in the second harmonic output. These reported signatures are expected to be ubiquitous in efficient, low dispersion SHG systems. Unless explicit steps are taken to avoid competition, the maximum observable second harmonic squeezing will likely be limited to 3 dB.

Chapter 7

Classical Properties of a Doubly Resonant Optical Parametric Oscillator

Sing it: 'tis no matter how it be in tune, so it make noise enough.

As you like it, William Shakespeare

Overview

This chapter is concerned with the classical properties of an all solid-state source of broadly tunable doubly resonant OPO pumped by a frequency doubled Nd:YAG NPRO laser. We observed a tuning range of 1007 nm to 1128 nm and a combined signal and idler output power of nearly 400 mW. Continuous tuning of over 8 GHz through the precise control of pump laser frequency is also achieved and stable operation on a single axial mode pair is obtained for several hours without mode hops. The relevant published paper to this chapter is

- *" Continuously-tunable doubly resonant optical parametric oscillator"*,
  M. Bode, P. K. Lam, I. Freitag, A. Tünnermann, H. -A. Bachor, and H. Welling, Opt. Commun. **148**, 117 (1998).

7.1 Introduction

Continuous-wave (CW) OPOs have regained attention in the last decade as broadly tunable light sources due to significant improvements in laser technology [14, 70], nonlinear materials [71] and new cavity designs [58, 72]. First demonstrated nearly 30 years ago [73], their development lagged far behind that of pulsed devices, which are now well established and commercially available. Because of threshold constraints, CW systems had to be operated as doubly resonant oscillators (DROs), resonating both the signal and idler waves, with stringent tolerances of the pump frequency and cavity length fluctuations. Such requirements were hardly compatible with lamp pumped solid state or argon ion (Ar+) lasers. DROs are thus known to be highly unstable and difficult to tune. Singly resonant optical parametric oscillators (SRO's) on the other hand have two or three orders of magnitude higher thresholds [74].

The advent of frequency and amplitude stable diode pumped solid state lasers with high single frequency output powers [14, 70] together with monolithic nonlinear OPO cavities [71] created an ideal combination for low threshold single frequency devices with high efficiency [75]. The high spectral purity of such DROs makes them especially useful for high resolution spectroscopy, injection locking and optical frequency division [76]. Because of the strong quantum correlation of the signal and idler waves, it also facilitates the investigation into fundamental studies of quantum optics [77].

Until recently, the output powers of monolithic single frequency OPOs have been limited to levels around 100 mW and continuous tuning without mode hops were confined by the cluster condition [31] to significantly less than 1 GHz. One approach to expand this tuning range is to resort to a proposed dual cavity design [78]. However, this method is only applicable to type II phase matched OPOs and requires carefully selected low loss intra-cavity components. Another interesting solution to achieve large continuous tuning is the recently published subharmonic pumped OPO which combines a frequency doubler and an OPO in a single cavity. This method reduces the number of tuning constraints [62, 63]. Continuous tuning is only limited by the triply resonant conditions of the cavity which can significantly decrease the doubling efficiency for wavelengths far from degeneracy. 4.5 GHz of tuning has been demonstrated with a discrete two mirror cavity through the tuning of the pump source [79, 80]. However, mode hop free oscillation for longer periods is difficult to achieve and requires maximum acoustic isolation of the entire assembly.

If higher pump powers were applied, the inherent stability properties of monolithic cavities turn into a disadvantage, since thermal effects like lensing or induced absorption reduce the mode matching quality. In this chapter, we report on an approach to overcome these constraints using a hemilithic single cavity design [79, 80]. A continuous tuning range of 8 GHz, the highest value reported so far to the best of our knowledge is obtained. We also demonstrate that Watt level pump powers is not necessarily deteriorated by optical degradation due to thermal or photorefractive effects.

7.2 Experimental setup

A schematic of the OPO setup is shown in Figure 7.1. A Mephisto 1800 monolithic Nd:YAG ring laser crystal [14] is pumped by four diode lasers (Siemens SFH 487401), each delivering 1 W of optical power at 808 nm. Stable single frequency emission of 1.8 W CW at 1064 nm with diffraction limited beam quality and a 1 kHz linewidth is achieved. The output frequency is continuously tunable over a range of 8 to 10 GHz without mode hops by precise control of the crystal temperature, while fast tuning is possible by applying mechanical stress to the crystal with a piezoelectric actuator (PZT). A Faraday isolator (30 dB extinction) is used to avoid optical feedback from the SHG crystal to the laser crystal.

SHG of the 1064 nm light is achieved by non-critical type I phase matching of a $\mathrm{MgO:LiNbO_3}$ crystal in an external hemilithic cavity [81]. Maximum single frequency output power of 1.2 W CW at 532 nm is obtained. With respect to the power matched to the fundamental transverse mode ($\mathrm{TEM_{00}}$) of the cavity, this corresponds to internal conversion efficiencies of as much as 90%. Mode hop free operation of more than 10 hours with high intensity stability in combination with frequency drifts of less than 30 MHz per hour has been demonstrated [81]. Hence, the frequency and amplitude stability of the pump laser is directly transferred to the harmonic wave 2ω. No signs of optical degradation or photorefractive effects in the $\mathrm{MgO:LiNbO_3}$ crystal are observed after operation for several months. The hemilithic cavity design can also be used for the second harmonic generation of a Nd:YAG miniature ring laser operating on the 946 nm transition, resulting in 500 mW CW single frequency radiation at 473 nm [82].

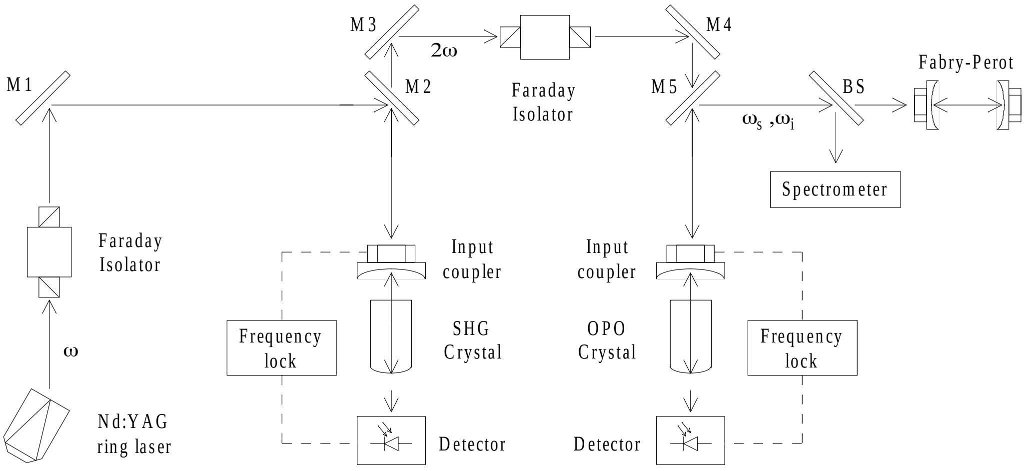

Figure 7.1: Schematic of the above threshold classical OPO experiment. The SHG and OPO crystals are both located in temperature stabilized ovens (not shown) for non-critical phase matching. Mirrors M1, M2 and M5 are highly reflecting at ω, ω_s and ω_i, and highly transmitting at 2ω. Mirrors M3 and M4 are highly reflecting at 2ω. BS: Beam splitter.

We used an identical cavity design to that of the SHG system for the setup of the OPO cavity. The cavity consists of a 7.5 mm long $\mathrm{MgO}:\mathrm{LiNbO_3}$ crystal and an external 25 mm radius of curvature mirror separated by approximately 23 mm. The back endface of the $\mathrm{MgO}:\mathrm{LiNbO_3}$ crystal is polished with a 25 mm radius of curvature and dielectrically coated as a high reflector (HR) for both 1064 nm and 532 nm. The front endface is flat and antireflection (AR) coated for both wavelengths. The external mirror, mounted on a PZT for cavity length adjustment, has transmittivities of 4% and $>$ 94% for 1064 nm and 532 nm, respectively. The nonlinear crystal for the OPO was initially tested in the frequency doubling setup to ensure nearly identical performance to the crystal finally used for the SHG. Its effective nonlinearity obtained from power measurements is

$$\eta_{\mathrm{nl}} = \frac{P_3}{P_1^2} \approx 4\ \mathrm{kW}^{-1} \tag{7.1}$$

The optical parametric oscillation is also achieved by non-critical type I phase matching in the $\mathrm{MgO}:\mathrm{LiNbO_3}$ crystal, temperature stabilized in an aluminium oven with better than 4 mK stability. The OPO cavity, which is of the single-cavity type, can be made doubly resonant for the infrared signal ω_s and idler ω_i waves, while the harmonic pump wave 2ω just double passes the resonator. Consequently, the spatial overlap between the harmonic pump wave and the fundamental transverse cavity modes ($\mathrm{TEM_{00}}$) of the signal and idler waves is difficult to quantify, but crucial for efficient nonlinear coupling.

Our approach to simplify the normally time consuming mode matching of the non-resonant second harmonic wave is to make the beam path of the harmonic wave starting at the endface of the SHG crystal to the endface of the OPO crystal symmetrical about a beam waist centered between the mirrors M3 and M4 (see Figure 7.1). As the two cavities have identical design, symmetry is the main factor to ensure efficient spatial mode matching.

Frequency stabilization of the DRO output while maintaining the possibility to tune the signal and idler frequencies via the control of the pump laser frequency can be achieved in two ways: Since the electro-optical modulation used to stabilize the doubler cavity is present on the harmonic pump wave, it is again transmitted to the OPO signal and idler waves and can be detected on the leakage field through the HR coated endface of the OPO. Mixing with the modulation source of the doubler and low pass filtering the mixer output results in a dispersion type error signal. This error signal is then fed back to the piezoelectric actuator by a servo loop for locking. Alternatively, the OPO crystal can be electro-optically modulated analogous to the doubler crystal. Two copper electrodes in contact with the OPO crystal faces perpendicular to the optical axis are used to generate a different modulation frequency (10 MHz) and frequency stabilization is achieved with similar Pound-Drever-Hall technique.

Both methods were investigated and the latter proved to yield better stability. Although the signal and idler waves each generate a respective error signal, the employed detector does not discriminate between them. Instead a sum error signal corresponding to the average deviation of the signal and idler frequencies from the cavity resonances is generated. By locking to the zero point of this error signal, the sum of the signal and idler detunings is kept to a zero, which is equivalent to the fulfillment of the cluster condition discussed in reference [31]. Therefore it was not necessary to attempt to separate the two error signals.

7.3 Output power and pump depletion

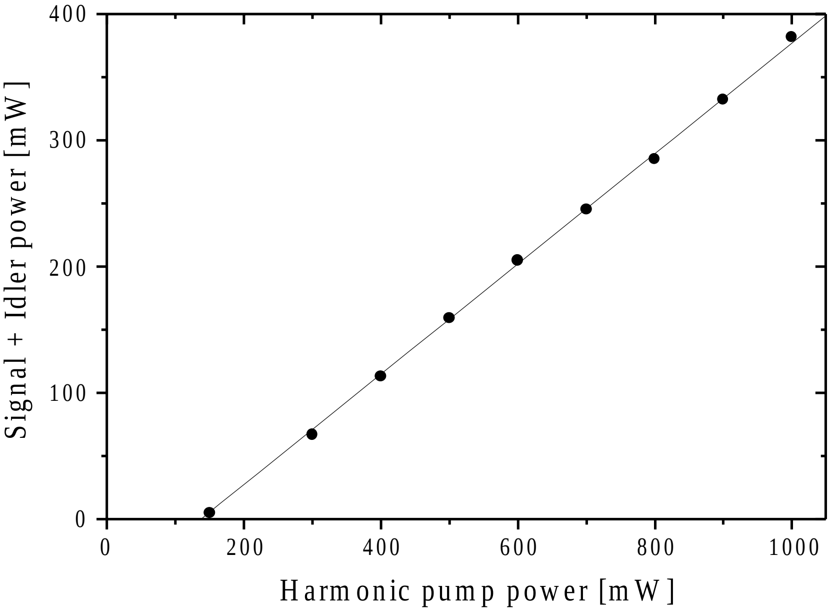

Figure 7.2: Combined signal and idler output power as a function of the harmonic pump power at 532 nm. The experimental data are obtained in front of the beam splitter (BS, see Figure 7.1). A threshold of 150 mW and a linear slope efficiency of 44% are measured.

The combined signal and idler output power in CW single frequency operation generated by the DRO as a function of the harmonic pump power at 532 nm is shown in Figure 7.2. For the maximum harmonic pump power of 1 W CW a combined signal and idler output power of 385 mW is obtained behind the dichroic mirror M5 (see Figure 7.1). This represents the highest value reported so far for single frequency DRO‘s, to the best of our knowledge. In this context, single frequency operation refers to a single signal and a single idler axial mode, or two unique frequencies. The input-output characteristics were measured by changing the polarization of the harmonic pump wave with a half-wave plate in front of the 532 nm Faraday isolator. A linear slope efficiency of 44% and an oscillation threshold of approximately 150 mW are obtained. No signs of optical degradation due to thermal or photorefractive effects are observed up to the maximum harmonic pump power of 1 W CW. Similar to the pump and harmonic waves, the signal and idler waves of the OPO have diffraction limited beam quality.

A theoretical value for the minimum oscillation threshold of a DRO can be calculated using the well known expression

$$P^{\mathrm{thr}} = \frac{(T+A)^2}{4\eta_{\mathrm{SHG}}} \tag{7.2}$$

where η_{SHG} $[\mathrm{W}^{-1}]$ is the effective nonlinearity for SHG. T is the input transmission of the cavity mirror and A the total cavity losses [83]. Using the values obtained from operating the $\mathrm{MgO:LiNbO_3}$ crystal as a frequency doubler, a calculated minimum threshold for zero detunings and optimum mode matching of approximately 110 mW is obtained. As explained in the preceding section, an accurate value for the quality of the overlap between the harmonic pump wave and the cavity modes is difficult to attain as the pump wave is not resonating in the OPO cavity. Hence, the difference between the theoretical and experimental values can be attributed to imperfect mode matching. For the same reason no attempt was made to calculate the conversion efficiency with respect to the harmonic pump power coupled into the fundamental cavity mode (TEM00).

A way to characterize the performance of an OPO independent of the spatial mode matching is to measure the depletion of the reflected pump wave. In our setup, this is easily done at the exit port of the 532 nm Faraday isolator (see Figure 7.1). The relative pump depletion as a function of the harmonic pump power is shown in Figure 7.3. For the maximum pump power of 1 W CW a value of more than 70% is reached, indicating that the internal conversion efficiency with respect to the mode matched pump power is significantly above 50%.

7.4 Coarse and fine tuning capabilities

The tuning characteristics of a doubly resonant OPO are determined by the conservation of energy condition , the phase matching condition and the cluster condition [31].

$$\begin{aligned} \omega_p &= \omega_s + \omega_i && (7.3)\\ k_p &= k_s + k_i && (7.4)\\ \delta\omega_s + \delta\omega_i &= \delta\omega_s^c + \delta\omega_i^c && (7.5) \end{aligned}$$

Of these conditions, phase matching ensures high parametric gain while the other two conditions determine the actual signal and idler oscillation frequencies. Coarse wave-

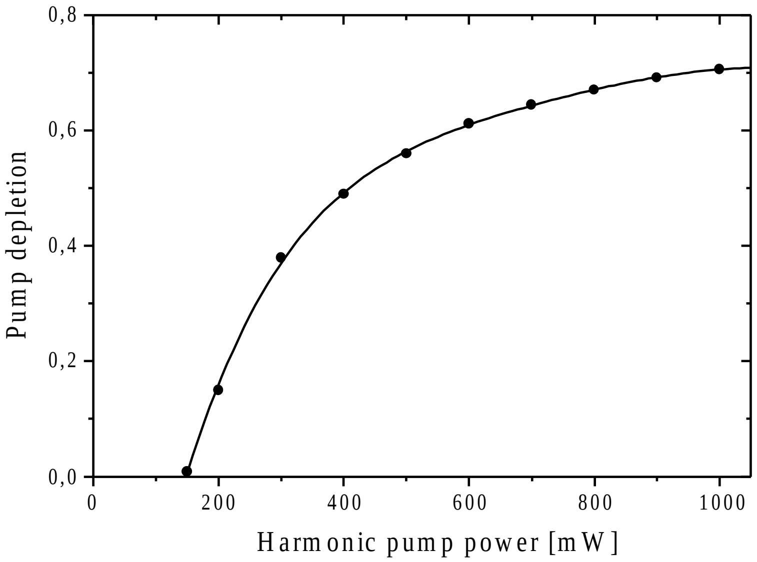

Figure 7.3: Depletion of the harmonic power above the parametric oscillation threshold. The experimental data are obtained by measuring the reflected harmonic power at the exit port of the 532 nm Faraday isolator. For the maximum pump power a depletion of more than 70% is obtained.

length tuning of the non-critically type I phase matched $\mathrm{MgO:LiNbO_3}$ crystal is achieved by the control of temperature. The discrete tuning range for a fixed pump frequency and stabilized single frequency operation is shown in Figure 7.4. The solid curve indicates the phase matching condition $\Delta k = 0$ calculated from published Sellmeier equations [58, 72] with a fitted reference temperature. Although useful parametric gain exists for numerous cluster curves of which $|\Delta k| \le \pi/l$, where l is the length of the nonlinear crystal [31]. In locked operation, a course tuning range from 1007 nm to 1128 nm for signal and idler is achieved. In transient mode with the scanning of the external mirror, parametric oscillation is detected from 980 nm to 1164 nm. These coarse tuning ranges are limited only by the bandwidth of the dielectric coatings on the output coupling mirror and the OPO crystal. With improved mirror bandwidth, it was recently demonstrated that bulk $\mathrm{MgO:LiNbO_3}$ in a CW doubly resonant setup can achieve a coarse tuning range of 788 nm to 1640 nm [67].

The wavelengths of signal and idler are measured with a spectrometer with 0.2 nm resolution, while single frequency operation on a single axial mode pair is confirmed with a confocal scanning Fabry-Perot interferometer with a free spectral range of 3.8 GHz as shown in Figure 7.1. A typical scanning interferometer trace confirming single frequency operation for both signal and idler waves is shown in Figure 7.5. The higher peaks are signal and the lower peaks are idler. The slight difference between the powers is due to the wavelength dependent sensitivity of the detector and the coating bandwidth of the interferometer. Stable operation on a single axial mode pair is obtained for several hours without mode hops, owing to the high frequency and amplitude stability of the pump source as well as the stable locking scheme.

Continuous frequency tuning of doubly resonant OPOs through tuning of the pump source has provided the largest tuning ranges so far [79, 80]. Our setup, using resonant

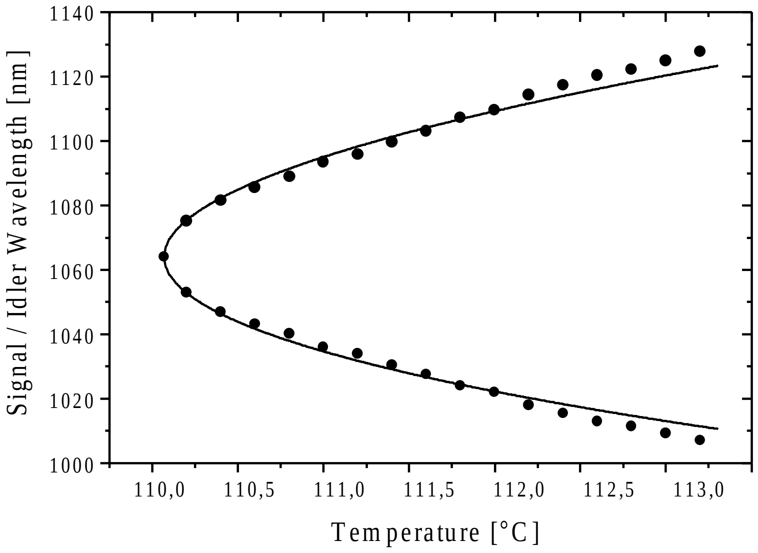

Figure 7.4: Phase matching versus temperature. Signal and idler wavelengths generated by the DRO in single frequency operation as a function of the phase matching temperature. The solid curve indicates the phase matching condition $\Delta k = 0$ calculated from published Sellmeier [72] equations with a fitted reference temperature.

hemilithic cavities locked to the laser frequency for both frequency doubling and optical parametric oscillation, is ideally suited for this approach. Consequently, a continuous tuning range for a signal and idler mode pair of 8 GHz without mode hops is achieved, limited only by the mode hops of the Nd:YAG ring laser. Tuning of the laser frequency via precise control of the Nd:YAG crystal temperature with tuning rates of up to 3 GHz/s resulted in a modulation of the OPO output power of less then 4% over the whole range, demonstrating the stability of the system. As the DRO is pumped by a single frequency laser with a linewidth of 1 kHz, the linewidth of both signal and idler waves is also linewidth limited in the kHz range.

7.5 Summary

We have demonstrated an all solid-state source of broadly tunable single frequency radiation from a CW, doubly resonant optical parametric oscillator with remarkable spectral properties. Based on non-critically phase matched magnesium oxide doped lithium niobate ($\mathrm{MgO} : \mathrm{LiNbO_3}$) and pumped by a frequency doubled Nd:YAG miniature ring laser at 532 nm, the OPO has a combined signal and idler output powers of nearly 400 mW CW with a linear slope efficiency of 44%. The overall efficiency with respect to the diode pump power reaches 10%. Identical nonlinear crystal assemblies were used for the SHG and the OPO resulting in an experimental setup with symmetrical beam path. This is demonstrated to be a convenient setup as it simplifies the normally time consuming spatial mode matching of the harmonic pump wave. Owing to the high frequency and amplitude stability of the single frequency pump laser, stable OPO operation on a single axial mode pair is achieved for several hours without mode hop using a standard Pound-Drever-Hall locking technique. Continuous tuning of the signal and idler frequencies

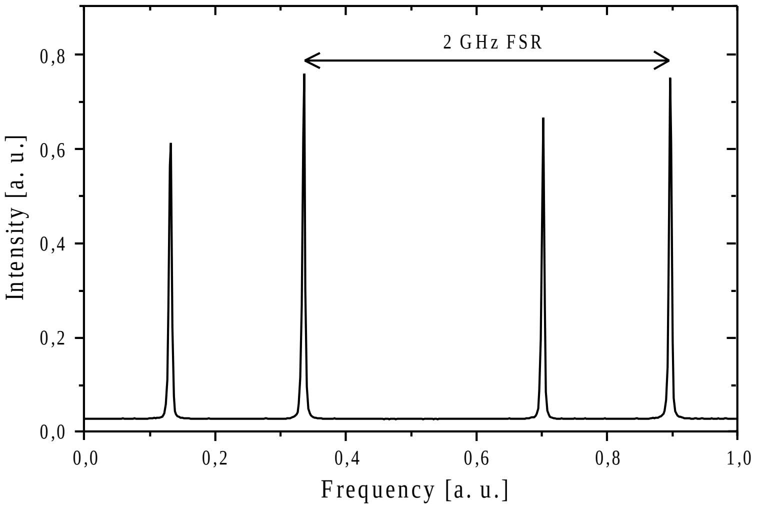

Figure 7.5: Scanning interferometer trace of the DRO output ensuring operation on a single axial mode pair. The higher peaks are signal, the lower peaks are idler. The difference is attributed to the wavelength dependent detector sensitivity and the coating bandwidth of the interferometer. FSR: Free spectral range of the confocal Fabry-Perot interferometer.

over a range of 8 GHz is achieved via precise control of the pump laser frequency with kHz linewidths. The OPO output tuning range of 1007 nm to 1128 nm is achieved.

The study of the classical properties of the above threshold doubly resonant OPO is an important prelude to the study of its quantum noise properties which will be the discussion of the next chapter.

Chapter 8

Squeezed Vacuum Generation

It is contrary to reason to say that there is a vacuum or space in which there is absolutely nothing.

Principia Philosophiae, René Descartes (1644).

Overview

In the previous chapter the classical properties of an above threshold OPO was discussed. This chapter describes the generation of optical squeezed vacuum states using a degenerate below threshold optical parametric oscillator. We report the observation of more than 7 dB of vacuum squeezing and discuss design criteria and experimental considerations for its optimization. We also report 4 dB of bright intensity squeezing by running the OPO as a parametric de-amplifier.

8.1 Introduction

In Chap. 5, we found that second harmonic generation can produce bright amplitude squeezed light. For singly resonant systems, however, the largest observed squeezing reported to date was very much smaller than that predicted by theory. This is due to two main reasons: The onset of parasitic intra-cavity NDOPO and pump noise degradation at low frequencies. The latter effect can be alleviated by using high finesse mode cleaner. In order to combat the former, intra-cavity dispersion has to be introduced to the SHG. This is a technically very challenging task, since losses cannot be introduced along with dispersion for the generation of large squeezing.

In this chapter, we investigate the various limits to squeezing from the reverse process of SHG. Compared to SHG, vacuum state squeezing via OPO has many advantages. Due to the existence of a threshold, the maximum squeezing from the OPO is not limited to 1/9 as in the case of the singly resonant SHG. Ideally, the zero frequency squeezing at the OPO threshold is perfect. Since the generation of the squeezed vacuum state occurs below threshold, we find that to first order, the noise from the OPO pump source does not degrade the squeezed vacuum. Furthermore, competing nonlinearities cannot occur in a parametric downconversion system due to the existence of a threshold.

The first demonstration of vacuum squeezing from a below threshold OPO was done by Wu *et al.* [84, 85] in 1986 where more than 3 dB of squeezing was observed. Polzik *et al.* [86] reported 6 dB of squeezed vacuum from $\mathrm{KNbO_3}$ at 856 nm with a Ti:Sapphire pump laser. The squeezed light obtained was later applied in spectroscopic measurements. In the same year Ou *et al.* [19] also reported 4 dB of vacuum squeezing at

1.08μm from a Type-II KTP crystal pumped by Nd:YAP laser. Improved performance in both the magnitude and the stability of squeezing were achieved with the use of monolithic and hemilithic OPO crystals where 5.5 dB of stable vacuum squeezing was reported by Breitenbach *et al.* [83] from the quantum optics group of Universität Konstanz. The Wigner function, photon number distribution as well as the density matrix of the squeezed vacuum were carefully characterized through optical homodyne tomography (see Appendix G for details). With similar setup, Schneider *et al.* [87] observed 4.3 dB of amplitude squeezing by running the OPO as an amplifier with an input seed wave. Subsequent work [88] improved the magnitude to an observed amount of 6.5 dB after electronic noise floor correction.

Apart from vacuum squeezing from the OPO and bright intensity squeezing from an OPA, the parametric downconversion process can also produce twin beam intensity squeezing [89–92]. Recently, Gao et. al. at Shanxi University [93] reported 9 dB of twin beam sub-quantum correlation from an α-cut KTP crystal. An improvement of 7 dB with respect to the standard quantum limit [20] was achieved in a weak absorption measurements using the strongly correlated twin beam.

Our aim of this chapter is to describe the production and optimization of vacuum squeezing from an OPO. With the hindsight gained from previous experiments, we set out to design an OPO solely for the purpose of obtaining large vacuum squeezing. We show that an important requisite for large vacuum squeezing is to have an OPO with high escape efficiency. However, the threshold power of such OPO is large, making above threshold operation difficult. Nevertheless, characterization of the OPO can still be done by running the OPO as an amplifier and by measurements of the magnitudes of output squeezing and anti-squeezing.

8.2 Experimental setup

The experimental setup for the generation of squeezed vacuum is as shown in Figure 8.1. A Nd:YAG NPRO laser (Mephisto 700) with a maximum output power of 700 mW at 1064 nm is used to pump a SHG crystal. The second harmonic output from the crystal is retrieved via a dichroic and directed to the front face of an OPO crystal. When necessary the OPO can be seeded with an input signal from the back face with some of the light tapped off from the laser before the SHG stage. A local oscillator beam is set up after passing some of the light from the laser output ($\approx$ 8 mW) through a high finesse mode cleaner. This local oscillator beam is mixed with the output of the OPO via a 50/50 beam splitter and measured in a homodyne configuration. The individual elements of the experiment will be described in more detail in the following sections.

8.2.1 The second harmonic generator

The second harmonic generator is constructed from bulk $\mathrm{MgO:LiNbO_3}$ in a hemilithic configuration and second harmonic generation is achieved via Type-I non-critical temperature phase matching. The dimensions of the crystal are $5.0(x) \times 7.5(y) \times 2.5(z)$ mm, where z denotes the optical axis. These dimensions are chosen for several reasons. Firstly a thin (2.5 mm) crystal along the optical axis provides a more efficient modulation of the crystal cavity via the electro-optic effect for a fixed applied voltage. This is because the change in refractive index of the material is proportional to the applied electric field gra-

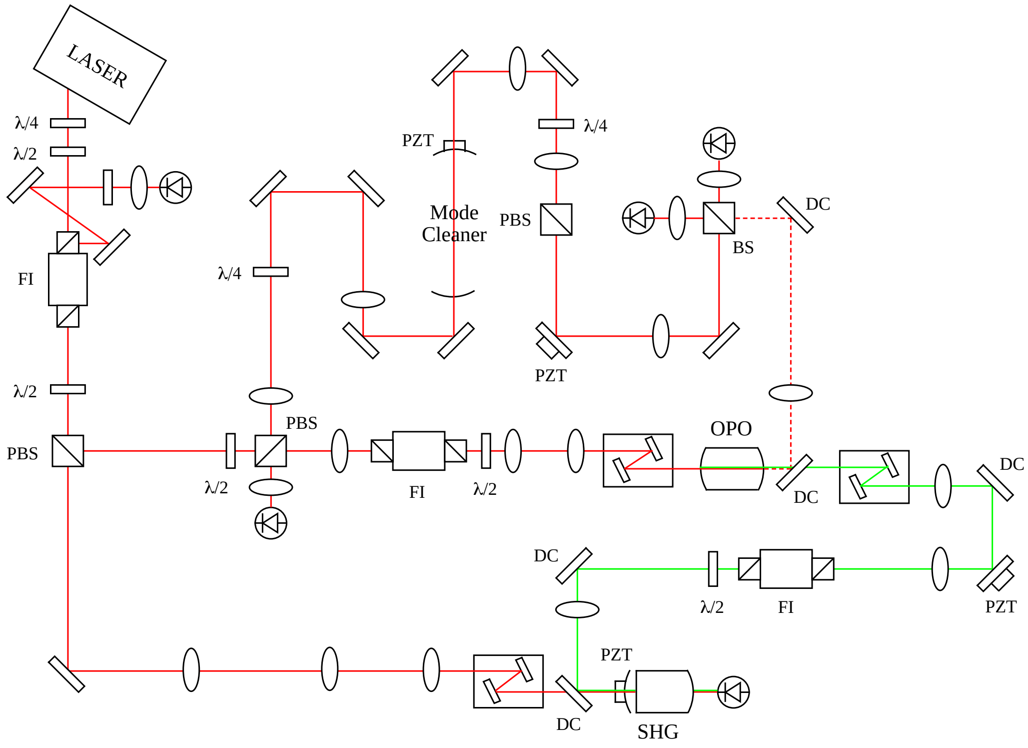

Figure 8.1: The experimental setup of the squeezed vacuum generator. $\lambda/2$, $\lambda/4$: half, and quarter wave plates; FI: Faraday isolator; BS: 50/50 beam splitter; PBS: Polarizing beam splitter; DC: Dichroic; PZT: Piezo-electric actuator.

dient

$$\Delta n = 1.137 \times 10^{-10} E \tag{8.1}$$

where E is in units of $\mathrm{V m^{-1}}$. Consequently, a smaller voltage is required for a thinner crystal. However, when the front and back faces of the crystal are too small, dielectric coatings may not be able to adhere to the crystal under thermal and electro-optic stresses [94]. A compromise to this is to make the x-dimension of the crystal larger. Hence dielectric layers are instead coated on the 2.5×5.0 mm surfaces. For the detection of squeezed light, a shorter crystal with larger cavity linewidth is desirable. However, a Boyd-Kleinman factor calculation [95] suggests that longer crystals have higher total nonlinearities , assuming all else unchanged. In order to improve the nonlinearity of a shorter crystal, the cavity has to be made nearer to concentric. We require that the waist of the cavity mode and the radius of curvature of the end faces to be smaller. This lead us to use a length of 7.5 mm along the y-axis with a comfortable 10 mm radius of curvature on the back face of the crystal. The coating on the curved back face of the crystal has $R =$ 99.96% for both 1064 nm and 532 nm and anti-reflection coating with $R <$ 0.1% for both modes is used for the front flat face of the hemilith.

A cavity is formed by placing an external output coupling mirror ≈ 23 mm in front of the crystal. The reflectivities of the mirror are 96% and 10% for 1064 nm and 532 nm, respectively. The radius of curvature of the output coupling mirror is 25 mm. The hemilithic cavity thus has a finesse of $\mathcal{F} = 146$, a free spectral range of FSR = 3.8 GHz and a cavity linewidth of FWHM = 25.8 MHz. The crystal is sandwiched between two electrodes along the optical axis and surrounded with a layer of macor. The entire assembly is finally housed in an aluminium casing which is temperature controlled to a stability of within ± 2 mK using a home built temperature controller (see Figs. D.1, D.2 and D.3 in Appendix D). The locking of the SHG is achieved by feedback control of the Pound-Drever-Hall error signal on a PZT mounted behind the output coupling mirror. Although higher second harmonic conversion efficiency is possible at lower power, 300 mW of 532 nm light is obtained with a maximum pump power of 600 mW .

8.2.2 The optical parametric oscillator

The optical parametric oscillator is based on the same technology as the second harmonic generator but with some minor differences. In order to minimize the intra-cavity losses, the OPO is formed by a monolithic cavity with the similar dimensions of $5.0(x)\times 7.5(y)\times 2.5(z)$ mm to the SHG. Both of the end faces of the OPO have radius of curvatures of 10 mm. The front face is coated with R = 95.6% for 1064 nm and R = 4% for 532 nm. The end face is again high reflectivity coating with R = 99.96% for both 1064 nm and 532 nm. The measured intra-cavity losses for the monolith is $\approx$ 0.1% cm^{-1} for 1064 and $\approx$ 4% cm^{-1} for 532 nm. The other cavity parameters are $\mathcal{F} = 136$, FSR = 9 GHz and FWHM = 66 MHz.

Since the cavity has no movable parts, tuning of the OPO cavity is difficult. The use of electro-optic effect can only produce tuning of small fractions of the cavity FSR even with very high applied voltage [1]. Although large tuning can be achieved by temperature control, this degree of freedom was not used due to the slow time response. Furthermore, temperature tuning of the nonlinear crystal also affects the strength of the nonlinear interaction, thus creating further operational complications. Although this is an apparent disadvantage of the monolithic system compare with hemilithic, the significantly smaller intra-cavity loss of the monolith remains an attractive attribute.

8.2.3 The mode cleaner

A standing wave mode cleaner is constructed for the purpose of both providing spatial as well as high frequency intensity noise filtering for the local oscillator beam. The advantages of frequency noise filtering has already been discussed in Chap. 5 and a quantum noise limited local oscillator is likewise essential for the homodyning of the squeezed vacuum states. Moreover, the output of an NPRO laser usually possesses some degree of astigmatism [96]. Since the squeezed vacuum beam is produced from a monolithic standing wave cavity, it has a very well defined diffraction limited Gaussian profile, which is non-astigmatic. The direct homodyne mixing of these two beams will hence yield interference with low visibility. In our experiment, we found that without spatial mode cleaning, the best visibility of the interference is $\mathrm{VIS} = 90\%$. Because the homodyne efficiency of the detection system is dependent on the square of visibility $\eta_{hom} \propto \mathrm{VIS}^2$, this alone is a significant limit to the maximum observable squeezing. We used two supermirrors from Newport (part number:10CV005R50T) to construct a standing wave cavity with a length of 170 mm. The radii of curvature of the mirrors are 1 m. Using Eq. (3.10), we found that the non-degeneracy of the higher order spatial modes for this cavity to be

---

[1] 1000V has been applied to the crystal while it was pumped with 300 mW of 532 nm light. No apparent photo-refractive damage was observed.

excellent. The mirrors have the following parameters:

$$R_1 = 99.89\%, \qquad R_2 = 99.98\% \tag{8.2}$$

$$A_1 = 3190\mathrm{ppm}, \qquad A_2 = 2810\mathrm{ppm} \tag{8.3}$$

$$T_1 = 0.103\%, \qquad T_2 = 0.0196\% \tag{8.4}$$

This gives a cavity finesse of $\mathcal{F} = 5000$, a free spectral range of FSR = 880 MHz and a cavity linewidth of 176 kHz. Impedance matching of $P_{\mathrm{trans}}/P_{\mathrm{inc}} \approx 60\%$ was obtained.

8.2.4 The homodyne system

The homodyning of the OPO output is done by combining the local oscillator and the OPO output via a 50/50 beam splitter. Since an imbalance in the power of the beam splitter outputs leads to a lower homodyning efficiency, care was taken in angle tuning the beam splitter to ensure that the 50/50 splitting ratio was accurate to less than ± 2%. The photodetectors used in the final detection are as shown in Figure B.1. An Epitaxx ETX-500 photodiode is used in a two stage transimpedance amplification circuit using two Comlinear operational amplifiers (CLC420 and CLC430). This type of photodetector can take up to 10 mW of optical power without any observable saturation effect [29]. The frequency range of this photodetector is from DC to around 20 MHz, which is more than suffices for the detection of squeezed vacuum which is normally performed at frequencies lower than 5 MHz. The quantum efficiency of the photodiodes were measured to be $94\pm$ 2%.

The homodyne efficiency of the system is determined by a measurement of the interference visibility form by two optical beams with equal intensity. We inject a small amount of laser light into the back face of the OPO and interfere this output with the spatially filtered local oscillator beam. The visibility of the interference fringes were found to be (98.5 ± 1.0)% give a homodyne efficiency of $\eta_{hom} = 0.97 \pm 0.02$.

8.3 A simple theory for OPO

We model the parametric process with the following simple approach. The Hamiltonian of the parametric downconversion process can be written as

$$H = Ea^\dagger a^\dagger - Eaa \tag{8.5}$$

where E is, in general, a complex constant that is dependent on the nonlinearity and the pump intensity. a and $a^\dagger$ are the annihilation and creation operators of the degenerate OPO output mode. The equations of motion of the OPO can then be written as

$$\dot{a} = Ea^\dagger - \gamma a + \sqrt{2\gamma_b}A_b + \sqrt{2\gamma_l}\,\delta A_l + \sqrt{2\gamma_c}\,\delta A_c \tag{8.6}$$

$$\dot{a}^\dagger = E^* a - \gamma a^\dagger + \sqrt{2\gamma_b}A_b^\dagger + \sqrt{2\gamma_l}\,\delta A_l^\dagger + \sqrt{2\gamma_c}\,\delta A_c^\dagger \tag{8.7}$$

where γ_b, γ_c and γ_l are the decay rates due to the back and front reflectivities and the intra-cavity losses of the OPO. $\gamma = \gamma_b + \gamma_c + \gamma_l$ is the total cavity decay rate. A_b is the seed wave injected at the back face of the OPO and δA_c and δA_l are the vacuum fluctuations terms associated with the respective losses. The steady state solution of the expectation of a, $\langle a \rangle = \alpha$, can be found by setting the above derivatives to zero and ignoring quantum fluctuations. This gives

$$\alpha = \frac{E}{\gamma}\alpha^* + \frac{\sqrt{2\gamma_b}}{\gamma}A_b \tag{8.8}$$

$$\alpha^* = \frac{E^*}{\gamma}\alpha + \frac{\sqrt{2\gamma_b}}{\gamma}A_b^* \tag{8.9}$$

where we have again used the linearization convention of $a = \alpha + \delta a$. By assuming that $\langle A_b \rangle = A_b$ is a real number, we obtained a simple expression for the intra-cavity field,

$$\alpha = \frac{(1 + E/\gamma)\sqrt{2\gamma_b}A_b}{\gamma(1 - |E|^2/\gamma^2)} \tag{8.10}$$

We note that in the absence of a pump amplitude, $A_b = 0$, the intra-cavity field has no coherent amplitude $\alpha = 0$. Using the input-output formalism, we can then work out the extra-cavity transmitted and reflected fields, $A_{\mathrm{trans}} = \sqrt{2\gamma_c}\alpha$ and $A_{\mathrm{refl}} = \sqrt{2\gamma_b}\alpha - A_b$. The reflected and transmitted photon number expressions are

$$n_t = \left|\frac{2\sqrt{\gamma_b\gamma_c}(1 + E/\gamma)}{\gamma(1 - |E|^2/\gamma^2)}\right|^2 A_b^2 \tag{8.11}$$

$$n_r = \left|\frac{2\gamma_b(1 + E/\gamma)}{\gamma(1 - |E|^2/\gamma^2)} - 1\right|^2 A_b^2 \tag{8.12}$$

The quantum noise behaviour of the OPO can be obtained from Eqs. (8.6) and (8.7). By taking the Fourier transform of the linearized equations, we obtained expressions for the fluctuations $\delta X^+ = a + a^\dagger$ of the amplitude quadrature and $\delta X_- = i(a - a^\dagger)$ of the phase quadrature of the field

$$i\Omega\,\delta X^+ = (\Re[E] - \gamma)\delta X^+ + \Im[E]\delta X^- + \sqrt{2\gamma_b}\delta X_b^+ + \sqrt{2\gamma_l}\delta X_l^+ + \sqrt{2\gamma_c}\delta X_c^+ \tag{8.13}$$

$$i\Omega\,\delta X^- = \Im[E]\delta X^+ + (\Re[E] + \gamma)\delta X^- + \sqrt{2\gamma_b}\delta X_b^- + \sqrt{2\gamma_l}\delta X_l^- + \sqrt{2\gamma_c}\delta X_c^- \tag{8.14}$$

where all $\delta X_i = \delta X_i(\Omega)$ are now operators as a function of the detection angular frequency, and $\Re[E]$ and $\Im[E]$ denote the real and imaginary part of the complex number E. The internal and external fields are again linked by the input-output formalism, $\delta X_1^+(\Omega) = \sqrt{2\gamma_c}\delta X^+ - \delta X_c^+(\Omega)$, where the subscript 1 is used to denote the measurable output mode of the OPO. The noise spectrum $V^+(\Omega)$ of the output is then obtained using,

$$V^+(\Omega) = \langle \delta X_1^{+*}(\Omega)\, \delta X_1^+(\Omega) \rangle \tag{8.15}$$

This spectrum contains information about the amplitude quadrature of the OPO which is measured in our experiment. The expression for the phase quadrature variance of the OPO, $V^-(\Omega)$, can be similarly obtained.

8.4 Classical regenerative gain

Because of the large escape efficiency of our OPO, the available second harmonic power is insufficient to pump the OPO above threshold. The initial investigation into the characteristic of the OPO is therefore performed by running the OPO as an amplifier with an input seed wave. Assuming that the pump power not significantly depleted, Fig-

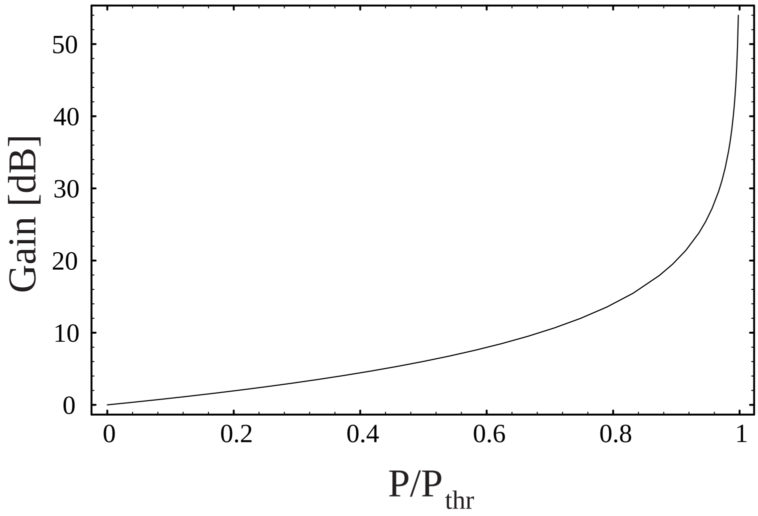

Figure 8.2: Calculated classical gain of the OPO operating as an amplifier. The gain is calculated by considering the ratio of transmitted powers with OPO pump power on and off, $P_{\text{inc}} = P$ and $P_{\text{inc}} = 0$.

ure 8.2 shows the calculated results of the OPA gain using Eq. (8.11). We note that at close to the threshold, the OPA gain obtained from the transmitted beam can be very large ($G > 10,000$ or 50 dB). This is due in part to the parametric amplification and in part to the improvement of the cavity impedance matching.

The impedance matching condition of a cavity is given by [16]

$$\Delta M = \sqrt{R_c} - \sqrt{R_b}(1 - L) = 0 \tag{8.16}$$

where R_c and R_b are the reflectivities of the back and front surfaces, and L is the total intra-cavity loss. We note that without any incident pump field, the coupling and transmission of the seed wave from the back of the OPO is very small, due to the poor impedance matching (large ΔM due to $R_c > R_b(1-L)$) of the OPO cavity. When the OPO is pumped by an incident wave, parametric gain is experienced by the sub-harmonic mode. This corresponds to having a negative loss $L < 0$, thus making the cavity better impedance matched. Thus, more of the seed wave is coupled into the OPO, resulting in even more gain. Figure 8.3 shows a regenerative OPO gain of $\approx 10,000$ when all of the available pump power from the SHG is incident on the OPO. We note that according to the theoretical calculation, this corresponds to within 2% of the threshold. However, in spite of attempts to increase the second harmonic output, above threshold oscillation of the OPO was not observed.

8.5 Limits to vacuum squeezing

In most publications squeezing is analysed as a function of pump power. This is because the pump level normally determines the amount of squeezing. In the case of a below threshold OPO, 100% squeezing is predicted at the threshold in an ideal set-up. However, while the OPO is experimentally running below threshold, this is not the easiest quantity

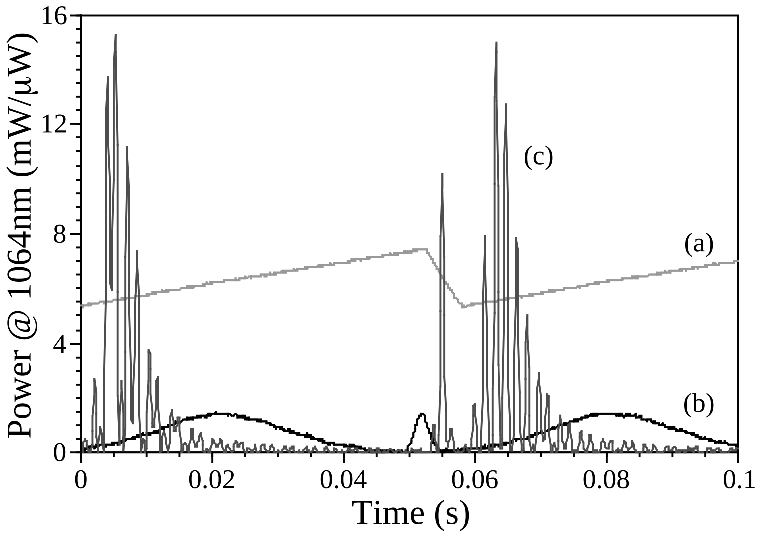

Figure 8.3: Classical gain of the OPO operating as an amplifier. The OPO is electro-optically modulated by application of a ramp voltage with a period of 55 ms as shown in trace (a). Trace (b) shows the small input signal beam injected at the back face of the OPO, the peak power of the input beam corresponds to 1.5 μW of optical power. With the pump field of the OPO turned to the maximum of 300 mW, trace (c) shows the transmitted output. We note that the presence of the pump field slightly shifted the resonance of the OPO due to the thermal effect caused by pump absorption. The pump field is modulated at a much shorter period of 3 ms. Parametric amplification or de-amplification is observed when the pump field is in-phase or in-quadrature with the signal field. The maximum classical gain achieved with this setup is $\approx 10,000$ (15 mW).

to measure since many other experimental conditions may vary. For example, the phase matching of the OPO crystal may have drifted due to the variation of pump light, thus causing a change in the OPO threshold.

A more systematic way of analysing the situation is a plot of the anti-squeezing quadrature versus the squeezing quadrature. As reported by Wu *et al.* [85], the output of a below threshold OPO can be inferred to be a minimum uncertainty state. This piece of information can then be used to determine the efficiencies of the system and the amount of parametric action occurring at the below threshold condition.

The quantum noise analysis of the OPO gives us the following analytic expressions of the squeezing and anti-squeezing quadrature noise variance,

$$V^{+}(\Omega) = 1 - \eta_{\rm esc}\,\eta_{\rm det}\,\eta_{\rm hom}\frac{4\sqrt{P/P_{\rm thr}}}{((\Omega/\gamma)^2 + (1+\sqrt{P/P_{\rm thr}})^2)} \qquad (8.17)$$

$$V^{-}(\Omega) = 1 + \eta_{\rm ese}\,\eta_{\rm det}\,\eta_{\rm hom}\frac{4\sqrt{P/P_{\rm thr}}}{((\Omega/\gamma)^2 + (1-\sqrt{P/P_{\rm thr}})^2)} \qquad (8.18)$$

Where $\eta_{\rm esc}, \eta_{\rm det}, \eta_{\rm hom}$ are the escape, detection and homodyne efficiencies of the OPO system; P and $P_{\rm thr}$ are the pump and threshold powers. Unlike in the case of SHG squeezing, the pump noise of the OPO does not contribute significantly to the squeezing spectrum of the OPO below threshold. We now examine each limiting factor in detail.

- *Escape efficiency*

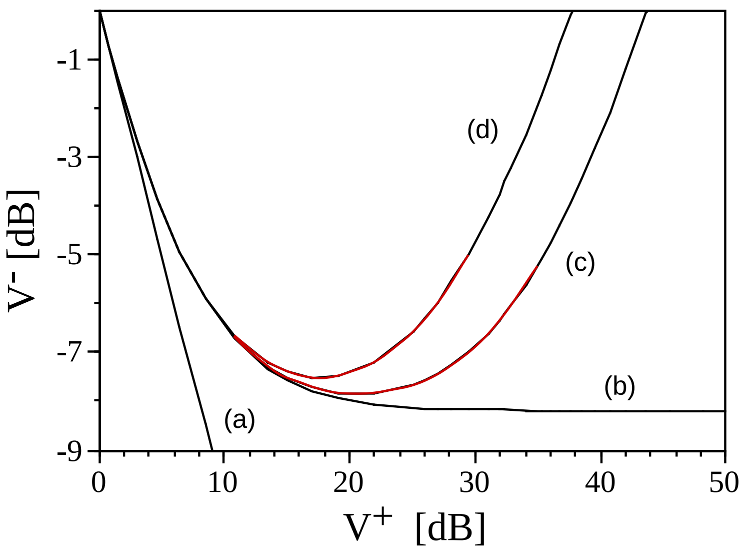

Figure 8.4: Limits of the OPO squeezing. The anti-squeezing quadrature V^+ is plotted against the orthogonal squeezing quadrature V^- of the OPO vacuum output. Trace (a) shows the theoretical prediction for an ideal squeezed vacuum state, where $V^+V^- = 1$; Trace (b) is the calculated squeezed vacuum state based on the experimental efficiencies; In traces (c) and (d), phase jitter of $\Delta\phi = 0.05$ rad ($3°$) and 0.10 rad ($6°$) are added onto the vacuum output, respectively. The results shows that there is an optimum value below threshold where the vacuum squeezing is maximum.

The escape efficiency of the OPO is the ratio of output coupling decay rate to the total cavity decay rate given by

$$\eta_{\mathrm{esc}} = \frac{\gamma_c}{\gamma} \tag{8.19}$$

From the parameter values of the OPO crystal, we obtained $\eta_{\mathrm{esc}} = 0.96 \pm 0.01$. Obviously, the escape efficiency can be further increased by reducing the reflectivity of the OPO front face. However, this is at the expense of a much larger OPO threshold. From the previous section, we have already acknowledged that insufficient pump power is available to bring the OPO to above threshold. Thus a further increase in the escape efficiency is only feasible with a more efficient SHG source or a more powerful pump laser.

- *Detection efficiency*

  The Epitaxx 500 InGaAs photodiodes were used in the RF amplification circuit given in Figure B.1. The quantum efficiency of these photodetectors is $\eta_{\mathrm{det}} = 0.94 \pm 0.02$ and the detectors are capable of detecting 10 mW of optical power without saturation. In our experiment, the squeezed vacuum is measured in a homodyne setup with a 6 mW optical local oscillator. More than 10 dB of quantum noise floor clearance from the dark noise of the photodetector was present and hence the squeezed vacuum measurement does not require any electronic noise floor correction.

- *Homodyne efficiency*

  A detailed discussion of the homodyne efficiency is presented in Chap. 2. With the use of the spatial mode cleaner described in Sec. 8.2.3, the homodyne efficiency of

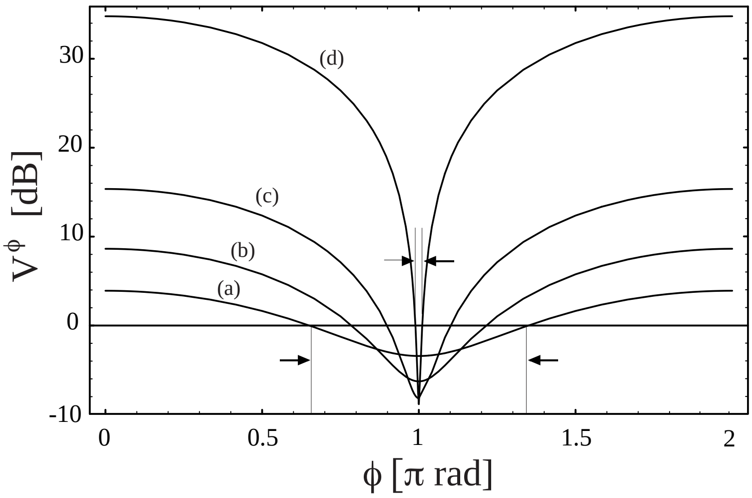

Figure 8.5: Plot of V^{ϕ} for 25, 50, 75, 100% of threshold pump power for (a), (b), (c) and (d) respectively. The total efficiency used is $\eta_{\rm tot} = \eta_{\rm esc}\eta_{\rm det}\eta_{\rm hom} = 0.90$. The quadrature angles which have sub-quantum noise variance become narrower as shown by the arrows for trace (a) and (d).

our OPO system is $\eta_{\rm hom} = 0.97 \pm 0.02$.

- *Cavity linewidth*
  Another advantage of lowering the reflectivity of the OPO front face, or increasing the escape efficiency is the broadening of the OPO cavity linewidth. Since squeezing is only observable within the cavity linewidth due to the input-output coupling, a larger linewidth is desirable. The linewidth of our OPO system is 67 MHz. At the detection frequency of this experiment (3 MHz), linewidth considerations are unimportant.

- *Threshold power*
  Investigation into the regenerative gain of the OPO has revealed that the available second harmonic power of the system is sufficient to get within 2% of the threshold power. From Eq. (8.17) and (8.18), we note that the amount of vacuum squeezing has only a square-root dependence on the pump power of the OPO. Hence, this factor is not crucial. In fact, most of the best vacuum squeezing results from OPO were obtained at a level significantly lower than the OPO threshold due to the phase stability of the system.

- *Phase jitters*
  Phase angle resolution becomes more and more acute with larger squeezing. The vibration of the reflecting surfaces causes jitter in the relative phase of the local oscillator and the squeezed beam. If these vibrations are faster than the time required for the spectrum analyser to gather a single pixel of information, then that point will not be a pure measurement of the noise at quadrature phase angle θ. Instead it will be a measurement of the noise integrated over some range of angles $\theta \pm \delta\theta$. If this happens, then some of the noise from the anti-squeezed quadrature is coupled into what was intended to be a measurement of the squeezed quadrature. This will reduce the amount of squeezing which can be observed. Figure 8.4 shows theoretical

predictions of the observable squeezing of V^+ as a function of the anti-squeezing quadrature V^-. With a perfectly efficient system, trace (a) shows the reduction of noise in the squeezed quadrature V^+ and the corresponding increase of noise in the anti-squeezed quadrature V^- predicted by Eqs. (8.17) and (8.18). When experimental efficiencies are included, trace (b) shows that as the OPO approaches threshold, the observable squeezing is limited by the experimental efficiencies to a maximum of 8.5 dB close to threshold, while the anti-squeezing noise still increases. The addition of phase jitter, shown in traces (c) and (d), means that as the OPO approaches threshold, increasingly large amounts of noise are coupled into the measurement of V^+ and the amount of squeezing observed actually decreases.

From Figure 8.5, we note that when the OPO is operating close to threshold, the increase of the anti-squeezing quadrature noise is large. This effectively reduces the quadrature angles that will exhibit sub-quantum noise variance. Any small phase jitters about the squeezing quadrature therefore couple large amount of noise from the anti-squeezing quadrature.

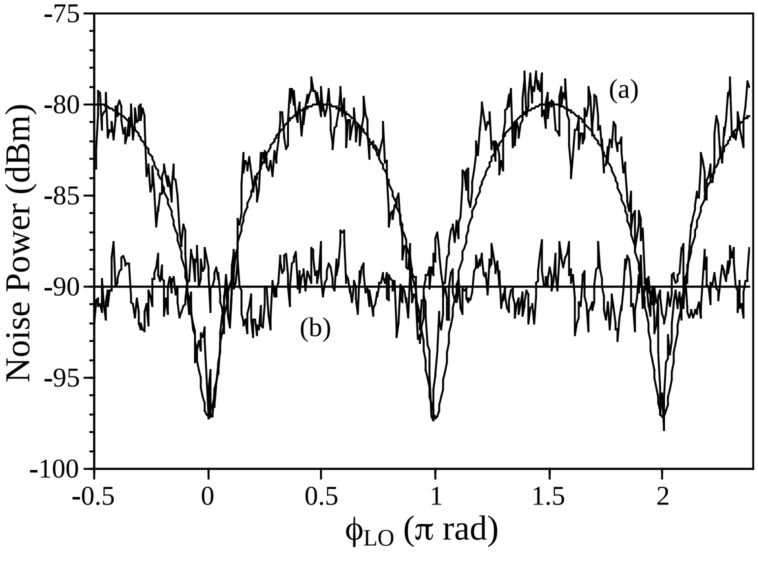

Figure 8.6: Noise variance of the squeezed vacuum. Trace (a) shows experimental results of the noise variance measurement of the squeezed vacuum state. The scan measurement of the quadrature phase shows a variation of noise variance from 10 dB above the standard quantum limit to more than 7 dB of quadrature squeezing. The smooth line are fitted values of a 7.1 dB squeezed vacuum assuming the given experimental efficiencies. The standard quantum noise level is at -90 dBm as shown by trace (b). ResBW = 50 kHz and VBW = 1 kHz.

8.6 Squeezing results

Figure 8.6 shows the end results of our optimization of all experimental parameters. At a pump power of around 60%±10%, we observed our best vacuum squeezing results of more than 7.0 ± 0.2 dB at the detection frequency of 3 MHz. Since the linewidth of the OPO was 67 MHz, the vacuum squeezing produced by our system should exhibit

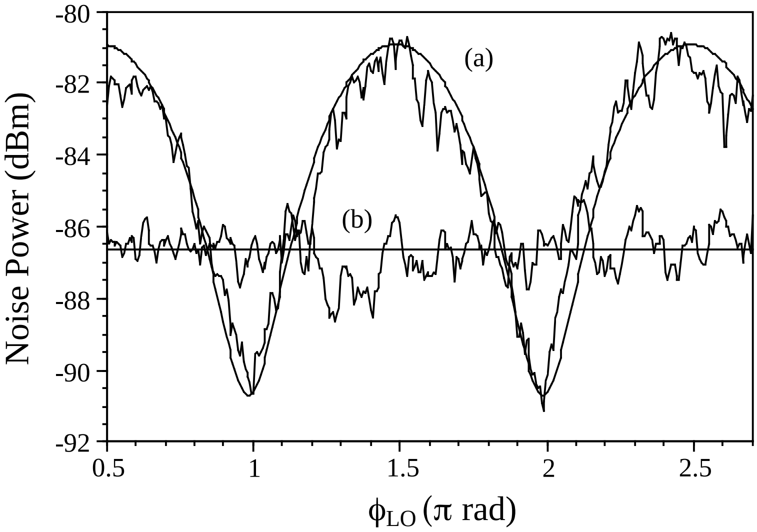

Figure 8.7: Noise variance of the OPA output. Trace (a) shows the noise variance scan of the OPA output. The noise variance varies from 5.5 dB above the standard quantum limit to close to 4 dB of quadrature squeezing. (b) shows the quantum noise limit at -86.6 dBm. The measurement obtained by the OPA are not as reliable as the OPO vacuum squeezing due to problems with the locking system.

broadband squeezing from DC to 10's of MHz. We obtained more than 4 dB of vacuum squeezing with detection frequencies from 1 MHz to 20 MHz. The limit of spectral investigation was set by the frequency response of the photodetectors. The local oscillator power used in this measurement was 6 mW.

Figure 8.7 shows the bright intensity squeezing observed with a small seed wave is injected from the back face of the OPO. The relative phase of the pump with the injected seed were locked by observing the minimum DC level of the sum photocurrents of the homodyne detectors. This corresponds to the de-amplification condition of the OPA which is predicted to produce amplitude quadrature (intensity) squeezing. More than 4 dB of intensity squeezing is observed. However, the intensity squeezing obtained from the parametric de-amplification process provides a squeezed beam of relatively low intensity. When higher input seed powers are used, the intensity noise of the input beam becomes dominant. Unless the seed is quantum noise limited, squeezing obtained from the parametric process will be buried by the residual intensity noise of the seed wave.

8.7 Summary

In this chapter, we have reported the observation of 7.0 ± 0.2 dB of vacuum squeezing from the OPO. To date, this is the one of the best results of vacuum squeezing reported worldwide. We found that the observed squeezing was limited by the phase stability of our system. Without phase jitter, the predicted value for the best observable vacuum squeezing with the current system should be at around 8.5 dB. We have also shown that bright intensity squeezed light can be obtained by operating the OPO as an intensity de-amplifier. The best results obtained was 4 dB.

Part III

Applications of Quantum Electro-Optic Control

Chapter 9

Quantum Electro-Optic Control of Light

The control of a large force is the same principle as the control of a few men: it is merely a question of dividing up their numbers.

The Art of War, Sun Tzu

Overview

This chapter introduces the electro-optic feedforward scheme and shows that it can be used to produce, in principle, perfect noiseless signal amplification (signal transfer coefficient[1] of $T_s = 1$). Experimental demonstrations of the scheme are presented. The scheme is subsequently used to amplify a small signal carried by amplitude squeezed light. We demonstrate that, unlike the fragile squeezed input, the signal amplified output is robust to propagation losses. Finally, when used in combination with an injection locking scheme, we demonstrate that an independently variable noiseless signal and power optical amplifier can be constructed. The relevant published papers to this chapter are

- *"Noiseless signal amplification using positive electro-optic feedforward"*, P. K. Lam, T. C. Ralph, E. H. Huntington, and H.-A. Bachor, Phys. Rev. Lett. **79**, 1471 (1997).
- *" Noiseless electro-optic processing of optical signals generated with squeezed light"*, P. K. Lam, T. C. Ralph, E. H. Huntington, D. E. McClelland, and H.-A. Bachor, Opt. Ex. **2**, 100 (1998).
- *"Noiseless independent signal and power amplification"*, E. H. Huntington, P. K. Lam, T. C. Ralph, D. E. McClelland, and H.-A. Bachor, Opt. Lett. **23**, 540 (1998).

9.1 Introduction

The classical control theory of a feedback or feedforward loop is a very well researched topic for many scientists and engineers. With many of the modern appliances relying on automation and robotics, an understanding of the classical control theory is a common

---

[1] see section 10.2 for a definition of signal T_s and meter T_m transfer coefficients.

requisite for many technologists. In the field of optical physics, control theory is also commonly used in many situations. From temperature controlling of nonlinear crystals, auto-alignment of optical elements to the locking of optical resonators and suppression of laser intensity noise, all make use of electronics control theory in their operations. In optical communication systems, the electro-optic effect is also widely used for the encoding and decoding of modulation signals on a light beam.

An obvious question to a quantum optician in relation to control theory is this: Can classical control theory be utilized in quantum optics to control observables beyond the standard quantum limit? The answer to this question seems to have changed several times in the past decade. At first thought, it is apparent that the quantum counterpart to the classical control theory will not be as simple. In electronic systems where control theory are most frequently used, a tap off point of information (a circuit junction) in general partitions the flow of current to both the readout arm and the transmitted arm almost identically. Electrons, being fermions, only exhibit quantum noise at extremely low-current low-noise situations. Optical quantum noise however, easily manifests itself at every junction point (beam splitter) of an optical system. This is one of the consequences of photons being bosons. An optical beam splitter hence does not behave similarly to an electronic circuit junction. The photon statistics in the readout arm of an optical junction in general have rather different photon statistics to the transmitted arm. However, there is still no reason to discount the possibility that controlling of photon statistics can be achieved by some novel optical control scheme.

The size of amplitude fluctuations on a light beam limits its ability to detect or carry small amplitude signals [97]. In principle, coherent light with fluctuations at the quantum noise limit (QNL), or even squeezed light with fluctuations below the QNL, would be ideal for the detection and transmission of small signals. However, such signals are very fragile to losses, which introduce fluctuations at the QNL that rapidly reduce the signal to noise ratio. A solution to this problem is to amplify the signal until it is much larger than the QNL and hence robust to losses [98]. However, this too has problems as phase insensitive amplifiers (PIA's), such as laser amplifiers, inevitably introduce excess quantum noise. In the case of coherent light, this excess noise halves (reduces by 3 dB) the signal to noise ratio in the high gain limit [99]. This is often referred to as the 3 dB penalty for PIA's.

In this chapter, we propose and demonstrate a simple, electro-optic, signal amplification scheme which retains optical coherence while not requiring any non-linear optical process. Our scheme is based on partial detection of the light with a standard beam splitter and detector (Figure 9.3). The light reflected from the beam splitter is detected and the resultant photo-current is amplified and fedforward to an amplitude modulator in the transmitted beam. By correct choice of the electronic gain and phase, we show that intensity signals carried by the input light are amplified, whilst the vacuum fluctuations which enter through the empty port of the beam splitter are cancelled. Since not all of the input light is destroyed, the output is still coherent with the input beam.

9.2 Classical and quantum control theory

9.2.1 Classical feedback and feedforward

Before proceeding to the quantum optical control schemes, it is worthwhile to review the fundamentals of classical control theory. For an electronic feedback loop as shown in

Figure 9.1(a), the transfer function of the loop is given by [100]

$$V_{\text{out}}(\Omega) = \frac{|G(\Omega)|^2}{|1 + G(\Omega)H(\Omega)|^2} V_{\text{in}}(\Omega), \tag{9.1}$$

where $V_{\text{in}}(\Omega)$ and $V_{\text{out}}(\Omega)$ are the input and output noise variance spectra of the system, respectively; Ω is the RF frequency of interest, $G(\Omega)$ and $H(\Omega)$ are the gains at different stages of the feedback loop as indicated in Figure 9.1(a). The derivation of Eq. (9.1), known as Mason's gain formula, is based on the simple junction partition assumption mentioned in the previous section. In the high gain limit where $G(\Omega) \to \infty$, the output noise variance exactly equals that of the input noise variance.

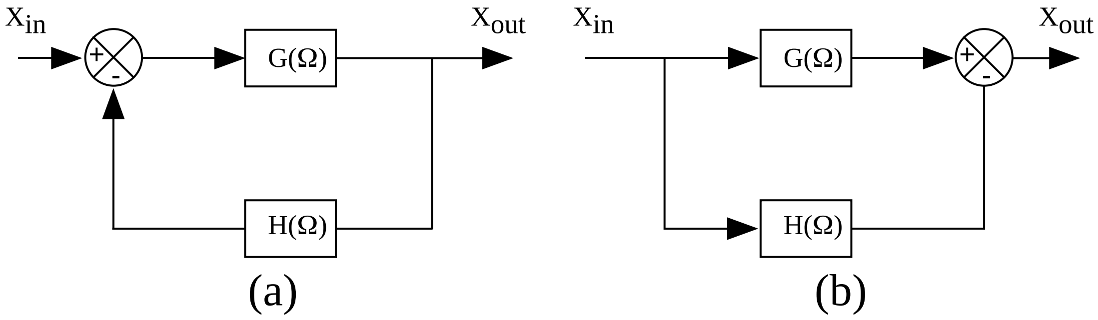

Figure 9.1: Two simple classical control loops: (a) Feedback loop and (b) Feedforward loop.

The effect of time delay τ in a feedback loop gives rise to a bandwidth limit of the control loop which can be modelled by a simple substitution of $H(\Omega) \to e^{-i\Omega\tau}H(\Omega)$. For signal frequencies much higher than a given maximum bandwidth of $\Omega_{max} \approx \pi/\tau$, this simple feedback loop experiences significant phase delay and is unable to achieve any form of useful control.

Stability of the feedback loop can be determined by mapping out the complex value function of the *open loop gain* of the system. The Nyquist stability theorem states that the closed loop feedback system is stable if and only if the locus of the open loop gain from $\Omega = (-\infty, \infty)$ does not enclose the $(-1, 0)$ point in the complex plane. For the purpose of this thesis, it is suffice to say that the feedback loop can be unstable if precautions are not taken during the designing of the feedback control gain $H(\Omega)$. A more rigorous discussion of the feedback loop is available in reference [100].

We now examine a feedforward loop as shown in Figure 9.1(b). The transfer function is given by

$$V_{\text{out}}(\Omega) = |G(\Omega) - H(\Omega)|^2 V_{\text{in}}(\Omega). \tag{9.2}$$

In spite of the diagrammatic similarity between the two control loops, feedforward control is a much simpler system. The open loop gain of a feedforward loop is identical to the closed loop gain and we can have the output equal the input by letting $|G(\Omega) - H(\Omega)| = 1$. In principle, a feedforward loop can have no time delay at all. This is done by simply making sure that there is no time difference in the arrival of the in-loop and the transmitted signal at the summing stage. This is a condition that cannot be satisfied by a feedback loop. Thus, a feedforward loop can in principle work at any given frequency without any bandwidth constraint. Another simplicity of the feedforward loop is in its inherent stability. Since the transfer function of the feedforward loop contains no poles, stability of the system is always guaranteed.

Because of these advantages of the feedforward loop over the feedback loop, the quantum optical study of electro-optic control done in this chapter is exclusively done with the electro-optic feedforward scheme.

9.2.2 Quantum limit of control theory

In electronic control circuits, signals carried by electrons can be split into in-loop and out-of-loop signals with almost no noise added. The quantum nature of electrons does not easily manifest itself because of several reasons. Since electrons are fermions and they obey the Pauli's exclusion principle, they have the tendency to partition themselves evenly between the in-loop and the out-of-loop. We can also choose to think that the repulsion between electrons will mean that their partition will be 'anti-bunched'. This resembles intensity squeezing and is in fact the reason why a diode laser with a quiet pump would be squeezed [101].

When control loops are employed to control light, the situation becomes more tricky. Since photons are bosons, they have the tendency to bunch up amongst themselves. At a beam splitter 'junction', we will find that the quantum nature of photons is easily observable due to this underlying difference. In order to correct for this effect, the analysis of any optical control loop requires that quantum noise or vacuum partition noise be added at every tap-off junction of the control loop. An immediate consequence of the added vacuum partition noise is that the in-loop and the out-of-loop light beams no longer share identical photon statistics. Thus rendering the control imperfect.

A detailed quantum mechanical analysis of feedback control theory is given in reference [46] and reference [102]. For the remainder of this chapter we will focus our discussions on quantum electro-optic feedforward control of light. We will show that in spite of the presence of vacuum partition noise in the feedforward control loop it is still possible to gain control of the transmitted beam beyond the quantum limit. This enable the noiseless amplification of light using only electro-optic feedforward.

9.3 Noiseless optical amplification

In 1982, Caves [103] showed that optical amplification which is phase insensitive will suffer some amount of signal to noise degradation. This is again due to the bosonic nature of photons. In the limit of large gain, this degradation can be as large as 50% or 3 dB. This noise penalty is commonly known as the "3 dB noise penalty".

In order to overcome the 3 dB noise penalty, a phase sensitive amplifiers must be used. Phase sensitivity of an optical amplifier is defined as follows. If an optical device amplifies an input signal equally independent of any relative phase (or whether the signal is encoded in any quadrature amplitude), then the amplifier is called a *phase insensitive amplifier*. In a phase space representation, a phase insensitive amplifier will isotropically enlarge a given input state as shown in Figure 9.2(a). A very well known example of a phase insensitive amplifier is the laser amplifier. For a laser amplifier, the input signal field determines completely the phase of the output field. The amplifier itself has no internal mechanism for phase discrimination since atomic inversions to a metastable level are used as the gain mechanism. In contrast, a *phase sensitive amplifier* amplifies an input state by a variable amount depending on the relative phase or the quadrature amplitude of the signal. Thus in phase space representation, the phase sensitive amplifier is anisotropic in gain. Figure 9.2(b) shows the optical parametric amplifier response which is a phase sensitive amplifier. In this case, the pump phase of the OPA provide the phase reference to the input signal. When the input signal is in phase with the pump, it is amplified. The amplification factor decreases gradually to de-amplification when the input signal phase changes from in-phase to in-quadrature (90°) with the input pump.

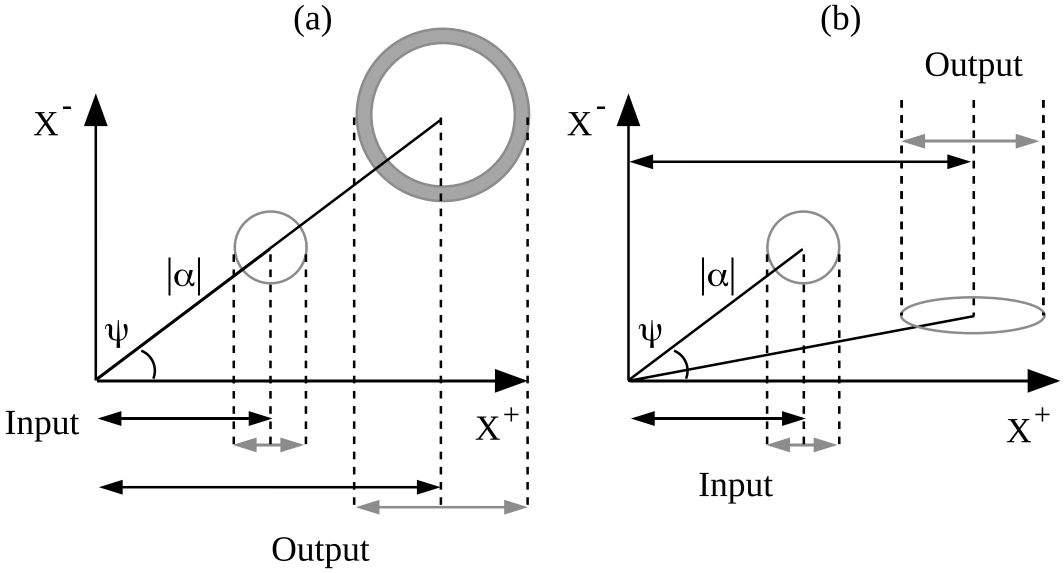

Figure 9.2: A phase space representation of (a) a phase insensitive amplifier. The input signal is amplified in both the X^{+} and X^{-} quadratures. However, noise indicated by grey shade were added on the amplified output. (b) a phase sensitive OPA amplifier. The input signal is amplified along the X^{+} quadrature whilst de-amplified along the X^{-} quadrature. Grey arrows denote noise and black arrows, signals.

In the following we use a simplified argument similar to that given in reference [103] to show that the 3 dB noise penalty for a linear phase insensitive amplifier is a direct consequence of the bosonic nature of photons. Let a and $a^{\dagger}$ be the boson annihilation and creation operators of the input light field and their amplitude and phase quadrature amplitudes as defined in the usual way are X_a^{+} and X_a^{-}, respectively. A phase-insensitive linear amplifier with gain G would give an output field of

$$X_b^{+} = \sqrt{G} X_a^{\phi} + N_1, \tag{9.3}$$

$$X_b^{-} = \sqrt{G} X_a^{\phi+\pi} + N_2, \tag{9.4}$$

where b is the output state of the amplifier and N_i are the noise of the amplifier for the corresponding quadrature. Since the output field is also optical and must thus obey the same boson commutation relation as the input field a, we can write

$$\left[a, a^{\dagger}\right] = 1, \tag{9.5}$$

$$\left[b, b^{\dagger}\right] = 1, \tag{9.6}$$

or equivalently, we can re-write this relation in terms of the quadrature amplitudes as,

$$
\begin{aligned}
[X_a^+, X_a^-] &= \frac{1}{2}i, & (9.7)\\
\left[X_b^+, X_b^-\right] &= \frac{1}{2}i. & (9.8)
\end{aligned}
$$

Substituting Eq. (9.4) into the commutation relation equation for b and $b^\dagger$, we obtain

$$
[N_1, N_2] = \frac{1}{2}i(1-G) \tag{9.9}
$$

Equation (9.9) thus is the first condition for the noise terms required by the boson commutation relation. Using the Heisenberg uncertainty relation on Eq. (9.9), we obtain

$$
\langle \Delta N_1^2 \rangle \langle \Delta N_2^2 \rangle \leq \frac{1}{16}(1-G)^2. \tag{9.10}
$$

We can further conclude that

$$
\langle \Delta N_1^{1,2} \rangle = \frac{1}{4}\left|(1-G)\right| \tag{9.11}
$$

because of the symmetry implied by phase insensitivity. We now make the following assumptions to proceed. Firstly, we can assume that the noise terms on average have no net contribution to the output field. Furthermore, we do not anticipate any form of correlations between the noise terms and the input field. These conditions give us

$$
\begin{aligned}
\langle N_1 \rangle &= 0 & (9.12)\\
\langle N_2 \rangle &= 0 & (9.13)\\
[a_1, N_2] &= 0 & (9.14)\\
[a_2, N_1] &= 0. & (9.15)
\end{aligned}
$$

The variance of the output field becomes

$$
\begin{aligned}
\langle \Delta b_1^2 \rangle &= G\langle \Delta a_1^2 \rangle + \langle \Delta N_1^2 \rangle & (9.16)\\
\langle \Delta b_2^2 \rangle &= G\langle \Delta a_2^2 \rangle + \langle \Delta N_2^2 \rangle. & (9.17)
\end{aligned}
$$

The output signal to noise ratio is defined by

$$
\mathrm{SNR}_{\mathrm{out}} = \frac{\langle X^\theta \rangle^2}{(\Delta X^\theta)^2}, \tag{9.18}
$$

where θ is the quadrature angle. Finally, solving for the SNR expression gives the following inequality

$$
\mathrm{SNR}_{\mathrm{out}} \leq \mathrm{SNR}_{\mathrm{in}} \left(1 + \frac{|1 - 1/G|}{4\langle (\Delta X^\theta)^2 \rangle}\right)^{-1} \tag{9.19}
$$

This is the *fundamental theorem of phase-insensitive linear amplifiers*. In the limit of large gain $G \to \infty$, an input signal encoded on a coherent state gives

$$
\mathrm{SNR}_{\mathrm{out}} \leq \frac{1}{2}\mathrm{SNR}_{\mathrm{in}} \tag{9.20}
$$

It is interesting to note that the derivation given above assumes very little: the canonical boson commutation relations for the input and the output field. As long as the output field of the amplifier is still bosonic, the consequence of amplification is a '3 dB' noise penalty. We can think of this 3 dB penalty as arising from the fact that a PIA amplifies the two conjugate observables, intensity and phase, simultaneously. If additional noise was not added in this process, the uncertainty relation for the variables would be violated.

To avoid this penalty, amplification must be phase sensitive. In which case Eqs. (9.14) and (9.15) no longer hold, in general. This will eventually lead to an asymmetry in the quadrature amplitudes which can be exploited to avoid the noise penalty for one quadrature at the expense of worsening the amplifier performance of the conjugate observable.

9.3.1 Examples of noiseless amplification

Many different schemes of noiseless amplification have been proposed and demonstrated. Since phase sensitivity is intrinsic to many of the non-linear interactions, one method of phase sensitive amplification is to make use of a non-linear optical process. For example, optical parametric amplification has been used to amplify intensity signals with almost no noise penalty. Levenson *et al.* [104] in 1993 demonstrated noiseless amplification using a type-II pulsed OPA. They reported a best performance of $T_s + T_m = 1.32$. The advantage of using the OPA is that the output state of the amplifier is a minimum uncertainty state that is optically coherent with the input field. Unfortunately such experiments are complex and difficult to setup and control.

In the same year, Goober *et al.* [105] and Roch *et al.* [106] independently demonstrated noiseless amplification using another phase sensitive amplification method. In both of their schemes, they used the electronically amplified photocurrent from a directly detected input signal to drive an LED. Because electronic amplification has very little or no noise penalty, the re-emitted output LED light is a noiseless amplified version of the input. This method is phase sensitive as only the intensity is measured and amplified after the direct detection. They reported a performance of $T_s + T_m = 1.77$. However, the drawback of this method is that all phase information is destroyed by the direct detection process. Because the output field is from an LED source, it also has no temporal or spatial optical coherence with the input light.

9.4 Experimental setup

The experimental setup for electro-optic feedforward is shown schematically in Figure 9.3. A polarizing beam splitter taps off part of the input beam to the in-loop detector. The transmittivity of the beam splitter, ε, is controlled by a half-wave plate. A balanced detector pair denoted by $\mathrm{D_{il}}$ is set up to enable self-homodyne measurements on the in-loop beam. This in-loop balanced detector pair has a total efficiency of $\eta_m = 0.92 \pm 0.02$. The photon statistics of the beam can then be determined relative to the QNL and will be used to measure the noise variance of the input light. The detected photo-currents of the balanced detector pair are summed and passed through stages of RF amplification and filtering.

The purpose of the in-loop RF amplification and filtering is to provide high gain at a well define region of the RF spectrum around the input signal. This is needed because unlike optical feedback control, optical feedforward is less efficient in the electro-optic transfer of modulation signals. An example of a completed in-loop electronics is shown

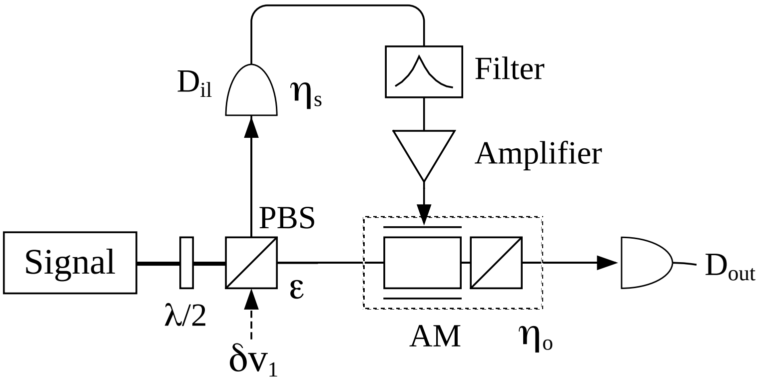

Figure 9.3: Schematic of the experimental setup. $\mathrm{D_{il}}$: in-loop balanced detector pair; $\mathrm{D_{out}}$: Out-of-loop detector; PBS: Polarizing beam splitter; $\lambda/2$: Half-wave plate; AM: Amplitude modulator.

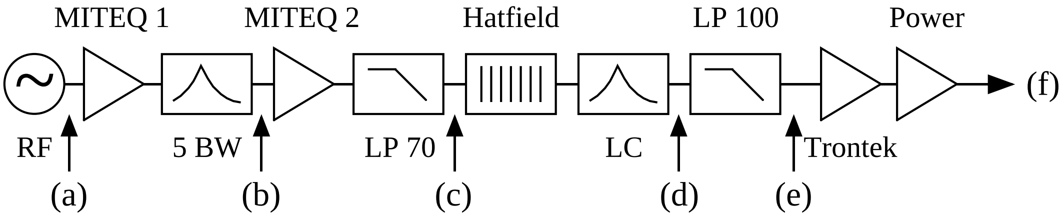

Figure 9.4: Schematic of in-loop electronics circuit. A total of three signal amplifiers (MITEQ 1, MITEQ 2 and Trontek) and one power amplifier (Power) are used. The filters are 5 BW: 5^{th} order Butterworth filter; LP70: Low pass filter @ 70 MHz; LC: Bandpass filter; LP100: Low-pass filter @ 100 MHz. Hatfield: Variable attenuator and RF: RF tracking generator.

in Figure 9.4. The transfer function plots of the in-loop circuit at various stages of the loop are shown in Figure 9.5. These transfer function plots were obtained by replacing the photodiodes with a tracking generator. Broadband RF signals at around -50 dBm are used as input to the in-loop as shown in Figure 9.5(a). Without any form of amplification or filtering, the spectrum is a flat line. At the end of the amplification and filtering stages, the final output of the in-loop signal is shown in plot (f) of Figure 9.5. For this particular setup, a maximum RF power of +15 dBm is deliverable without any sign of electronic saturation. An amplitude modulator is formed by using the EOM in conjunction with a polarizer to electro-optically convert the in-loop signal to the transmitted light. The availability of high RF power means that strong amplitude modulation of light is possible while maintaining relatively high transmittivity at the electro-optic modulator. Finally a spectrum analyser is used to measure the noise and signal power spectrum of the output photo-current of detector $\mathrm{D_{out}}$. The out-of-loop detection efficiency, including the modulator losses, is $\eta_o = 0.80 \pm 0.05$.

9.5 Theoretical modelling

We model the electro-optic feedforward scheme as follows. Suppose the beam splitter has a transmittivity ε and negligible losses. The reflected beam is directed to a detector

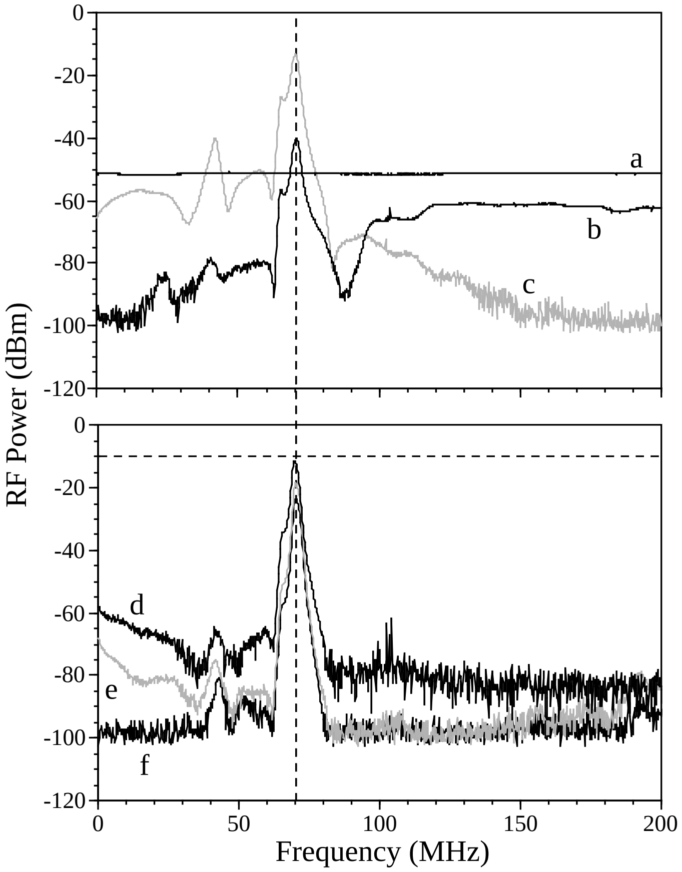

Figure 9.5: The in-loop electronics transfer function at various points. (a) A tracking generator produces -50 dBm of broadband RF power (b) after the 5^{th} order Butterworth filter; (c), (d), (e) are transfer functions taken at points indicated in the in-loop circuit. (f) Output of the in-loop signal. The peak of the transfer function is at 70 MHz with a -3 dB full width of < 2 MHz. The suppression of frequencies outside the region of interest is > 65 dB. This in-loop circuit is thus ideally suited for signal amplification at 70 MHz.

of efficiency η_m. We can write the input laser beam in the linearized form

$$\hat{A}_{\mathrm{in}}(t) = A_{\mathrm{in}} + \delta\hat{A}_{\mathrm{in}}(t), \tag{9.21}$$

where $\hat{A}_{\mathrm{in}}$ is the field annihilation operator; A_{in} is the classical steady state value of the field; and $\delta\hat{A}_{\mathrm{in}}$ is a zero-mean operator which carries all the classical and quantum fluctuations. The detected output field is given by

$$\hat{A}_{\mathrm{out}} = \sqrt{\eta_o}\left(\sqrt{\varepsilon}\,A_{\mathrm{in}} + \sqrt{\varepsilon}\,\delta\hat{A}_{\mathrm{in}} + \sqrt{1-\varepsilon}\,\delta\hat{v}_1 + \delta\hat{r}\right) + \sqrt{1-\eta_o}\,\delta\hat{v}_3, \tag{9.22}$$

where η_o is the combined efficiency due to the transmittivity of the modulator and the quantum efficiency of the out-of-loop detector. As usual, vacuum fluctuations from the unused port of the beam splitter, $\delta\hat{v}_1$, and due to out-of-loop losses , $\delta\hat{v}_3$, appear on the transmitted beam. We have assumed that the feedforward does not affect the steady state value of the field but just adds a small fluctuating term $\delta\hat{r}$ which can be written as a convolution over time [107],

$$\begin{aligned}\delta\hat{r} &= \int_0^\infty k(\tau)\sqrt{(1-\varepsilon)\eta_m}\,A_{\rm in}\Big(\sqrt{(1-\varepsilon)\eta_m}\,\delta\hat{X}_A(t-\tau)\\ &\quad -\sqrt{\varepsilon\eta_m}\,\delta\hat{X}_{v1}(t-\tau)+\sqrt{(1-\eta_m)}\,\delta\hat{X}_{v2}(t-\tau)\Big)\,d\tau. \end{aligned} \tag{9.23}$$

$\delta\hat{r}$ expresses the changes in the phase and amplitude of the feedforward signal due to the electronics by a function $k(t)$. This convolution embodies the storage effect of the feedforward process [108]. However, unlike the feedback loop where time delay is unavoidable, the feedforward loop can in principle have zero time delay. In this situation, the above convolution is unnecessary.

The amplitude fluctuations of the input field and its accompanying vacuum fluctuations from the beam splitter δv_1, and the non-unity detector efficiency δv_2, are defined by $\delta\hat{X}_{A\rm in} = \delta\hat{A}_{\rm in} + \delta\hat{A}^\dagger_{\rm in}$ and $\delta\hat{X}_{vi} = \delta\hat{v}_i + \delta\hat{v}_i^\dagger$. Note that energy conservation requires that the vacuum fluctuations introduced on the reflected beam are anti-correlated with those on the transmitted beam. The amplitude fluctuation spectrum of the output field is the expectation value of the Fourier transform of the absolute squared amplitude fluctuations, ie. $V_{\rm out}(\Omega) = \langle|\delta\tilde{X}_{A\rm out}|^2\rangle$. Experimentally $V_{\rm out}$ is obtained by normalizing the power spectrum from the spectrum analyser to the QNL for the same optical power. We find

$$\begin{aligned}V_{\rm out}(\Omega) &= \eta_o|\sqrt{\varepsilon}+\lambda\sqrt{(1-\varepsilon)\eta_m}|^2 V_{\rm in}(\Omega)\\ &\quad +\eta_o|\sqrt{(1-\varepsilon)}-\lambda\sqrt{\varepsilon\eta_m}|^2 V_1\\ &\quad +\eta_o|\lambda\sqrt{(1-\eta_m)}|^2\,V_2\\ &\quad +(1-\eta_o)\,V_3, \end{aligned} \tag{9.24}$$

where various parameters have been rolled into the electronic gain $\lambda(\Omega)$, which is in general a complex number. $V_{\rm in}(\Omega) = \langle|\delta\tilde{X}_{A\rm in}|^2\rangle = V_{\rm s,in}(\Omega) + V_{\rm n,in}(\Omega)$ is the amplitude fluctuation spectrum of the input field. The vacuum noise spectra originate from the empty port of the beam splitter V_1, the in-loop detector efficiency V_2 and the out-of-loop losses V_3, are shown explicitly to emphasise their origins. All vacuum inputs are quantum noise limited, ie., $V_1 = V_2 = V_3 = 1$. We define the signal and meter transfer coefficients of the optical amplifier as follow [104]

$$T_s = \frac{{\rm SNR}_s^{\rm out}}{{\rm SNR}_s^{\rm in}} \tag{9.25}$$

$$T_m = \frac{{\rm SNR}_m^{\rm out}}{{\rm SNR}_s^{\rm in}} \tag{9.26}$$

Where ${\rm SNR}_i = V_{s,i}/V_{n,i}$ are signal to noise ratio of the i port. An ideal noiseless amplifier should therefore have $T_s = 1$ and a phase insensitive linear amplifier has $T_s = 0.5$ in the limit of large gain.

Due to the opposite signs accompanying the feedback parameter λ in the signal and vacuum fluctuations terms of Eq. (9.24), it is possible to amplify the input signal (first term), while cancelling the vacuum noise from the feedforward beam splitter (second term). The third and fourth terms of Eq. (9.24) represent unavoidable experimental losses.

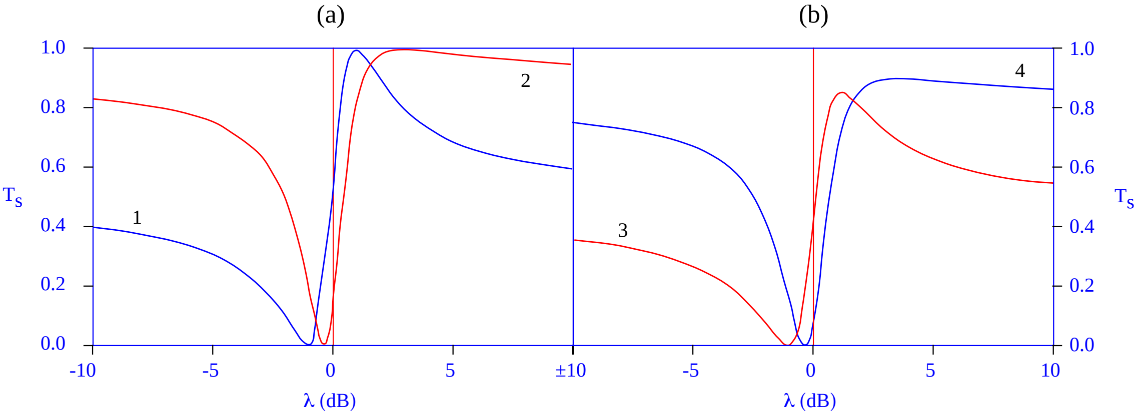

Figure 9.6: Plots of signal transfer coefficient for varying electronics gain λ. *Left*: Ideal lossless electro-optic feedforward for ε = 50% and 90% (plot 1 and 2, respectively). The plots show that there is always a positive feedforward gain which yields $T_s = 1$ corresponding to noiseless amplification. *Right*: Realistic system with in-loop detector efficiency $\eta_m = 0.9$ and total down stream efficiency $\eta_o = 0.8$.

In particular if we choose

$$\lambda = \frac{\sqrt{1-\varepsilon}}{\sqrt{\varepsilon\eta_m}}, \tag{9.27}$$

the vacuum fluctuations from the beam splitter V_1 are exactly cancelled, thus allowing noiseless amplification. Under the optimum condition of unit detection efficiency and negligible out-of-loop losses ($\eta_m = \eta_o = 1$), we find

$$V_{\text{out}}(\Omega) = \frac{1}{\varepsilon}V_{\text{in}}(\Omega) = \frac{1}{\varepsilon}(V_{\text{s,in}}(\Omega) + V_{\text{n,in}}(\Omega)). \tag{9.28}$$

That is, the fluctuations are noiselessly amplified by the inverse of the beam splitter transmittivity. The signal and quantum noise are amplified by the same amount and there is no noise added, hence there is no degradation of the signal to noise ratio. Thus our system ideally can attain a transfer coefficient of $T_s = 1$ for a signal gain of $G = 1/\varepsilon$. It is also worth noting that if the feedforward is chosen to be negative with

$$\lambda = -\frac{\sqrt{\varepsilon}}{\sqrt{(1-\varepsilon)\eta_m}}, \tag{9.29}$$

the output variance becomes,

$$V_{\text{out}} = \frac{1}{(1-\varepsilon)}V_1. \tag{9.30}$$

The output of the feedforward loop is now completely independent of the input noise variance. This is the principle of laser intensity *noise eater* which is used for the suppression of the resonant relaxation oscillation of a laser (contained in V_{in}). However, we observed that the resulting output field is always noisier than the quantum noise limit. This is the result obtained by Taubman *et al.* [102], where it is shown that electro-optic control of light is insufficient to generate squeezing.

Figure 9.6(a), and Figure 9.7(a) and (b) show the ideal case results of varying the feed-

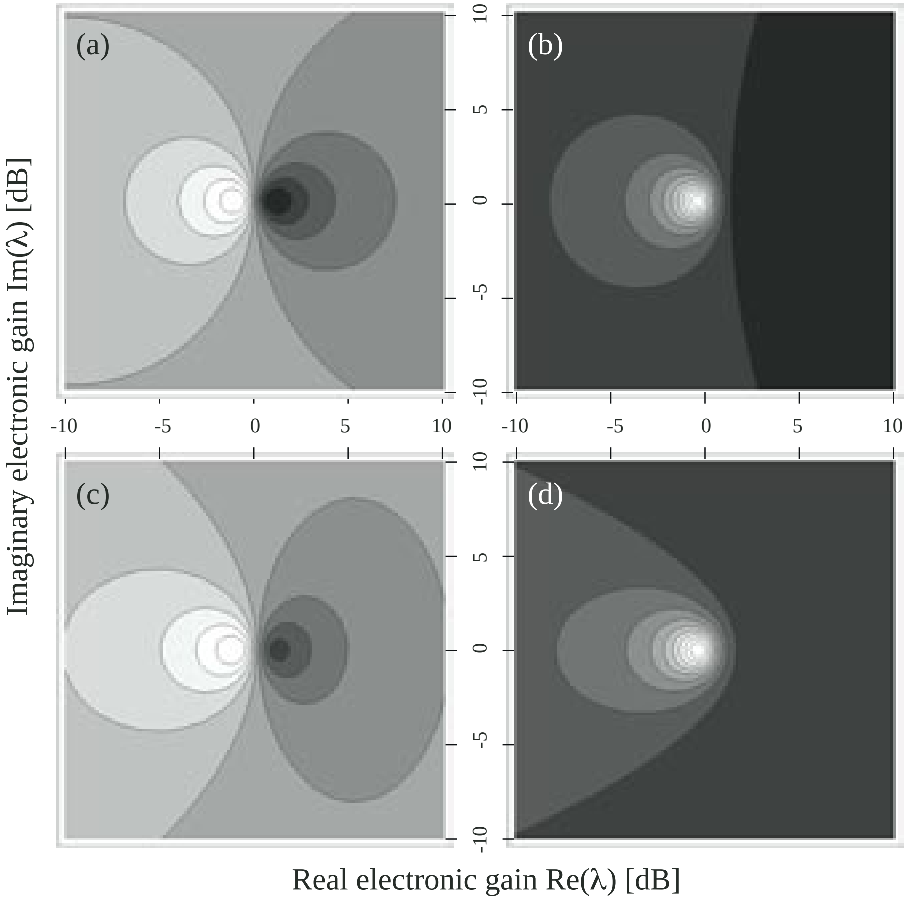

Figure 9.7: Contour plots of the signal transfer coefficient T_S. The 2-dimensional space represent the magnitude and phase of the electronic gain λ. Points along the x-axis corresponds to in-phase gain where λ is real. Points along the y-axis corresponds to in-quadrature gain where λ is purely imaginary. (a) and (b): Ideal feedforward with $\varepsilon = 0.5$ and $\varepsilon = 0.1$, respectively. (c) and (d): The corresponding feedforward with realistic experimental parameters $\eta_m = 0.9$ and $\eta_o = 0.8, \varepsilon = 0.5$ and $\varepsilon = 0.1$.

forward gain for different in-loop beam splitter reflectivities. Each plot in Figure 9.6(a) shows that noiseless amplification of $T_s = 1$ occurs at some positive gain whilst $T_2 = 0$ at some negative gain corresponding to ideal noise eater operation[2].

The effect of non-unity in-loop detector efficiency and total downstream efficiencies is to limit the optimum signal transfer coefficient to $T_s^{\max} = \eta_m$ in the limit of large in-loop reflection $\varepsilon \to 0$. Extra losses downstream from the feedforward affect the output in the same way as losses due to the out-of-loop efficiency η_o. Figure 9.6(b), and Figure 9.7(c) and (d) show the same plots of signal transfer coefficient versus feedforward gain but with realistic experimental parameters.

---

[2] This noise eater operation for the feedforward configuration only works at one gain value. In contrast, feedback control of intensity noise works at any high enough gains.

9.6 Experimental results of noiseless amplification

9.6.1 Quantum noise limited input

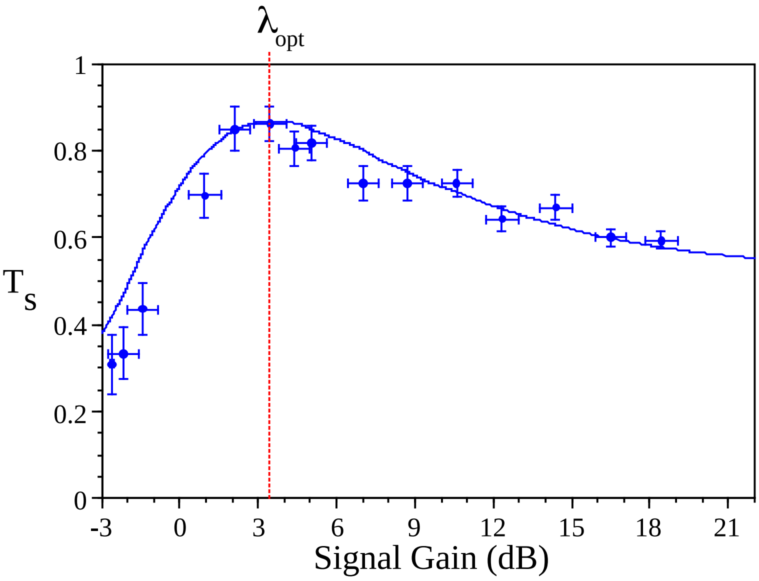

Figure 9.8: Signal transfer coefficient, T_s, vs signal gain, G. $\varepsilon = 0.5$. The optimum value of $T_s = 0.86 \pm 0.02$ occurs at a gain of $G = 3.4\pm$ 0.6 dB.

In our initial experiments, the input light used for signal amplification is within 0.2 dB of the QNL at a detection frequency of 20 MHz. We impose an input signal at 20 MHz with $\mathrm{SNR}_{\mathrm{in}} = 9.7\pm$ 0.1 dB. The highest T_s of our scheme does not occur at arbitrarily large feedforward. There is an optimum magnitude and phase for the electronic gain, which corresponds to the complete cancellation of vacuum fluctuations introduced by the feedforward beam splitter. The half-wave plate is adjusted to tap half of the input light, $\varepsilon = 0.5$, for feedforward. The signal transfer coefficient, T_s, and the signal gain, G, are obtained for various feedforward electronic gains. As can be seen from Figure 9.8, there is clearly an optimum feedforward gain where $T_s = 0.86 \pm 0.02$ is a maximum at $G = 3.4\pm$ 0.6 dB. For higher signal gains, the value of T_s value degrades and asymptotes to the value corresponding to direct in-loop detection. This is because for high feedforward gains, the contribution from the in-loop signal overwhelms the transmitted signal.

A theoretical curve calculated from the experimental parameters is also plotted on Figure 9.8. The optimum feedforward gain λ_{opt} corresponds to a signal gain of $G =$ 3.4 dB and a signal transfer coefficient of $T_s = 0.87$, in good agreement with the experimental values.

To obtain optimum performance at higher signal gain requires a greater reflectivity at the beam splitter (see Eq. (9.28)). For higher beam splitter reflectivity, the transmitted beam is dominated by the vacuum fluctuations. Thus, higher feedforward gain is required to completely cancel the vacuum fluctuations, resulting in a shift of the optimum operating point λ_{opt} to a higher value. This is demonstrated in Figure 9.9 where the beam splitter reflectivity was increased to 90%, ie. $\varepsilon = 0.1$. With maximum available feedforward gain, we achieve $T_s = 0.88 \pm 0.02$ with a signal gain of $G = 13.4\pm$ 0.5 dB. We have

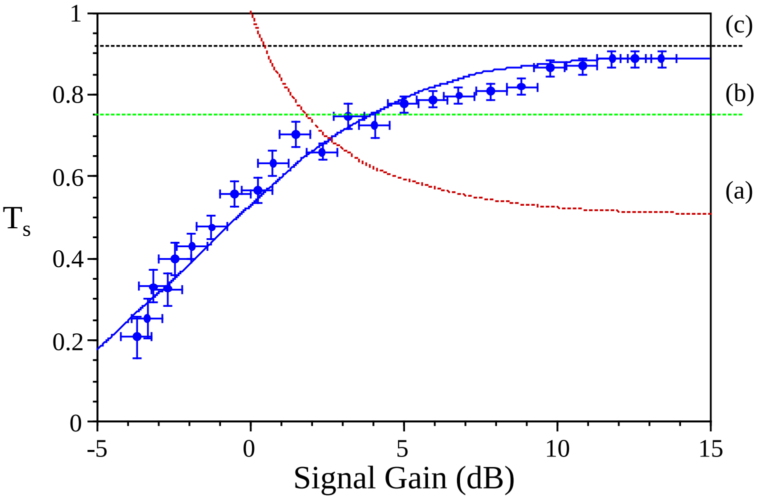

Figure 9.9: Signal transfer coefficient, T_s, vs signal gain, G, for transmittivity of $\varepsilon = 0.1$. Dotted curves are limiting cases: (a) is the best possible performance of a PIA, points above this curve are evidence of phase sensitive amplification; (b) is the T_s value when feedforward signal dominates, points above this line are evidence of vacuum fluctuations cancellation. (c) is the T_s^{max} of the scheme set by the efficiency of the in-loop detector $\varepsilon = 0.92 \pm 0.02$.

also calculated the T_s as a function of signal gain for a PIA, as shown by curve (a), a PIA with the same signal gain would be limited to a transfer coefficient of $T_s = 0.51$. Our system clearly exceeds this limit.

9.6.2 Squeezed input

It is important to note that the absolute power of the amplified output signal, as measured by the spectrum analyser, is not necessarily larger than that of the input signal. This is because the absolute signal power is scaled by the intensity of the light field and in our scheme the intensity of the light field is unavoidably decreased. This reduction in intensity also reduces the QNL of the output beam. However the size of the amplified signal with respect to the QNL is increased. It is this relative amplification of the signal (as measured by G) which reduces the fragility of the signal.

To illustrate this, we use our system to amplify squeezed light, which is notoriously sensitive to losses. As our squeezed source, we use the second harmonic output from the singly resonant frequency doubler described in Chap. 5. The SHG produces squeezing in the amplitude quadrature which can then be amplified by our feedforward scheme. The top half of Figure 9.10 shows the input noise spectrum. This is obtained from the in-loop balanced detector pair by setting the beam splitter to total reflection. Trace (i) shows the QNL, which is obtained by subtracting the photo-currents in the balanced detector pair. Trace (ii) is the sum of the photo-currents, which gives the noise spectrum of the input light. Regions where (ii) is below (i) are amplitude squeezed. The maximum measured squeezing of 1.6 dB is observed in the region of 8-10 MHz on a 26 mW beam. The inferred value, after taking into account the detection efficiency and electronic noise floor, is 1.8 dB. A small input modulation signal (2.80 dB observed) is introduced at 10 MHz which, allowing for detection losses, has $\mathrm{SNR_{in}} = 1.10 \pm 0.03$. Other features of the spec-

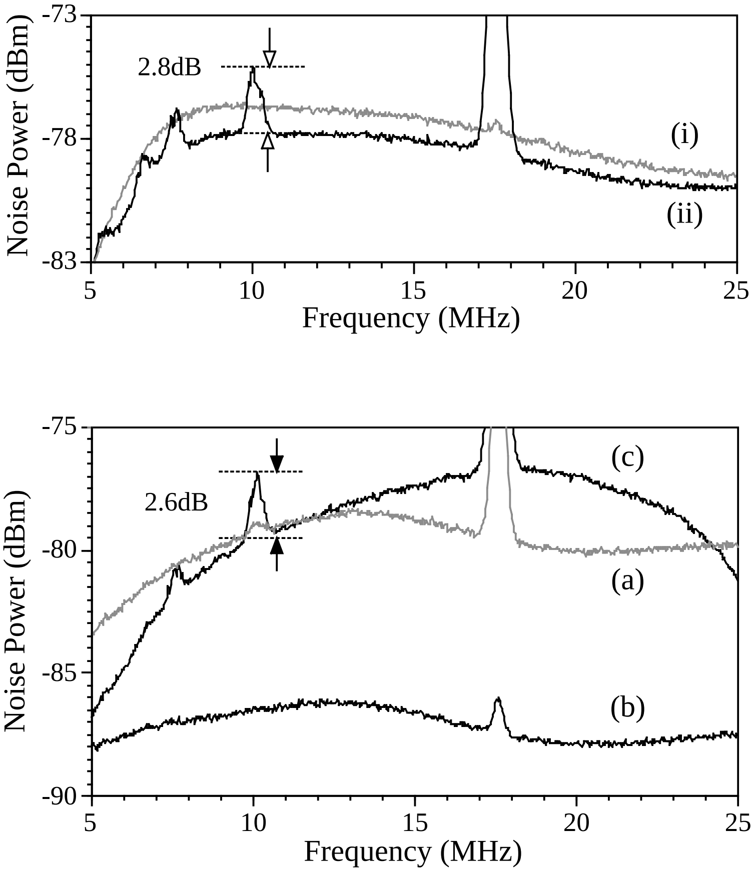

Figure 9.10: Top: Noise spectra of the squeezed input beam. Trace (i) and (ii) are the difference and sum of the balanced photo-currents, respectively. A modulation signal of $\mathrm{SNR_{in}}$ = 2.8 dB is introduced at 10 MHz. Bottom: Noise spectra of the output beam. (a) Direct detection of the input light using the single output detector. Because of the presence of loss $\eta_o = 0.14$, the signal degrades to SNR = 0.4 dB. (b) Output noise spectrum without feedforward and with large loss $\eta_{\mathrm{tot}} = 0.014$. The signal is completely destroyed. (c) With optimum feedforward gain, the signal is reconstructed with $\mathrm{SNR_{in}}$ = 2.6 dB. This corresponds to $T_s = 0.75 \pm 0.02$ and $G = 9.3\pm$ 0.2 dB.

tra include the residual 17.5 MHz locking signals of the frequency doubling system [109] and the low frequency roll-off of the photo-detector, introduced to avoid saturation due to the large relaxation oscillation of the laser at $\approx$ 0.5 MHz.

The bottom half of Figure 9.10 shows the noise spectra obtained from the single output detector. Setting the beam splitter reflectivity to zero, $\varepsilon = 1$ the transmitted beam is made to experience 86% downstream loss, $\eta_o = 0.14$, after the feedforward loop. As trace (a) shows, the SNR is strongly degraded by the attenuation such that the signal is now barely visible above the noise. We now perform signal amplification by setting the beam splitter reflectivity to 90%, $\varepsilon = 0.1$. This further attenuates the output beam to $\eta_{\mathrm{tot}} = \varepsilon\eta_o = 0.014$. With no feedforward gain, as trace (b) shows, the modulation signal is now too small to be seen above the noise. Due to the large amount of attenuation, trace (b) is quantum noise limited to within 0.1 dB over most of the spectrum. Finally, by choosing the optimum signal gain, $G = 9.3\pm$ 0.2 dB, trace (c) shows the amplified input signal with $\mathrm{SNR_{out}} = 0.82 \pm 0.03$. Traces (b) and (c) are of the same intensity, hence we can see that the output signal is significantly above the QNL. This is the reason why the amplified output is far more robust to losses then the input. This result corresponds to a signal transfer coefficient of $T_s = 0.75 \pm 0.02$, again in good agreement with the theoretically calculated result of $T_s = 0.77$. This is to be compared with the best performance of a PIA, with similarly squeezed light, of $T_s \approx 0.4$. Note that trace (c) has a different shape to (a) and (b) due to the transfer function of the in-loop electronics and the phase variation of the feedforward across the frequency spectrum. As can be seen, the bandwidth of the RF gain is from 7 MHz to 21 MHz. However the optimum feedforward gain is only satisfied in a limited region of the spectrum around 10 MHz.

9.7 Signal and power amplification

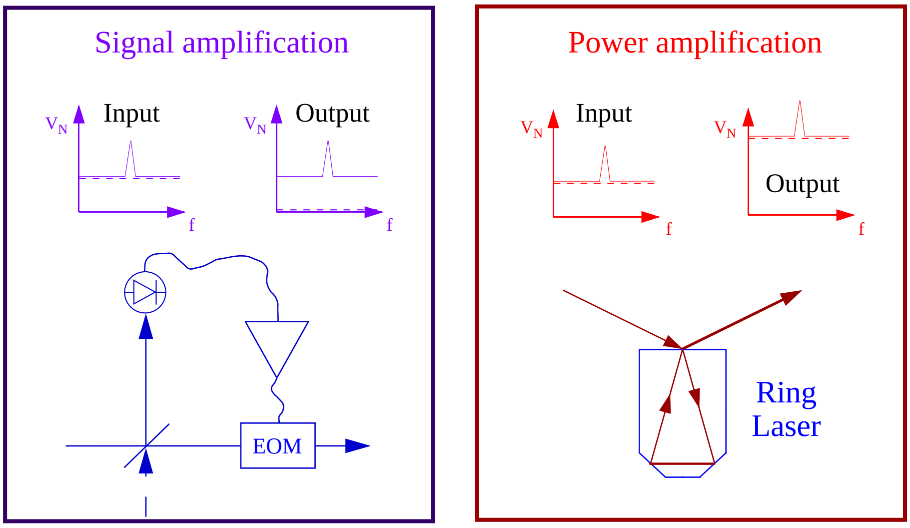

Figure 9.11: Signal and power amplifiers. *Left*: electro-optic feedforward loop. *Right*: injection locked ring laser. Dotted lines in the insert spectra represent the standard quantum limit of the light field.

The direct detection of an optical signal gives a photocurrent signal strength that is proportional to both the DC optical intensity as well as the RF fluctuations or modulation encoded in the light field. A spectrum analyser noise variance measurement of the light field $\mathcal{V}_{\rm meas}$ is thus proportional to

$$\mathcal{V}_{\rm meas} \propto I V_{\rm norm} \tag{9.31}$$

where $V_{\rm norm}$ is the normalized variance of the field and I is the optical intensity. An amplification of light can therefore be either an amplification of the optical intensity or an amplification of the field fluctuations (modulation) or both. We thus define the following gain factors

$$G_s = \frac{V_{\rm out}}{V_{\rm in}} \tag{9.32}$$

$$G_p = \frac{I_{\rm out}}{I_{\rm in}} \tag{9.33}$$

$$G_{\mathrm{tot}} \;=\; G_p G_s \tag{9.34}$$

Hence a signal amplifier is one which amplifies the fluctuations of the input state whilst a power amplifier is one which amplifies the intensity. The total gain of an optical amplifier is the product of both the signal and power gains.

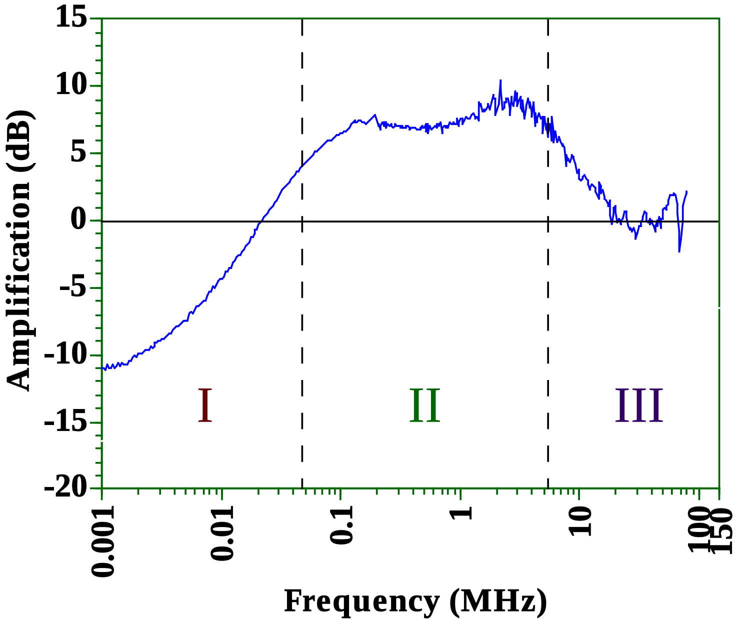

Figure 9.12: Transfer function of an injection locked laser. (I) This region corresponds to the geometric summing of the noise of the slave and master lasers. (II) This region corresponds to phase insensitive laser amplification. (III) At frequencies larger than the linewidth of the laser cavity, the seed wave is simply reflected.

In most amplification schemes, power and signal amplifications occur simultaneously. This is not always desirable. For example, in gravitational wave detection high power quantum noise limited lasers are required. However, the amplification of optical power of a laser source using the standard laser amplifier means that the noise variance of the field will be amplified to levels much high than the standard quantum limit. In this case, it would be ideal to have power amplification without signal amplification. On the other hand, in an optical communication network, signal amplification is preferred since this would lead to a robust transmission of optical signal as demonstrated in the Sec. 9.6.2. Corresponding increase in the optical power however, could lead to the saturation of the detection photodiodes. In this case, signal amplification with little or no power amplification is desirable.

The electro-optic feedforward scheme can noiselessly amplify the signal of an input beam. However, it cannot increase the optical intensity of the transmitted beam. Instead the transmitted beam intensity is attenuated by the reflectivity of the beam splitter and non-ideal downstream loss. Hence as shown in Figure 9.11 the measured noise power $\mathcal{V}_{\mathrm{meas}}$ of the output may not have increased through the feedforward loop. Again assuming an ideal situation, the signal and power gains of the electro-optic feedforward loop at the optimum electronic gain point is given by

$$\begin{aligned} V_{\mathrm{out}} &= \frac{1}{\varepsilon}V_{\mathrm{in}} && (9.35)\\ I_{\mathrm{out}} &= \varepsilon I_{\mathrm{in}}. && (9.36) \end{aligned}$$

This gives a total gain of $G_{\mathrm{tot}} = 1$.

We now turn our attention to the injection locking of a ring laser with an input signal field. The transfer function of the injection locked ring laser system [15, 110–112] is measured and modelled by Harb *et al.* [113] and Ralph *et al* [45], respectively. The results are summarized in Figure 9.12. We can divide the frequency spectrum of the injection locked transfer function into three regimes. At frequencies much smaller than the resonant relaxation oscillation of the slave laser (region I), the output noise variance of the injection locked laser is given by

$$V_{\mathrm{out}} \simeq \frac{I_{\mathrm{in}}V_{\mathrm{in}} + I_{\mathrm{free}}V_{\mathrm{free}}}{I_{\mathrm{in}} + I_{\mathrm{free}}} \tag{9.37}$$

where I_x denote the intensities and V_x the variances. The subscripts indicate the input, output and free running parameters. Hence in this low frequency regime, the output variance is a weighted sum of both the input noise variance and the free running slave laser noise variance.

At frequencies around the laser resonance (region II), we find the noise variance transfer function to be

$$V_{\mathrm{out}} \simeq HV_{\mathrm{in}} + (H - 1) \tag{9.38}$$

where H is the semiclassical intensity amplification factor of the injection locked system. This is similar to that of the transfer function of a phase insensitive laser amplifier.

At even higher frequencies (region III), we move to the regime outside the laser cavity linewidth. High frequency fluctuations of the injected field are thus directly reflected off the front face of the ring laser. In this case, the transfer function of the noise variance is simply

$$V_{\mathrm{out}} \simeq V_{\mathrm{in}} \tag{9.39}$$

This regime is thus ideal for power amplification [114] since signal on the input field is unchanged whilst the optical intensity of the input field is amplified by the injection locked slave laser as illustrated in Figure 9.11.

In all three regimes, the optical intensity gain is given by

$$I_{\mathrm{out}} = G_p I_{\mathrm{in}} \tag{9.40}$$

where $G_p = (I_{\mathrm{in}} + I_{\mathrm{slave}})/I_{\mathrm{in}}$.

For our combined amplification system, we thus predict that the signal will undergo a gain of $G_s = 1/\varepsilon$ and the power, a gain of $G_p = G_{p,\mathrm{ff}}G_{p,\mathrm{inj}} = H\varepsilon$. The total gain and signal transfer coefficient is then the product of the gains and the coefficients of the individual stages.

$$\begin{aligned} G_{\mathrm{tot}} = &= G_s \times G_p && (9.41)\\ T_{s,\mathrm{tot}} &= T_{s,\mathrm{sig}} \times T_{s,\mathrm{pow}} && (9.42) \end{aligned}$$

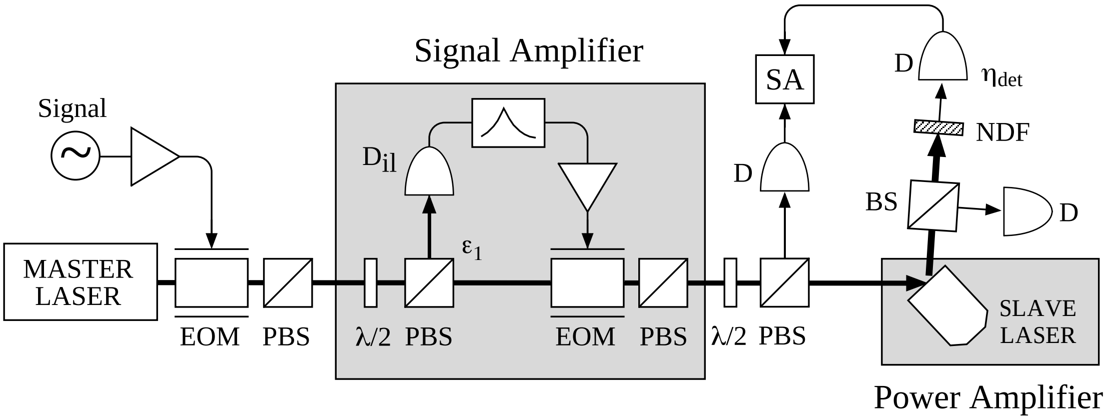

Figure 9.13: Schematic of the combined feedforward-injection locked amplifier.

9.7.1 Experimental setup and results

The schematic of the combined signal and power amplifier is shown in Figure 9.13. Unlike in the previous section, this experiment was done with 1064 nm light because of the use of the Nd:YAG NPRO as the slave laser (LZH350). We took $10.00\pm$ 0.02 mW of power from the master laser (LZH700) and introduced an input signal at 73 MHz with an amplitude modulator so that the frequency region of interest was well outside the cavity linewidth of the slave laser. The signal imposed had a SNR $= 13.0\pm$ 0.1 dB with the noise level at the standard quantum limit. A half-wave plate and polarizing beam splitter combination was placed before the slave laser to enable separate investigation of the signal amplifier. The slave laser was capable of generating 360 mW of light and had a FSR of 5.8 GHz. At the output of the laser, we tapped off 2% of the optical intensity and used this as a locking signal by monitoring the beat between the master and the slave lasers. Finally, the remainder of the slave output was attenuated with neutral density filters to a measurable level before the final analysis was done using a RF spectrum analyser.

Figure 9.14 shows the locus of the maximum signal transfer coefficient for various signal gains G_s. Again, this figure demonstrates the noiseless amplification capability of the electro-optic feedforward loop. A wide range of signal amplification gains with $T_s > 0.8$ was obtained. With the noiseless signal amplification confirmed, we injected the output into the slave Nd:YAG NPRO laser. It is worth noting that the signal transfer coefficients reported in Figure 9.14 is the measured value using a photodetector with efficiency of $\eta_{\rm det} = 0.93 \pm 0.02$. By direct injection of the output signal into the NPRO laser, this efficiency is irrelevant and thus signal transfer is only limited by the mode-matching efficiency of the injection locking. Typically, the mode-matching efficiency is $\eta_{\rm mode} = 0.96 \pm 0.02$.

Our measurement of the power amplification performance is shown in Figure 9.15. The output variances $V_{\rm out}$ were taken for a range of power gains and input variances. The photodetection system used in this experiment has a saturation level at around 20 mW making direct measurement of the slave output impossible most of the time. The use

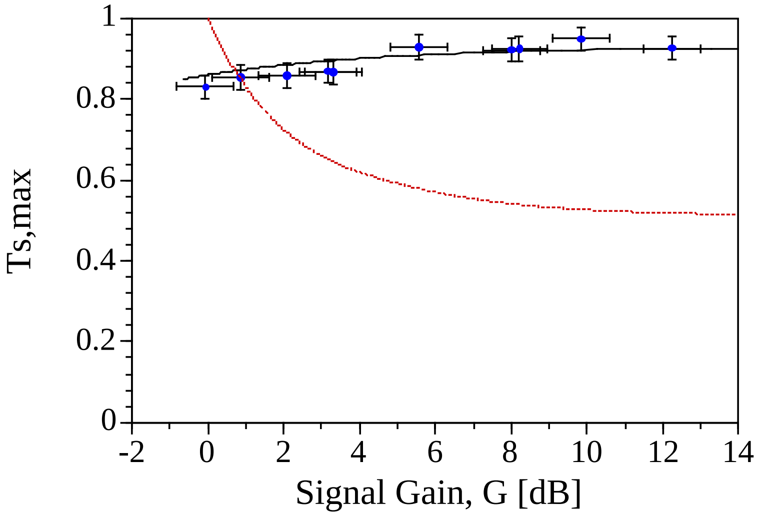

Figure 9.14: Locus of maximum signal transfer coefficient with varying beam splitter reflectivity.

Total gain G	Signal gain G_s	Power gain G_p	Signal transfer coef. T_s	Measured % power η
9.8	9.8	1.0	$0.86(0.86) \pm 0.02$	1
10.0	2.5	4.0	$0.88(0.88) \pm 0.05$	1
15.8	15.8	1.0	$0.88(0.88) \pm 0.05$	1
23.0	14.4	1.6	$0.86(0.91) \pm 0.05$	0.69
73.3	14.1	5.2	$0.74(0.89) \pm 0.05$	0.29
225	2.5	90	$0.15(0.9) \pm 0.3$	0.05
311	16.7	18.6	$0.30(0.66) \pm 0.2$	0.025

Table 9.1: Signal transfer coefficients for the combined amplifier setup for various signal and power gain levels. η represent the fraction of output measured by the final detection system and values in bracket are the inferred values of the combined system.

of neutral density filter means that the output variance has to be inferred from partial detection. Nevertheless, all of the measurements suggests a close to perfect transfer of signal variance.

Finally, Table 9.1 summarizes for the various cases of composite amplifications. From pure signal amplification of $G_s = 15.8$ to large power amplification of $G_p = 90$, all of which have demonstrated noiseless amplification with signal transfer coefficient $T_s > 0.5$. The largest gain achieved in our experiment correspond to a total gain of 311 (25 dB).

9.8 Summary

This chapter has demonstrated several fundamental characteristics of the electro-optic feedforward control loop. We have shown that with the correct amount of positive electronic gain, the feedforward can completely cancel the vacuum fluctuations introduced at a beam splitter. As a result, we were able to achieve noiseless signal amplification

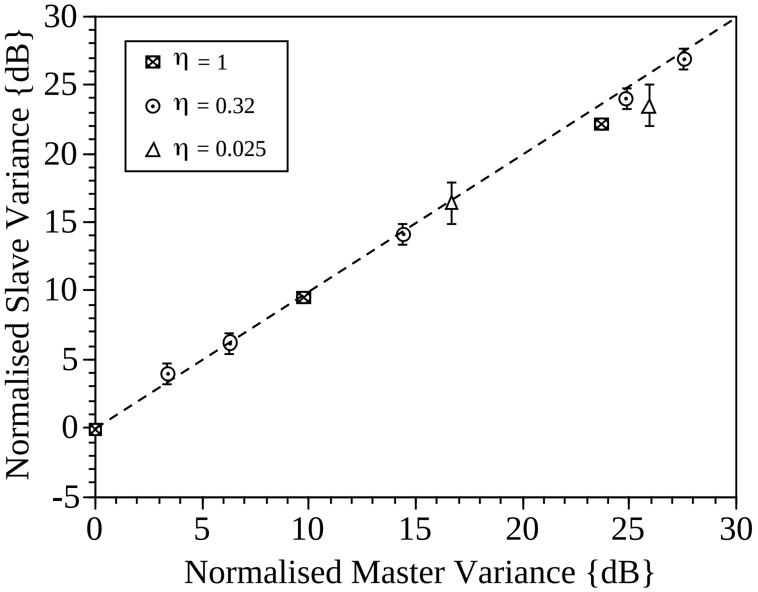

Figure 9.15: Normalized variance of the injection locked laser as a function of the normalized variance of the master laser at the detection frequency of 73 MHz. η represent the attenuation of the output field before detection. The dotted line denotes perfect signal transfer of $T_s = 1$.

with performance limited only by the detection efficiency of the photodetectors. With an amplitude squeezed beam as input, we demonstrated that noiseless signal amplification made the modulated signals on the squeezed beam robust to lossy transmission. Finally, when the feedforward loop was used in combination with an injection locked laser, independently variable noiseless signal and power amplifications were demonstrated.

Chapter 10

Quantum Nondemolition Measurement with Electro-Optic Control

Vizzini: Inconceivable!
Inigo: You keep using that word. I do not think it means what you think it means . . .

The Princess Bride

Overview

This chapter introduces the concept of quantum nondemolition (QND) measurements and shows that the electro-optic feedforward loop when used in combination with a squeezed vacuum meter input is a QND device. More generally, the squeezed vacuum meter input can be thought of as a pre-enhancement stage and the electro-optic feedforward as a post-enhancement stage of most QND measurements.

10.1 Introduction

As early as the 1930's, von Neumann, Bohr, Heisenberg and others [115] have hinted on the quantum limit and the irrepeatability of precision measurements. It is not until the 1970's that Braginsky [116] suggested the possibility of QND measurement. The example he used was that of a mechanical bar for the detection of gravitational wave called the *Weber bar*. Subsequently, many scientists [117–120] have translated this idea to the QND measurement of electro-magnetic fields. Since then QND studies took off in nonlinear optics more successfully than its mechanical counterpart, because of the more advanced techniques available in optical systems. In fact, for similar reasons, the detection of gravitational waves has also been shifted from a mechanical paradigm to one of optics. There are many experimental demonstrations of QND measurements [104–106, 121–128]. Most of them use nonlinear optical properties to establish some form of coupling between the input signal beam with an input meter beam. The idea is that after the nonlinear interaction, the output meter and signal beam will possess information of the original input signal.

Bruckmeier *et al.* [128, 129] in recent years has also demonstrated that with the introduction of a squeezed meter input as proposed by Shapiro [130], QND measurements can be significantly improved. In this chapter we will show that the electro-optic feedforward loop can be use to provide another level of enhancement for QND measurements.

Furthermore, when combined with a squeezed meter input beam the electro-optic feedforward loop can itself be a QND device.

10.2 Criteria for QND measurements

A sequence of repeated measurements of an observable on a stationary classical system will always yield the same results, to within experimental errors. In another words, the act of measurement does not have to significantly affect the system that is being measured in the classical world. However, for quantum systems this is in general not true because of the collapse of the wavefunction of the quantum system and the Heisenberg uncertainty principle. In the quantum world, the act of measurement will always introduce perturbations on the system that is being measured. For small quantum system, this effect can be very significant. One standard example frequently found in textbook is the position and momentum measurement of a particle. It can be easily shown that, as a consequence of Heisenberg uncertainty principle, the successive accurate measurements of position affect the uncertainty in the momentum of the given system. This in turn results in an indeterminacy in subsequent results of position measurements. On the other hand, the accurate determination of the momentum of a quantum system seems to not have such devastating effect on subsequent momentum measurements. The type of measurement similar to the measurement of a particle momentum is called *quantum nondemolition* (QND) measurement.

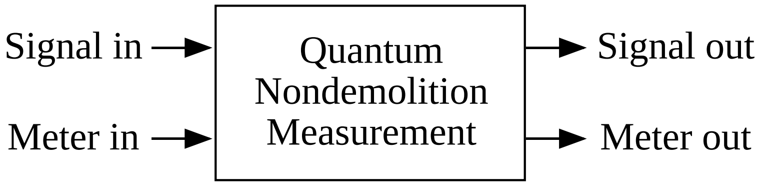

Figure 10.1: Schematic of a QND experiment. The input signal is the state of interest and normally contains interesting information which we are trying to extract. The meter out is where the information is obtained. This is normally classical in nature (eg. photocurrent). The meter input is the probe sent into the measurement system. Sometimes, the probe can simply be the vacuum fluctuations.

Several more precise definitions of a QND measurement will be presented in the remaining of this section. From here onwards, we use the symbol s to denote the system of interest (signal) and m to denote the meter introduced to measure the system. A QND measurement can then be thought of as a special interaction between the system and the meter as shown in Figure 10.1. We also restrict ourselves in the linearizable , travelling-wave regime of quantum optics. So that all quantum fluctuations can be considered to only the first order. A consequence of this is that the quadrature amplitudes can be used and we avoid the complexity of dealing with photon number and phase operator for light.

Braginsky [116] defines the QND observable A as an observable which satisfies the following equation

$$[U, A] = 0, \tag{10.1}$$

where U is the evolution operator for the system and meter. This equation defines well the non-demolition property of the observation of A by the meter, but does not address the efficacy of the measurement itself. Subsequently Caves *et al.* in one of their papers [120] decomposed this general definition of a QND measurement into two separate conditions. The first condition is that the QND observable must commute with the system Hamiltonian.

$$[H_s, A] = 0 \tag{10.2}$$

This is called the *QND variable condition*. Secondly, the interaction Hamiltonian between the system and meter must also commute with the observable,

$$[H_{\rm int}, A] = 0. \tag{10.3}$$

The second condition ensure that the interaction between the system and meter is QND. The simultaneous fulfilment of both equations is sufficient to satisfy the original definition of Eq. (10.1).

An even more practical version of the criteria for QND is later given by Holland *et al.* and Poizat *et al* [8, 131, 132]. We will list the criteria and discuss them individually:

- *Efficiency of meter transfer*
  The meter transfer coefficient, T_m, is a figure of merit for the amount of information that is obtained by the QND measurement.

  $$T_m = \frac{\rm SNR_m^{out}}{\rm SNR_s^{in}} \tag{10.4}$$

  where we have used the superscripts to represent the input and output of the signal and the meter beam. A $T_m = 1$ is therefore a perfect measurement of the input signal. However, this criteria does not actually guarantee that the output signal still retain its original information. Thus we require another transfer coefficient.

- *Efficiency of signal transfer*
  As defined in Chap. 9 the signal transfer coefficient of a measurement is given by

  $$T_s = \frac{{\rm SNR}_s^{\rm out}}{{\rm SNR}_s^{\rm in}} \tag{10.5}$$

  Again, a $T_s = 1$ means that the input signal experiences no degradation or change from the measurement and is thus an ideal condition. The sum of both signal and meter transfer coefficients, called the total transfer coefficient $T = T_s + T_m$, thus tells us the *information performance* of the QND measurement.

Apart from information considerations, a quantum system is also characterized by its fluctuations and correlations. The next three criteria are their measures:

- *Information retrieval*
  The correlation between the meter output and the signal input is given by

  $$C(X_m^{\rm out}, X_s^{\rm in}) = \frac{\langle X_s^{\rm in} X_m^{\rm out}\rangle_{\rm sym} - \langle X_s^{\rm in}\rangle\langle X_m^{\rm out}\rangle}{\sqrt{V_s^{\rm in} V_m^{\rm out}}} \tag{10.6}$$

  Where the subscript sym denotes the *symmetric ordering* of the operators. This criterion is therefore a measure of information retrieval, since a strong correlation between the signal input and the meter output means that a good amount of information has been retrieved by the meter.

- *Back action evasion*
  The formal equation to describe back action evasion is given by the following equation
  $$[H_{\mathrm{d:m}}, A] = 0 \tag{10.7}$$
  Where $H_{\mathrm{d:m}}$ is the interaction Hamiltonian between the detector and the meter. However, this is not very intuitive. A more practical measure of back action evasion is given by the following correlation
  $$C(X_s^{\mathrm{out}}, X_s^{\mathrm{in}}) = \frac{\langle X_s^{\mathrm{in}} X_s^{\mathrm{out}} \rangle_{\mathrm{sym}} - \langle X_s^{\mathrm{in}} \rangle \langle X_s^{\mathrm{out}} \rangle}{\sqrt{V_s^{\mathrm{in}} V_s^{\mathrm{out}}}} \tag{10.8}$$
  Similar to the signal transfer coefficient, strong correlation between the input and the output signal suggest that the measurement introduce no significant degradation of the signal beam. Back action due to the measurement process is thus evaded by the system.

- *Quantum state preparation*
  The final meaningful correlation that can be obtained from the 4-port QND as shown in Figure 10.1 is the correlation between the signal output and meter output.
  $$C(X_s^{\mathrm{out}}, X_m^{\mathrm{out}}) = \frac{\langle X_s^{\mathrm{out}} X_m^{\mathrm{out}} \rangle_{\mathrm{sym}} - \langle X_s^{\mathrm{out}} \rangle \langle X_m^{\mathrm{out}} \rangle}{\sqrt{V_s^{\mathrm{out}} V_m^{\mathrm{out}}}} \tag{10.9}$$
  When the two outputs are strongly correlated, a measurement of the meter output can determine the state of the signal output. Hence the correlation coefficient given is known as the state preparation correlation.

The correlation coefficients given above can take any value between -1 and 1. For measurements where fluctuations are Gaussian, it is more convenient to express these characteristics in terms of their covariances,

$$V_{\mathrm{info}} = V_m^{\mathrm{out}} \left(1 - C(X_m^{\mathrm{out}}, X_s^{\mathrm{in}})^2\right) \tag{10.10}$$
$$V_{\mathrm{bae}} = V_s^{\mathrm{out}} \left(1 - C(X_s^{\mathrm{out}}, X_s^{\mathrm{in}})^2\right) \tag{10.11}$$
$$V_{\mathrm{qsp}} = V_s^{\mathrm{out}} \left(1 - C(X_s^{\mathrm{out}}, X_m^{\mathrm{out}})^2\right) \tag{10.12}$$

Which takes value of 0 to $+\infty$. Obviously, it is an overkill to have all five of the figures of merit given above since there are overlapping information between the covariances. Poizat *et al.* [132] proposed that in most situations, a 2-dimensional representation of the figures of merit is sufficient for a given QND measurement.

Figure 10.2 shows the QND representation in the 2-dimensional diagram. On the x-axis, the total transfer coefficient is chosen. A good measurement in terms of information is therefore located to the right of the 2-D diagram. On the y-axis, the quantum state preparation covariance is chosen. We follow the conventional notation and represent the covariance as $V_{s|m} = V_{\mathrm{qsp}}$. This covariance is chosen instead of the others because it is the only covariance given above that does not depend on the input meter and signal states. Thus, this is a more practical measurement in real experiment. With these two figures,

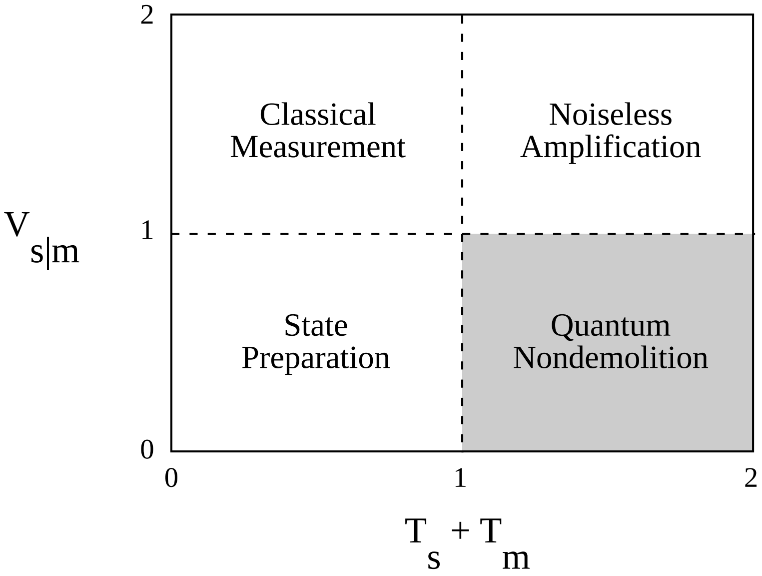

Figure 10.2: A two dimensional representation of QND measurement. The x-axis is the total transfer coefficient and the y-axis is the quantum state preparation covariance $V_{s|m}$

the 2-D space is divided into 4 quadrants by the $V_{s|m} = 1$ and the $T = 1$ lines. As we shall shortly see in the next section, these lines represent the boundaries between quantum and classical measurements. The top left quadrant is called the *classical* quadrant, where the performances of both the information transfer and quantum correlation can be reached entirely classically. The top right quadrant is the *noiseless amplification* or *quantum optical tap* quadrant. In this regime, information transfer has exceeded the quantum limit. However, strong correlation does not yet exist between the output states of the measurement. The results obtained in Chap. 9 thus lie within this quadrant since the in-loop signal does not correlate beyond the quantum limit with the output amplified signal. The bottom left quadrant is the *quantum state preparation* quadrant. In this regime, the output states are strongly correlated to each other. Hence, the measurement of one can be use to determine and prepare the quantum state of the other. Finally, the QND quadrant is the bottom right quadrant where performances in both information transfer and quantum correlation exceed the quantum limit.

In the next section, we examine the use of a normal beam splitter as a measurement device and show that it corresponds to the intersection point of the quadrants with a coherent vacuum meter and a quantum noise limited signal inputs.

10.3 The beam splitter

Let us consider a lossless beam splitter as a measurement device where the two input ports are now regarded as the signal and meter inputs. The transmitted output beam is now our signal output and the reflected beam our meter output. We restrict ourselves in the linearizable regime and only consider all quantum fluctuations to the first order. Our analysis can therefore be restricted to the quadrature amplitude of interest by simply writing the small fluctuating terms δX_i for both the signal and meter inputs. The output beams are thus given by

$$\begin{aligned} \delta X_s^{\rm out} &= \sqrt{\varepsilon}\,\delta X_s^{\rm in} + \sqrt{1-\varepsilon}\,\delta X_m^{\rm in} && (10.13)\\ \delta X_m^{\rm out} &= \sqrt{1-\varepsilon}\,\delta X_s^{\rm in} - \sqrt{\varepsilon}\,\delta X_m^{\rm in} && (10.14) \end{aligned}$$

where ε is the transmittivity of the beam splitter. The noise variances are easily calculated as $V_i = \langle \delta X_i^\dagger\, \delta X_i \rangle$, giving

$$\begin{aligned} V_s^{\rm out} &= \varepsilon V_s^{\rm in} + (1-\varepsilon) V_m^{\rm in} && (10.15)\\ V_m^{\rm out} &= (1-\varepsilon) V_s^{\rm in} + \varepsilon V_m^{\rm in} && (10.16) \end{aligned}$$

In terms of these noise variances, the signal to noise ratios and transfer coefficients are thus given by

$$\begin{aligned} {\rm SNR}^{\rm in} &= \frac{V_s^{\rm in}}{V_{s,n}^{\rm in}} - 1 && (10.17)\\ {\rm SNR}_m^{\rm out} &= \frac{V_m^{\rm out}}{V_{m,n}^{\rm out}} - 1 && (10.18)\\ {\rm SNR}_s^{\rm out} &= \frac{V_s^{\rm out}}{V_{s,n}^{\rm out}} - 1 && (10.19)\\ T_m^{\rm out} &= \frac{{\rm SNR}_m^{\rm out}}{{\rm SNR}_s^{\rm in}} && (10.20)\\ T_s^{\rm out} &= \frac{{\rm SNR}_s^{\rm out}}{{\rm SNR}_s^{\rm in}} && (10.21) \end{aligned}$$

similar to the convention used in Chap. 9, where V_i and denotes the total signal and noise variance of i and $V_{i,n}$ is the noise variance level of i (see Eq. (9.28)). We shall now restrict ourselves to a quantum noise limited signal input, $V_{s,n}^{\rm in} = 1$. The signal and meter transfer coefficients of the beam splitter can then be obtained by making simple substitutions of the above equations,

$$\begin{aligned} T_s &= \tfrac{V_s^{\rm out} - V_{s,n}^{\rm out}}{V_{s,n}^{\rm out}(V_s^{\rm in} - 1)} = \frac{\varepsilon}{[\varepsilon + (1-\varepsilon)V_m^{\rm in}]} && (10.22)\\ T_m &= \tfrac{V_m^{\rm out} - V_{m,n}^{\rm out}}{V_{m,n}^{\rm out}(V_s^{\rm in} - 1)} = \frac{(1-\varepsilon)}{[(1-\varepsilon) + \varepsilon V_m^{\rm in}]} \end{aligned}$$

For a coherent vacuum meter input $V_m^{\rm in} = 1$, the total transfer coefficient of the beam splitter is $T = 1$, independent of its transmittivity. This suggest that an increase in the signal transfer is at the expense of the meter transfer coefficient and vice versa.

The covariance of the beam splitter is given by

$$\begin{aligned} V_{s|m}^{\rm out} &= V_s^{\rm out}\left(1 - C(X_s^{\rm out}, X_m^{\rm out})^2\right)\\ &= V_s^{\rm out} - \frac{|\langle\, \delta X_s^{\rm out} X_m^{\rm out} \rangle|^2}{V_m^{\rm out}}\\ &= \frac{V_s^{\rm in} V_m^{\rm in}}{(1-\varepsilon)V_s^{\rm in} + \varepsilon V_m^{\rm in}} && (10.23) \end{aligned}$$

We note that for uncorrelated fields

$$\langle \delta X_i \, \delta X_j \rangle = \delta_{ij} \langle \delta X_i^2 \rangle, \tag{10.24}$$

ie. the average contribution of the product of uncorrelated fields is zero. Again when both the signal and meter input are quantum noise limited, $V_{s|m}^{\mathrm{out}} = 1$ independent of the transmittivity of the beam splitter. Thus, we have shown that a beam splitter measurement with quantum noise limited signal and meter inputs corresponds to the intersection point of quadrants in the 2-D QND representation.

The introduction of a squeezed vacuum meter input can improve the beam splitter measurement. Eqs. (10.22) shows that a smaller value of the input meter variance leads to improvements in the transfer coefficients. Furthermore, Eq. (10.23) also show likewise improvement to the covariance of the beam splitter outputs. This suggests that a beam splitter with a squeezed vacuum meter input is a QND device as proposed by Shapiro [130] and demonstrated in recent years by Bruckmeier *et al.* [128, 129]. Figure 10.3 shows the results of the calculation with 0 to 6 dB of vacuum squeezing as meter input for the beam splitter.

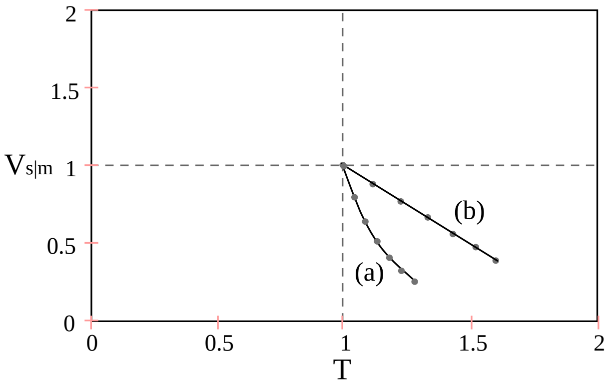

Figure 10.3: Beam splitter with squeezed vacuum input. (a) $\varepsilon = 0.5$ and (b) $\varepsilon = 0.1$. Both plots show the locus of 0 to 6 dB squeezing. Circles represents meter squeezing with integer number of decibels.

10.4 Electro-optic feedforward as a QND measurement

Let us now examine the electro-optic feedforward loop in light of the QND criteria. Figure 10.4 again shows the schematic of the feedforward loop. The previously unused beam splitter port is now our meter input port which can be injected with a squeezed vacuum. The in-loop beam is now the meter output beam and the transmitted beam is the signal output beam. We use the superscripts to denote the three stages of the signal and meter: The input ($^{\mathrm{in}}$), the output ($^{\mathrm{out}}$), and the final (^{f}). The signal and meter outputs are simply the respective output *fields* of the beam splitter. The final stage of the meter however, denotes the measured *photocurrent* of the feedforward loop and is thus dependent on the efficiency of the in-loop meter detector η_m. Similarly, the final stage of the signal represents the photocurrent of the signal detector after the feedforward loop. For convenience, we can lump all downstream losses after the feedforward loop into a total output efficiency η_o.

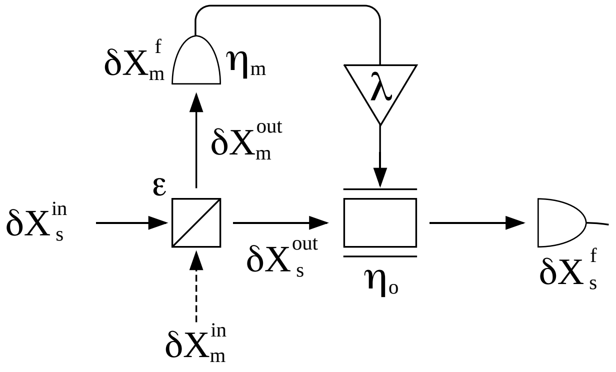

Figure 10.4: Electro-optic feedforward used as a QND measurement scheme

The photocurrents of the meter and signal are given by,

$$
\begin{aligned}
\delta X_m^f &= \sqrt{\eta_m(1-\varepsilon)}\; \delta X_s^{\rm in} + \sqrt{\eta_m \varepsilon}\; \delta X_m^{\rm in} + \sqrt{1-\eta_m}\; \delta X_{v,m} && (10.25)\\
\delta X_s^f &= \sqrt{\eta_o}\left[(\sqrt{\varepsilon} + \lambda\sqrt{\eta_m(1-\varepsilon)})\; \delta X_s^{\rm in} + \right. && (10.26)\\
&\quad (\sqrt{1-\varepsilon} - \lambda\sqrt{\eta_m \varepsilon})\; \delta X_m^{\rm in} + \\
&\quad \left. \lambda\sqrt{(1-\eta_m)}\; \delta X_{v,m} \right] + \\
&\quad \sqrt{1-\eta_o}\; \delta X_{v,o}
\end{aligned}
$$

where $\delta X_{v,m}$ and $\delta X_{v,o}$ are the vacuum fluctuations introduced by the efficiency of the meter detector and the total output loss. Note that the output and the meter vacua are uncorrelated and therefore cannot be combined together as field amplitudes.

Similar to the previous section, we find the transfer coefficients of the feedforward loop by making substitutions

$$
\begin{aligned}
T_m^f &= \frac{V_m^f - V_{m,n}^{\rm f}}{V_{m,n}^f (V_s^{\rm in} - 1)} && (10.27)\\
T_s^f &= \frac{V_s^f - V_{s,n}^{\rm f}}{V_{s,n}^{\rm out} (V_s^{\rm in} - 1)} && (10.28)
\end{aligned}
$$

and we obtained

$$
T_m^f = \frac{\eta_m(1-\varepsilon)}{\eta_m(1-\varepsilon) + \eta_m \varepsilon V_m^{\rm in} + (1-\eta_m)} \qquad (10.29)
$$

$$
T_s^f = \frac{\eta_o |\sqrt{\varepsilon} + \lambda\sqrt{\eta_m(1-\varepsilon)}|^2}{\eta_o \left(|\sqrt{\varepsilon} + \lambda\sqrt{\eta_m(1-\varepsilon)}|^2 + |\sqrt{1-\varepsilon} - \lambda\sqrt{\eta_m \varepsilon}|^2 V_m^{\rm in} + |\lambda|^2(1-\eta_m) \right) + (1-\eta_o)} \qquad (10.30)
$$

The covariance of the scheme is given by

$$\begin{aligned} V_{s|m}^{f} &= \langle\, \delta X_s^{f\,2} \rangle - \frac{|\langle\, \delta X_s^{f}\, \delta X_m^{f} \rangle|^2}{\langle\, \delta X_m^{f\,2} \rangle} && (10.31)\\ &= V_s^f - \frac{|\langle \mathcal{X} \rangle|^2}{V_m^f} && (10.32)\end{aligned}$$

where

$$\begin{aligned} \mathcal{X} &= \sqrt{\eta_o \eta_m (1-\varepsilon)}(\sqrt{\varepsilon} + \lambda\sqrt{\eta_m (1-\varepsilon)})\ \delta X_s^{\mathrm{in}\,2} + \\ &\quad \sqrt{\eta_o \eta_m \varepsilon}(\sqrt{1-\varepsilon} - \lambda\sqrt{\eta_m \varepsilon})\ \delta X_m^{\mathrm{in}\,2} + \\ &\quad \sqrt{\eta_o}\lambda(1-\eta_m)\ \delta X_{v,m}^{2} && (10.33)\end{aligned}$$

With some algebra, the covariance can be shown to be

$$\begin{aligned} V_{s|m} &= [\eta_o \eta_m V_s^{\mathrm{in}} V_m^{\mathrm{in}} + (1-\eta_m)\eta_o(\varepsilon V_s^{\mathrm{in}} + (1-\varepsilon)V_m^{\mathrm{in}}) \\ &\quad +(1-\eta_o)\eta_m((1-\varepsilon)V_s^{\mathrm{in}} + \varepsilon V_m^{\mathrm{in}}) + (1-\eta_o)(1-\eta_m)] \\ &\quad /[(1-\eta_m) + \eta_m(\varepsilon V_m^{\mathrm{in}} + (1-\varepsilon)V_s^{\mathrm{in}})] && (10.34)\end{aligned}$$

A surprising results since it shows that the covariance is independent of the gain of the feedforward loop.

From the results of Eqs. (10.29), (10.30) and (10.34), it is clear that electro-optic feedforward can only affect the signal transfer coefficient. Leaving the meter transfer coefficient and the covariance unchanged. The improvement of the signal transfer can be explained as follows. Any anti-correlations between the signal input and output fields will reduce the signal transfer. However, the anti-correlation as explained in Chap. 9, is entirely due to the input meter fluctuations and is still information stored in the in-loop photocurrent. We can therefore make use of electro-optic feedforward control to cancel and correct for the anti-correlation. The optimum amount of electro-optic feedforward gain is obtained by differentiating Eq. (10.30) in terms of λ,

$$\lambda_{\mathrm{opt}} = \frac{\sqrt{\eta_m(1-\varepsilon)}(\eta_o V_m + 1 - \eta_o)}{\eta_o\sqrt{\varepsilon}(\eta_m V_m + 1 - \eta_m)}. \qquad (10.35)$$

This gives an optimum final signal transfer coefficient of

$$T_{s,\mathrm{opt}}^{f} = \frac{\eta_m(1-\varepsilon) + \eta_o(\varepsilon + V_m - \eta_m)}{\eta_m(1-\varepsilon) + \eta_o(\varepsilon - V_m\varepsilon + V_m - 1) + 1} \qquad (10.36)$$

The QND results after feedforward is therefore shifted towards the right hand side of the 2-D QND diagram without any detrimental effect on the covariance of the measurement (see Figure 10.5). The numerical calculations performed are all based on realistic experimental parameters. The electro-optic feedforward with a squeezed vacuum meter input is hence a very good QND device with performance potentially comparable to many of the best QND proposals.

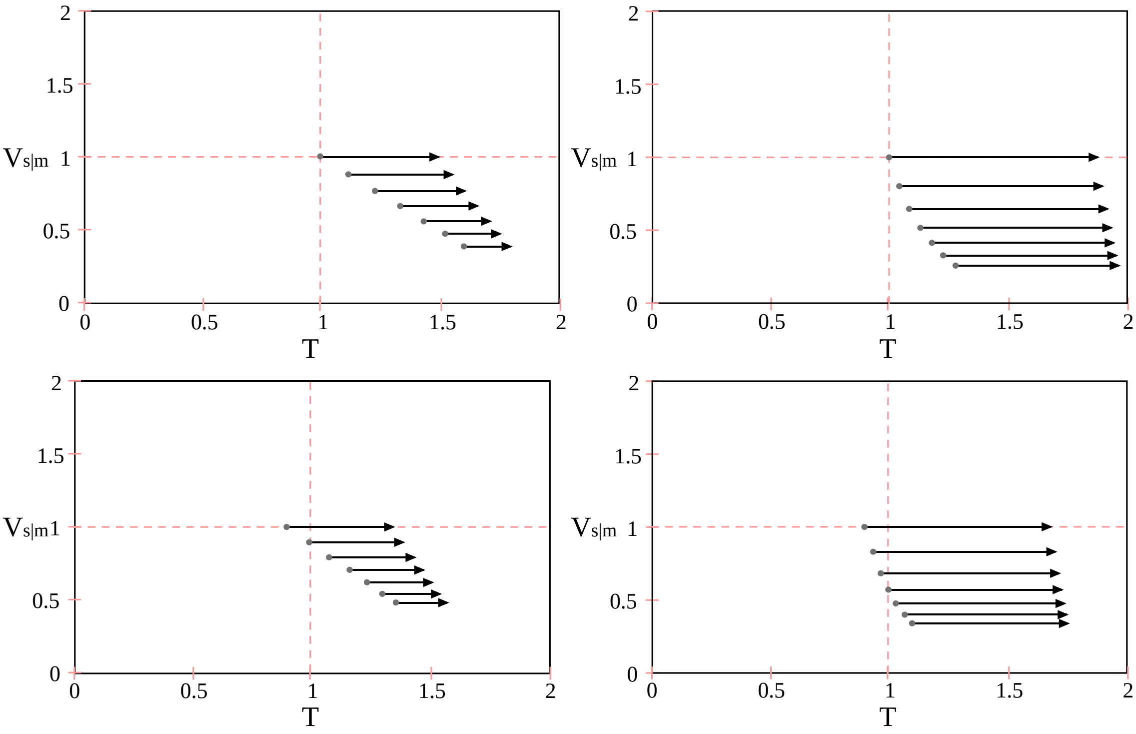

Figure 10.5: QND performances with squeezed vacuum meter input and optimum electro-optic feedforward gain λ_{opt}. Circles represent points without electro-optic feedforward but with a squeezed vacuum meter input of 0, 1, 2, 3, 4, 5, and 6 dB squeezing. Arrows represent the improvements with optimum electro-optic feedforward. *Top*: Results with perfect efficiencies $\eta_m = \eta_o = 1$. *Bottom*: Results with realistic efficiencies $\eta_m = \eta_o = 0.90$ *Left*: Beam splitter transmittivity $\varepsilon = 0.5$. *Right*: Beam splitter transmittivity $\varepsilon = 0.1$

10.5 Pre- and post- enhancement of a QND measurement

Since we are restricting the analysis to the linearizable regime, we can make use of matrix representation to describe QND measurements. In general, we can write the signal and meter outputs as a vector obtained by the multiplication of a QND matrix with an input state vector,

$$\begin{bmatrix} \delta X_s^{\text{out}} \\ \delta X_m^{\text{out}} \end{bmatrix} = \begin{bmatrix} S_s & S_m & S_{v1} & \dots \\ M_s & M_m & M_{v1} & \dots \end{bmatrix} \begin{bmatrix} \delta X_s^{\text{in}} \\ \delta X_m^{\text{in}} \\ \delta X_{v1} \\ \vdots \end{bmatrix} \tag{10.37}$$

Where $\delta X_{v,i}$ are the vacuum fluctuations due to losses; S_i and M_i represent the coupling coefficient of the signal and meter outputs with the ith input mode, respectively. The conditions for QND can then be expressed as

$$S_s \approx 1, \tag{10.38}$$

$$S_i \ll S_s, \qquad \forall i \neq s, \tag{10.39}$$

$$M_s \gg M_i. \tag{10.40}$$

Most linear processes have the principle diagonal terms S_s and M_m strongly coupled (as well as the off diagonal terms S_m and M_s) and are thus unsuitable for QND measurement. Eqs. (10.38) and (10.39) are basically the conditions for back action evasion. This condition is normally achieved via the phase sensitivity of some nonlinear interaction process. Eq. (10.40) on the other hand, ensures high measurement precision by the meter.

We can express the feedforward loop as a matrix equation and obtained

$$\begin{bmatrix} \delta X_s^f \\ \delta X_m^f \end{bmatrix} = \begin{bmatrix} \sqrt{\eta_o}(\sqrt{\varepsilon} + \lambda\sqrt{\eta_m(1-\varepsilon)}) & \sqrt{\eta_o}(\sqrt{1-\varepsilon} - \lambda\sqrt{\eta_m\varepsilon}) & \lambda\sqrt{\eta_o(1-\eta_m)} & \sqrt{1-\eta_o} \\ \sqrt{\eta_m(1-\varepsilon)} & \sqrt{\eta_m\varepsilon} & \sqrt{1-\eta_m} & 0 \end{bmatrix} \times \begin{bmatrix} \delta X_s^{\text{in}} \\ \delta X_m^{\text{in}} \\ \delta X_{v,m} \\ \delta X_{v,o} \end{bmatrix} \tag{10.41}$$

Thus in the limit of $\eta_m, \eta_o \to 1$ and $\varepsilon \to 0$, the QND measurement becomes perfect.

Another example of this representation is given by reference [128] for the QND measurement using an OPA

$$\begin{bmatrix} \delta X_s^{\text{out}} \\ \delta X_m^{\text{out}} \end{bmatrix} = \begin{bmatrix} 1-r & -\sqrt{r} & -r^{3/2} \\ \sqrt{r} & -r^2/2 & r \end{bmatrix} \begin{bmatrix} \delta X_s^{\text{in}} \\ \delta X_m^{\text{in}} \\ \delta X_v \end{bmatrix} \tag{10.42}$$

where $r^2 = A/\kappa$ is the ratio of losses to parametric interaction strength. In the limit of $r \to 0$ this system is again a perfect QND device. However, in any nonlinear interaction process, loss is inevitable. One way to alleviate the problem is to pre-enhance the measurement by the injection of squeezed vacuum making $\delta X_m^{\text{in}} \to 0$. This thus relaxes the QND conditions given in Eqs. (10.39) and (10.40).

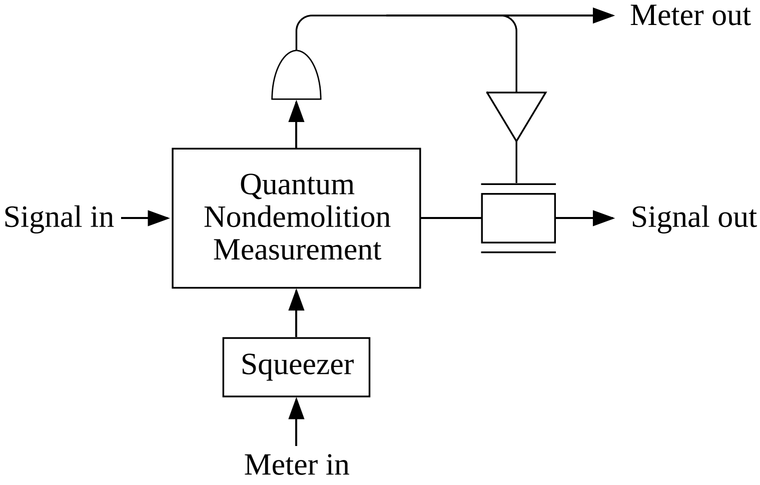

Figure 10.6: QND measurement with pre- and post- enhancements from a squeezed meter input and a meter feedforward, respectively.

We can, by the same token regard the electro-optic feedforward control as a post-enhancement stage of a given QND measurement. Since in most situations the meter output field is measured and converted into photocurrent readout, this information can be used to correct and further improve the signal output. Figure 10.6 shows the conceptual schematic of a pre- and post- enhanced QND device. The final output of the scheme is given by

$$\begin{bmatrix} \delta X_s^{\text{out}} \\ \delta X_m^{\text{out}} \end{bmatrix} = \begin{bmatrix} \mathcal{A}+\lambda\mathcal{B} & \mathcal{C}-\lambda\mathcal{D} \\ 0 & 1 \end{bmatrix} \begin{bmatrix} S_s & S_m & S_{v1} & \dots \\ M_s & M_m & M_{v1} & \dots \end{bmatrix} \begin{bmatrix} \delta X_s^{\text{in}} \\ \mathcal{R}\delta X_m^{\text{in}} \\ \delta X_{v1} \\ \vdots \end{bmatrix} \tag{10.43}$$

Where $\mathcal{R}$ is the squeezing parameter; $\mathcal{A}, \mathcal{B}, \mathcal{C}$ and $\mathcal{D}$ denote the expressions for feedforward control. Both the pre- and post- enhancements are widely applicable to many QND devices, since no assumption was made on the form of the QND matrix.

Chapter 11

Quantum Teleportation of Continuous Variables

Kirk: ”You’d think they have people beaming down everyday.”
Spock: ”Yes, curious lack of interest.”

Errand Of Mercy, Star Trek.

Overview

This chapter examines the quantum teleportation of the quadrature amplitudes of electro-magnetic field from a small signal communication point of view. We show that mixed bright squeezed beams can provide the entanglement required for teleportation. Specific experimental criteria for teleportation of bright beams in terms of the information transfer and quantum correlations are discussed. The relevant published paper to this chapter is

- *“Teleportation with bright squeezed lights”*,
  T. C. Ralph and P. K. Lam, Phys. Rev. Lett. **81**, 5668 (1998).

11.1 Introduction

The word “teleportation” seems to always inevitably conjure up images from science fiction movies, in which machines can make material object spontaneously disappear into thin air and reconstitute itself at some remote sites. In common language, teleportation is simply “the disembodied transport of an object from one place to another” [133, 134]. For classical information, teleportation seems to be rather ubiquitous nowadays. A simple telephone call for example, has already satisfied the description of the statement and can be known as voice teleportation. The sound wave which impacts on the microphone is disembodied and converted into electrical current, and in some cases optical field, during transport and then synthesized back to voice via a speaker at the receiver phone. Another everyday example of teleportation is telefaxing, where information written on a piece of paper is teleported to another fax machine[1]. The fax machine at the remote site, can even provide material (paper) identical to the original for the reconstruction

---

[1] The wireless telegraph is not difficult to understand. The ordinary telegraph is like a very long cat. You pull the tail in New York, and it meows in Los Angeles. The wireless is the same, only without the cat. – Albert Einstein

of information. Hence, more technically, teleportation is a process with the following qualitative attributes:

- *Information or material must be transported from a sender to a receiver.*
  Although the teleportation of atomic system has been proposed and demonstrated to a limited extent [135], we will only devote our attention to the transport of optical states in this chapter.
- *Information or material must involve some form of disembodiment during transport.*
  This is to ensure that the direct propagation of a light beam or the throwing and normal transporting of an object is not classified as teleportation. A property that is perhaps useful in situation where interception is undesirable as in a quantum cryptographic system.
- *Information or material transport must be speedy.*
  Depending on the form of disembodiment, the speed of transport can be the speed of light, electrical current or sound wave.
- *The reconstruction process at the receiver must preserve as many physical properties of the original as possible.*
  In particular, we would like to consider the simultaneous transportation of pairs of canonically conjugate observables. We can therefore no longer regard remote QND reconstruction [136] as an example of teleportation since QND measurements are only concerned with a single observable.

The statements above are still rather vague and qualitative. In particular, we need to find figures of merit on the quality of the reconstructed copy. Furthermore it seems that because the observables in consideration here are canonical conjugates of each other, the Heisenberg uncertainty principle (HUP) implies that teleportation of information will not surpass a given quantum limit. This is because HUP precludes the simultaneous precise determination of conjugate observables. A remarkable discovery by Bennett et al. [137] however, found that the unknown state of a spin-$1/2$ particle could be “teleported” beyond this quantum limit to a remote station through the transmission of classical information, provided the sender and receiver share an Einstein-Podolsky-Rosen type (EPR) entangled quantum pair [138]. We call this type of transport “quantum teleportation”.

Experimental realizations of quantum teleportation have so far been achieved by several groups on different systems. Boschi *et al.* [139] and Bouwmeester *et al.* [140] demonstrated that the polarization state of a single photon can be quantum teleported. Their demonstration have been restricted by the efficiency inherent in photon counting experiments. Davidovich *et al.* [135] have also proposed a scheme for the teleportation of atomic state between two high-Q microwave cavities. Developments by Vaidman [141], Braunstein and Kimble [142] have shown the possibility of the teleportation of continuous quantum variables, such as the quadrature amplitudes of the electromagnetic field. This enables high efficiency homodyne detection techniques to be used. The initial scheme proposed was to make use of below threshold OPO as an EPR source [143]. Furusawa *et al.* [134] recently proceeded to demonstrate the first quantum teleportation of continuous variables by a method using the mixing of squeezed light similar to the proposal of this chapter.

In this chapter, we will show that two bright squeezed sources can be used to produce the required EPR state for quantum teleportation. The significance of this to the below threshold OPO is three-fold: (i) It illustrates that EPR state twin beams can be produced from individual squeezed inputs. This is of practical as well as general interest as compact and reliable, bright squeezed sources (eg. pump suppressed diode lasers [144]) appear feasible in the short term; (ii) As all beams are "bright", it provides additional degrees of freedom in the experimental setup. This is an improvement to using parametric down conversion as the EPR source since the necessary quantum correlations for teleportation only exist near threshold [69] and; (iii) It highlights the physics by enabling a direct analogy with electro-optic feedforward described in Chap. 9 to be drawn.

We proceed to analyze the setup from a small signal, quantum optical communications point of view. Success is measured by the precision with which the spectral variances of the conjugate input variables (intensity and phase) can be reconstructed on the teleported output. Specific experimental criteria for teleportation of bright beams are proposed.

11.2 Teleportation with classical channels

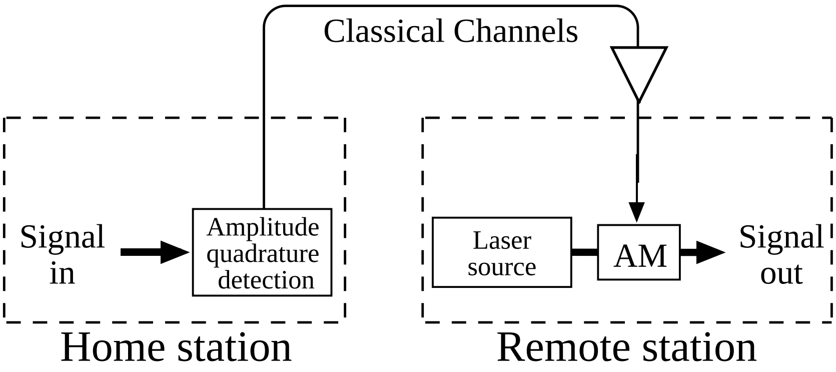

Figure 11.1: Simple transmission scheme.

Let us start off with a rather simple optics experiment to attempt the teleportation of an optical state. Figure 11.1 depict schematically a setup where an input signal encoded in a light beam is detected and its amplitude fluctuations is converted into photocurrent. This photocurrent is then fedforward to a remote station where the information is used to reconstruct the original signal beam by encoding the photocurrent signal on a new laser beam. Obviously, the act of detection at the home station constitutes a valid disembodiment of the original optical state. However, it is also equally obvious that such a system at best can only be able to reconstruct the amplitude quadrature information since no phase information has actually been measured.

In order to overcome this problem, we now add another detection system and measure simultaneously both the amplitude and phase quadratures of the input light as shown in Figure 11.2. The reconstruction of the original light beam at the remote site is similarly done in two stages, where the amplitude and phase fluctuations of the new laser beam are modulated by the respective information carried by the respective measured photocurrents.

Again using the linearized formalism, we write the input field as $\hat{A}_{\rm in}(t) = A_{\rm in} + \delta\hat{A}_{\rm in}(t)$, where $\hat{A}_{\rm in}$ is the field annihilation operator; $A_{\rm in}$ is the classical, steady state, co-

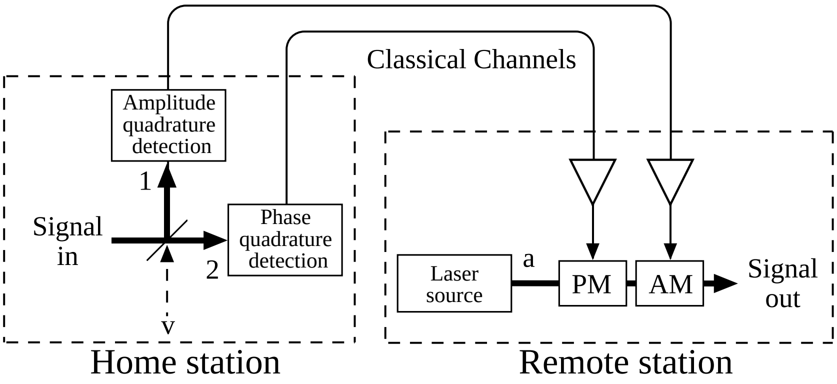

Figure 11.2: Classical teleportation scheme.

herent amplitude of the field (taken to be real); and $\delta\hat{A}_{\text{in}}$ is a zero-mean operator which carries all the classical and quantum fluctuations. For bright beams the amplitude noise spectrum is given by

$$V_{\text{in}}^{+}(\Omega) = \langle|\delta A_{\text{in}}(\Omega) + \delta A_{\text{in}}^{\dagger}(\Omega)|^2\rangle = \langle|\delta X_{\text{in}}^{+}(\Omega)|^2\rangle \tag{11.1}$$

where the absence of hats indicate Fourier transforms have been taken. We denote all amplitude quadrature parameters by a "$+$" subscript or superscript and phase quadrature parameters by "$-$". The phase noise spectrum is then given by

$$V_{\text{in}}^{-}(\Omega) = \langle|\delta A_{\text{in}}(\Omega) - \delta A_{\text{in}}^{\dagger}(\Omega)|^2\rangle = \langle|\delta X_{\text{in}}^{-}(\Omega)|^2\rangle \tag{11.2}$$

We can write the input light amplitude noise spectrum as $V_{\text{in}}^{+} = V_s^{+} + V_n^{+}$. Where V_s^{+} is the signal power and V_n^{+} is the quantum noise power. Similarly the phase noise spectrum can be written $V_{\text{in}}^{-} = V_s^{-} + V_n^{-}$. Suppose the input light is split into two equal halves with a beam splitter as shown in Figure 11.2. The amplitude spectrum is detected in arm 1 and the phase spectrum is detected in arm 2 leading to the following spectra

$$\begin{aligned} V_1^{+} &= 1/2V_{\text{in}}^{+} + 1/2V_v^{+}, \qquad (11.3)\\ V_2^{-} &= 1/2V_{\text{in}}^{-} + 1/2V_v^{-}, \qquad (11.4)\end{aligned}$$

As the amplitude and phase quadratures are conjugate observables, Heisenberg uncertainty principle states that it is not possible to obtain perfect knowledge of both simultaneously. This is ensured by the noise penalties, V_v^{+} and V_v^{-} introduced by the beam splitter. For the case of only vacuum entering at the empty port of the beam splitter $V_v^{+} = V_v^{-} = 1$.

The measurement penalty may be reduced for one quadrature by introducing squeezed vacuum into the empty port such that either $V_v^{+} < 1 < V_v^{-}$ or $V_v^{+} > 1 > V_v^{-}$, however any improvement in the measurement of one quadrature is always at the expense of degrading the measurement of the other. To quantify this we consider the transfer coefficients of the two quadratures defined by two signal transfer coefficients,

$$T^{+} = \text{SNR}_1^{+}/\text{SNR}_{\text{in}}^{+}, \tag{11.5}$$

$$T^- = \mathrm{SNR}_2^- / \mathrm{SNR}_{\mathrm{in}}^-, \tag{11.6}$$

for the amplitude quadrature and for the phase quadrature, respectively. Here SNR stands for the signal to noise ratios of the input quadratures, in, and the detected fields, $1, 2$. We find quite generally

$$\begin{aligned} T^+ + T^- &= \frac{V_n^+}{V_n^+ + V_v^+} + \frac{V_n^-}{V_n^- + V_v^-} \\ &= 1 + \frac{V_n^+ V_n^- - V_v^+ V_v^-}{V_n^+ V_n^- + V_n^+ V_v^- + V_v^+ V_n^- + V_v^+ V_v^-} \end{aligned} \tag{11.7}$$

Since we wish to derive a quantum limit to the measurement scheme, we assume that our input beam is in a minimum uncertainty state by making $V_n^+ V_n^- = 1$. Using the Heisenberg uncertainty principle for the quadratures $V_v^+ V_v^- \geq 1$, we find

$$T_s^+ + T_s^- \leq 1 \tag{11.8}$$

for any simultaneous measurement of both quadratures using the measurement scheme shown in Figure 11.2. This places an absolute upper limit on the information that can possibly be transmitted through the classical channel.

The information arriving at the receiver is imposed on an independent beam of light using amplitude and phase modulators. We now wish to consider how well this can be achieved. The problem is that the light beam at the receiver must carry its own quantum noise. For small signals the action of the modulators can be considered additive and we will assume that they are ideal in the sense that loss is negligible and the phase modulator produces pure phase modulation and similarly for the amplitude modulator. The output field is given by

$$\hat{A}_{\mathrm{out}} = \hat{A}_a + \delta \hat{R}_+ + \delta i \hat{R}_-, \tag{11.9}$$

and the fluctuations imposed by the modulators can be written as the following convolutions over time [107]

$$\begin{aligned} \delta \hat{R}_+ &= \int_0^\infty k_+(\tau) \frac{1}{2} A_{\mathrm{in}} \left(\delta \hat{X}_{\mathrm{in}}^+(t-\tau) + \delta \hat{X}_v^+(t-\tau) \right) d\tau \\ \delta \hat{R}_- &= \int_0^\infty k_-(\tau) \frac{1}{2} A_{\mathrm{in}} \left(\delta \hat{X}_{\mathrm{in}}^-(t-\tau) + \delta \hat{X}_v^-(t-\tau) \right) d\tau \end{aligned} \tag{11.10}$$

where k_+ and k_- describe the action of the electronics in the amplitude and phase channels respectively. The amplitude and phase quadrature fluctuations of the receiver beam are represented by $\delta \hat{X}_a^+$ and $\delta \hat{X}_a^-$ respectively. The amplitude and phase quadrature noise spectra of the output field are

$$V_{\mathrm{out}}^+ = V_a^+ + |\lambda_+(\Omega)|^2 (V_{\mathrm{in}}^+ + V_v^+) \tag{11.11}$$

$$V_{\mathrm{out}}^- = V_a^- + |\lambda_-(\Omega)|^2 (V_{\mathrm{in}}^- + V_v^-) \tag{11.12}$$

where various parameters have been rolled into the electronic gain of the amplitude channel, λ_+ and λ_-, which is proportional to the Fourier transform of $k_\pm$.

By making $|\lambda_+|^2, |\lambda_-|^2 >> 1$, the signal transfer coefficient for the output $T_s^\pm = \mathrm{SNR}_{\mathrm{out}}^\pm / \mathrm{SNR}_{\mathrm{in}}^\pm$ can satisfy the equality in Eq. (11.8), thus realizing the maximum allowable information transfer. However the output beam would then be much noisier than the input beam and hence yield a very dissimilar state. A measure of the similarity of the input and output beams is given by the amplitude and phase conditional variances [131];

$$V_{\mathrm{cv}}^{+} = V_{\mathrm{out}}^{+} - \frac{|\langle \delta X_{\mathrm{in}}^{+} \delta X_{\mathrm{out}}^{+} \rangle|^2}{V_{\mathrm{in}}^{+}} \tag{11.13}$$

$$V_{\mathrm{cv}}^{-} = V_{\mathrm{out}}^{-} - \frac{|\langle \delta X_{\mathrm{in}}^{-} \delta X_{\mathrm{out}}^{-} \rangle|^2}{V_{\mathrm{in}}^{-}} \tag{11.14}$$

If $V_{\mathrm{cv}}^{+} + V_{\mathrm{cv}}^{-} = 0$ then the input and output are maximally correlated. For our system we find

$$V_{\mathrm{cv}}^{+} + V_{\mathrm{cv}}^{-} = V_a^{+} + V_a^{-} + |\lambda_1|^2 V_v^{+} + |\lambda_2|^2 V_v^{-} \tag{11.15}$$

Once again any attempt to suppress the noise penalty in one quadrature, say by squeezing the receiver beam, results in a greater penalty in the other quadrature. The best result is obtained for $\lambda_+ = \lambda_- = 0$ and a coherent receiver beam giving

$$V_{\mathrm{cv}}^{+} + V_{\mathrm{cv}}^{-} \geq 2 \tag{11.16}$$

That is the best correlation between the states is achieved by not transferring any information. In principle one could measure V_{cv}^{+} directly by performing a perfect QND measurement of the amplitude quadrature of the input field and electronically subtracting it from an amplitude quadrature measurement of the output field. In a similar way V_{cv}^{-} could in principle be measured using a perfect QND measurement of the phase quadrature of the input field. Clearly this is impractical. However the correlations can be inferred quite easily from individual measurements of the transfer coefficients and the absolute noise levels of the output field via

$$\begin{aligned} V_{\mathrm{cv}}^{+} &= (1 - T_s^{+}) V_{\mathrm{out}}^{+} \\ V_{\mathrm{cv}}^{-} &= (1 - T_s^{-}) V_{\mathrm{out}}^{-} \end{aligned} \tag{11.17}$$

These results are summarized in Figure 11.3 where $T_s^{+} + T_s^{-}$ versus $V_{\mathrm{cv}}^{+} + V_{\mathrm{cv}}^{-}$ are plotted as a function of increasing $|\lambda_\pm|$. The dotted lines represent the limits set by purely classical transmission with symmetric emphasis on both quadrature amplitudes.

11.3 Teleportation with quantum and classical channels

11.3.1 The requisite EPR state

We now consider the electro-optical arrangement that is shown in Figure 11.4. It is similar to that proposed by Braunstein and Kimble [142]. However in contrast to reference [142] we have replaced the parametric down converter with two coherently related amplitude squeezed sources which are mixed on a 50:50 beam splitter (BS1). One of the sources is phase shifted by $\pi/2$ with respect to the other before mixing.

The results of the mixing at the beam splitter of these two amplitude squeezed sources, is two output fields with EPR-type entanglement. Figure 11.5 shows the ball-on-stick picture of the situation. As originally proposed by Einstein-Podolsky-Rosen [138], an EPR entanglement is the condition of a pair of quantum states correlated to each other via two canonically conjugate variables. For example, two particles are said to have EPR entanglement when they are correlated with each other via both position and momentum. Similarly, a quantum optical analogue of the situation is that two optical states

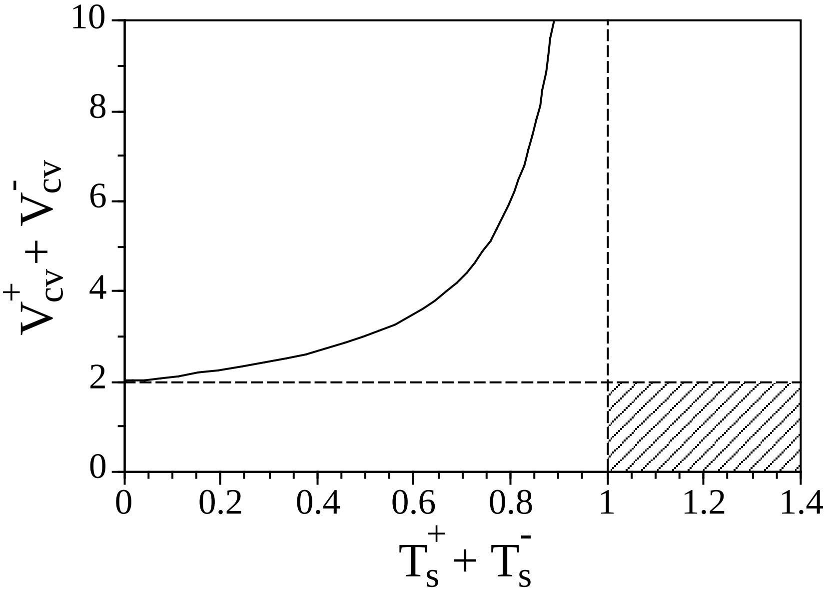

Figure 11.3: Performance of classical teleportation arrangement. Information transfer ($T_s^+ + T_s^-$) is plotted versus state reconstruction ($V_{\rm cv}^+ + V_{\rm cv}^-$) for $\lambda_\pm = \lambda_+ = -\lambda_-$ running from 0 to 2.0. Dashed lines indicate the classical limits.

are EPR entangled when correlations exist in both the amplitude and phase quadratures between the two states. Ou *et al.* [143] have demonstrated that such a optical entanglement does exist between the two output light fields of a nondegenerate below threshold OPO. When two the detection systems were set to measure the amplitude quadrature of the output fields, the difference of the photocurrents will show intensity squeezing [20]. Conversely, when the detection systems are measuring the phase quadrature of the two output light field, the sum of the photocurrents will exhibit phase squeezing. Using the ball-on-stick picture presented in Chap. 2, we obtain similar results with the mixing of two bright amplitude squeezed beams.

11.3.2 Quantum teleportation results

Once the EPR entanglement is confirmed, one of the beams is sent to where we wish to measure the input signal. There it is mixed with the input signal beam (which is of similar intensity) on another 50/50 beam splitter (BS2). We combine them in phase such that there are "bright" and "dark" outputs. The bright beam is directly detected to obtain its amplitude quadrature. The dark beam is mixed with a local oscillator (LO) and homodyne detection is used to measure its phase quadrature (represented schematically in Figure 11.4). The photocurrents obtained are sent to amplitude and phase modulators situated in the other beam coming from the mixed squeezed sources.

Following the approach of Chap. 9, the amplitude noise spectrum of the output field is found to be

$$V_{\rm out}^+ = \left|\frac{1}{\sqrt{2}} + \frac{1}{2}\lambda_+\right|^2 V_a^+ + \left|\frac{1}{\sqrt{2}} - \frac{1}{2}\lambda_+\right|^2 V_b^- + \left|\frac{1}{\sqrt{2}}\lambda_+\right|^2 V_{\rm in}^+ \tag{11.18}$$

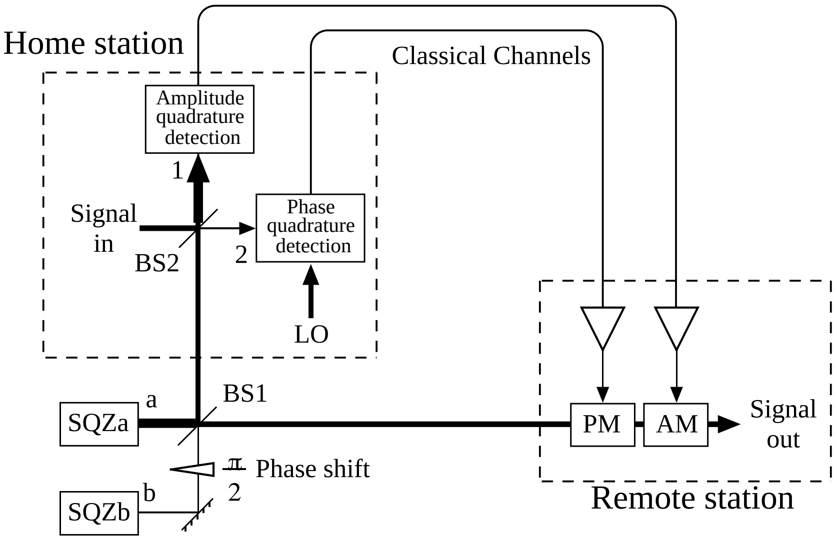

Figure 11.4: Schematic of quantum teleportation arrangement. SQZa and SQZb are coherently related squeezed sources with the intensity of a much greater than that of b. The signal input and local oscillator (LO) must also be coherently related to the squeezed sources. BS1 and BS2 are 50:50 beam splitters.

and similarly the phase noise spectrum is given by

$$V_{\text{out}}^{-} = \left|\frac{1}{\sqrt{2}} + \frac{1}{2}\lambda_{-}\right|^{2} V_{a}^{-} + \left|\frac{1}{\sqrt{2}} - \frac{1}{2}\lambda_{-}\right|^{2} V_{b}^{+} + \left|\frac{1}{\sqrt{2}}\lambda_{-}\right|^{2} V_{\text{in}}^{-} \tag{11.19}$$

Here the amplitude (phase) spectra of beams a and b are given by V_a^+ (V_a^-) and V_b^+ (V_b^-), respectively. The cross coupling of the phase spectrum of the weak beam, b, into the amplitude spectrum of the output is due to the $\pi/2$ phase shift. Consider first the situation if beams b and the signal are blocked so that just vacuum enters the empty ports of the beam splitters. The setup is then just a feedforward loop. We have shown in Chap. 9 and in reference [145] that the measurement penalty at the feedforward beam splitter (BS1) can be completely cancelled by correct choice of the electronic gain, allowing noiseless amplification of V_a^+ to be achieved. This cancellation can be seen from Eq. (11.18) with the electronic gain set to $\lambda_+ = \sqrt{2}$. The remaining penalty is due to the in-loop beam splitter (BS2) which, here, is allowing us to detect both quadratures. But now suppose we inject our signal into the empty port of the in-loop beam splitter. With $\lambda_+ = \sqrt{2}$ we find Eq. (11.18) reduces to

$$V_{\text{out}}^{+} = 2V_{a}^{+} + V_{\text{in}}^{+} \tag{11.20}$$

and if beam a is strongly amplitude squeezed such that $V_a^+ << 1$ then

$$V_{\text{out}}^{+} \simeq V_{\text{in}}^{+} \tag{11.21}$$

Now consider the phase noise spectrum of Eq. (11.19). If we impose the same electronic gain condition on the fed-forward phase signal as we have for the amplitude signal we will get an output spectrum

$$V_{\text{out}}^{-} = 2V_{a}^{-} + V_{\text{in}}^{-} \tag{11.22}$$

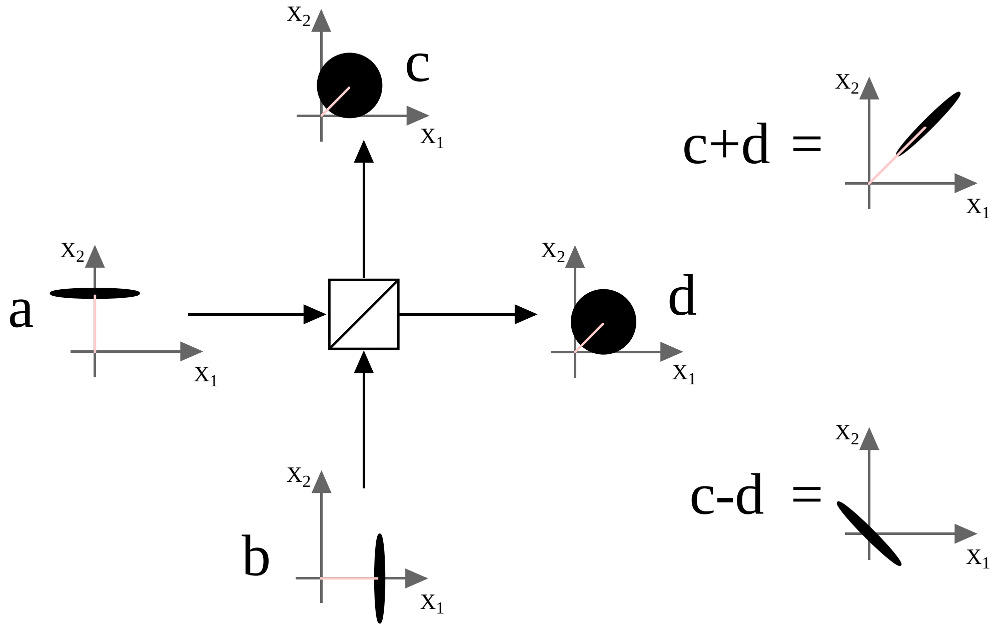

Figure 11.5: EPR entanglement.

If beam a is strongly amplitude squeezed then the uncertainty principle requires $V_a^- \gg 1$ so this is not a useful arrangement. However if we perform negative rather than positive feedforward on our phase signal such that $\lambda_- = -\sqrt{2}$ then we will cancel the phase noise of beam a and instead see the vacuum noise entering at the empty port of the feedforward beam splitter. Finally by injecting our low intensity beam b at this port we find

$$V_{\rm out}^- = 2V_b^+ + V_{\rm in}^- \tag{11.23}$$

Beam b can be made strongly amplitude squeezed without affecting Eq. (11.21) thus giving us

$$V_{\rm out}^- \simeq V_{\rm in}^- \tag{11.24}$$

Hence we have the remarkable result that we can satisfy both Eqs. (11.21) and (11.24) simultaneously even though the only direct connection between the input and output fields is classical. More generally, the spectral variance at some arbitrary quadrature phase angle (θ) is given by

$$\begin{aligned} V_{\rm out}^\theta &= \left\langle \left| \delta A_{\rm out}^\dagger e^{+i\theta} + \delta A_{\rm out} e^{-i\theta} \right|^2 \right\rangle \\ &= V_{\rm in}^\theta + 2\cos^2\theta\, V_a^+ + 2\sin^2\theta\, V_b^+ \end{aligned} \tag{11.25}$$

This form makes it clear that, provided beam a and beam b are both strongly amplitude squeezed, the input and output spectral variances will be approximately equal for any arbitrary quadrature angle (not just amplitude and phase). Note that neither the sender or receiver obtain quantum limited information about the teleported field due to the presence of a noisy anti-squeezed quadrature in both the phase and amplitude measurements.

Experimental conditions will in general be non-ideal. We define teleportation as having been unconditionally achieved when both the correlation and the information transfer have exceeded the classical limits (ie. $T_s^+ + T_s^- \geq 1$ and $V_{\rm cv}^+ + V_{\rm cv}^- \leq 2$) at some RF detection frequency. In Figure 11.6 we plot $T_s^+ + T_s^-$ versus $V_{\rm cv}^+ + V_{\rm cv}^-$ as a function of feedforward gain for various values of squeezing. Notice that although moderate values of squeezing allow either information transfer or state reconstruction to be superior to the classical channel limit, squeezing must be greater than 50% before both conditions can be met simultaneously and hence teleportation achieved.

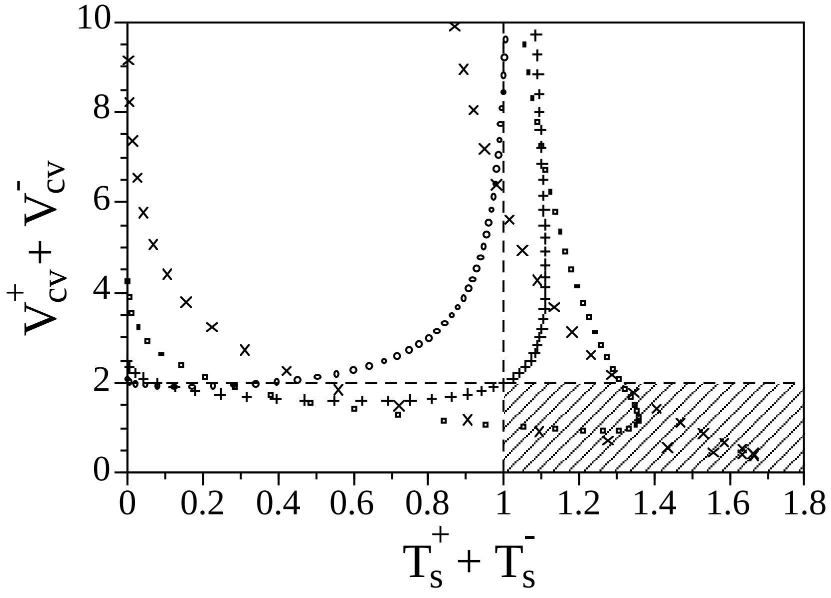

Figure 11.6: Performance of quantum teleportation arrangement. Information transfer ($T_s^+ + T_s^-$) is plotted versus state reconstruction ($V_{\rm cv}^+ + V_{\rm cv}^-$) for $\lambda_\pm = \lambda_+ = -\lambda_-$ starting from 0 with increments of 0.05. Circles, pluses, squares and crosses are for 25%, 50%, 75% and 90% squeezing from both sources, respectively. Dashed lines indicate the classical limits and shaded region are region of unconditional quantum teleportation.

In summary we have shown that the EPR type correlation needed to produce teleportation of continuous variables can be established using two bright squeezed sources. We have analyzed the setup from a small signal quantum optical point of view. We have established criteria for deciding if teleportation has been achieved and have shown that the mechanism can be understood in terms of electro-optic feedforward control.

Chapter 12

Conclusions

Roads? Where we're going we don't need...roads.

Dr. Emmet Brown, Back to the Future

12.1 Summary of the squeezing results

This thesis reports the generation of optical squeezed state by $\chi^{(2)}$ nonlinear processes.

In the SHG experiment, we have observed 2.1 dB of intensity quadrature squeezing from the second harmonic output. A modular theory for noise propagation in our SHG experiment is developed. The experimental data and the theoretical predictions are shown to be in excellent agreement with each other.

Our investigations into the limiting factors of SHG squeezing reveal that competition between nonlinearities can occur within a single monolithic nonlinear crystal. We find that in the presence of competition, the second harmonic output power can be optically clamped. Our study of the quantum noise of competition suggests that the onset of competition degrades the second harmonic squeezing. This is a hitherto unpredicted limit for SHG squeezing. An improvement on the SHG squeezing by suppressing the onset of competition with intra-cavity dispersion is proposed.

The classical study of the OPO process has facilitated us with crucial information for the optimal design of an OPO for squeezed vacuum generation. Using a low loss OPO with large escape efficiency, we have observed more than 7 dB of vacuum squeezing at 70% of threshold. Limits to the observed vacuum squeezing are discussed. In particular, we find that the phase jitters of the OPO system becomes the dominant limiting factor for strong vacuum squeezing when the other efficiencies of the system are optimized. The OPO can be operated as an amplifier when an input seed wave is used. By locking the relative phase of the seed wave in quadrature with the second harmonic pump, the input seed wave underwent parametric de-amplification and 4 dB of intensity squeezing is observed from the OPA output.

12.2 Summary of the electro-optic feedforward control results

With the use of an electro-optic feedforward loop, we demonstrate that vacuum fluctuations introduced at a beam splitter can be compensated with the correct amount of feedforward gain.

The first application of this quantum noise control via an electro-optic feedforward loop is the noiseless signal amplification of a coherent input. The results achieved,

$T_s = 0.90$, with this simple setup is limited only by the efficiency of the photodetectors and is comparable to most of the proposed noiseless amplification schemes. When used in combination with an injection locked laser, we have proceeded to demonstrate the independently variable signal and power amplifications. Large total gain, as high as $G > 300$, has been achieved while maintaining excellent signal transfer.

More interesting applications were demonstrated when the feedforward loop is used in conjunction with squeezed light. We have shown that the noiseless signal amplification of a squeezed input can lead to robust transmission of modulation signals in the squeezed beam. Even in the presence of large downstream loss (86%), our results obtained by the feedforward amplifier still exceed the performance of an ideal (no loss) phase insensitive amplifier.

The injection of squeezed vacuum into a feedforward loop is shown to corresponds to a QND measurement. Theoretical modeling using achievable experimental parameters suggest excellent performance of the QND device. In a more general sense, we can utilize the injection of squeezed vacuum state and the electro-optic feedforward control as two pre- and post- enhancement stages of a QND measurement.

Finally, we propose the possibility of quantum teleportation using two electro-optic feedforward loops and two sources of squeezed light. Measures based on information transfer and quantum correlation are also proposed for the characterization of quantum teleportation.

12.3 Future research

12.3.1 Mode-locked OPO via competing nonlinearities

The competing nonlinearities described in the SHG experiment of Chap. 6 are surprisingly ubiquitous in many experiments. Since the onset of competition leads to a degradation of the second harmonic squeezing, it is regarded as a parasitic effect for squeezed state generation. However, a precise control of the onset of competition can lead to useful application as a frequency comb generator. When the nonlinear crystal cavity is driven with a modulation frequency equal to its cavity FSR, two effects will occur. Firstly, the incident fundamental beam entering the cavity will experience an energy transfer to its sidebands due to the existence of the modulation. Since these sidebands are at one FSR away, they are themselves resonant modes of the nonlinear cavity. The build up of these intra-cavity sideband fields can possibly lead to the production of an optical frequency comb [17, 146, 147]. Secondly, the generation of intra-cavity NDOPO can facilitate large frequency tuning of the optical comb [148] which may be useful as an optical frequency reference. We also anticipate that such systems will produce pulsed outputs similar to a mode-locked laser. Perhaps, with the variation of temperature and cavity length, the pulse width of the mode-locked OPO can be controlled. The device mode-locked OPO can hence potentially be a frequency and pulse width tunable light source.

12.3.2 Implementations of QND measurement and quantum teleportation

The proposals of Chap. 10 and Chap. 11 have not yet been implemented experimentally. The author feels that experimental implementation of these two ideas can possibly lead to more interesting physics not yet discovered by the theoretical models used.

With the availability of a strongly squeezed vacuum and a carefully designed electro-optic control loop, calculations done in Chap. 10 suggest that the QND measurement achievable by the proposed method should have excellent performances in both the quantum correlations and the total signal transfer coefficients.

Although quantum teleportation has been demonstrated in many experimental systems [134, 139, 140], many questions still exist in the characterization of the results and the possible applications of quantum teleportation. Our proposal of characterizing the performance of the teleporter by measurements of quantum correlations and signal transfer coefficients are different to the characterization via a measurement of the fidelity

$$\mathcal{F} = \langle \psi_{\rm in} | \rho_{\rm out} | \psi_{\rm in} \rangle \tag{12.1}$$

where $|\psi_{\rm in}\rangle$ is the input ket and $\rho_{\rm out}$ is the density function of the output state. Depending on the optical state undergoing teleportation and its application, one measure may have advantage over the other.

12.3.3 The squashed state of light

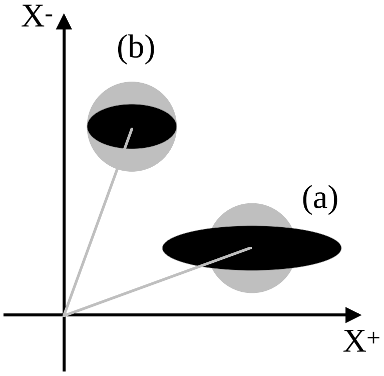

Figure 12.1: The squashed state of light. (a) The squeezed state (black) and a minimum uncertainty coherent state (grey). (b) The squashed state (black) has a squeezed quadrature whilst the orthogonal quadrature is still quantum noise limited.

The observation of sub-shot-noise photocurrent within an electro-optic control loop was observed by Walker *et al.* [149] and Machida *et al.* [150] not long after the first demonstration of squeezed light. The generation of this *in-loop squeezing* or *squashed light* [151], as is commonly called, is much easier than the generation of real squeezing. Shapiro *et al.* [152] pointed out that this sub-shot-noise in-loop light beam does not obey the free field boson commutation relation. Consequently the reduction in the noise of one quadrature does not necessarily accompany an increase of noise in the orthogonal quadrature as shown in Figure 12.1. However, attempts to utilize this sub-shot noise light by directly coupling it out of the electro-optic control loop only yield, at best, quantum noise limited results.

Recently, Buchler *et al.* [153] proposed that the sub-shot-noise statistics of the squashed state can be utilised to suppress the classical and quantum radiation pressure noise on the mirrors of an optical cavity. Wiseman [154] proposed that an in-loop atom will experience fluorescence line narrowing when illuminated by the squashed state. In both cases, the in-loop squashed state can be thought of as being utilized via an in-loop QND measurement: The use of an optical cavity or the coupling of in-loop light to an atom. Experimental investigations into the application and generation of squashed state can potentially yield important breakthrough and further extend the use of quantum electro-optic control of light.

Appendix A

Measuring Signal and Noise with a Spectrum Analyser

In this appendix, we work through a numerical example of a signal-to-noise ratio measurement using a spectrum analyser. The details of the correction factors used in this calculation are provided in reference [30].

Suppose that we have measured simultaneously using a spectrum analyser a signal level of $\kappa = -79$ dBm and noise level (assume that the measurement is in a quantum noise limited environment) of $\delta = -88$ dBm. From a separate measurement of the photodetector used in the setup, we found that the photodetector has a quantum efficiency of $\eta = 0.92$. The following tables provide a step-by step guide to working out the actual signal and noise power.

The measured quantities listed in Table A.1 are the quantities displayed by the RF spectrum analyser and the values are calculated based on these uncorrected values. the SNR figure used throughout this thesis is based on the usual definition of the ratio of signal power to noise power. However, at the signal frequency the measurement obtained by the spectrum analyser is the sum of signal and noise power. Hence δ and κ are the only two quantities directly measurable.

Based on the explanation given in Chap. 3 and reference [30], the noise levels of the measurements are suitably corrected in Table A.2. The true values are therefore the actual values of quantities as measured by the photodetector. The S/N value given in Table A.2

Measured quantity	*mathematical expression*	*value*
N (dBm)	δ	-88.00 dBm
(mW)	$10^{\delta/10}$	1.585×10^{-9} mW
$S+N$ (dBm)	κ	-79.00 dBm
(mW)	$10^{\kappa/10}$	1.259×10^{-8} mW
S (dBm)	$10\log(10^{\kappa/10} - 10^{\delta/10})$	-79.58 dBm
(mW)	$10^{\kappa/10} - 10^{\delta/10}$	1.101×10^{-8} mW
$(S+N)/N$ (dB)	$\kappa - \delta$	9.00 dB
	$10^{(\kappa-\delta)/10}$	7.94
S/N (dB)	$10\log(10^{\kappa/10} - 10^{\delta/10}) - \delta$	8.42 dB
	$(10^{\kappa/10} - 10^{\delta/10})/10^{\delta/10}$	6.95

Table A.1: Measured spectrum analyser quantities

True quantity	*mathematical expression*	*value*
N (dBm)	$\delta + 2$	-86.00 dBm
(mW)	$1.585 \times 10^{\delta/10}$	2.512×10^{-9} mW
$(S+N)$ (dB)	$10\log(10^{\kappa/10} + 0.585 \times 10^{\delta/10})$	-78.69 dB
	$10^{\kappa/10} + 0.585 \times 10^{\delta/10}$	1.352×10^{-8}mW
S (dBm)	$10\log(10^{\kappa/10} - 10^{\delta/10})$	-79.58 dBm
(mW)	$10^{\kappa/10} - 10^{\delta/10}$	1.101×10^{-8} mW
$(S+N)/N$ (dB)	$10\log(10^{\kappa/10} + 0.585 \times 10^{\delta/10}) - (\delta + 2)$	7.31 dB
	$(10^{\kappa/10} + 0.585 \times 10^{\delta/10})/(1.585 \times 10^{\delta/10})$	5.38
S/N (dB)	$10\log(10^{\kappa/10} - 10^{\delta/10}) - (\delta + 2)$	6.42 dB
	$(10^{\kappa/10} - 10^{\delta/10})/(1.585 \times 10^{\delta/10})$	4.38

Table A.2: Corrected values

Inferred quantity	*mathematical expression*	*value*
$(S+N)/N$ (dB)	$10\log(10^{\kappa/10} + 0.585 \times 10^{\delta/10}) - (\delta + 2 + 10\log\eta)$	7.67 dB
	$(10^{\kappa/10} + 0.585 \times 10^{\delta/10})/(1.585\eta \times 10^{\delta/10})$	5.85
S/N (dB)	$10\log[(10^{\kappa/10} + 0.585 \times 10^{\delta/10})/(1.585\eta \times 10^{\delta/10}) - 1]$	6.85 dB
	$(10^{\kappa/10} + 0.585 \times 10^{\delta/10})/(1.585\eta \times 10^{\delta/10}) - 1$	4.85

Table A.3: Inferred values

is thus the usual SNR value reported in all of the measurements in this thesis. Note that when the measured signal size is comparable to the quantum noise, the SNR's can be significantly different before and after correction ($\mathrm{SNR}_{\mathrm{meas}} = 6.95$ and $\mathrm{SNR}_{\mathrm{true}} = 4.38$).

Finally, we can infer the values of the measured quantities by assuming that the non-ideal efficiency of the photodetector will lead to the weakening of signals toward the standard quantum limit. The S/N value given in Table A.3 is used only as limit of compliance to theoretical predictions.

Appendix B

Photodetector Circuit Diagrams

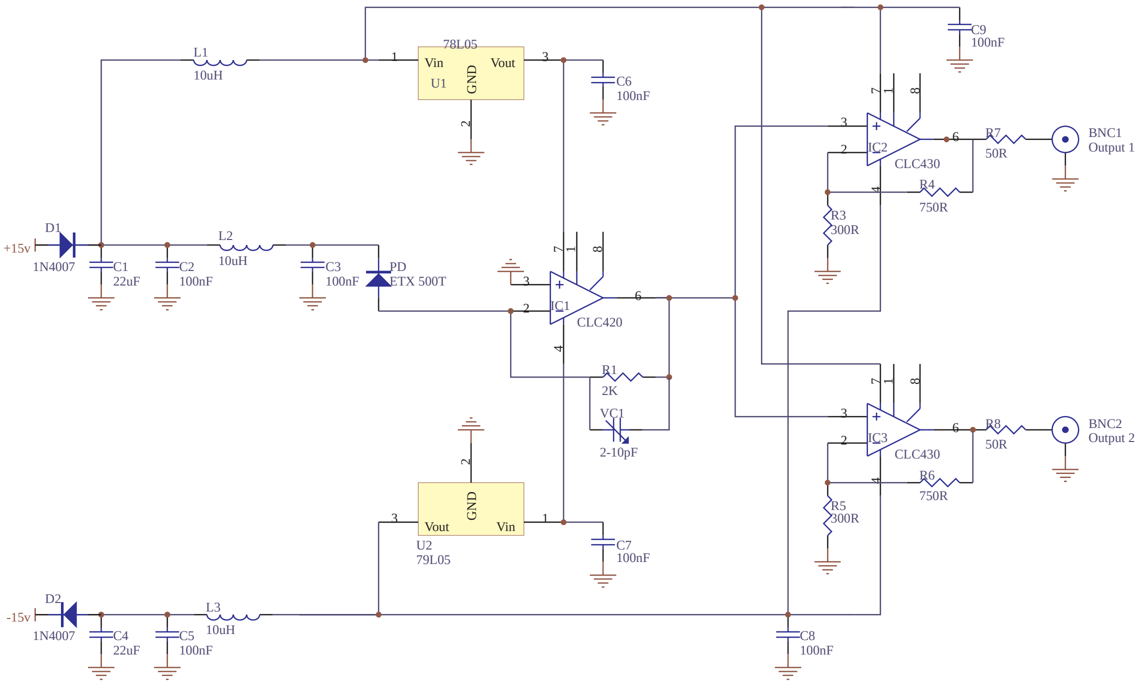

Figure B.1: Circuit diagram of 1064 nm photodetector. The photodiode used is ETX-500 from Epitaxx. RF operational amplifiers use are Comlinear CLC-420 and CLC-430.

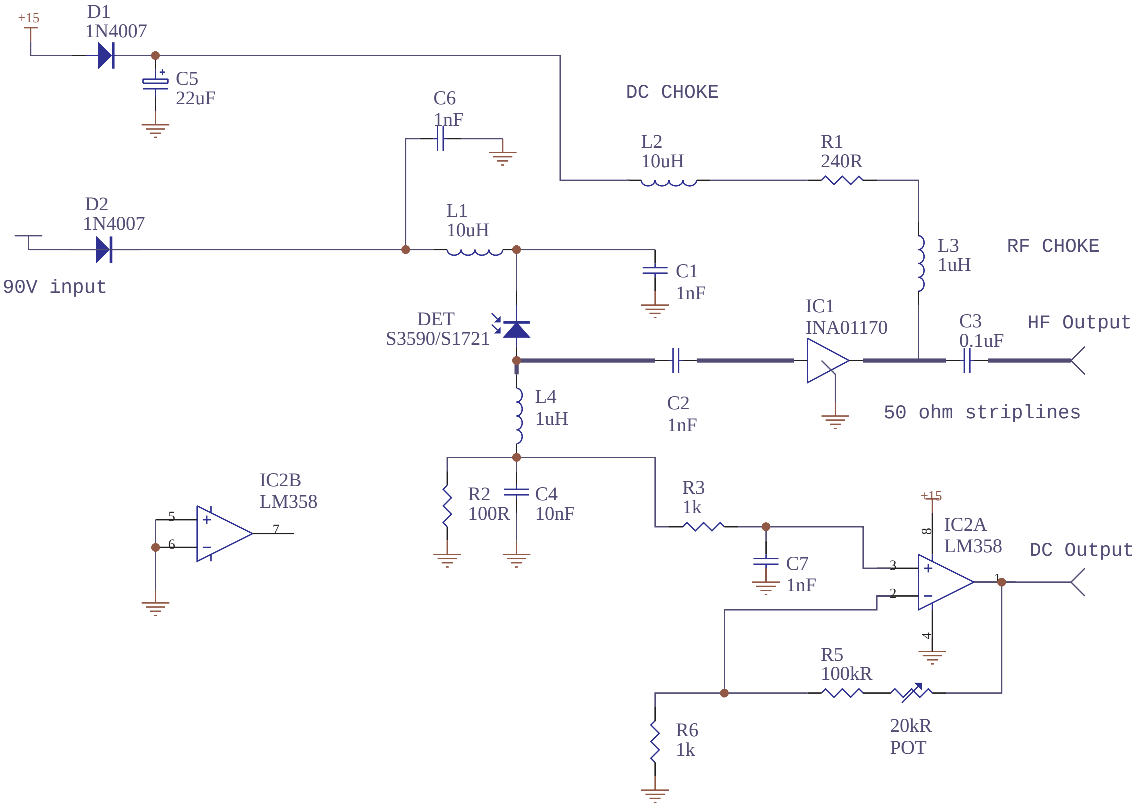

Figure B.2: Circuit diagram of 532 nm photodetector. Hamamatsu S-1721 and S-3590 photodiodes were used in this circuit. The RF amplification is done using Hewlett-Packard INA-01170 MMIC. DC amplification is done separately using LM 358 operational amplifier.

Appendix C

PID Controller Circuit Diagrams

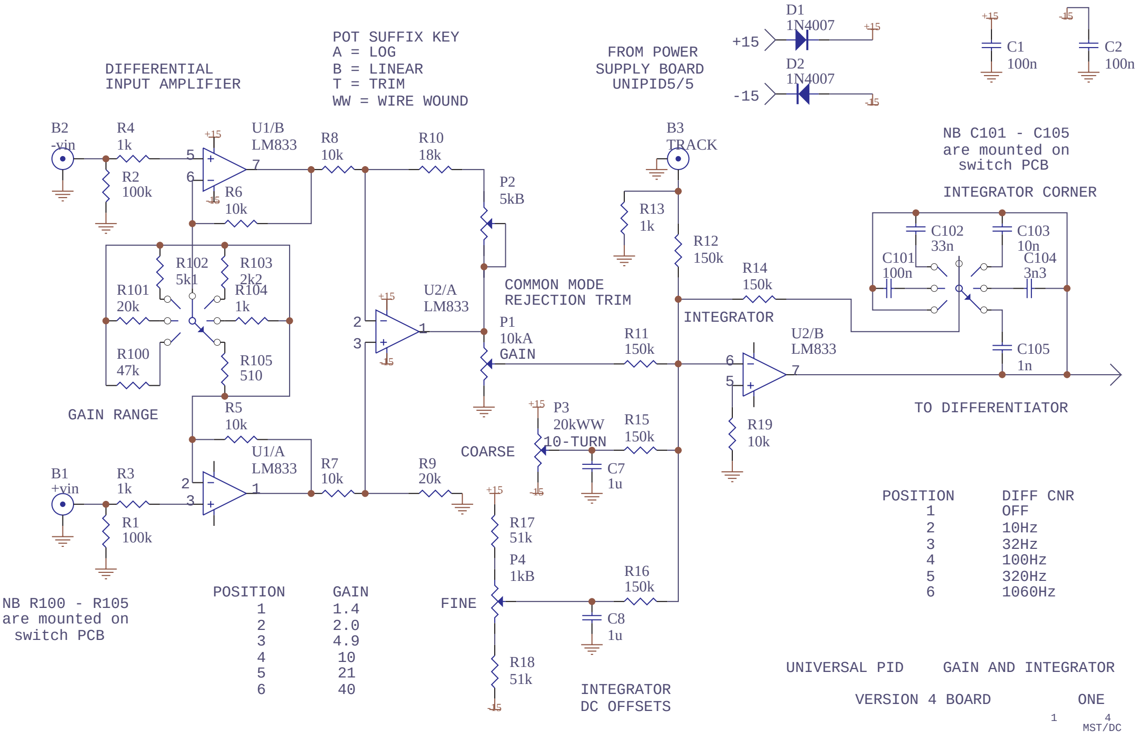

Figure C.1: Gain and integration stages of UniPID 5.0.

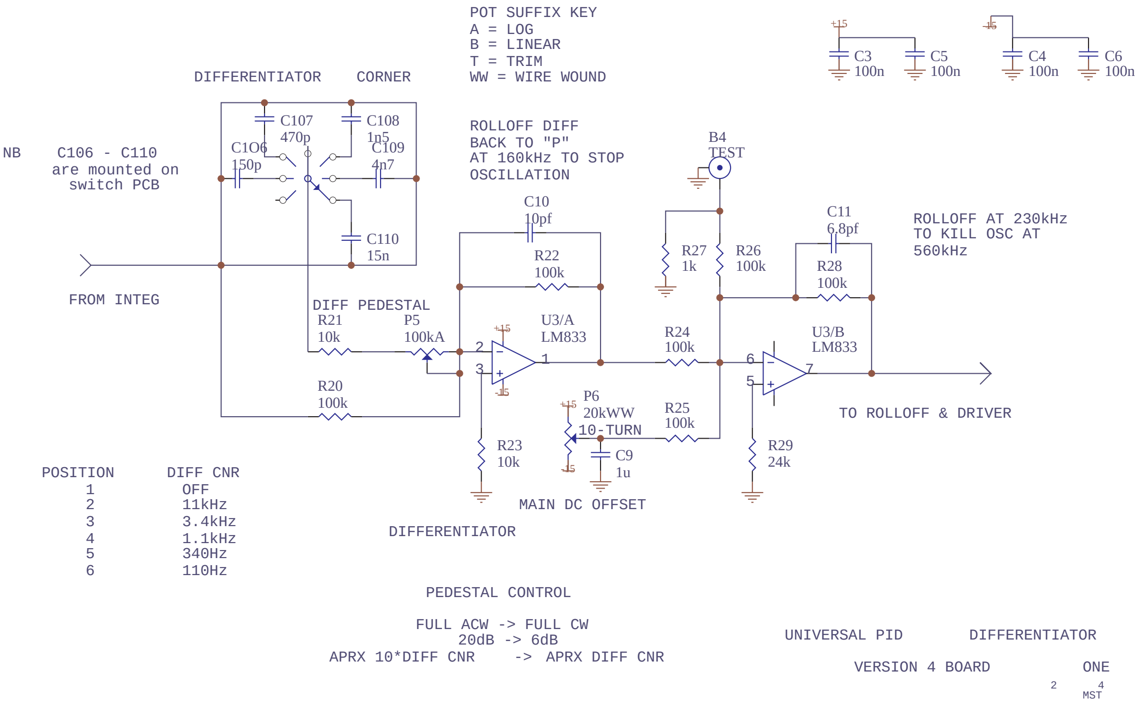

Figure C.2: Differentiator stage of UniPID 5.0.

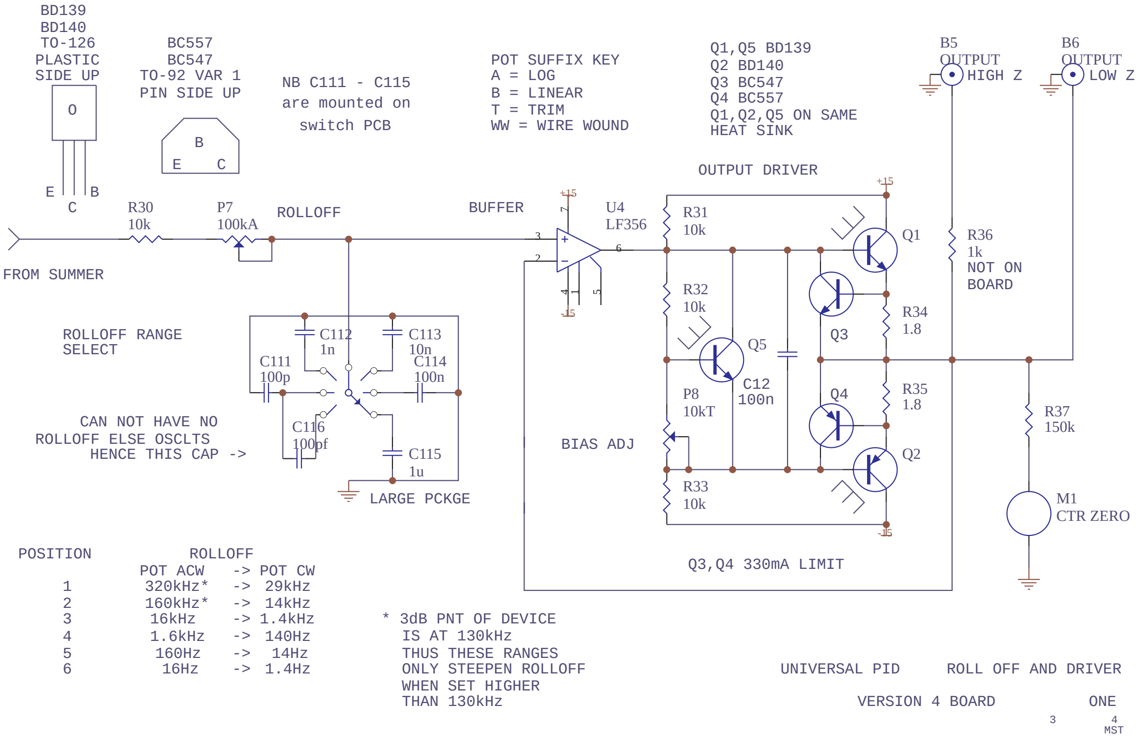

Figure C.3: Driver and roll-off stage of UniPID 5.0.

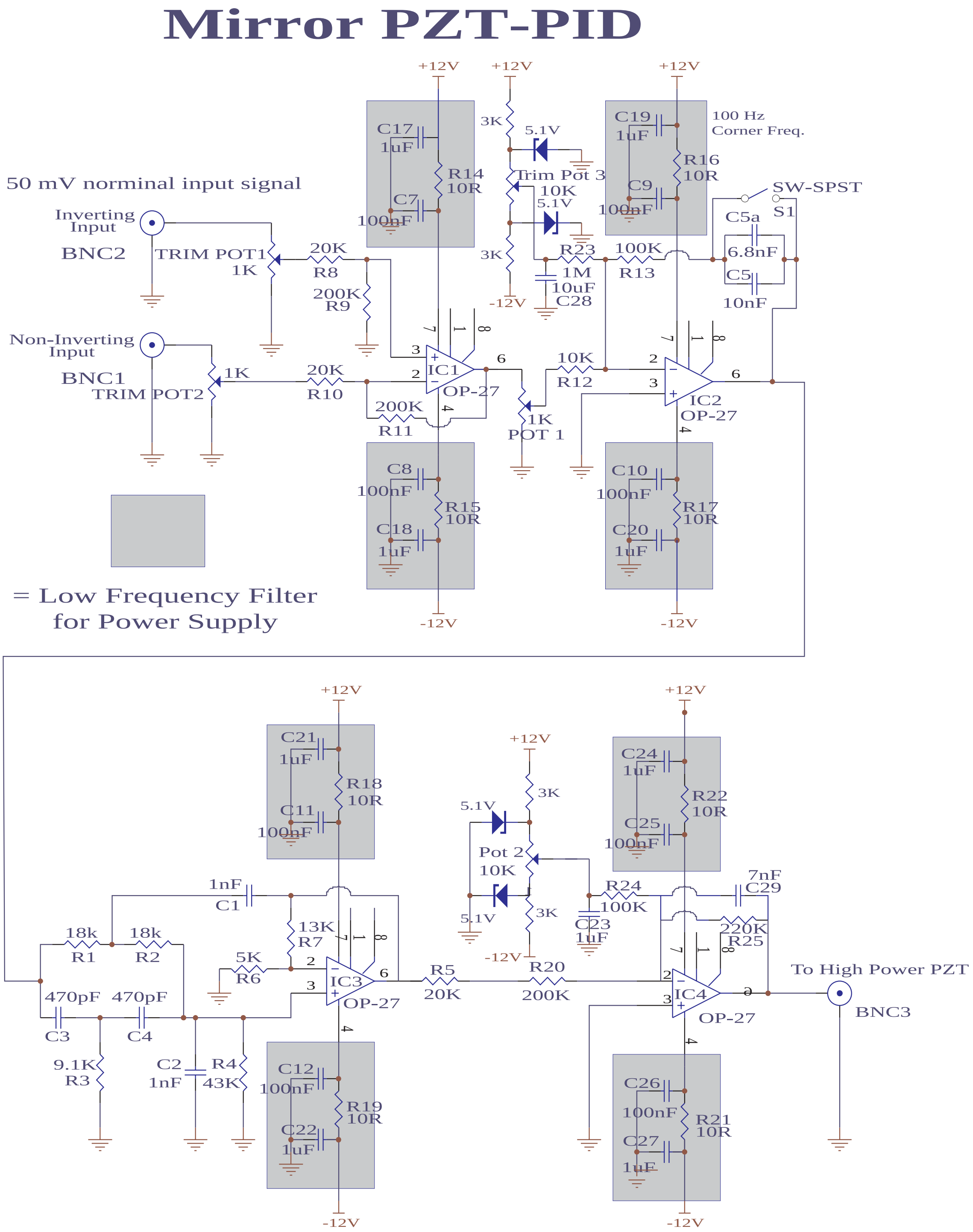

Figure C.4: Circuit diagram of piezo-electric actuator M1 PID.

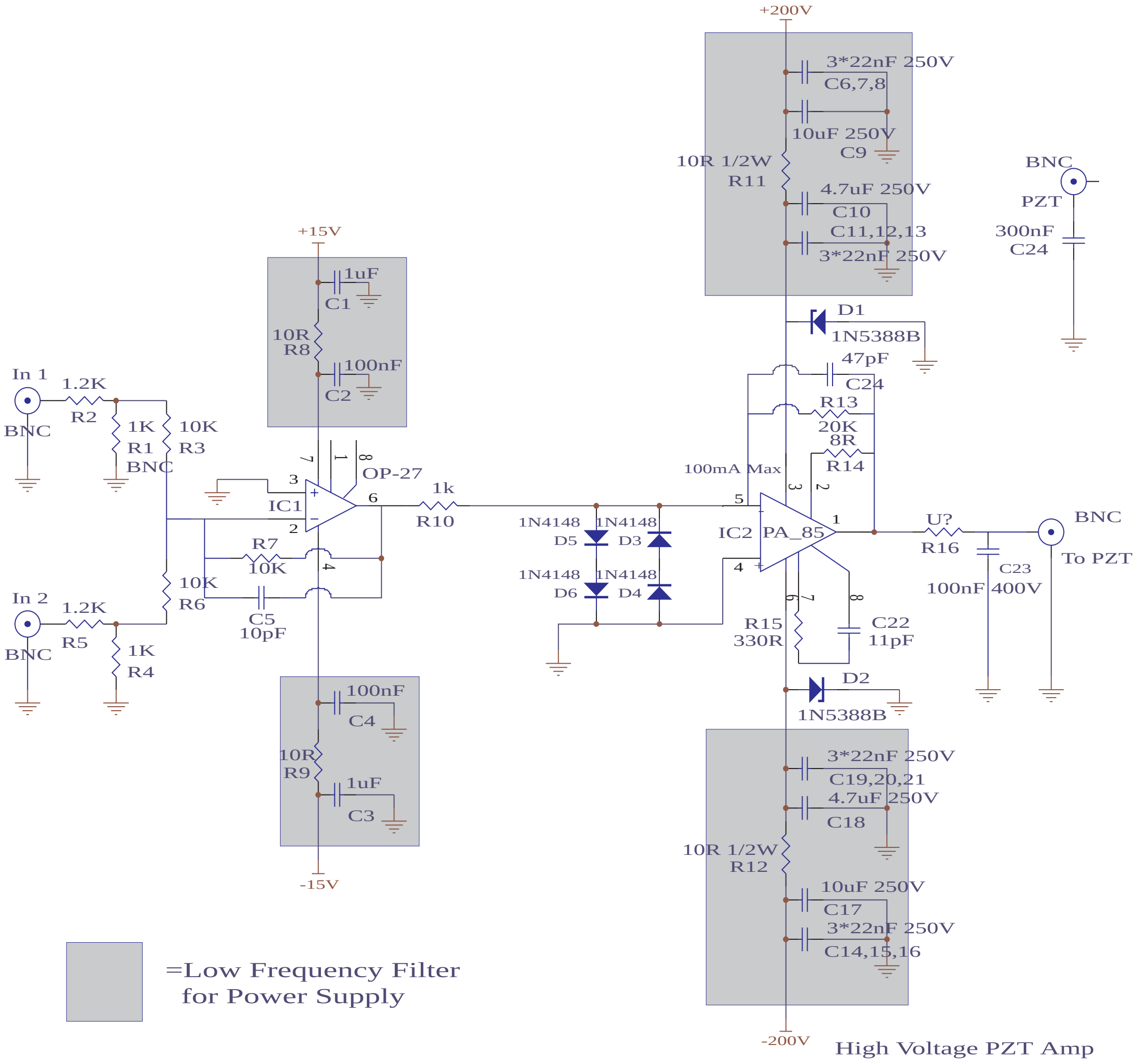

Figure C.5: Circuit diagram of high voltage M1 amplifier.

Appendix D

Temperature Controller Circuit Diagrams

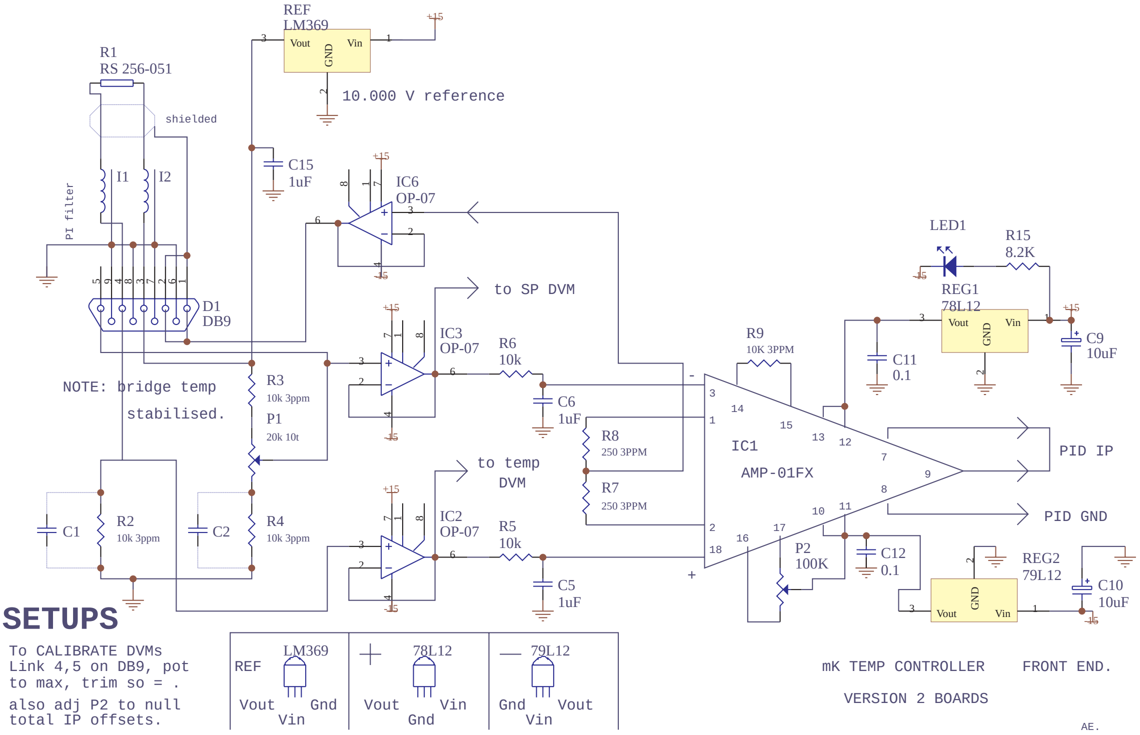

Figure D.1: Front end interface of milli-Kelvin temperature controller.

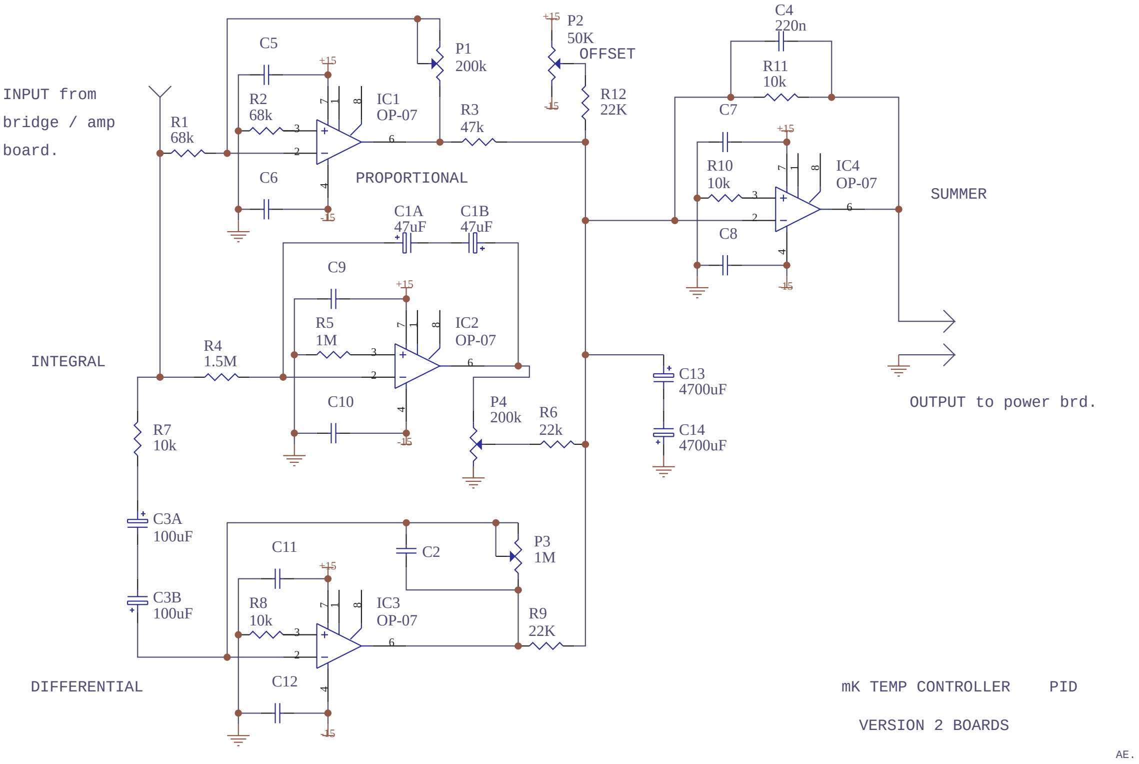

Figure D.2: PID circuit of milli-Kelvin temperature controller.

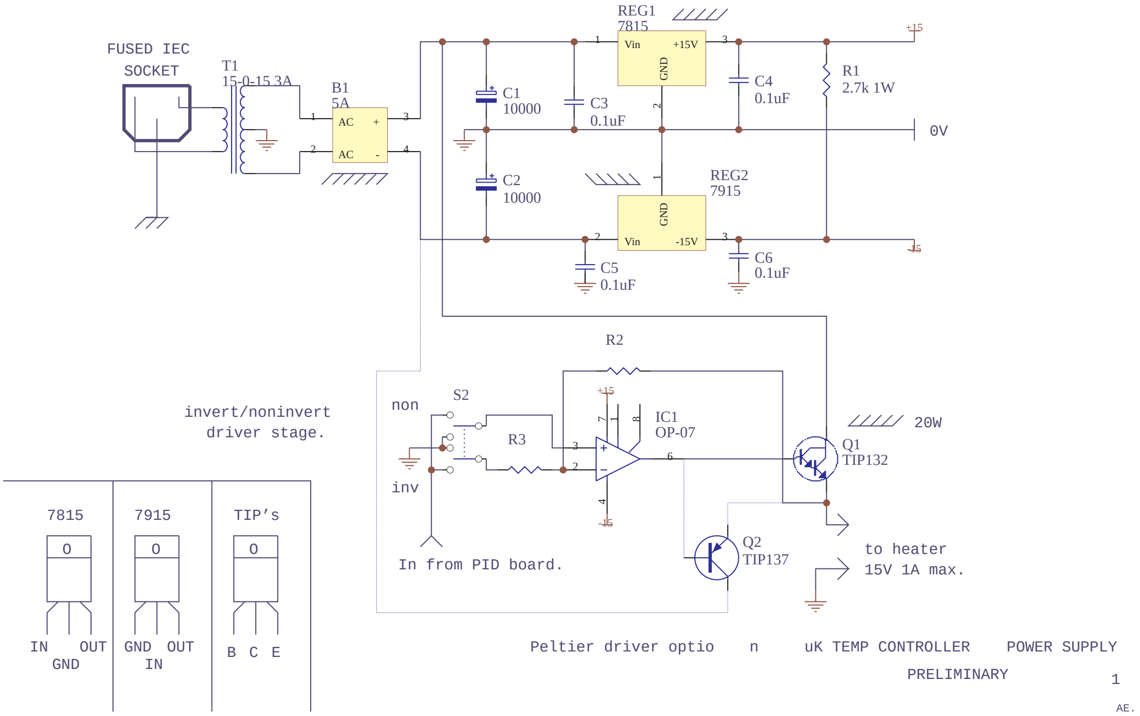

Figure D.3: Power supply of milli-Kelvin temperature controller.

Appendix E

Laser Controller Circuit Diagrams

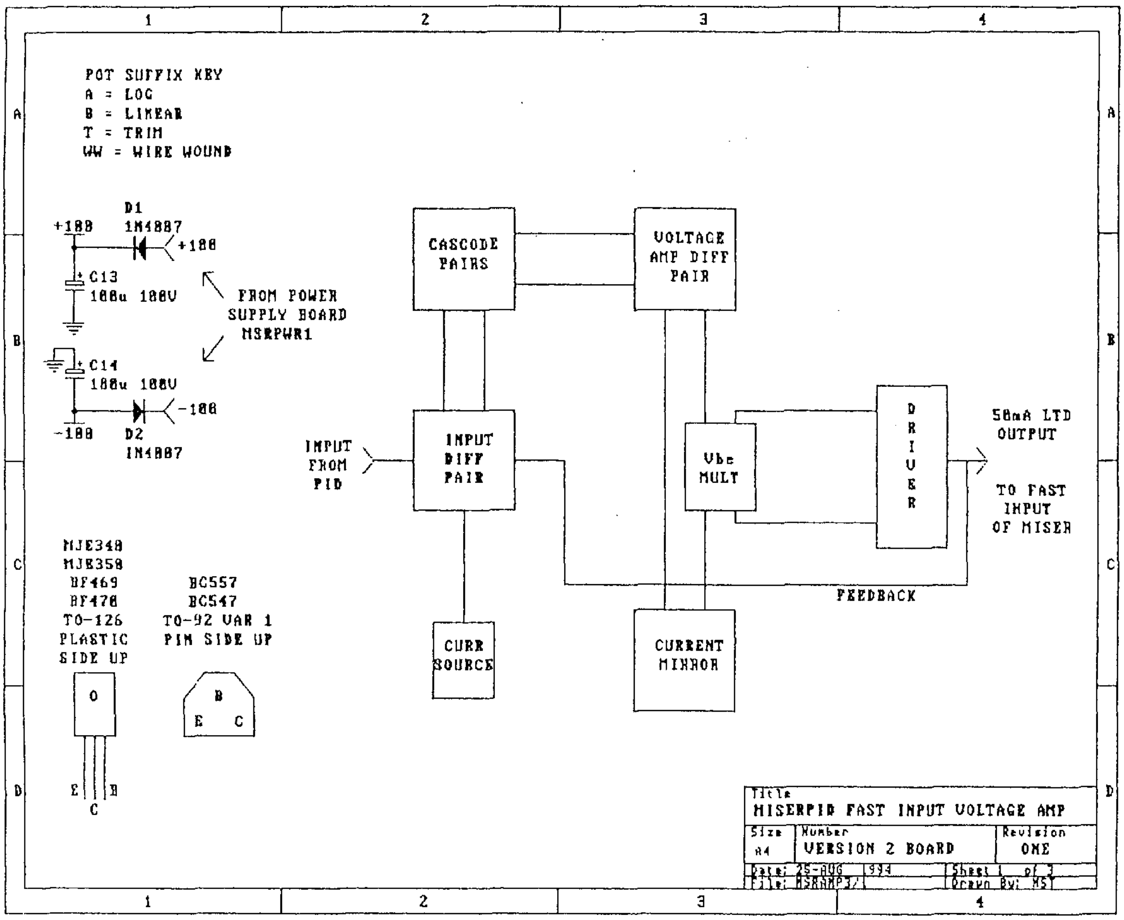

Figure E.1: Schematic of fast input (HV) amplifier of laser controller.

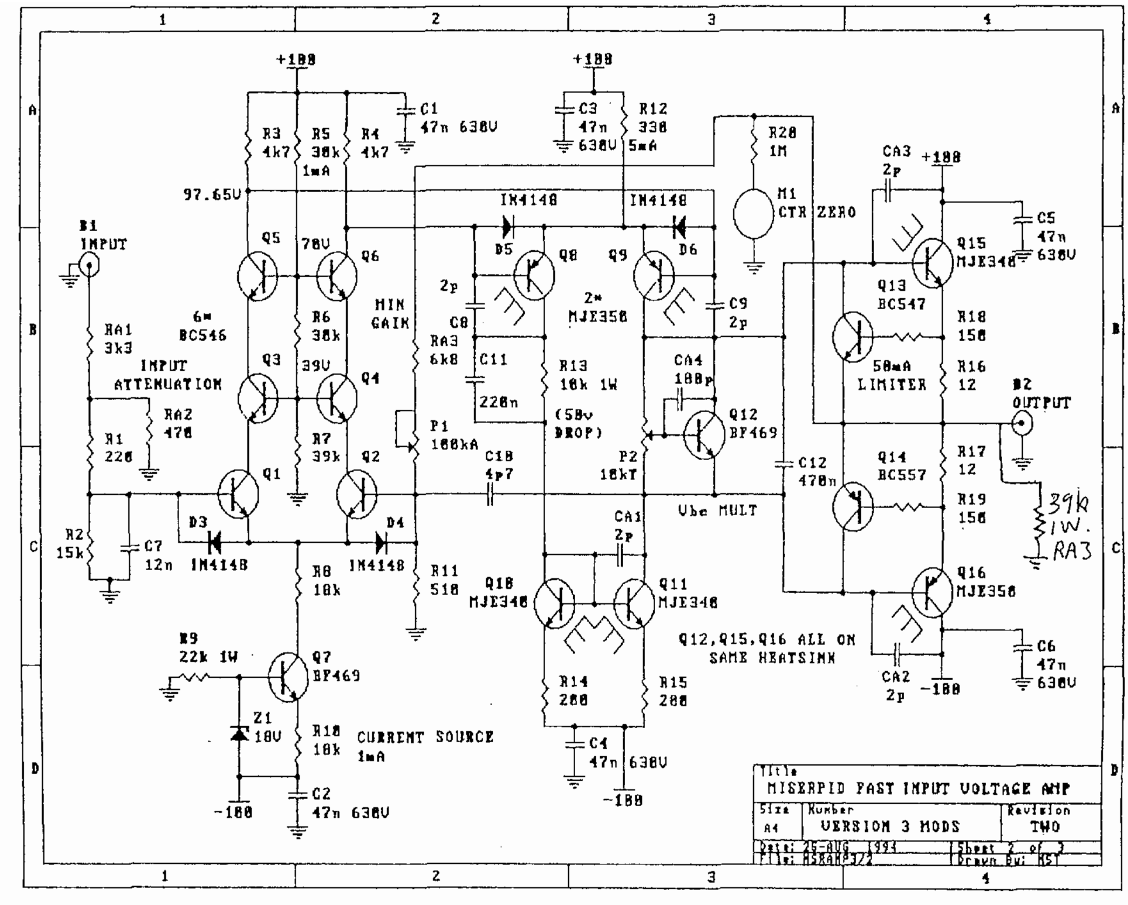

Figure E.2: Fast input (HV) amplifier of laser controller.

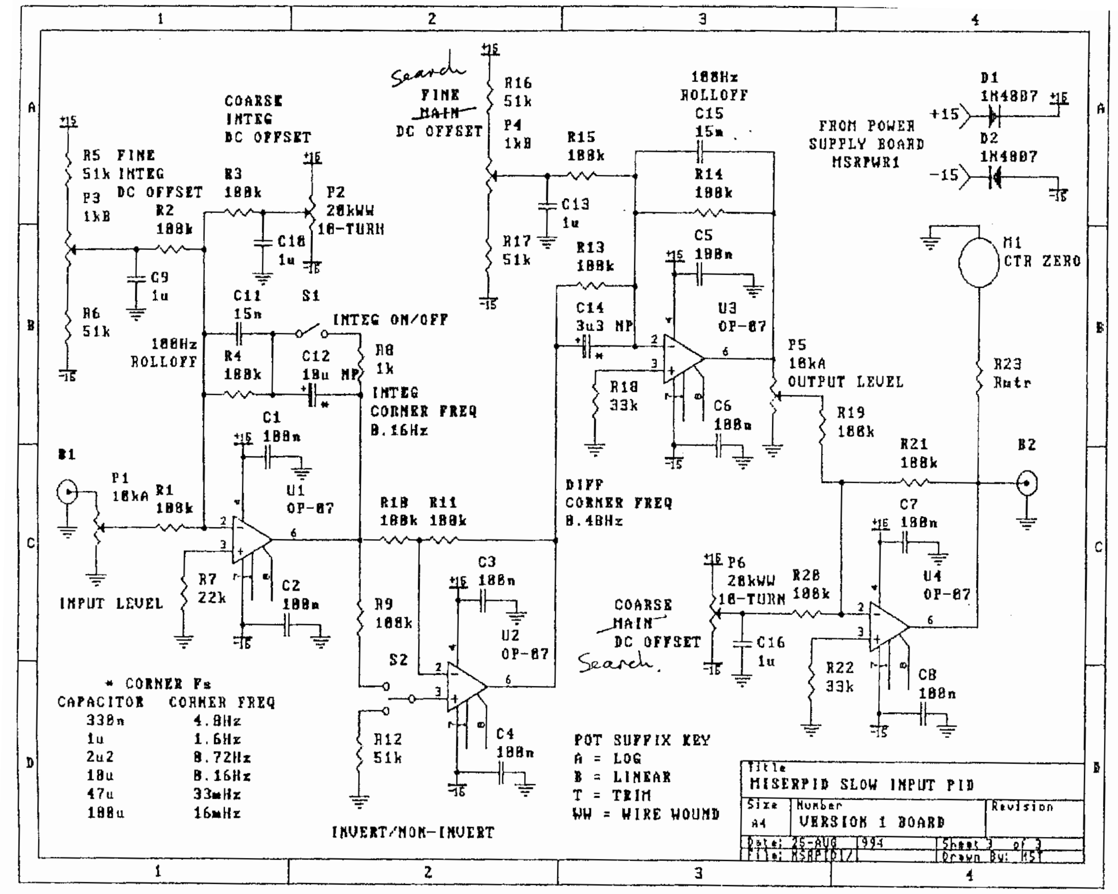

Figure E.3: Slow input of laser controller.

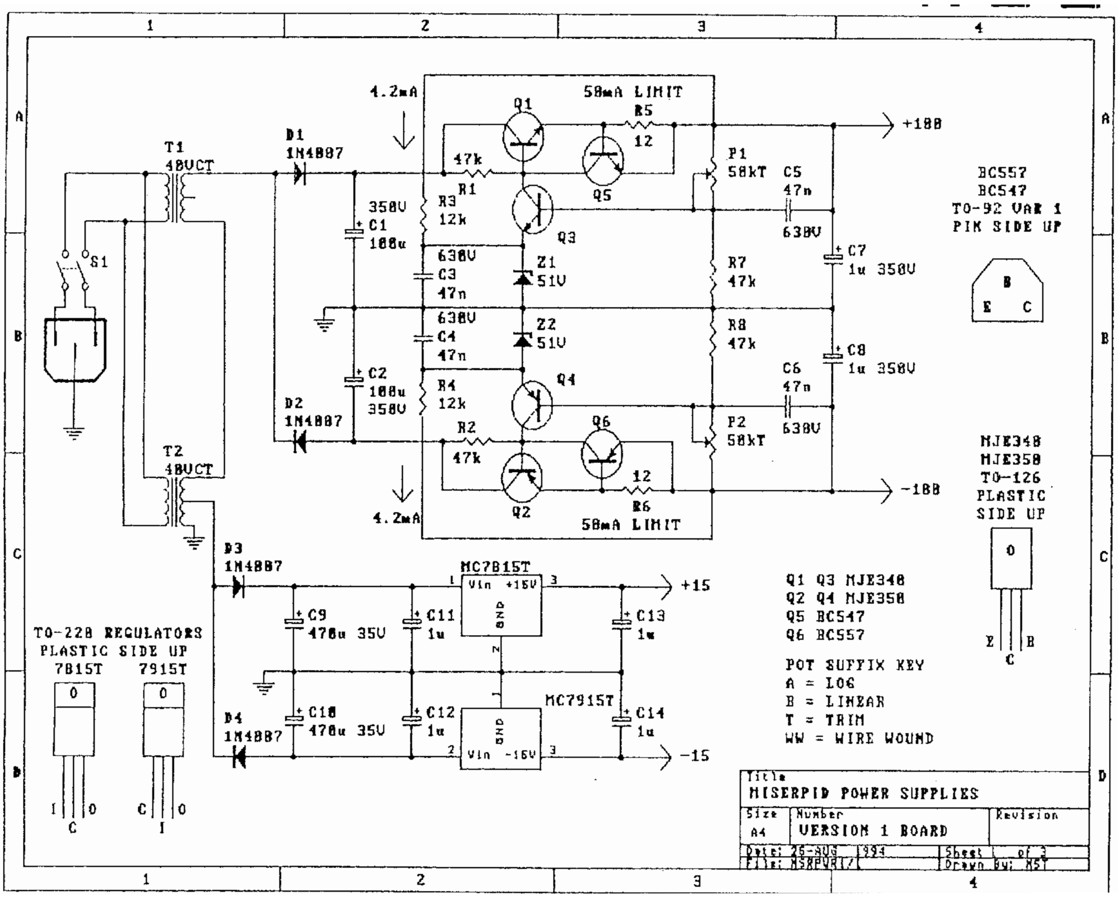

Figure E.4: Laser controller power supply.

Appendix F

Q-Switched Second Harmonic Generation

This appendix discusses the generation of optical second harmonic with a Q-switched diode pumped Nd:YAG laser. Reliable single-pass second harmonic generation of more than 400 mW of 532 nm average power is reported. The maximum conversion efficiency of the setup is 65% and the output mode of the second harmonic is single mode and has diffraction limited beam quality. Results presented here are from the following publication:

- *"High average power Q-switched second harmonic generation with diode pumped Nd:YAG Laser"*,
  P. K. Lam, I. Freitag, M. Bode, A. Tünnermann, and H. Welling, Electron. Lett. **34**, 666 (1998).

F.1 Introduction

Since its conception, the non-planar Nd:YAG ring laser [14] has been demonstrated to be an ideal pump source for efficient CW generation of single-frequency second harmonics [81, 155]. Owing to its unique geometry, single-frequency mode, unidirectional output, with excellent frequency stability is guaranteed, allowing problem free operation for second harmonic generation (SHG).

We demonstrate that a passively Q-switched non-planar ring Nd:YAG laser [4] is an ideal source for pulsed SHG. In particular, we have shown that similar to its CW counterpart, the pulsed second harmonic beam generated is also single-frequency mode and inherits the diffraction limited beam quality of the pump source. High conversion efficiency for average power of up to 400 mW can be achieved by simply single-passing the fundamental beam through a nonlinear medium. Neither the passive Q-switching nor the single-pass SHG require any control electronics, thus making the set up easy to assemble, economical and compact.

F.2 Q-switched NPRO

The Q-switched laser crystal assembly used for pulsed SHG is shown in Figure F.1. It consists of a piece of $\mathrm{Cr}^{4+}:\mathrm{YAG}$ sandwiched between two pieces of Nd:YAG crystal. The first piece of Nd:YAG crystal has a dimension of 3 mm x 8 mm x 6 mm and functions as the active medium which provides large atomic inversions necessary for efficient Q-switching. As observed from previous work [156], 6mm length of active medium is used to ensure that all of the pump light from the diode lasers is absorbed before the reaching the saturable absorber. The front face of the crystal is coated for high transmittance at the 808 nm pump frequency and T = 36% for 1064 nm. The flat surfaces formed an unstable resonator cavity which relies entirely on thermal lensing for stability. The $\mathrm{Cr}^{4+}:\mathrm{YAG}$ crystal is a 1 mm thick 10 mm diameter disc. At low optical intensity, it has a starting transmission of T_{st} for 1064 nm, which is dependent on the Cr^{4+} doping concentration. This transmittance increases with increasing intensity, thus providing the saturable absorption necessary for Q-switched operation [157, 158]. The final piece of Nd:YAG crystal acts as a reflector which provides the non-planar geometry for inducing an optical diode effect when placed in a strong magnetic field [14]. All surfaces internal to the laser cavity are anti-reflection coated for 1064 nm.

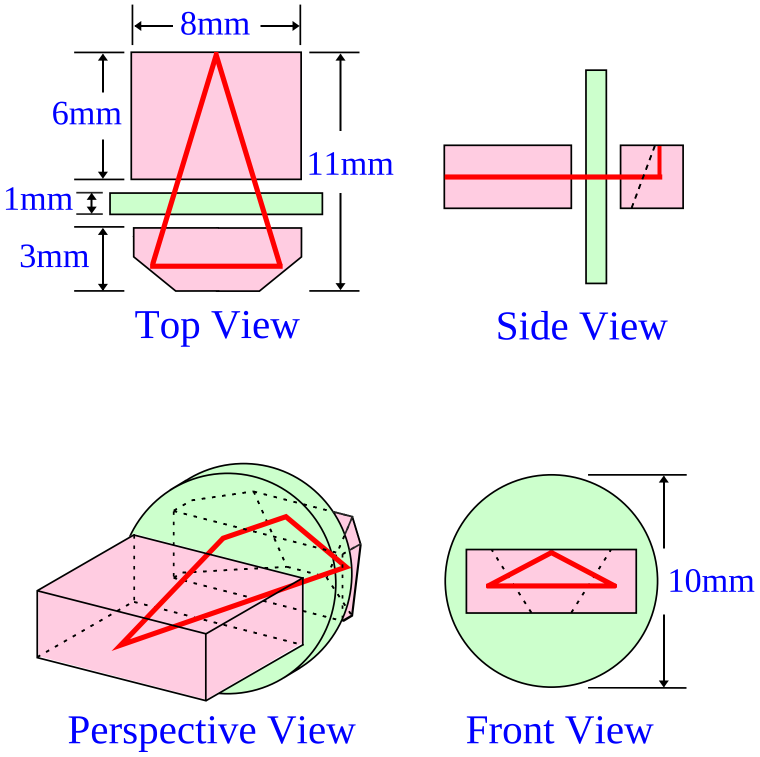

Figure F.1: Top and front views of the crystal assembly. The shaded areas are the $\mathrm{Cr}^{4+}:\mathrm{YAG}$ disc and the white areas are the Nd:YAG crystals. The lasing mode is shown in black lines.

For the purpose of optimizing for a high average output power, we set up the Q-switched laser as shown in Figure F.2. The crystal assembly is bi-directionally pumped by four diode laser arrays capable of delivering up to 6.5 W of 808 nm light. The pump beams are mode-selectively directed into the laser cavity to ensure single TEM_{00} mode operation. Two polarizing beam splitters are used to combine the p- and s- polarized light, from the transmitted and reflected diode laser beams, respectively. Owing of the Q-switched operation, some of the optical power is inevitably absorbed by the saturable absorber and can cause the crystal assembly to heat up. At high pump powers, we found this to have a detrimental effect on the stability of the laser operation. The laser can sometimes oscillate in both directions in the presence of excessive heating. However, this instability can be controlled by using a water-cooled crystal mount to drain away the heat absorbed thus re-activating efficient operation of the Peltier element which is in direct contact with the crystal assembly. Active stabilization of the crystal assembly temperature is then controlled via a temperature controller.

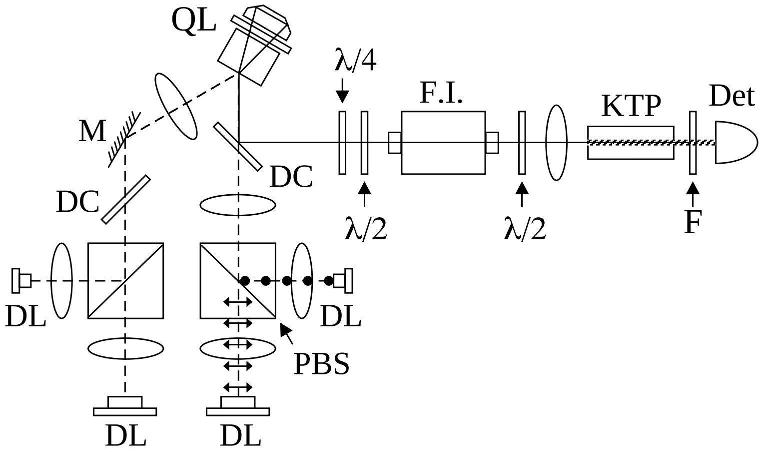

Figure F.2: Schematic of the Q-switched second harmonic generator. PBS: Polarizing beam splitter; DC: Dichroic beam splitter; DL: Diode laser array; QL:Q-switched laser; M: Mirror; $\lambda/2, \lambda/4$: Half and quarter wave plates, respectively; FI: Faraday isolator and F: IR Filter.

As shown in Figure F.2, two dichroic plates are placed in front of the crystal assembly to safeguard against reflection of any pulsed light on the pump diode arrays. One of these dichroics is also used to output the fundamental radiation. Because of the high peak power achievable during Q-switching, efficient SHG can be achieved without the need of a resonator cavity for the nonlinear medium. To demonstrate the simplicity of SHG with the Q-switched source, we single-pass the output beam through a 15mm long room temperature type II phase matched KTP crystal, which is anti-reflection coated for both the fundamental and second harmonic frequencies. Due to the lower damage threshold for the second harmonic light in the KTP crystal, a long crystal in combination with a long focal length lens is more desirable. This is to ensure that the high peak power of the Q-switched laser is not over-focused beyond the damage threshold. Once this precaution is taken, high conversion to the second harmonic is readily observed and can be optimized by translating the mode-matching lens.

F.3 Results

Figure F.3 shows both the fundamental peak power (and pulse width) of the laser as a function of average output power for the $\mathrm{Cr}^{4+}:\mathrm{YAG}$ disc with $T_{\mathrm{st}} = 71\%$. We found that by reducing the starting transmittance of the $\mathrm{Cr}^{4+}:\mathrm{YAG}$ to $T_{\mathrm{st}} < 61\%$, peak powers of more than 30 kW (≈2.3 ns) are achievable. However, this is attained at the expense of lowering the average power to less than 300 mW. On the other hand, an average power of as much as 1W is attainable by increasing the starting transmittance to $T_{\mathrm{st}} > 83\%$. This, however, reduces the peak power of the system to less than 4 kW (≈5 ns), making the SHG less efficient. Hence, a compromise is necessary to ensure that sufficient peak

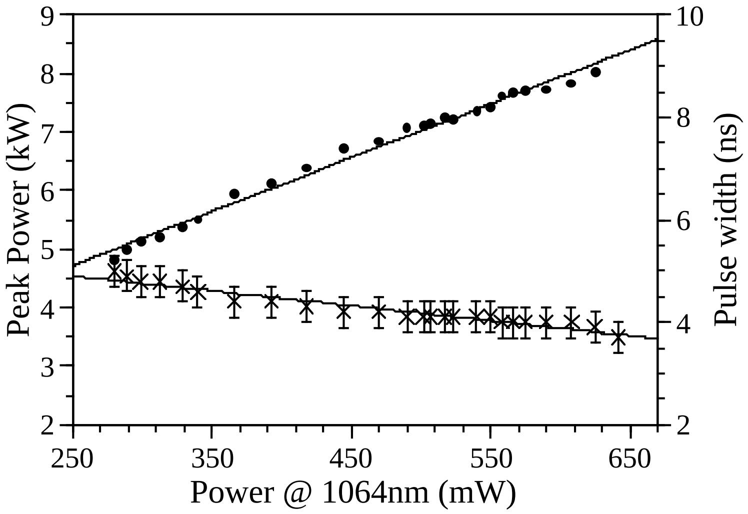

Figure F.3: Q-switched output pulse frequency (dots) and pulse width (crosses) vs average fundamental power.

power is attained for the SHG without significantly reducing the average output power. With the present setup of $T_{\mathrm{st}} = 71\%$, the peak power of the Q-switched output can reach as much as 8 kW (≈3.7 ns) and the average power 670 mW.

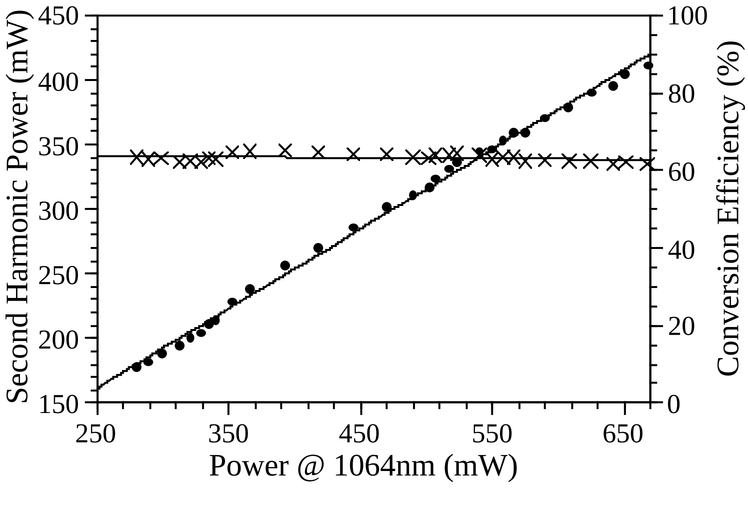

Figure F.4: Single pass conversion efficiency (dots) and average output power (crosses) of the second harmonic output vs fundamental power.

Figure F.4 shows both the second harmonic power and its conversion efficiency as a function of average fundamental power. For an average fundamental power of 670 mW, as much as 411 mW of 532 nm second harmonic is obtained. The highest single-pass conversion efficiency is 65.2% at a fundamental average power of around 370 mW. Similar to the fundamental output, the second harmonic beam is measured to be single-frequency mode and has a diffraction limited quality Gaussian profile. We note that the single-pass conversion efficiency is independent of the fundamental intensity to about $\pm 2\%$ making the second harmonic power to be almost linearly proportional to the fundamental power. This is attributed to the increasing thermal lensing effect experienced by the KTP crystal due to the traversal of high peak power beams.

F.4 Conclusions

We have reported a compact and efficient source of stable, single-frequency Q-switched 1064 nm ideal for pulsed SHG. A maximum single-pass conversion efficiency of 65% is achieved and average 532 nm power as high as 411 mW is obtained. Similar to the CW non-planar ring laser, the pulsed second harmonic generated by the Q-switched laser is highly single-frequency and inherits the Gaussian diffraction limited quality of the fundamental beam. Because both the passive Q-switching and the single pass SHG are completely devoid of any control electronics, this system is economical, compact and simple to assemble.

Appendix G

Optical Homodyne Tomography of Information Carrying Laser Beams

Overview

Optical homodyne tomography (OHT) is a tool that allows the reconstruction of Wigner functions for each detection frequency of a propagating optical beam. It can measure probability distribution functions (PDF's) of the field amplitude for any given quadrature of interest. In this appendix, we demonstrate OHT for a range of classical optical states with constant and time varying modulations and show the advantage of OHT over conventional homodyne detection. The OHT simultaneously determines the signal to noise ratio in both amplitude and phase quadratures. We show that highly non-Gaussian Wigner functions can be obtained from incoherent superpositions of optical states.

G.1 Introduction

Optical homodyne tomography (OHT) allows the reconstruction of the Wigner function $W(x_1, x_2)$ [159] representation of an optical state. The theoretical foundation of quantum state reconstruction was outlined by Vogel and Risken [160] and has inspired a series of experiments, initially with optical pulses [161, 162] and more recently with CW light [83, 163, 164].

In practical applications, such as sensing or communication, a laser beam is modulated in order to carry information. This can occur at different modulation frequencies or channels Ω_m. Each modulation frequency has its own Wigner function $W_{\Omega m}(x_1, x_2)$, and can vary dramatically from channel to channel [165]. Hence, a realistic laser beam with signal modulations is a propagating multi-mode quantum state, which is quite different to the single mode intra-cavity description of an optical state. Such a realistic light beam can only be described by a spectrum of Wigner functions W_Ω, one for each frequency Ω.

In the early experiments [161] of pulsed laser OHT, only one single Wigner function was reconstructed. This Wigner function contains all statistical moments of the photon number in the pulses and individual Fourier components of a pulse could not be separated. In more recent experiments with CW lasers, Wigner functions $W_{\Omega d}$ for squeezed and classical states were reported for specific detection frequencies Ω_d. In the case of squeezed light, Wigner functions with elliptical two-dimensional Gaussian quasi-probability distributions were demonstrated [83, 163, 164].

In this appendix, we use the Wigner function representation to describe coherent states with different forms of classical sinusoidal phase modulation (PM). At the modulation frequency we observe that the Wigner functions are displaced away from the origin of the phase space and the results allow us to directly determine the signal to noise ratio (SNR) for both amplitude and phase signals. At all other frequencies, the Wigner functions are always centred at the origin. We demonstrate how the Wigner functions are controlled by the quadrature and depth of modulation.

One of the advantages of OHT over conventional homodyne measurements [166, 167] is that OHT can show any non-Gaussian features in the Wigner functions of more complex optical states. Such features are contained in the higher order moments of the noise statistics with the result that a simple measurement of the noise variance (2nd order moment) alone is an insufficient description. The additional complexity means Wigner function reconstruction demands more sophisticated statistical analysis. Unfortunately, unlike experiments in atom optics [168], complex optical states are extremely difficult to generate [47]. They require highly nonlinear processes which have fluctuations comparable to the average steady state amplitude. To date only a few proposals for the generation of such non-classical states exist [169]. We test the ability of OHT to reconstruct highly non-Gaussian Wigner functions by using laser beams with time varying modulation to produce classical superpositions of optical states. We discuss the accuracy of the OHT technique and some of the practical limitations.

This work demonstrates the capability of OHT for the diagnosis of realistic laser beams and establishes techniques that will be important once highly non-Gaussian, eg. “Schrödinger’s cat”, states can be experimentally realised.

G.2 Standard homodyne detection

The conventional approach for the measurement of a laser beam is the balanced homodyne detection. The light generated by a CW laser with an optical frequency ν is processed by an interferometric arrangement (Black components in Figure G.1). The majority of the optical power (P_{LO}) is split off by mirror M1 as the optical local oscillator beam and sent via mirror M3 to the combining beamsplitter M4. A small part of the optical power (P_{test}) reaches M4 via the mirror M2 as the test beam. The relative phase between the beams is controlled by moving M3 with a piezo position controller (PZT). The two optical outputs are converted into photocurrents $i_1(t)$ and $i_2(t)$ using matched, high efficiency detectors PD1 and PD2, respectively. The difference $i_-(t) = i_1(t) - i_2(t)$ between the currents is analysed. The fluctuations of the test beam can be described with the generalised quadratures $\hat{x}(\theta) = (\hat{a}e^{-i\theta} + \hat{a}^\dagger e^{i\theta})/2$. Here $\hat{x}_1 = \hat{x}(0)$ is the amplitude quadrature, $\hat{x}_2 = \hat{x}(\pi/2)$ is the phase quadrature. Under the condition of $P_{LO} \gg P_{test}$ this device will provide a photocurrent i_- which contains information about the fluctuations of the test beam alone, and is immune to the fluctuations , or noise, of the local oscillator beam.

The variance $V_{\Omega d}(\theta)$ describes the properties of the test beam at one detection frequency Ω_d and is normalised to the standard quantum limit so that for a coherent state, $V_\Omega(\theta) = 1$. The difference photocurrent $i_-(t)$ is analysed using an RF spectrum analyser. The electric noise power $P_{i\Omega d}$ is proportional to the optical power of the local oscillator P_{LO} and the variance $V_{\Omega d}(\theta)$

$$P_{i-}(\Omega d, \theta) \propto P_{LO} V_{\Omega d}(\theta) \tag{G.1}$$

Due to the strong attenuation in the neutral density filter ND (transmission $\sim 1\%$), the

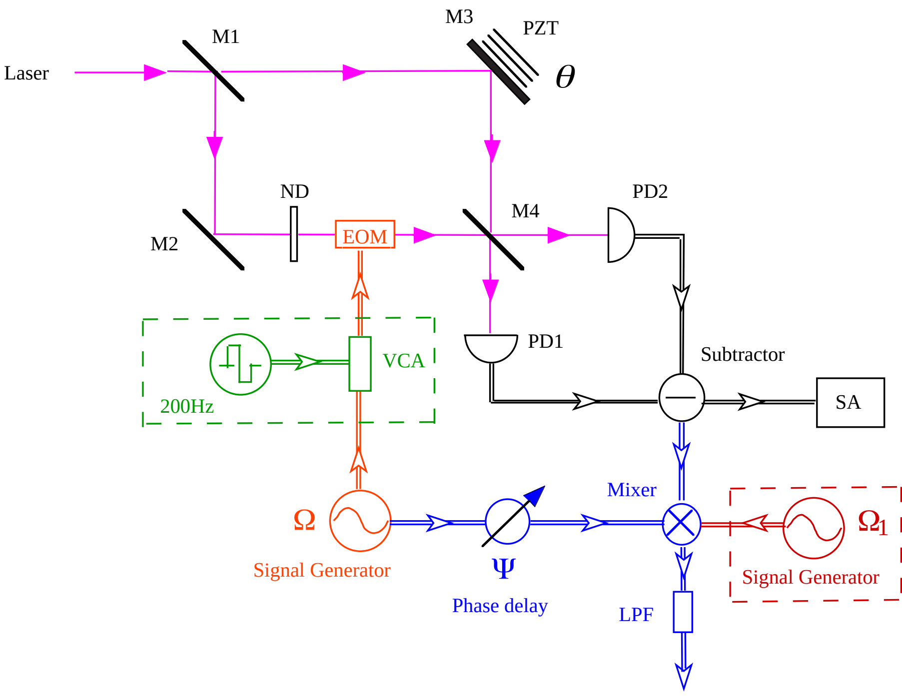

Figure G.1: Experimental setup of OHT. EOM: Electro-optic modulator; ND: neutral-density filter; PZT: Piezo; PD: photodetector; LPF: low-pass filter; VCA: Voltage controlled attenuator; SA: Spectrum Analyser.

test beam does not contain the actual noise spectrum of the laser but rather fluctuations introduced by the vacuum. If the output of the laser was squeezed, ($V_{\Omega d} < 1$) or slightly noisy ($V_{\Omega d} > 1$) the test beam would still have a noise spectrum close to the quantum noise limit of $V_{\Omega d} = 1$. This device is not particularly sensitive to laser noise. However, any modulation or squeezing generated inside the interferometer is clearly detectable. For example, a phase modulation introduced by driving the electro-optical modulator (EOM) within the interferometer at frequency Ω_m would increase $V_{\Omega m}(\theta = \pi/2)$.

G.3 Modulation

The output of the modulator is given by $E_{\text{out}} = E_0 \cos[2\pi\nu t + \delta \sin(\Omega_m t)]$ and the phase modulation generates sideband pairs at $\nu_L \pm n\Omega_m$. For $\delta \ll 1$, only the first order sidebands ($n = 1$) are important. The linearized annihilation operator for the quantum mode after the modulator is given by

$$\begin{aligned} \hat{a}(t) &= [E_0 + \delta\hat{a}(t)](1 + \beta e^{-i\Omega_m t} - \beta e^{i\Omega_m t}) \\ &\approx E_0 - 2i\beta E_0 \sin(\Omega_m t) + \delta\hat{a}(t), \end{aligned} \tag{G.2}$$

where $\beta = J_1(\delta)$, the first order Bessel function, and the operators contain the quantum fluctuations. The output current from the homodyne detector for a projection angle θ is

$$i_-(\theta, t) \propto E_0 \cos(\theta) - 2\beta E_0 \sin(\Omega_m t) \sin(\theta) + \delta\hat{X}(\theta, t). \tag{G.3}$$

The factor of proportionality depends on the efficiencies of the detectors, losses and the electronic gain. $\delta\hat{X}(\theta,t)$ describes the quantum fluctuation in this particular quadrature. In conventional experiments, the analysis of a particular Fourier component of the photocurrent is done by an RF spectrum analyser with the phase θ of the local oscillator kept constant. The result is a spectrum as given in Eq. (G.1). As a consequence the phase variance $V_{\Omega m}(\theta=\pi/2)$ increases in proportion to the modulation depth while all other parts of the spectrum $V_\Omega(\theta=\pi/2)$ with $\Omega\neq\Omega_m$ remain unchanged.

G.4 Optical homodyne tomography

In order to obtain the Wigner function of a light beam, only small modifications to the balanced homodyne apparatus are required [163]. Phase synchronous detection is introduced by replacing the spectrum analyser with a mixer demodulator (Blue components in Figure G.1). The mixer is gated by an electronic local oscillator signal derived from the same generator that drives the EOM. This electronic signal is shifted by a phase ψ giving a mixed down difference current $i_{\Omega m}(\theta,\psi;t)$. Starting with Eq. (G.2) and using Fourier transforms we can derive the output current from the mixer as :

$$i_{\Omega m}(\theta,\psi;t)=-\beta E_0\cos(\psi)\sin(\theta)-\cos(\psi)\delta X_{ci}(\theta,\Omega_m;t)+\sin(\psi)\delta X_{cr}(\theta,\Omega_m;t) \qquad \text{(G.4)}$$

where $\delta X_c(\theta,\Omega_m;t)$ can be understood as the total quantum fluctuations centered around $\pm\Omega_m$. $\delta X_{ci}(\theta,\Omega_m;t)$ and $\delta X_{cr}(\theta,\Omega_m;t)$ are the imaginary and real parts of $\delta X_c(\theta,\Omega_m;t)$ respectively. For $\psi=0$, we obtain

$$i_{\Omega m}(\theta,0;t)=-\beta E_0\sin(\theta)-\delta X_{ci}(\theta,\Omega_m;t). \qquad \text{(G.5)}$$

The first term contains all the modulation and the second term all the quantum fluctuations. Note that for synchronous detection, the phase of the modulation has to be known to the observers. In practice, this is not always possible.

If the modulation phase ψ is unavailable to the detection system, as would be the case for the monitoring of remotely generated signals, then either a phase recovery technique or asynchronous demodulation is required. Asynchronous demodulation can be simulated by equation (4) where the demodulation phase ψ is a linear function of time. This corresponds to an uncorrelated demodulation generator operating at Ω_1 in Figure G.1.

A typical synchronously demodulated photocurrent plot is shown in Figure G.2, where the phase angle θ is repetitively scanned. By selecting data that correspond to the same value inside the vertical intervals $\delta\theta$, we obtain measurements of, $w_{\Omega d}(\theta,t)$, for any given quadrature interval $(\theta,\theta+\delta\theta)$. Next a histogram of this current is formed by binning the data in intervals $\delta\theta$ for a coherent state. This results in the PDF $w_{\Omega d}(x,\theta)$ of the quadrature amplitude for various projection angle θ. Figure G.3 shows a series of such PDF's for a full scan of θ.

The width of a PDF corresponds to the variance $V(\theta)$ of the given quadrature. For any realistic, and thus linearizable state with photon number $N\gg 1$, the shape of the PDF is a Gaussian. For a coherent state the width of the Gaussian is equal to the photon number, thus identical to a Poissonian distribution. Squeezed states have sub-Poissonian PDF's at one particular angle θ_s, the squeezing quadrature.

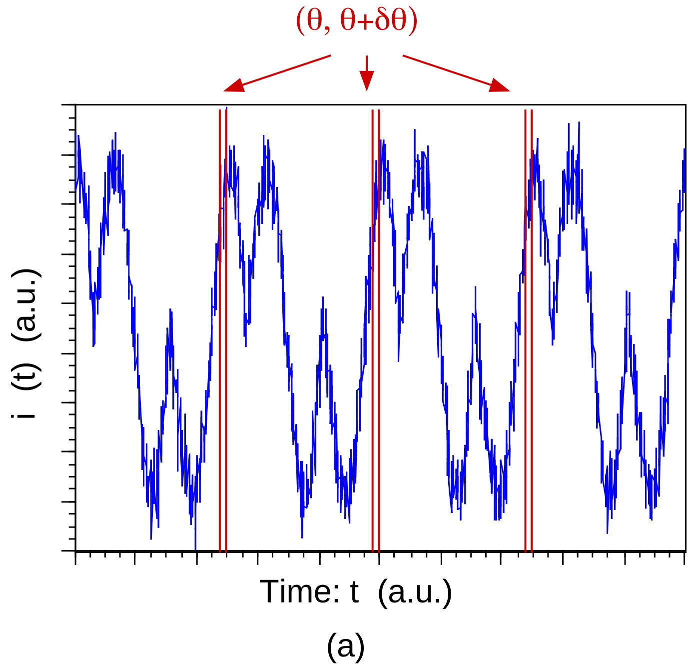

Figure G.2: The data processing of a typical OHT experiment. (a) One segment of the measured time trace of quadrature amplitude value by scanning the PZT

G.5 Wigner function reconstruction

Wigner functions can be reconstructed from the PDF's using the inverse Radon transform [160, 170].

$$W_{\Omega d}(x_1, x_2) = \frac{1}{4\pi^2}\int_{-\infty}^{+\infty}\int_{-\infty}^{+\infty}\int_{0}^{\pi} w_{\Omega d}(x,\theta) exp[i\eta(x - x_1\cos\theta - x_2\sin\theta)]|\eta| dx d\eta d\theta \quad \text{(G.6)}$$

The resulting Wigner function $W_{\Omega d}(x_1, x_2)$ is shown in Figure G.4. For a coherent state the function is symmetric - with concentric contour lines. For a squeezed state the function is asymmetric, with elliptical contour lines. For all coherent or squeezed states, without modulation ($\beta = 0$), the Wigner function is centered at the origin. This can be seen from equation Eq. (G.5) where only the second term contributes in this case. The orientation of the ellipse gives the squeezing quadrature. Since the Wigner function is normalized to the standard quantum limit, its position and size is independent of the optical power. Thus, a squeezed vacuum state has the same Wigner function as a bright squeezed state, provided that $P_{LO} \gg P_{test}$. Note that the Wigner function should not be confused with the widely used picture of a "ball on a stick" which tries to describe several properties of an optical state simultaneously. The "stick" indicates the average, DC optical power while the "ball" represents high frequency, AC fluctuations. The Wigner function which can be measured at a particular frequency depends only on the noise and signals at that frequency. Hence, Wigner functions can only be displaced from the origin by introducing a modulation.

The distance of the centre of the Wigner function from the origin is a direct measurement of the modulation depth. Amplitude modulation causes displacement along the

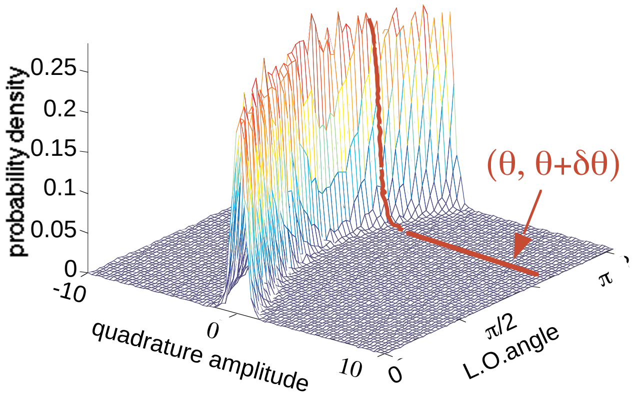

(b)

Figure G.3: The data processing of a typical OHT experiment. (b)The PDF after binning the time trace.

x_1 axis whilst PM along the x_2 axis. The Wigner function gives us immediately information about the signal quadrature, strength and noise. It provides the conventional signal to noise ratio, where both signal and noise are measured in the same quadrature, as well as the relative size of the noise in the orthogonal quadrature. The later is of interest in applications where some degree of crosstalk between the quadratures is unavoidable. Amongst others, this includes any application of resonantly locked cavities where a small imperfection of the locking can introduce cavity detunings and thus a mixing of the quadratures.

G.6 Experimental results

G.6.1 Varying the depth of phase modulation

The process of reconstructing Wigner functions and the effect of modulation depth is clearly demonstrated in Figure G.5. Here we use phase modulation and synchronous detection for four different modulation depths. For $\beta = 0$ (no modulation, i.e. a coherent state) the Wigner function is circular and centred at the origin. As the frequency modulation depth is increased, the Wigner function is displaced along the "x_2" (phase variance) axis. For large modulation, it is apparent that the phase modulation process has introduced significant amplitude modulation, resulting in the Wigner function being displaced vertically from the x_1 axis (amplitude variance). This is due to the imperfection of the phase modulator.

It is important to note that synchronous demodulation requires the optimization of the demodulation phase ψ. This ensures that the modulation component is detected with maximum efficiency and results in the optimum SNR being recorded on the Wigner function.

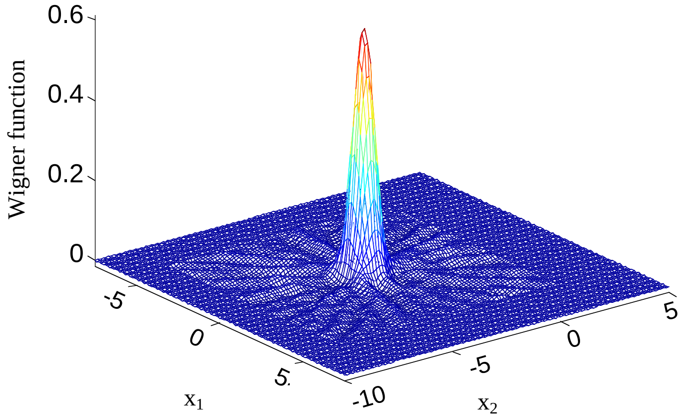

(c)

Figure G.4: The data processing of a typical OHT experiment. (c) The reconstructed Wigner function.

G.6.2 Switched phase modulation

In order to demonstrate the ability of our OHT system to record the details of a highly non-Gaussian distribution, we added a low frequency modulation to gate the PM on and off. By selecting this gating frequency at 200 Hz, within the detection bandwidth (100 kHz) we can then record the resulting distribution. The resulting Wigner function is plotted in Figure G.6. As can be seen, the gating process (square wave signal generator in Figure G.1) produces a Wigner function with 2 peaks: one peak corresponds to zero modulation and is located at the origin, whilst the other corresponds to phase modulation.

G.6.3 Asynchronous detection (variable phase ψ).

Finally we demonstrate the results of asynchronous detection. This is achieved experimentally by using a separate Ω_1 as the demodulation signal, which is different from the modulation frequency Ω_m used to drive the EOM. It is necessary to ensure that Ω_m and Ω_1 differ in frequency by an amount small compared with the detection bandwidth. Under these conditions the detected Wigner function then represents the weighted average of all possible demodulation phase values ψ. The resulting Wigner function, for phase modulation, is shown in Figure G.7. The distribution is now centred on the origin and spread symmetrically along the phase quadrature axis. The peaks at the extreme of the modulation correspond to the turning points where the dwell time of the modulation, as a function of phase, is greatest.

G.7 Discussion and summary

In conclusion, we have demonstrated that the reconstruction of Wigner functions provides clear information about the modulation and information carried by a laser beam at

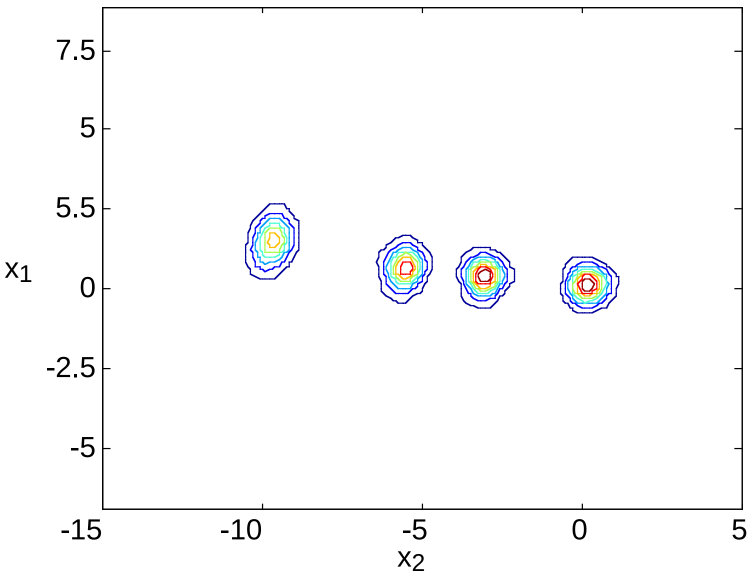

Figure G.5: Wigner functions of states with phase modulation of different depths. Four Wigner function contours are shown.

a given detection frequency. For the coherent and the squeezed states with modulations, the Wigner functions contain the same information as could be obtained with homodyne detection but they are easier to interpret. In particular, the displacement of a Wigner function $W_{\Omega d}$ provides information on the quadrature and strength of the modulation and the width of $W_{\Omega d}$ describes the noise. The signal to noise ratio at any given quadrature can be read directly.

In general, most optical states which can be generated can be described by a linearized theory and thus has a two dimensional Gaussian $W_{\Omega d}(x_1, x_2)$. In order to demonstrate the ability of measuring highly non-Gaussian Wigner functions, an asynchronous demodulation scheme is used.

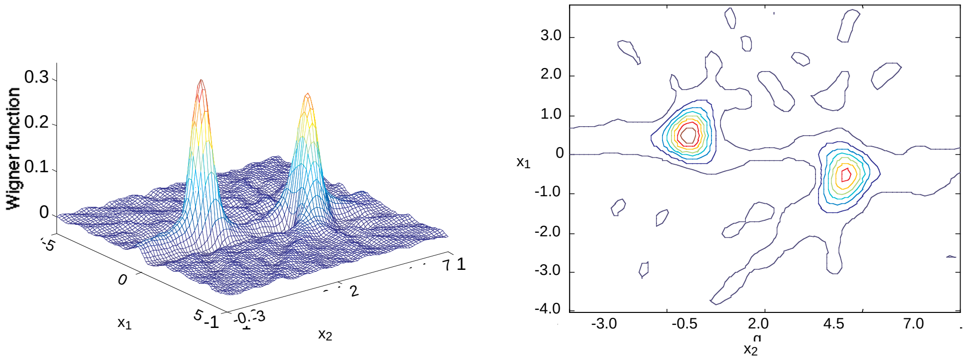

(a) (b)

Figure G.6: The reconstructed Wigner function and contour plot of a classical mixture state. (a) Wigner function; (b) contour plot.

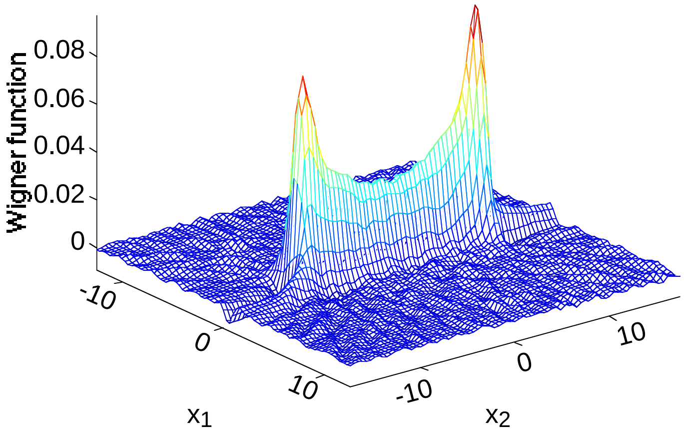

Figure G.7: The reconstructed Wigner function and contour plot by using a phase-unlocked scheme. (a) Wigner function; (b) contour plot.

Bibliography

[1] R. E. Slusher, L. W. Hollberg, B. Yurke, J. C. Mertz, and J. F. Valley, *Observation of Squeezed States Generated by Four-Wave Mixing in an Optical Cavity*, Phys. Rev. Lett. **55**, 2409 (1985).

[2] M. Born, Z. Phys. **37**, 863 (1926).

[3] V. Weisskopf and E. Wigner, Z. Phys. **63**, 54 (1930).

[4] C. Gardiner, *Quantum Noise*, Springer-Verlag, Berlin, 1 edition, 1991.

[5] V. Acosta, C. L. Cowan, and B. J. Graham, *"Essentials of Modern Physics"*, Harper and Row, Singapore, 1 edition, 1973.

[6] H. Haken, *"Laser theory", in Encyclopedia of Physics, Vol. XXV/2c, Light and Matter 1c*, Springer-Verlag, Berlin, 1 edition, 1970.

[7] H. P. Yuen, *Two-photon coherent states of the radiation field*, Phys. Rev. A **13**, 2226 (1976).

[8] D. F. Walls and G. J. Milburn, *Quantum Optics*, Springer-Verlag, Berlin, 1 edition, 1994.

[9] W. H. Louisell, *Quantum Statistical Properties of Radiation*, Wiley-Interscience, New York, 1 edition, 1973.

[10] P. Meystre and M. Sargent III, *Elements of quantum optics*, Springer-Verlag, Berlin, 2 edition, 1991.

[11] B. Yurke, *Use of cavities in squeezed state generation*, Phys. Rev. A **20**, 408 (1984).

[12] S. Reynaud, C. Fabre, E. Giacobino, and A. Heidmann, *Photon noise reduction by passive optical bistable systems*, Phys. Rev. A **40**, 1440 (1989).

[13] B. C. Buchler, 1998, Private communication.

[14] T. J. Kane and R. L. Byer, *Monolithic, unidirectional single-mode Nd:YAG ring laser*, Opt. Lett. **10**, 65 (1985).

[15] I. Freitag and H. Welling, *Investigation on amplitude and frequency noise of injection-locked diode-pumped Nd:YAG lasers*, Appl. Phys. B **58**, 537 (1994).

[16] A. E. Siegman, *Lasers*, University Science Books, California, 1 edition, 1986.

[17] M. B. Gray, 1998, Private communication.

[18] N. Uehara, *Ring mode cleaner for the initial LIGO 10 Watt laser*, Internal report, Ginzton Laboratory, Stanford University (1997).

[19] Z. Y. Ou, S. F. Pereira, and H. J. Kimble, *Realization of the Einstein-Podolsky-Rosen paradox for continuous variables in nondegenerate parametric amplification,* Appl. Phys. B **55**, 265 (1992).

[20] J. Gao, F. Cui, C. Xue, C. Xie, and K. Peng, *Generation and application of twin beams from an optical parametric oscillator including an α-cut KTP crystal,* Opt. Lett. **23**, 870 (1998).

[21] V. Pruneri, R. Koch, P. G. Kazansky, P. St. J. Russel W. A. Clarkson, and D. C. Hanna, *49 mW of cw blue light generated by first-order quasi-phase-matched frequency doubling of a diode-pumped 946-nm Nd:YAG laser,* Opt. Lett. **20**, 2375 (1995).

[22] W. R. Bosenberg, A. Drobshoff, J. I. Alexander, L. E. Myers, and R. L. Byer, *Continuous-wave singly resonant optical parametric oscillator based on periodically poled LiNbO*$_3$, Opt. Lett. **21**, 713 (1996).

[23] W. R. Bosenberg, A. Drobshoff, J. I. Alexander, L. E. Myers, and R. L. Byer, *93% pump depletion, 3.5-W continuous-wave, singly resonant optical parametric oscillator,* Opt. Lett. **21**, 1336 (1996).

[24] S. H. Youn, S.-K. Choi, P. Kumar, and R.-D. Li, *Observation of sub-Poissonian light in a travelling-wave second-harmonic generation,* Opt. Lett. **21**, 1597 (1996).

[25] K. Bergman and H. A. Haus, *Squeezing in fibers with optical pulses,* Opt. Lett. **16**, 663 (1991).

[26] S. Spälter, N. Korolkova, F. König, A. Sizmann, and G. Leuchs, *Observation of multimode quantum correlations in fiber optical solitons,* Phys. Rev. Lett. **81**, 786 (1998).

[27] S. Schmitt, J. Ficker, M. Wolff, F. König, A. Sizmann, and G. Leuchs, *Photon-number squeezed solitons from an asymmetric fiber-optic sagnac interferometer,* Phys. Rev. Lett. **81**, 2446 (1998).

[28] R. W. P. Drever, J. L. Hall, F. W. Kowalski, J. Hough, G. M. Ford, A. J. Munley, and H. Ward, *Laser phase and frequency stabilization using an optical resonator,* Appl. Phys. B **31**, 97 (1983).

[29] M. B. Gray, D. A. Shaddock, C. C. Harb, and H.-A. Bachor, *Photodetector designs for low-noise, broadband, and high power applcations,* Rev. Sci. Instrum. **69**, 3755 (1998).

[30] *Hewlett-Packard Technical Note, Application Note 150: Spectrum Analyser Basics,* 1992.

[31] R. C. Eckardt, C. D. Nabors, W. J. Kozlovsky, and R. L. Byer, *Optical parametric oscillator frequency tuning and control,* J. Opt. Soc. Am. B **8**, 646 (1991).

[32] P. D. Drummond and D. F. Walls, *Quantum theory of optical bistability. I: Nonlinear polarisability model,* J. Phys. A **13**, 725 (1980).

[33] H. Goldstein, *Classical Mechanics,* Addison-Wesley, Reading, 2 edition, 1980.

[34] S. F. Pereira, Min Xiao, H. J. Kimble, and J. L. Hall, *Generation of squeezed light by intracavity frequency doubling,* Phys. Rev. A **38**, 4931 (1988).

[35] A. Sizmann, R. J. Horowicz, G. Wagner, and G. Leuchs, *Observation of amplitude squeezing of the up-converted mode in second harmonic generation*, Opt. Commun. **80**, 138 (1990).

[36] P. Kürz, R. Paschotta, K. Fiedler, and J. Mlynek, *Bright Squeezed Light by Second-Harmonic Generation in a Monolithic Resonator*, Appl. Phys. B **55**, 216 (1992).

[37] P. Kürz, R. Paschotta, K. Fiedler, and J. Mlynek, *Squeezing by Second-Harmonic Generation in a Monolithic Resonator*, Europhys. Lett. **24**, 449 (1993).

[38] R. Paschotta, M. Collett, P. Kürz, K. Fiedler, H.-A. Bachor, and J. Mlynek, *Bright Squeezed Light from a Singly Resonant Frequency Doubler*, Phys. Rev. Lett. **72**, 3807 (1994).

[39] T. C. Ralph, M. S. Taubman, A. G. White, D. E. McClelland, and H.-A. Bachor, *Squeezed light from second-harmonic generation: experiment versus theory*, Opt. Lett. **20**, 1316 (1995).

[40] H. Tsuchida, *Generation of amplitude-squeezed light at 431 nm from a singly resonant frequency doubler*, Opt. Lett. **20**, 2240 (1995).

[41] E. S. Polzik, J. C. Carri, and H. J. Kimble, *Spectroscopy with squeezed light*, Phys. Rev. Lett. **68**, 3020 (1992).

[42] C. W. Gardiner, *Driving a quantum system with the output field from another driven quantum system*, Phys. Rev. Lett. **70**, 2269 (1993).

[43] H. J. Carmichael, *Quantum Trajectory Theory for Cascaded Open Systems*, Phys. Rev. Lett. **70**, 2273 (1993).

[44] C. W. Gardiner and M. J. Collett, *Input and output in damped quantum systems: Quantum stochastic differential equations and the master equation*, Phys. Rev. A **31**, 3761 (1985).

[45] T. C. Ralph, C. C. Harb, and H.-A. Bachor, *Intensity noise of injection-locked lasers: Quantum theory using a linearised input-output method*, Phys. Rev. A **54**, 4359 (1996).

[46] M. S. Taubman, *The quantum mechanics of electro-optic feedback, second harmonic generation, and their interaction*, PhD thesis, Physics Department, Australian National University, Canberra, Australia, 1995.

[47] H.-A. Bachor, M. B. Taubman, A. G. White T. C. Ralph, and D. E. McClelland, *Experiments with lasers and frequency doublers*, Proceedings of the Fourth International Conference on Squeezed States and Uncertainty Relations, NASA, Goddard Space Flight Center, Greenbelt, Maryland , 381 (1996).

[48] W. Koechner, *Solid-State Laser Engineering*, Springer-Verlag, Berlin, 4 edition, 1996.

[49] A. E. Siegman, *Nonlinear Optical Effects: An Optical Power Limiter*, Appl. Opt. **1**, 739 (1962).

[50] G. Stegeman, M. Shei-Bahae, E. W. Van Stryland, and G. Assanto, *Large nonlinear phase shifts in second-order nonlinear-optical processes*, Opt. Lett. **18**, 13 (1993).

[51] G. Assanto, G. I. Stegeman, M. Sheik-Bahae, and E. Van Stryland, *Coherent Interactions for All-Optical Signal Processing via Quadratic Nonlinearities,* J. Quantum. Electron. **31**, 673 (1995).

[52] Z. Y. Ou, *Observation of nonlinear phase shift in CW harmonic generation,* Opt. Commun. **124**, 430 (1996).

[53] A. G. White, J. Mlynek, and S. Schiller, *Cascaded second-order nonlinearity in an optical cavity,* Europhys. Lett. **35**, 425 (1996).

[54] P. L. Chu, B. A. Malomed, and G. D. Peng, *Nonlinear amplification in a second-harmonic-generating system,* Opt. Commun. **128**, 76 (1996).

[55] G. T. Moore and K. Koch, *Optical Parametric Oscillation with Intracavity Sum-Frequency Generation,* IEEE J. Quant. Elec. **29**, 961 (1993).

[56] E. C. Cheung, K. Koch, and G. T. Moore, *Frequency upconversion by phase-matched sum-frequency generation in an optical parametric oscillator,* Opt. Lett. **19**, 1967 (1994).

[57] K. Koch, G. T. Moore, and E. C. Cheung, *Optical parametric oscillation with intracavity difference-frequency mixing,* J. Opt. Soc. Am. B **12**, 2268 (1995).

[58] S. Schiller and R. L. Byer, *Quadruply resonant optical parametric oscillation in a monolithic total-internal-reflection resonator,* J. Opt. Soc. Am. B **10**, 1696 (1993).

[59] M. A. M. Marte, *Competing nonlinearities,* Phys. Rev. A **49**, 3166 (1994).

[60] G. T. Moore, K. Koch, and E. C. Cheung, *Optical parametric oscillation with intracavity second-harmonic generation,* Opt. Commun. **113**, 463 (1995).

[61] S. Schiller, G. Breitenbach, S. F. Pereira, R. Paschotta, A. G. White, and J. Mlynek, *"Generation of continuous-wave bright squeezed light", in laser frequency stabilization and noise reduction,* Proc. SPIE **2378**, 91 (1995).

[62] S. Schiller, G. Breitenbach, R. Paschotta, and J. Mlynek, *Subharmonic-pumped continuous-wave parametric oscillator,* Appl. Phys. Lett. **68**, 3374 (1996).

[63] A. G. White, P. K. Lam, M. S. Taubman, M. A. M. Marte, S. Schiller, D. E. McClelland, and H.-A. Bachor, *Classical and quantum signatures of competing* $\chi^(2)$ *nonlinearities,* Phys. Rev. A **55**, 4511 (1997).

[64] M. A. M. Marte, *Sub-Poissonian Twin Beams via Competing Nonlinearities,* Phys. Rev. Lett **74**, 4815 (1995).

[65] M. A. M. Marte, *Mutual influence of two* $\chi^{(2)}$*-nonlinearities and the generation of sub-Poissonian twin beams,* Acta Physica Slovaca **45**, 253 (1995).

[66] M. A. M. Marte, *Nonlinear dynamics and quantum noise for competing* $\chi^{(2)}$ *nonlinearities,* J. Opt. Soc. Am. B **12**, 2296 (1995).

[67] M. Tsunekane, S. Kimura, M. Kimura, N. Taguchi, and H. Inaba, *Continuous-wave broadband tuning from 788nm to 1640nm by a doubly resoant,* $\mathrm{MgO : LiNbO_3}$ *optical parametric oscillator,* Appl. Phys. Lett. **72**, 3414 (1998).

[68] A. G. White, *Classical and quantum dynamics of optical frequency conversion*, PhD thesis, Physics Department, Australian National University, Canberra, Australia, 1995.

[69] S. Reynaud, C. Fabre, and E. Giacobino, *Quantum fluctuations in a two-mode parametric oscillator*, J. Opt. Soc. Am. B **4**, 1520 (1987).

[70] I. Freitag, A. Tünnermann, and H. Welling, *Passively Q-switched Nd:YAG ring lasers with high average output power in single-frequency operation*, Opt. Comm. **115**, 511 (1995).

[71] D. A. Bryan, R. R. Rice, R. Gerson, H. E. Tomaschke, K. L. Sweeney, and L. E. Halliburton, *Magnesium-doped lithium niobate for higher optical power applications*, Opt. Eng. **24**, 138 (1985).

[72] W. J. Kozlovsky, C. D. Nabors, R. C. Eckardt, and R. L. Byer, *Monolithic* $\mathrm{MgO}:\mathrm{LINbO}_3$ *doubly resonant optical parametric oscillator pumped by a frequency doubled diode-laser-pumped Nd:YAG laser*, Opt. Lett. **14**, 66 (1989).

[73] R. G. Smith, J. E. Geusic, H. J. Levinstein, J. J. Rubin, S. Singh, and L. G. Uitert, Appl. Phys. Lett. **12**, 308 (1968).

[74] S. T. Yang, R. C. Eckardt, and R. L. Byer, *Power and spectral characteristics of continuous-wave parametric oscillators - the doubly to singly resonant transition*, J. Opt. Soc. Am. B **10**, 1684 (1993).

[75] G. Breitenbach, S. Schiller, and J. Mlynek, *81% conversion efficiency in frequency-stable continuous-wave parametric oscillation*, J. Opt. Am. Soc. B **12**, 2095 (1995).

[76] N. C. Wong, *Optical frequency division using an optical parametric oscillator*, Opt. Lett. **15**, 1129 (1990).

[77] J. J. Snyder, E. Giacobino, C. Fabre, A. Heidmann, and M. Ducloy, *Sub-shot-noise measurements using the beat note between quantum-correlated photon beams*, J. Opt. Soc. Am. B **7**, 2132 (1990).

[78] F. G. Colville, M. J. Padgett, and M. H. Dunn, *Continuous-wave, dual-cavity, doubly resonant, optical parametric oscillator*, Appl. Phys. Lett. **64**, 1490 (1994).

[79] A. J. Henderson, M. J. Padgett, J. Zhang, W. Sibbett, and M. H. Dunn, *Continuous frequency tuning of a cw optical parametric oscillator through tuning of its pump source*, Opt. Lett. **20**, 1029 (1995).

[80] S. Schiller et al., Novel lasers, devices and applications, topical meeting laser 97, Munich (1997).

[81] K. Schneider, S. Schiller, J. Mlynek, M. Bode, and I. Freitag, *1.1-W single-frequency 532-nm radiation by second-harmonic generation of a miniature Nd:YAG ring laser*, Opt. Lett. **21**, 1999 (1996).

[82] M. Bode, I. Freitag, A. Tünnermann, and H. Welling, *Frequency-tunable 500-mW continuous-wave all-solid-state single-frequency source in the blue spectral region*, Opt. Lett. **22**, 1220 (1997).

[83] G. Breitenbach, T. Müller, S. F. Pereira, J.-Ph. Poizat, S. Schiller, and J. Mlynek, *Squeezed vacuum from a monolithic optical parametric oscillator*, J. Opt. Am. Soc. B **12**, 2304 (1995).

[84] L.-A. Wu, H. J. Kimble, J. L. Hall, and H. Wu, *Generation of squeezed states by parametric down conversion*, Phys. Rev. Lett. **57**, 2520 (1986).

[85] L. A. Wu, M. Xiao, and H. J. Kimble, *Squeezed states of light from an optical parametric oscillator*, J. Opt. Soc. Am. B **4**, 1465 (1987).

[86] E. S. Polzik, J. Carri, and H. J. Kimble, *Atomic spectroscopy with squeezed light for sensitivity beyond the vacuum-state limit*, Appl. Phys. B **55**, 279 (1992).

[87] K. Schneider, R. Bruckmeier, H. Hansen, S. Schiller, and J. Mlynek, *Bright squeezed-light generation by a continuous-wave semimonolithic parametric amplifier*, Opt. Lett. **21**, 1396 (1996).

[88] K. Schneider, M. Lang, J. Mlynek, and S. Schiller, *Generation of strongly squeezed continuous-wave light at 1064 nm*, Opt. Ex. **2**, 59 (1997).

[89] A. Heidmann, R. J. Horowicz, S. Reynaud, E. Giacobino, C. Fabre, and G. Camy, *Observation of quantum noise reduction on twin laser beams*, Phys. Rev. Lett. **59**, 2555 (1987).

[90] J. Mertz, T. Debuisschert, A. Heidmann, C. Fabre, and E. Giacobino, *Improvements in the observed intensity correlation of optical parametric oscillator twin beams*, Opt. Lett. **16**, 1234 (1991).

[91] H. Wang, C. D. Xie, J. R. Gao, and K. C. Peng, Acta Opt. Sin. **16**, 1144 (1996).

[92] Q. Pan, Y. Zhang, T. C. Zhang, C. D. Xie, and K. C. Peng, *Experimental investigation of intensity difference squeezing using Nd:YAP laser as pump source*, J. Phys. D **30**, 1588 (1997).

[93] J. Gao, 1998, Private communication.

[94] A. G. White, 1996, Private communication.

[95] G. D. Boyd and D. A. Kleinman, *Parametric Interaction of Focussed Gaussian Light Beams*, J. Appl. Phys. **39**, 3597 (1968).

[96] I. Freitag, 1997, Private communication.

[97] Y. Yamamoto, S. Machida, S. Saito, N. Imoto, T. Tanagawa, M. Kitagawa, and G. Björk, Progress in Optics **28**, 87 (1990).

[98] H. P. Yuen, *Generation, detection, and application of high-intensity photon number eigenstate fields*, Phys. Rev. Lett. **56**, 2176 (1986).

[99] H. A. Haus and J. A. Mullen, *Quantum noise in linear amplifiers*, Phys. Rev. **128**, 2407 (1962).

[100] R. C. Dorf, *Modern control systems*, Addison-Wesley, Sydney, 5 edition, 1990.

[101] Y. Yamamoto and H. A. Haus, *Effect of electrical partition noise on squeezing in semiconductor lasers,* Phys. Rev. A **45**, 6596 (1992).

[102] M. S. Taubman, H. Wiseman, D. E. McClelland, and H.-A. Bachor, *Intensity feedback effects on quantum-limited noise,* J. Opt. Soc. Am. B **12**, 1792 (1995).

[103] C. M. Caves, *Quantum limits on noise in linear amplifiers,* Phys. Rev. D **26**, 1817 (1982).

[104] J. A. Levenson, I. Abram, T. Rivera, P. Fayolle, J. C. Garreau, and P. Grangier, *Quantum optical cloning amplifier,* Phys. Rev. Lett. **70**, 267 (1993).

[105] E. Goobar, A. Karlsson, and G. Björk, *Experimental realization of a semiconductor photon number amplifier and a quantum optcial tap,* Phys. Rev. Lett. **71**, 2002 (1993).

[106] J.-F. Roch, J.-Ph. Poizat, and P. Grangier, *Sub-shot-noise manipulation of light using semiconductor emitters and receivers,* Phys. Rev. Lett. **71**, 2006 (1993).

[107] H. M. Wiseman, M. S. Taubman, and H.-A. Bachor, *Feedback-enhanced squeezing in second harmonic generation,* Phys. Rev. A **51**, 3227 (1995).

[108] H. M. Wiseman, *Feedback in open quantum system,* Mod. Phys. Lett. **9**, 629 (1995).

[109] A. G. White, M. S. Taubman, T. C. Ralph, P. K. Lam, D. E. McClelland, and H.-A. Bachor, *Experimental test of modular noise propagation theory for quantum optics,* Phys. Rev. A **54**, 3400 (1996).

[110] H. Wang, M. J. Freeman, and D. G. Steel, *Squeezed light from injection-locked quantum well lasers,* Phys. Rev. Lett. **71**, 3951 (1993).

[111] S. Inoue, S. Machida, Y. Yamamoto, and H. Ohzu, *Squeezing in an injection-locked semiconductor laser,* Phys. Rev. A **48**, 2230 (1993).

[112] A. D. Farinas, E. K. Gustafson, and R. L. Byer, *Frequency and intensity noise in an injection-locked, solid state laser,* J. Opt. Am. Soc. B **12**, 328 (1995).

[113] C. C. Harb, T. C. Ralph, E. H. Huntington, I. Freitag, D. E. McClelland, and H.-A. Bachor, *Intensity noise properties of injection-locked lasers,* Phys. Rev. A **54**, 4370 (1996).

[114] T. C. Ralph and H.-A. Bachor, *Noiseless amplification of the coherent amplitude of bright squeezed light using a standard laser amplifier,* Opt. Commun. **122**, 94 (1995).

[115] J. A. Wheeler and W. H. Zurek, Princeton University Press, 1983.

[116] V. B. Braginsky and Yu. I. Vorontsov, Usp. Fiz. Nauk **114**, 41 (1974).

[117] V. B. Braginsky, Yu. I. Vorontsov, and F. Ya. Khalili, Sov. Phys. JETP **46**, 705 (1977).

[118] K. S. Thorne, R. W. P. Drever, C. M. Caves, M. Zimmermann, and V. D. Sandberg, *Quantum nondemolition measurements of harmonic oscillators,* Phys. Rev. Lett. **40**, 667 (1978).

[119] W. G. Unruh, *Quantum nondemolition and gravity-wave detection,* Phys. Rev. D **19**, 2888 (1979).

[120] C. M. Caves, K. S. Thorne, R. W. P. Drever, V. D. Sandberg, and M. Zimmermann, *On the measurement of a weak classical force coupled to a quantum-mechanical oscillator. I. Issues of principle*, Rev. Mod. Phys. **52**, 341 (1980).

[121] J.-Ph. Poizat and P. Grangier, *Experimental realization of a quantum optical tap*, Phys. Rev. Lett. **70**, 271 (1993).

[122] M. D. Levenson, R. M. Shelby, M. Reid, and D. F. Walls, *Quantum nondemolition detection of optical quadrature amplitudes*, Phys. Rev. Lett. **57**, 2473 (1986).

[123] A. La Porta, R. E. Slusher, and B. Yurke, *Back-action evading measurements of an optical field using parametric down conversion*, Phys. Rev. Lett. **62**, 28 (1989).

[124] P. Grangier, J.-F. Roch, and G. Roger, *Observation of backaction-evading measurement of an optical intensity in a three-level atomic nonlinear system*, Phys. Rev. Lett. **66**, 1418 (1991).

[125] S. R. Friberg, S. Machida, and Y. Yamamoto, *Quantum-nondemolition measurement of the photon number of an optical soliton*, Phys. Rev. Lett **69**, 3165 (1992).

[126] K. Bencheikh, J. A. Levenson, Ph. Grangier, and O. Lopez, *Quantum nondemolition demonstration via repeated backaction evading measurements*, Phys. Rev. Lett. **75**, 3422 (1995).

[127] J.-F. Roch, K. Vigneron, Ph. Grelu, A. Sinatra, J.-Ph. Poizat, and Ph. Grangier, *Quantum Nondemolition Measurements using Cold Trapped Atoms*, Phys. Rev. Lett. **78**, 634 (1997).

[128] R. Bruckmeier, K. Schneider, S. Schiller, and J. Mlynek, *Quantum Nondemolition Measurement Improved by a Squeezed Meter Input*, Phys. Rev. Lett. **78**, 1243 (1997).

[129] R. Bruckmeier, H. Hansen, S. Schiller, and J. Mlynek, *Realization of a paradigm for quantum measurements: The squeezed light beam splitter*, Phys. Rev. Lett. **79**, 43 (1997).

[130] J. H. Shapiro, *Optical waveguide tap with infinitesimal insertion loss*, Opt. Lett. **5**, 351 (1980).

[131] M. J. Holland, M. J. Collett, D. F. Walls, and M. D. Levenson, *Nonideal quantum nondemolition measurement*, Phys. Rev. A **42**, 2995 (1990).

[132] J.-Ph. Poizat, J.-F. Roch, and P. Grangier, *Characterization of quantum non-demolition measurement in optics*, Ann. Phys. Fr. **19**, 265 (1994).

[133] S. L. Braunstein, 1998, Private communication.

[134] A. Furusawa, J. L. Sorensen, S. L. Braunstein, C. A. Fuchs, H. J. Kimble, and E. S. Polzik, *Unconditional quantum teleportation*, Science **282**, 706 (1998).

[135] L. Davidovich, N. Zagury, M. Brune, J. M. Raimond, and S. Haroche, *Teleportation of an atomic state between two cavities using nonlocal microwave fields*, Opt. Commun. **107**, 420 (1994).

[136] T. C. Ralph, *Robust transmission and reconstruction of fragile optical state*, Phys. Rev. A **56**, 4187 (1997).

[137] C. H. Bennett, G. Brassard, C. Crépeau, R. Jozsa, A. Peres, and W. K. Wootters, *Teleporting an unknown quantum state via dual classical and Einstein-Podolsky-Rosen Channels*, Phys. Rev. Lett. **70**, 1895 (1993).

[138] A. Einstein, B. Podolsky, and N. Rosen, Phys. Rev. **47**, 777 (1935).

[139] D. Boschi, S. Branca, F. De Martini, L. Hardy, and S. Popescu, *Experimental realization of teleporting an unknown pure quantum state via dual classical and Einstein-Podolsky-Rosen channels*, Phys. Rev. Lett. **80**, 1121 (1998).

[140] D. Bouwmeester, J.-W. Pan, K. Mattle, M. Eibl, H. Weinfurter, and A. Zeilinger, *Experimental quantum teleportation*, Nature **390**, 575 (1997).

[141] L. Vaidman, *Teleportation of quantum states*, Phys. Rev. A **49** (1994).

[142] S. L. Braunstein and H. J. Kimble, *Teleportation of continuous quantum variables*, Phys. Rev. Lett. **80**, 869 (1998).

[143] Z. Y. Ou, S. F. Pereira, H. J. Kimble, and K. C. Peng, *Realization of the Einstein-Podolsky-Rosen paradox for continuous variables*, Phys. Rev. Letts. **68**, 3663 (1992).

[144] Y. Yamamoto and S. Machida, *High-impedance suppression of pump fluctuation and amplitude squeezing in semiconductor lasers*, Phys. Rev. A **35**, 5114 (1987).

[145] P. K. Lam, T. C. Ralph, E. H. Huntington, and H.-A. Bachor, *Noiseless signal amplification using positive electro-optic feedforward*, Phys. Rev. Lett. **79**, 1471 (1997).

[146] M. Kourogi, K. Nakagawa, and M. Ohtsu, *Wide-span optical frequency comb generator for accurate optical frequency difference measurement*, IEEE J. Quantum Electron. **29**, 2693 (1993).

[147] M. Kourogi, T. Enami, and M. Ohtsu, *A monolithic optical frequency comb generator*, IEEE Photon. Technol. Lett. **6**, 214 (1994).

[148] L. R. Brothers, D. Lee, and N. C. Wong, *Terahertz optical frequency comb generation and phase locking of an optical parametric oscillator at 665 GHz*, Opt. Lett. **19**, 245 (1994).

[149] J. G. Walker and E. Jakeman, *Optical dead time effects and sub-Poissonian photo-electron counting statistics*, Proceedings of Spie - the International Society for Optical Engineering **492**, 274 (1985).

[150] S. Machida and Y. Yamamoto, Opt. Commun. **57**, 290 (1986).

[151] D. A. Shaddock, 1998, Private communication.

[152] J. M. Shapiro, G. Saplakoglu, S.-T. Ho, P. Kumar, B. E. A. Saleh, and M. C. Teich, *Theory of light detection in the presence of feedback*, J. Opt. Soc. Am. B **4**, 1604 (1987).

[153] B. C. Buchler, M. B. Gray, D. A. Shaddock, T. C. Ralph, and D. E. McClelland, *Suppression of classical and quantum radiation pressure noise via electro-optic feedback*, Opt. Lett. (accepted) (1999).

[154] H. M. Wiseman, *In-loop squeezing is like real squeezing to an in-loop atom*, Phys. Rev. Lett. **81**, 3840 (1998).

[155] D. C. Gerstenberger, G. E. Tye, and R. W. Wallace, *Efficient second-harmonic conversion of cw single frequency Nd:YAG laser light by frequency locking to a monolithic ring frequency doubler*, Opt. Lett. **16**, 992 (1991).

[156] I. Freitag, A. Tünnermann, and H. Welling, *Passively Q-switched Nd:YAG ring laser with high average output power in single-frequency operation*, Opt. Lett. **22**, 706 (1997).

[157] S. Kuck, K. Petermann, and G. Huber, *Spectroscopic investigation of the* $\mathrm{Cr}^{4+}:\mathrm{YAG}$ *center in YAG*, OSA Proc. Advanced Solid State Lasers **10**, 92 (1991).

[158] S. Li, S. Zhou, P. Wang, Y. C. Chen, and K. K. Lee, *Self-Q-switched diode-end-pumped Cr,Nd:YAG laser with polarized output*, Opt. Lett. **18**, 203 (1993).

[159] E. P. Wigner, *On the quantum correction for thermodynamic equilibrium*, Phys. Rev. **40**, 749 (1932).

[160] K. Vogel and H. Risken, *Determination of quasiprobability distributions in terms of probability distributions for the rotated quadrature phase*, Phys. Rev. A **40**, 2847 (1989).

[161] D. T. Smithey, M. Beck, M. G. Raymer, and A. Faridani, *Measurement of the Wigner distribution and the density matrix of a light mode using optical homodyne tomography: Application to squeezed states and the vacuum*, Phys. Rev. Lett. **70**, 1244 (1993).

[162] M. Beck, D. T. Smithey, J. Cooper, and M. G. Raymer, *Experimental determination of number-phase uncertainty relations*, Opt. Lett. **18**, 1259 (1993).

[163] G. Breitenbach, S. Schiller, and J. Mlynek, *Measurement of the quantum states of squeezed light*, Nature **387**, 471 (1997).

[164] T. Coudreau, A. Z. Khoury, and E. Giacobino, *Quantum tomography of a laser beam interacting with cold atoms*, Laser Spectroscopy XIII international conference, World Scientific , 305 (1997).

[165] M. J. Collett and C. W. Gardiner, *Squeezing of intracavity and travelling-wave light fields produced in parametric amplification*, Phys. Rev. A **30**, 1386 (1984).

[166] H. P. Yuen and V. W. S. Chen, *Noise in homodyne and heterodyne detection*, Opt. Lett. **8**, 177 (1983).

[167] B. Schumaker, *Noise in homodyne detection*, Opt. Lett. **9**, 189 (1984).

[168] Ch. Kurtsiefer, T. Pfau, and J. Mlynek, *Measurement of the Wigner function of an ensemble of helium atoms*, Nature **386**, 150 (1997).

[169] T. Felbinger, S. Schiller, and J. Mlynek, *Oscillation and Generation of Nonclassical States in Three-Photon Down-Conversion*, Phys. Rev. Lett. **80**, 492 (1998).

[170] U. Leonhardt, *Measuring the Quantum State of Light*, Cambridge University Press, 4 edition, 1997.